USING OPTICAL TECHNIQUES TO MEASURE ALUMINUM BURNING IN POST-DETONATION EXPLOSIVE FIREBALLS

BY

JENNIFER MOTT PEUKER

DISSERTATION

Submitted in partial fulfillment of the requirements
for the degree of Doctor of Philosophy in Mechanical Engineering
in the Graduate College of the
University of Illinois at Urbana-Champaign, 2012

Urbana, Illinois

Doctoral Committee:

Professor Nick Glumac, Chair
Professor Herman Krier
Associate Professor Dimitrios Kyritsis
Associate Professor Joanna Austin

ABSTRACT

Metals are added to high explosives and propellants to increase the heat of explosion. Aluminum is commonly used because it has a high energy density, is relatively inexpensive, is easy to produce, and has a low toxicity. To optimize the performance and safety of aluminized explosives, it is necessary to understand where, when, and with what the aluminum is reacting in the explosive fireball. Efforts in aluminum combustion have focused on aluminum monoxide (AlO) emission because it is easy to measure, and it is a combustion marker in some cases; however, the first part of the current study has indicated that explosive fireballs are optically thick. Therefore, external measurements are biased toward conditions near the fireball surface. The objectives of the current study are twofold: (1) to further the understanding of aluminum combustion in an explosive fireball, specifically where, when, and with what the aluminum is reacting; and (2) to characterize AlO emission measurements from aluminized explosive fireballs in order to determine when and how AlO emission can be used as an indicator of aluminum combustion.

Experiments were completed in six different environments—air, pure O_2, pure CO_2, pure N_2, 40%/60% O_2/N_2 and 20%/80% CO_2/N_2—using four distinct aluminized charges of varying aluminum particle size—3 μm, 10 μm and 40 μm—and loading amount—20 and 50 percent by mass—to determine with what the aluminum is reacting. In addition, a charge containing 20 percent aluminum oxide (Al_2O_3) was used as an inert comparison. Contrasting results from optical—emission spectroscopy, pyrometry and high speed imaging—and non-optical techniques—recovered residue analysis and overpressure measurements—is used to challenge typical interpretations of optical measurements of aluminized explosive fireballs. The effect of the aluminum particle location with respect to the explosive material was tested by using end-loaded charges, and by placing a layer of grease on the aluminized charge

tip. Time-resolved overpressure measurements are used to determine when the aluminum is burning. Experiments employing an air-gap between the explosive charge and aluminum powder aid in determining how and when aluminum is activated and combusted in the initial blast wave and the subsequent fireball containing high pressure and high temperature detonation products.

Tests in four environments—air, pure O_2, pure CO_2, and pure N_2—show that even when AlO emission intensity is lower by 90 percent in N_2 or CO_2 than it is in air for a charge, it is possible to have significant—60 to 70 percent—aluminum particle oxidation. In addition, substantial AlO emission was measured in the absence of unburned aluminum—almost half of the peak AlO emission measured when unburned aluminum was present. Results show that AlO emission intensity measurements are skewed to higher AlO intensities by high transient temperatures within the first 30 μs when the peak AlO emission is usually measured. The aluminum particle location also affects the amount of AlO emission measured such that when more particles are on the fireball surface, then more AlO emission is measured. However, the end-loaded aluminum does not add to the energy output enhancement as much as the pre-loaded aluminum charges since the peak pressures and initial impulse are similar for different amounts of aluminum. A grease layer on the tip of the charge reduces the amount of AlO emission measured by 90 percent, but has the same energy output in the initial blast wave as the same charge not having a grease layer, indicating that the material at the tip of a charge changes the breakout and subsequent AlO emission production.

In addition, the overpressure measurements indicate that four distinct stages of aluminum combustion exist. The first stage is the detonation and the activation of the aluminum. In the second stage the aluminum burns to enhance the blast wave which is indicated by higher peak pressures and initial impulses than a charge not containing aluminum. During the third stage, the aluminum continues to burn to increase the overpressure of the chamber. The fireball cools during the fourth stage and any aluminum oxidation does not add to the energy release.

The variations in how much AlO emission is measured indicate that interpreting AlO emission measurements from explosive fireballs is not straightforward with respect to correctly determining the amount of aluminum combusted, how long the aluminum reacted, or

the energy released. If aluminum is available to burn and AlO emission is measured, then the aluminum is burning—even taking into account AlO emission from the oxide layer. However, when no AlO emission is measured, it does not necessarily mean that the aluminum is not burning. When AlO emission is measured it indicates that the temperatures are high enough to sustain aluminum combustion which produces AlO, and that oxidizers are present which react to produce the AlO emission. The relative intensities for the same time frame of AlO emission measured could be indicators about the temperature or number of reactions occurring.

AlO emission measured from explosive fireballs is a result of both anaerobic and aerobic reactions, and both types of reactions contribute to the aluminum combustion enhancement of the explosive charge. The aluminum combustion adds to the blast wave enhancement and the aluminum also burns to increase the overpressure of the chamber.

To my family, for their unconditional love and support

ACKNOWLEDGMENTS

This study was funded by the Defense Threat Reduction Agency under HDTRA1-07-1-0011. Dr. Suhithi Peiris is the program manager. The work was carried out in several combustion laboratories in the Mechanical Engineering Laboratory building that were developed by Professors Nick Glumac and Herman Krier. Material properties were determined in the Frederick Seitz Materials Research Laboratory Central Facilities, University of Illinois, which are partially supported by the U.S. Department of Energy under grants DE-FG02-07ER46453 and DE-FG02-07ER46471.

I want to thank my advisor, Professor Nick G. Glumac, for his support throughout my PhD studies. I especially appreciate his guidance and his training in order to carry out the measurements in the laboratory. Special gratitude goes toward my co-advisor Professor Herman Krier for his thought provoking discussions and his supervision of many of the experiments.

In addition, I want to thank the members of my dissertation committee—Professor Dimitrios C. Kyritsis and Professor Joanna Austin—for their suggestions, comments and recommendations. Special thanks goes to fellow graduate students in my research group—Lance Kingston, Patrick Lynch, Andrew Coverdill, John Rudolphi, Jeff Mason, David Chonowski and Michael Clemenson—for their assistance in and out of the lab, and to the undergraduates who have helped with the experiments—Chris Kvistad, Mark Janowski, and David Joyce.

Last, but not least, I want to thank my family and friends, especially my parents and my husband, Steffen, for their love and encouragement to keep going even when it gets tough.

TABLE OF CONTENTS

LIST OF TABLES ix

LIST OF FIGURES xi

CHAPTER 1 RESEARCH MOTIVATION AND BACKGROUND 1
1.1 Aluminum Combustion in Explosives 1
1.2 Aluminum Combustion Theory 3
1.3 Optical Measurements 8
1.4 Optical Measurement Limitations 10
1.5 Study Objectives 11

CHAPTER 2 REVIEW OF PREVIOUS WORK AND PLAN OF STUDY 12
2.1 Review of Previous Work 12
2.2 Plan of Study 23

CHAPTER 3 OPTICAL DEPTH OF ALUMINIZED FIREBALLS 26
3.1 Light Transmission through Media 26
3.2 Optical Depth Measurement Techniques 27
3.3 Results and Analysis 33
3.4 Optical Measurement Implications 41

CHAPTER 4 EXPERIMENTAL METHODS TO EVALUATE ALUMINUM COMBUSTION IN EXPLOSIVE FIREBALLS 42
4.1 Charge Descriptions 42
4.2 Diagnostics 45
4.3 Test Chambers Descriptions 54
4.4 Test Descriptions 57

CHAPTER 5 RESULTS FROM ALUMINUM COMBUSTION IN EXPLOSIVE FIREBALLS EXPERIMENTS 65
5.1 Energy Release Measurements 65
5.2 AlO Emission and Al Particle Oxidation 67
5.3 Effect of Fireball Confinement 77
5.4 Effect of Temperature 81
5.5 Effect of Hot Al_2O_3 94

5.6 Effect of Al Particle Location 95
5.7 Effect of Al Particle Size and Ambient Environment 109
5.8 High Speed Camera Visualization of the Fireball and Shock Wave Velocity Measurements 132

CHAPTER 6 ANALYSIS OF ALUMINUM BURNING IN AN EXPLOSIVE FIREBALL AND INTERPRETATION OF ALO EMISSION MEASUREMENTS . . . 150
6.1 Understanding Aluminum Burning in an Explosive Fireball 151
6.2 Influences to AlO Emission Measurement and Its Interpretation 168

CHAPTER 7 CONCLUSIONS AND RECOMMENDATIONS 205
7.1 Summary and Conclusions 205
7.2 Recommendations for Future Work 212

APPENDIX A EXPERIMENTAL PROCEDURES AND EQUIPMENT 216
A.1 Standard Operating Procedures 216
A.2 Equipment Settings 229
A.3 Setup Pictures 231

APPENDIX B EXPERIMENTAL EQUIPMENT 238
B.1 Equipment Technical Data 238
B.2 Pressure Ratio Analysis 239
B.3 Technical Drawings 243

APPENDIX C CALCULATIONS METHODOLOGY AND DETAILS 248
C.1 Effect of Temperature on AlO B State Population 248
C.2 Taylor Similarity Solution to Blast Equations 250
C.3 Explosive Energy Calculations 251
C.4 Comparison of Energy Calculations 252

REFERENCES 255

LIST OF TABLES

1.1 Properties of RDX and PETN. 3
1.2 Balanced reaction formula for RDX and PETN. 3
1.3 Aluminum combustion reactions. 6
1.4 Aluminum combustion gas-phase reaction rates. 8
1.5 AlO $B^2\Sigma^+ \rightarrow X^2\Sigma^+$ emission bands and intensity strength. 9

2.1 List of explosive mixtures referenced in the text. 13

3.1 Delay and exposure times for images taken using the High Speed Framing Cameras. 31
3.2 Attenuation length for each delay time and associated uncertainties. 40

4.1 Charges used in the study. 44
4.2 Mass measurements for heated aluminum particles. 51
4.3 Typical size, frames per second and frame interval used for high speed camera images. 54
4.4 Summary of tests completed in the tube chamber. 59
4.5 Tests completed for the weakly confined fireball comparison and test designations. 60
4.6 Tests completed for the Al_2O_3-, Al-, Al+grease-loaded charge tests and designations. 61
4.7 Tests completed for end-loaded and environments tests in the blast chamber and designations. 62
4.8 Tests completed for the gap tests and designations. 64

5.1 Aluminum particle percent oxidation and standard deviation (std dev.) determined from SEM/EDS analysis. 72
5.2 Results from Gordon-McBride equilibrium calculations of the aluminized RP80s. 75
5.3 Results from Gordon-McBride equilibrium calculations of the 20 percent Al RP80s, different environments. 77
5.4 Results from Gordon-McBride equilibrium calculations of the 50 percent Al RP80s, different environments. 77
5.5 Average temperatures for blast chamber experiements. 83
5.6 Initial blast wave impulse and peak pressures for the end-loaded charges. . . 102

5.7 Specific heat ratio and speed of sound for different ambient environments, at 20°C, assuming ideal gas. . . . 117

6.1 Comparison of blast driving energy release between the types of charges. . . 158
6.2 Comparison of peak pressures and initial blast wave impluses of 20 and 50 percent loading. . . . 158
6.3 Summary of combustion stages. . . . 166
6.4 Fiber probe AlO measurements for the 20%-3-μm-Al charge. . . . 180
6.5 Fiber probe AlO measurements for the 20%-40-μm-Al charge. . . . 180
6.6 Comparison of external AlO emission measurements to inside fireball measurements. . . . 181
6.7 List of tests completed to investigate the effect of the grease layer. . . . 192

A.1 Pulse Generator—Tube Chamber. . . . 229
A.2 FK Andor CCD Detector—Tube Chamber. . . . 229
A.3 Pulse Generator—Blast Chamber. . . . 230
A.4 FK Andor CCD Detector—Blast Chamber. . . . 230
A.5 Picoscope for pressure transducers. . . . 230
A.6 DC Amplifier for peizoresistive pressure transducers. . . . 231
A.7 Calibration equations for peizoresistive pressure transducers. . . . 231
A.8 Picoscope for pryometer. . . . 231

B.1 Spectrometer. . . . 238
B.2 Shadowgraph and High Speed Camera. . . . 238
B.3 Pyrometer. . . . 239
B.4 Pressure Transducers. . . . 239
B.5 Other Equipment. . . . 239

C.1 Comparison of methods to calculate explosive energy and tabulated values for pure RDX and PETN. . . . 253
C.2 Comparison of the Taylor blast solution. . . . 254

LIST OF FIGURES

1.1 Image of an aluminized explosive fireball. 4
1.2 AlO emission bands in instrument range—440–550 nm. 10
1.3 Schematic of emitted light observed from one side of a fireball. 11

3.1 Beam splitter test schematic. 29
3.2 Schematic of HSFC test setup. 30
3.3 Dot matrix setup. 31
3.4 Absorbance of laser beam as measured by the photo diodes and high speed camera images. 33
3.5 Transmission of the laser line through fireball at seven different times. 36
3.6 Transmission of the laser line for all delay times as a function of position from the initial charge surface. 37
3.7 Transmission of dot matrix beams through the fireball. 38
3.8 Absorbance within fireball as a function of the estimated path length through the fireball. 39

4.1 Schematic of original RP80 detonator. 43
4.2 Schematic of charges used. 45
4.3 Custom built spectrometer and CCD detector. 46
4.4 Pyrometer schematic. 48
4.5 Comparison of pressure traces from the two pressure transducers. 49
4.6 Fits to determine peak pressure. 50
4.7 Aluminum particle oxidation as a function of measured oxygen using the SEM/EDS. 52
4.8 Schematic of shadowgraph. 53
4.9 Tube chamber experiment setup. 55
4.10 Schematic of spectroscopy measurements for tube chamber. 56
4.11 Pressure vessel used as the blast chamber. 57
4.12 Spectroscopy and pyrometry setup schematic for the blast chamber. 57
4.13 Schematic of air gap experiment charge and Al (or SiO_2) pellet setup. 63
4.14 Examples of aluminum pellet suspended on 2.5-μm thick Mylar attached to a steel shim. 64

5.1 Comparison of the positive impulse from the initial blast wave from charges in air. 66

5.2 AlO emission intensities from the confined fireball tests for each aluminized charge in four environments. 68
5.3 20%-3-μm-Al charge in air repeated tests in the tube chamber. 69
5.4 20%-3-μm-Al charge in O_2 repeated tests in the tube chamber. 69
5.5 20%-40-μm-Al charge in air repeated tests in the tube chamber. 70
5.6 20%-40-μm-Al charge in O_2 repeated tests in the tube chamber. 70
5.7 50%-3-μm-Al charge in air repeated tests. 71
5.8 50%-3-μm-Al charge in O_2 repeated tests. 71
5.9 The residue percent oxidation from SEM/X-ray analysis is within the standard deviation—based on the average measured oxidation of 20 particles from individual tests (each data point)—for different charges in the same environment. 73
5.10 AlO Intensities from three tests using 50%-3-μm-Al charges. 78
5.11 The normalized AlO emission intensities from both experiment setups for each aluminized charge show different histories, which can affect measurement interpretation. The time resolutions for the confined (triangles) and unconfined (squares) setups are 2 μs, and 16 μs, respectively. 80
5.12 Schematic showing the difference in optical collection for the confined and unconfined setups, FB: fireball. 81
5.13 Comparison of temperatures from all charges. 83
5.14 Condensed phase temperature measurements from tube chamber tests for each aluminized charge in each environment (temperatures determined from spectrometer measurements). 85
5.15 Condensed phase temperatures each charge tests in air (temperatures determined from spectrometer measurements). 86
5.16 Condensed phase temperatures each charge tests in O_2 (temperatures determined from spectrometer measurements). 86
5.17 Condensed phase temperatures each charge tests in CO_2 (temperatures determined from spectrometer measurements). 87
5.18 Condensed phase temperatures each charge tests in N_2 (temperatures determined from spectrometer measurements). 87
5.19 Condensed phase temperatures from two measurement techniques compared to normalized AlO emission for each aluminized charge. 89
5.20 Comparision of temperatures to the AlO intensity for 20%-3-μm Al charge tests in each environment. 91
5.21 Comparision of temperatures to the AlO intensity for 20%-40-μm Al charge in air, (temperatures determined from spectrometer measurements). 92
5.22 Comparision of temperatures to the AlO intensity for 20%-40-μm Al charge in O_2, (temperatures determined from spectrometer measurements). 92
5.23 Comparision of temperatures to the AlO intensity for 50%-3-μm Al charge in air, (temperatures determined from spectrometer measurements). 93
5.24 Comparision of temperatures to the AlO intensity for 50%-3-μm Al charge in O_2, (temperatures determined from spectrometer measurements). 93

5.25 Average integrated AlO values at peak AlO emission, one 16 μs exposure frame, for each type of charge. 95
5.26 Average initial blast wave impulse for Al- and Al_2O_3-loaded charges. 96
5.27 Initial blast wave positive impulse for Al-loaded charges with and without a grease layer. 97
5.28 Normalized AlO emission signal for Al-loaded charges with and without a grease layer. 97
5.29 When the Al burns on the outer surface of the fireball, the AlO emission intensity is greater than when most of the Al burns inside the fireball. 98
5.30 End-loaded test results from the tube chamber using different ambient environments. 99
5.31 End-loaded bare charge in O_2 repeated tests. 100
5.32 Residue oxidation for the end-loaded tests in the tube chamber. 101
5.33 Blast chamber tests' AlO emission for end-loaded charges. 101
5.34 Impulse as a function of time for the end loaded charges. 103
5.35 Initial blast wave impulse comparison for gap tests—Al in air and N_2, and SiO_2 in air. 104
5.36 Net enhancement from the Al pellets—Al pellet impulse minus SiO_2 pellet impulse. 106
5.37 AlO emission from experiments in air. 106
5.38 AlO emission from experiments in N_2. 106
5.39 Total time integrated AlO emission as a function of gap distance. 107
5.40 Total AlO emission as a function of the initial blast wave impulse difference—Al minus SiO_2. 108
5.41 Temperature from gap tests in air. 109
5.42 Pressure trace analysis. 110
5.43 Peak pressures for 20 percent aluminized charges in four environments. . . . 112
5.44 Initial blast wave impulse for 20 percent aluminized charges in four environments. 114
5.45 Time of arrival of the pressure wave for 20 percent aluminized charges in four environments. 117
5.46 Aerobic vs. anaerobic components from the 20 percent aluminized charges at 21.3 cm from the blast site; comparison for $t < 5$ ms. 120
5.47 Aerobic vs. anaerobic components from the 20 percent aluminized charges at 32.1 cm from the blast site; comparison for $t < 5$ ms. 121
5.48 The aerobic fraction of the total impulse, i.e., $\text{Impulse}_{\text{air}-\text{N}_2}/\text{Impulse}_{\text{air}}$ at 32.1 cm from the blast site. 122
5.49 Impulses in air, N_2, and aerobic (air-N_2) component plotted to show aluminum particle size comparisons, at 21.3 cm from the blast site. 123
5.50 Impulses in air, N_2, and aerobic (air-N_2) component plotted to show aluminum particle size comparisons, at 32.1 cm from the blast site. 124
5.51 Impulse vs. time for 20 percent aluminized charges in four environments,at 21.3 cm from the blast site. 126

5.52 Impulse vs. time for 20 percent aluminized charges in four environments, at 32.1 cm from the blast site. . . . 127
5.53 Impulse vs. time for 20 percent aluminized charges in four environments. . . 128
5.54 AlO for 20 percent aluminized charges in four environments. . . . 129
5.55 Schematic of AlO emission collection. . . . 130
5.56 Temperature for 20 percent aluminized charges in four environments, (temperatures measured using the pyrometer). . . . 131
5.57 Images from 0514-bare-air test. . . . 133
5.58 Images from the 0506-alumina-air test. . . . 133
5.59 Images from 20%-3-μm-Al loaded charge tested in air. . . . 134
5.60 Images from 20%-10-μm-Al loaded charge tested in air. . . . 135
5.61 Images from 20%-40μm-Al loaded charge tested in air. . . . 136
5.62 Shock wave velocities for bare and aluminized charges in air. . . . 137
5.63 Images from 50%-3μm-Al loaded charge tested in air. . . . 138
5.64 Shock wave velocity for the 50%-3-μm-Al tests in air. . . . 138
5.65 Images from 20%-3-μm-Al loaded charge tested in O_2. . . . 139
5.66 Images from 20%-3-μm-Al loaded charge tested in N_2. . . . 140
5.67 Images from 20%-3-μm-Al loaded charge tested in CO_2. . . . 140
5.68 Shock wave velocity for the 20%-3-μm-Al loaded charge by environment. . . 141
5.69 Images from the end-loaded charge having 8.3 mg aluminum. . . . 142
5.70 Images from the end-loaded charge having 17.6 mg aluminum. . . . 143
5.71 Images from a 20%-3-μm-Al charge with a layer of grease on the tip. . . . 144
5.72 Images from the 0.021 inch gap and SiO_2 pellet test. . . . 145
5.73 Images from the 0.020 in gap, aluminum pellet tested in air. . . . 146
5.74 Images from the 0.028 in gap, aluminum pellet tested in air. . . . 146
5.75 Images from the 0.059 in gap, aluminum pellet tested in air. . . . 147
5.76 Images from the 0.141 in gap, aluminum pellet tested in air. . . . 147
5.77 Images from the 0.245 in gap, aluminum pellet tested in air. . . . 148
5.78 Images from the 0.562 in gap, aluminum pellet tested in air. . . . 148
5.79 Shock wave velocity for the gap test in air using an aluminum pellet. . . . 149

6.1 Ideal pressure traces for blast driving based on the Taylor blast similarity solution. . . . 157
6.2 Quasi-static Pressure (QSP) for 15 runs. . . . 160
6.3 QSP scaled to the bare charge in 40% O_2. . . . 161
6.4 Impulses for the energy released in an ideal stirring reactor in three different time frames for 20% aluminum additive and impulse curve from experiemental data. . . . 164
6.5 Schematic of combustion stages. . . . 167
6.6 Progression of fireball size with respect to time and compared to relative size of optical collection volume. . . . 173
6.7 Percent collection volume of total fireball volume captured, assuming no optical depth effects, and compared to typical time of AlO emission measurements. . . . 175

6.8 Particle density in fireball of each aluminized charge, assuming uniform distribution of Al particles. . . . 176
6.9 Particle density in fireball of 3 μm aluminized charges, assuming uniform distribution of Al particles, and end-loaded charges, assuming particles on leading surface of fireball. . . . 177
6.10 Based on measured attenuation length from the optical depth study, the shaded portion of the fireball shown is the approximate portion of the fireball that is less than one attenuation length from the fireball edge. . . . 178
6.11 Fireball dimensions and attenuation lengths at 10 μs, 20 μs and 45 μs. . . . 179
6.12 Fireball fraction not within one attenuation length of the leading fireball edge and compared to typical peak AlO time. . . . 179
6.13 Particle density in each test chamber. . . . 183
6.14 Comparision of optical collection volume fractions of the tube chamber and the blast chamber. . . . 184
6.15 AlO emission measurements from tube confinement experiments. . . . 186
6.16 Comparison of the late-time impulse for the end-loaded and 20 percent pre-loaded charges. . . . 188
6.17 Long term impulse from the Al pellets in air compared to the average impluse of the SiO_2 pellets. . . . 189
6.18 Long term inpulse from the Al pellets in N_2, and the average impluse of the SiO_2 pellets in air. . . . 189
6.19 Schematic of holder for the Mylar and glass strips used to test the effect of a grease layer on the charge tip. . . . 192
6.20 AlO emission from 20%-3-μm-Al charges—charge only, Mylar layer touching the charge tip, and Mylar layer offset 2 mm from the charge tip. . . . 193
6.21 AlO emission from 20%-10-μm-Al charges—charge only, Mylar layer touching the charge, and a glass layer touching the charge tip. . . . 194
6.22 Temperaure behind an ideal shock wave from a bare charge. . . . 197
6.23 The adiabatic combustion temperature for a bare charge and a 20 percent aluminum charge in air. . . . 198
6.24 Based on bare case and ideal blast equations, progression of pressure and shock radius as a function of time. The normalized AlO is typical for 20%3-μm-Al charge. . . . 200
6.25 Ideal blast pressure and AlO emission from the 50%-Al and 20%40-μm-Al charges in addition to the 20%3-μm charge. . . . 201

A.1 Collection and focusing optics for the tube chamber tests. . . . 232
A.2 Chuck mount for the tube chamber tests. . . . 232
A.3 Interior of the blast chamber—detonator mount, side-on piezoelectric pressure transducer and retroreflective screen. . . . 233
A.4 Charge mount blocks. . . . 234
A.5 Charge mount brass containments. . . . 234
A.6 Focusing optics from fiber optic to spectrometer slit. . . . 235
A.7 Fiber optic at tank top for the pyrometer and spectrometer. . . . 235

A.8 Schematic and picture of old pyrometer. 236
A.9 Optics for newer version of the pyrometer. 236
A.10 Front and side views of mounted piezoresistive pressure transducers. 237

B.1 Pressure ratio for all experiments as a function of day of test. 240
B.2 Pressure ratio for environment experiments as a function of ambient atmosphere and Al particle size. 241
B.3 Pressure ratio for gap experiments a function of the gap distance between the charge and the pellet. 242
B.4 Brass piece used to hold charge in block. 243
B.5 Top plate used with the first block for mounting in the blast chamber. 244
B.6 Cylindrical mount for knife edge and piezo-resistive pressure transducer. . . . 245
B.7 Knife edge flat plate for piezo-resistive pressure transducer mount. 246
B.8 Plastic mount for piezo-resistive pressure transducer. 247

C.1 Comparison of pressure traces for different energy determinations. 254

CHAPTER 1

RESEARCH MOTIVATION AND BACKGROUND

This experimental research focuses on understanding the nature of emission from the aluminum sub-oxide AlO in an explosive environment in order to evaluate the use of AlO as an indicator of the aluminum combustion events. As an introduction to the study, the first chapter introduces key background and theory necessary for understanding the motivation of the work, and its results and conclusions. Aluminum combustion in explosives and basic aluminum combustion theory are briefly described, while a more extensive discussion of aluminum combustion can be found in Section 2.1. Optical measurement techniques are described, including details on AlO emission theory, and the limitations of optical measurements. The study's objectives are summarized in Section 1.5.

1.1 Aluminum Combustion in Explosives

Metals are common additives to energetic applications to increase the heat of explosion. This method is generally used in the defense and aerospace industries to increase the energy release of high explosives and propellants. Aluminum powder is commonly used because it has a high energy density, is relatively inexpensive, easy to produce, and has a low toxicity[1].

The combustion of aluminum has been studied extensively in the past half century, and though combustion can be predicted in some circumstances, many unknowns remain regarding the chemistry and physics of aluminum burning in an explosive fireball. It is important to understand the details of aluminum burning in an explosive fireball so blast designs can be optimized and tailored to specific applications, such as improving munitions, explosives for

mining, and building destruction. There are many variables involved in modeling the explosive fireball including composition, mass and geometry of the charge, the amount of particle loading, particle placement, diameter, size distribution and chemical makeup of the particles. Most models are still inadequate with respect to the chemistry of metal combustion.

Recently, there has been evidence that aluminum combustion behind a detonation is much more rapid than in quiescent burning. Aluminum particle combustion using shock tubes has shown that the constant temperature/pressure burn time of 10 μm diameter particles is on the order of milliseconds[2], but in a detonation using aluminized explosives, the time frame is much shorter, on the order of tens of microseconds[3]. The aluminum burn time scales with pressure—which approaches several hundred kilobars—and shorter burn times are expected. If this prompt reaction can be exploited, the energetic nature of metals can be better implemented, enhancing performance by ensuring that the energy released from the metal additive is on the same time scale as the detonation, and enhancing safety by being able to predict when the energy will be released. Indeed, there is evidence that it is possible for the aluminum to react in the detonation wave, contributing to the early volume expansions, and increasing the detonation velocity[4, 5]. In general, it is understood that the aluminum burns with the detonation products (anaerobic reactions) and with the ambient atmosphere (aerobic reactions) behind the shock wave; however details of the physical and chemical mechanisms remain unknown.

The charges used in this research contain cyclotrimethylenetrinitramine, also known as Hexogen, Cyclonite, or RDX—$C_3H_6N_6O_6$—in a mixture called PBX-9407. PBX-9407 is made up of 94 percent RDX and 6 percent binder (Exon 461) by weight[6]. The RDX is initiated by pentaerythritol tetranitrate or PETN—$C_5H_8N_4O_{12}$. A bridge wire in the charge initiates the PETN. The resulting detonation wave then ignites the PBX-9407 (RDX) and the aluminum particles. The detonation velocity of the PBX-9407 is 8.1 mm/μs (8100 m/s) at an explosive density of 1.6 g/cm^3[6], and the Chapman-Jouguet (CJ) detontation pressure is 275 kbar at an explosive density of 1.63 g/cm^3[7]. At the speed of the detonation wave

and size of the RP80, the detonation wave travels through the charge in less than 1.2 μs, at which point the wave transitions to traveling through the atmosphere. The properties of RDX and PETN are listed in Table 1.1. The exact charges used in this study are described in Chapter 4.

Table 1.1: Properties of RDX and PETN, adapted from Akhavan[1].

Characteristics	RDX	PETN
Chemical Formula	$C_3H_6N_6O_6$	$C_5H_8N_4O_{12}$
Molecular Weight	222.1	316.1
Melting Temperature (°C)	202–204	141.3
Thermal Ignition Temperature (°C)	260	202
Energy of Formation (kJ/kg)	+417	-1509
Enthalpy of Formation (kJ/kg)	+318	-1683
Oxygen Balance (% weight)	-21.60	-10.16

PETN, RDX and PBX-9407 have negative oxygen balances. A negative oxygen balance indicates that the amount of oxygen present in the explosive material is not enough for complete oxidation. The balanced reactions for RDX and PETN are listed in Table 1.2. Adding aluminum to the explosive mixtures decreases the oxygen balance, i.e. makes it more negative. The amount of oxygen available in the explosive and the resulting detonation products influences the amount of aluminum combustion.

Table 1.2: Balanced reaction formula for RDX and PETN[1].

Explosive Substance	Balanced reaction formula for complete combustion
PETN	$C_5H_4N_4O_{12} \rightarrow 5CO_2 + 4H_2O + 2N_2 - 2O$
RDX	$C_3H_6N_6O_6 \rightarrow 3CO_2 + 3H_2O + 3N_2 - 3O$

1.2 Aluminum Combustion Theory

Experimental quantification of the reaction of aluminum will further the understanding of aluminum combustion in explosive fireballs, such as the one shown in Figure 1.1. Of interest is the ignition/combustion time as a function of aluminum particle diameter, oxidation

environment, temperature, and pressure. The energy release rate of the aluminum particles depends on when they ignite and how fast they burn. Explosives currently use large aluminum particles, but research is moving toward smaller particles because of decreased ignition delays[8, 9], and particles 1–10 μm in diameter burn more rapidly and have a more complete combustion[10], thus exploiting as much stored chemical energy as possible.

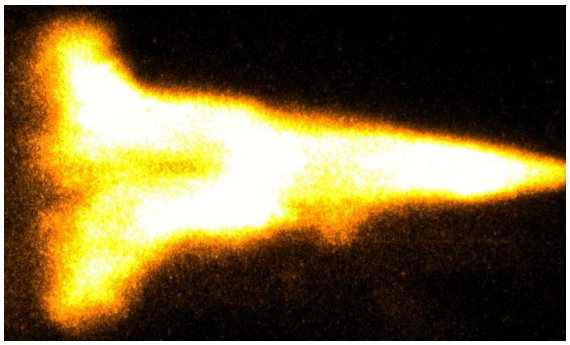

Figure 1.1: Image of an aluminized explosive fireball. False color added.

The oxidation of aluminum to form alumina (Al_2O_3) follows the global reaction of

$$2Al_{(s)} + 1\frac{1}{2}O_{2(g)} \rightarrow Al_2O_3 \tag{1.1}$$

and is exothermic producing -1590 kJ[1]. Aluminum particles have a thin ($\sim$3 nm) oxide shell[11] which must be penetrated before the aluminum vapor can react. When the oxide layer melts ($T_{melting} \sim 2330$ K), the aluminum is already molten since its melting temperature is 933 K.

The study of quiescent combustion of aluminum particles—of the order of 100 μm—has generally led to burn time correlations for a diffusion limited theory setting the burn time proportional to a power of the initial diameter—$t_b \sim d^n$ where $n \simeq 2$. [12, 13] While theory states the burning rate is independent of temperature and pressure, studies have shown that aluminum combustion burn time depends on pressure, and the burn time diameter exponent is between 1 and 2[14–17]. Ample evidence also exists that for particles less than 20 μm there is a deviation from diffusion limited toward kinetic limited combustion[2, 18, 19]. In

addition, a detonation wave interacting with the aluminum particles will change the physical properties and influence aluminum particle ignition and reaction.

While little information is available regarding the exact initiation mechanism of aluminum particles in an explosive, it is known that aluminum reacts not only with the oxygen in the explosive formulations (and environment if available), but also with detonation products—CO_2, H_2O, CO, NO, NO_2, N_2—most commonly with CO_2 and H_2O. The global reactions producing alumina from aluminum reactions with the detonation products are[1]:

$$3CO_{2(s)} + 2Al_{(s)} \rightarrow 3CO_{(g)} + Al_2O_{3(s)} \quad \Delta H_c = -741\ kJ \tag{1.2}$$

$$3H_2O_{(s)} + 2Al_{(s)} \rightarrow 3H_{2(g)} + Al_2O_{3(s)} \quad \Delta H_c = -866\ kJ \tag{1.3}$$

$$3CO_{(g)} + 2Al_{(s)} \rightarrow 3C_{(s)} + Al_2O_{3(s)} \quad \Delta H_c = -1290\ kJ \tag{1.4}$$

Aluminum can also react with nitrogen, especially in a depleted oxidizer environment, creating AlN and is an exothermic reaction.

$$2Al + N_2 \rightarrow 2AlN \quad \Delta H_c = -318\ kJ \tag{1.5}$$

Aluminum also reacts with nitrogen-oxide in fuel lean locations:

$$2Al + 3N_2O \rightarrow Al_2O_3 + 3N_2 \quad \Delta H_c = -1866\ kJ \tag{1.6}$$

All of the aluminum oxidation reactions are exothermic and contribute to the energy release of the explosive. The location of the aluminum particles influences which reactions take place. Inside the fireball, available oxidizers are detonation products only, but on the surface of the fireball, oxidizers in the environment is also available to react with the aluminum. Therefore, the detonation product reactions with the aluminum are important to the overall aluminum combustion and energy release.

1.2.1 Kinetic Pathways

The kinetic pathways for aluminum reactions in air are well documented, and the Al + O_2 reactions have been studied extensively[20, 21]. The reaction mechanisms for reactions with CO_2 and H_2O are not as thoroughly investigated, and many modelers assume similar pathways as in air. The aluminum combustion reactions, adapted from Beakstead et al.[20], are listed in Table 1.3. The (liq) and (g) refer to the liquid and gas phases, respectively. Reaction 1 is the surface reaction which generates gaseous Al. Reaction 2 is also at the droplet surface and occurs when AlO diffuses back to the surface. Reactions 3–7 are gas-phase reactions involving the oxidizers. Reaction 8 is the alumina dissociation reaction and controls the temperature. The alumina is formed from suboxides in reactions R9–R15.

Table 1.3: Aluminum combustion reactions, adapted from Beakstead et al.[20]. Note: not all of the reactions listed are fundamental reactions.

Surface reactions:	
R1	$Al(liq) \rightarrow Al(g)$
R2	$Al(liq) + AlO(g) \rightarrow Al_2O(g)$
Gas-phase reactions:	
R3	$Al(g) + O_2 \rightarrow AlO + O$
R4	$AlO + O_2 \rightarrow AlO_2 + O$
R5	$Al + CO_2 \rightarrow AlO + CO$
R6	$Al + H_2O \rightarrow AlO + H_2$
R7	$O + O + M \leftrightarrow O_2 + M$
Dissociation reaction:	
R8	$Al_2O_3(liq) \rightarrow 2AlO + \frac{1}{2}O_2$
Condensation reactions:	
R9	$2AlO + \frac{1}{2}O_2 \rightarrow Al_2O_3(liq)$
R10	$2AlO + CO_2 \rightarrow Al_2O_3(liq) + CO$
R11	$2AlO + H_2O \rightarrow Al_2O_3(liq) + H_2$
R12	$Al_2O + O_2 \rightarrow Al_2O_3(liq)$
R13	$Al_2O + 2CO_2 \rightarrow Al_2O_3(liq) + 2CO$
R14	$Al_2O + 2H_2O \rightarrow Al_2O_3(liq) + 2H_2$
R15	$AlO_2 + AlO_2 \rightarrow Al_2O_3(liq) + \frac{1}{2}O_2$

The condensation steps are Reactions 9–15. Beckstead et al.[20] proposed a 2-step condensation process. The first step yields gaseous aluminum oxide (R9–R15), and the second step is the condensation of gaseous Al_2O_3 to a liquid. While gaseous Al_2O_3 has not been ob-

served experimentally, Beckstead et al. assumes that the rate of condensation is much faster than the kinetic step—Al_2O_3(g) is an intermediate with a very short life. Bucher[21] proposed a 21-step mechanism for aluminum combustion with O_2, and includes reactions with the suboxide Al_2O_2. Zhang et al.[22] suggests that the aluminum-particle-air detonation mechanism model should also include the following irreversible aluminum reactions.

$$Al + \frac{3}{4}O_2 \rightarrow \frac{1}{2}Al_2O_3 \quad \Delta H_c = -838\ kJ \tag{1.7}$$

$$Al + \frac{1}{2}O_2 \rightarrow AlO \quad \Delta H_c = 91\ kJ \tag{1.8}$$

1.2.2 Thermochemistry

Little information is available in literature about the rates of the reaction steps listed in Table 1.3, in which only a few sources exist on the reactions of aluminum with oxygen, carbon dioxide and water vapor. The kinetic rate information available was compiled by Beckstead[20] for the purpose of modeling single aluminum particle combustion in O_2, CO_2 and H_2O. The rate of vaporization (R1) of the liquid aluminum depends of the surface temperature and the boiling point depends on the pressure of the system[20]. The reaction rates of the gas-phase reactions (R3–R7) are listed in Table 1.4. Reaction 3 is exothermic at -3.2 kcal/mol[23], while reaction 5 is endothermic at 4.8 kcal/mol[24], and reactions 6 is also exothermic at -5 kcal/mol[25]. The condensation reactions (R9–R15) rates were assumed to be identical in Beckstead's model[20].

Table 1.4: Aluminum combustion gas-phase reaction rates in units of cm^3/(mole-sec), adapted from Beakstead et al[20].

$k_{R3} = 9.76 \cdot 10^{13} exp(-80/T)$
$k_{R4} = 4.63 \cdot 10^{14} exp(-10,008/T)$
$k_{R5} = 2.5 \cdot 10^{-13} T^{0.5} exp(-1030/T) + 1.4 \cdot 10^{-9} T^{0.5} exp(-14,000/T)$
$k_{R6} = (1.9 \pm 1.5) \cdot 10^{-12} exp(-(442.87 \pm 221.44)/T) +$
$(1.6 \pm 0.47) \cdot 10^{-10} exp(-(2868.6 \pm 452.94)/T)$
$k_{R7} = 6.17 \cdot 10^{15} T^{-5} exp(0/T)$

1.3 Optical Measurements

Experimental quantification of when and where the additives burn using direct in situ measurements of explosive fireballs is difficult because of the short time scales—less than 100 μs—and extreme environments—thermally high temperatures and pressures. Therefore, using non-intrusive optical techniques to observe radiant emissions from the fireball is a possible alternative. Optical techniques can also provide knowledge of which gaseous or condensed species appear in the fireball, as well as data for the temperature of condensed and/or gas phase species. Time resolved spectroscopic techniques are commonly used to measure light emission intensity as a function of time and wavelength. High speed cine-photography—having a framing rate of $\Delta t \propto O(1\mu s)$—can also provide critical information about the size and location of the light emitting region(s).

1.3.1 AlO Emission Theory

Documented efforts for aluminum combustion focused on monitoring the aluminum monoxide (AlO) emission because it emits in the visible wavelength region and is a combustion marker in most cases. As seen by the reactions R9–R11, AlO is an intermediate in the aluminum combustion with O_2, CO_2 and H_2O. If the AlO intensity is proportional to the local

reaction of aluminum, then AlO emission can help identify when and where the aluminum burns in the fireball.

AlO has strong emission bands in the visible range, which have a high signal to noise ratio through the $B^2\Sigma^+ \rightarrow X^2\Sigma^+$ transition, where X is the ground energy state and B is the second excited electronic energy level. The B–X transition emission bands—rounded to the nearest 0.1 $\mathring{A}$—are listed in Table 1.5, and are shown in Figure 1.2. The intensity strength is qualitative—based on a visual scale as defined by Pearse and Gaydon[26] The intesity estimates are an order of precedence of the strength of the band—which is useful for identification of the bands—and is a 0–10 scale, in which 0 is assigned the weakest band and 10 to the strongest[26]. The AlO B–X transition emission bands observed are caused by electronic transitions and vibrational transitions within the $\Delta\nu = -1$ band.

Table 1.5: AlO $B^2\Sigma^+ \rightarrow X^2\Sigma^+$ emission bands and visual intensity strength. Adapted from [26].

λ (nm)	Intensity	ν'	ν''	λ (nm)	Intensity	ν'	ν''	λ (nm)	Intensity	ν'	ν''
540.97	4	4	6	510.20	6	1	2	453.76	4	5	3
539.23	4	3	5	507.94	5	0	1	451.62	5	4	2
537.69	4	2	4	486.62	8	1	1	449.38	5	3	1
535.78	3	1	3	484.22	10	0	0	447.04	4	2	0
533.70	3	0	2	469.44	7	3	2	437.38	3	6	3
514.26	5	3	4	467.19	8	2	1	435.24	3	5	2
513.31	6	2	3	464.81	9	1	0	433.04	2	4	1

The emission intensity from the AlO B state is a function of the local number density of the excited state—upper energy level—and the Einstein coefficient A for each transition. Emission will be strongest from the hottest regions of the fireball because the amount of AlO in the B state is exponentially dependent on the temperature.

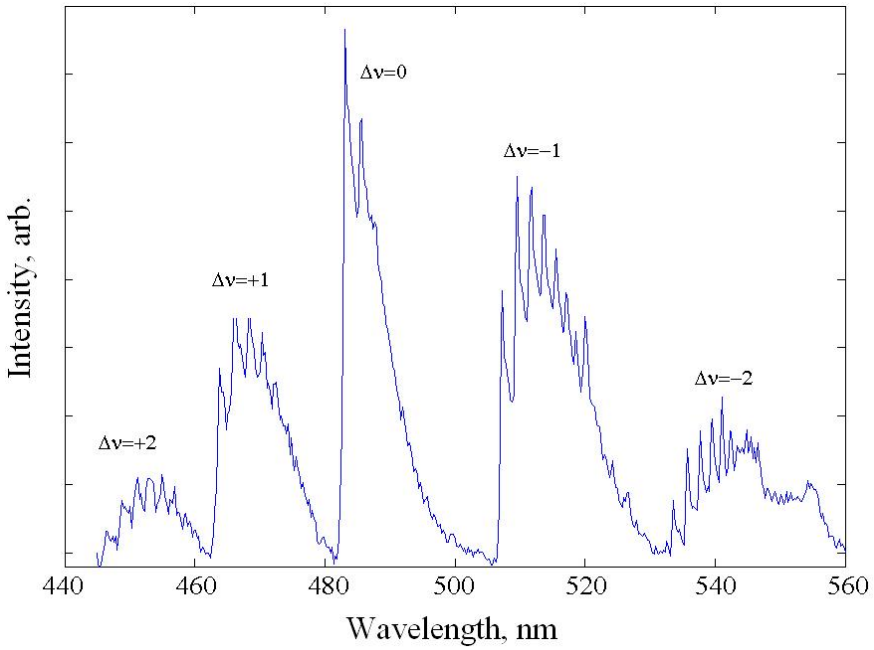

Figure 1.2: AlO emission bands in instrument range—440–550 nm.

1.4 Optical Measurement Limitations

Limitations to optical techniques exist, at least in part, as result of the optical depth variations and species temperature dependence. These limitations have not been investigated in detail to allow understanding of the applicability of AlO as a straightforward combustion marker. The optical depth study completed as a part of this research has demonstrated the need to address the optical thickness of an explosive fireball when using optical measurement techniques, such as emission spectroscopy in the visible region[27]. The results indicate that what is measured may not accurately represent the actual aluminum burning in an explosive fireball, because, typically, the fireball is optically thick, and the emission measured is from the outer region of the fireball, as shown in Figure 1.3. An optically thin media is one in which the light emitted is not absorbed within a set path length by the media before it can be seen or measured outside the media.

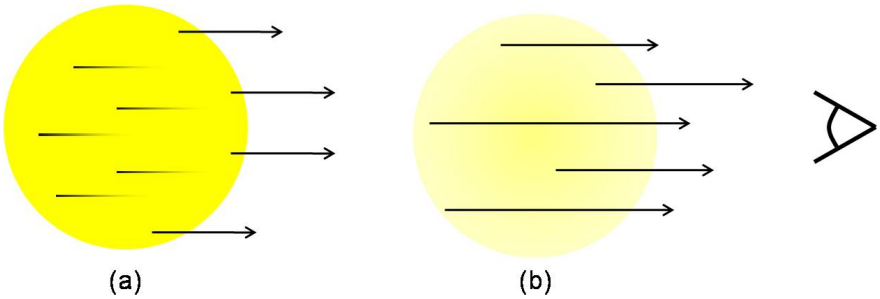

Figure 1.3: Schematic of emitted light observed from one side of a fireball that is (a) optically thick, and (b) and optically thin.

1.5 Study Objectives

As previously stated, this research focuses on understanding AlO emission from an explosive fireball. Therefore, the optical diagnostic characterization and the understanding of what can be accurately measured in the fireball when using optical techniques is the objective. Questions to be answered include: (a) For what circumstances are specific optical measurement interpretations of aluminized explosives valid, e.g. relating AlO intensity to the aluminum combustion rate? (b) What guidelines can be used to evaluate/interpret optical measurements?

An evaluation of the applicability of optical measurement techniques as quantitative measures of aluminum combustion in explosive fireballs must take into account the dependence of the AlO emission on the explosive gas temperature, ambient oxidizer, and metal particle size. In the process of understanding the optically thick explosive environments, it is desirable to develop alternative means to probe aluminum combustion, if AlO intensity does not suffice.

A second objective is to answer—at least qualitatively—when, where, and with what the aluminum burns during the explosive event.

CHAPTER 2

REVIEW OF PREVIOUS WORK AND PLAN OF STUDY

In this chapter, a summary of past studies in the area of aluminum combustion—both quiescent and in explosives—is presented. Section 2.1.3 summarizes studies which discuss the optical thickness of explosive fireballs, and serves to further motivate the work completed to measure the optical depth of an aluminized explosive fireball. Finally, a summary of the experimental work carried out in this study is presented.

2.1 Review of Previous Work

The literature review is broken into three sections. The first sections summarizes key conclusions from decades of studies on the combustion of aluminum particles. These results form a base to compare and build the knowledge of aluminum combustion in explosive fireballs. The section on aluminized explosives provides background on the current understanding of the role of aluminum additives in explosives. Explosive combinations referenced in the literature review are listed in Table 2.1. The final section reviews previous studies which indicate that an explosive fireball is optically thick under certain conditions.

Common Name	Formula or Composition
Ammonium phosphate (AP) (oxidizer)	$(NH_4)_3PO_4$
Bis(2,2,2-trinitro-ethly)nitramin (BTNEN)	$C_4H_4N_8O_{14}$
Nitromethane (NM)	CH_3NO_2
Tritanol	$C_{19}H_{16}O$
Cyclotetramethylenetetranitramine (HMX)	$C_4H_8N_8O_8$
Trinitrotoluene (TNT)	$C_7H_5N_3O_6$
Cyclotrimethylenetrinitramine (RDX)	$C_3H_6N_6O_6$
Pentaerythritol tetranitrate (PETN)	$C_5H_8N_4O_{12}$
H6	45% RDX, 29.2% TNT, 21% Al, 4.7% wax
PBXN-111	20% RDX, 43% AP, 25% Al, 12% HTPB binder
PBXN-113	45% HMX, 35% Al, 20% HTPB binder
PBXIH-135	45% HMX, 35% Al, 20% HTPB binder
C4	91% REX, 9% Plasticizer/Binder

Table 2.1: List of explosive mixtures referenced in the text.

2.1.1 Quiescent Aluminum Particle Combustion

Many researchers have studied quiescently burning aluminum particles. It has been shown that the burn time of aluminum particles depends on the oxidizer. An increase in effective oxidizer decreases the burn time;[16, 28] however, the burn time also depends on the particle size. Bazyn et al.[16] found for 10 μm particles oxygen has the fastest burn time, then CO_2 and H_2O, while Olsen[28] found that H_2O was a better oxidizer than CO_2. The aluminum burns differently in the different environments, such as aluminum particles burn simultaneously with CO_2 and O_2, but burn in stages in an H_2O/O_2 environment under certain conditions[29]. Servaites et al.[29] also determined that—for 5 to 10 μm aluminum particles—the burn time is a function of oxidation species concentration and type, the temperature, and the pressure. Other studies have also concluded that the pressure[16] and temperature[18] dependencies on the burn time are functions of the oxidizer for particles less than 10 μm. The flame temperature depends on the oxidizer such that higher temperatures exist in oxygen rich environments[20, 30, 31]. Furthermore, these studies have determined that the flame structure is also dependent on the oxidizer[30–33]. It is impor-

tant to note that Al/N species have only been observed in the products in oxygen deficient environments[33, 34], and thus N_2 is not a completely inert environment, which is a common assumption. These studies show the importance of common combustion products, such as CO_2 and H_2O, as oxidizers for aluminum combustion, and therefore it is expected that the aluminum will burn inside an explosive fireball with the detonation products—which include CO_2, H_2O, N_2, NO, and CO—as well as with the ambient environment.

As expected, the aluminum particle burn time has a strong dependence on the particle size. For larger particles, greater than 20 μm, the widely accepted Beckstead[13] correlation for aluminum in various temperatures, pressures, oxidizers, and sizes works well, and uses a $d^{1.8}$ diameter dependence. In this range, aluminum particle combustion has been observed to be in the diffusion limited regime, and is weakly dependent on the temperature and pressure[13]. For smaller particles—less than 10 μm and extending into the nanometer ranges—studies have reported major deviations from the $d^{1.8}$ diameter relationship, using $n < 1$ for 10 μm diameter particles[18]. Thus, studies report a transition from diffusion limited toward kinetic limited combustion[2, 18, 19, 35–37]. A burning rate dependence on temperature and pressure has also been observed for particles smaller than 20 μm[2, 17, 35, 36]. Therefore, micron sized aluminum particle combustion rates will be dependent on the temperature and pressure, and for an explosive fireball, the aluminum combustion will be dependent on the detonation properties—which inside the fireball are on the order of hundreds of kilobar during a microsecond time frame.

Many studies have demonstrated the dependence of the oxidizer on the burn time of aluminum particles. Some key results from the literature are as follows. Olsen[28], burning individual 70 μm Al particles in a H_2/O_2 diffusion flame—having an adiabatic flame temperature of 3000 $\pm$50 K—found that an increase in effective oxidizer reduced the burn time. It was also found that increasing the CO_2 mole fraction in the flame increased the burn time, and it was concluded that H_2O is a stronger oxidizer than CO_2. In [33], individual aluminum particles were ignited in N_2O, CO_2, CO, O_2/N_2, and O_2/Ar environments at room

temperature (no explicitly stated temperature). Envelope flames were seen in O_2, CO_2 and N_2O environments, in order of largest to smallest flames. In CO the flame was near the surface and had a weak envelope reaction. SEM of the quenched particles showed Al/N species in fuel rich environments. These species are formed near the particle surface where O is deficient. Using Planar Laser Induced Flourescence (PLIF), the flame temperature and relative AlO concentration were measured for 230 μm Al particles ignited in atmospheres of CO_2, N_2O and mixes of O_2 with N_2 and Ar at 298 K. In nitrogen containing atmospheres, Al-N-O species were found in condensed-phase measurements in lower temperature regions of the flame. In addition, the AlO profile measured was observed to be spatially narrower in the N_2 atmosphere, presumably as a result of the both aluminum and nitrogen species competing for available oxygen. Thus, the results showed the importance of AlN and NO species in the flame structure and on the combustion dynamics of aluminum particle combustion[30]. Dreizin[31] measured higher temperatures near burning particles in oxygen-rich environments—around 3000°C for tests having more than 10 percent O_2, and around 2600°C for tests having less than 10 percent O_2. Experiments were completed using free falling individual 250 μm and 90 μm aluminum particles burning in Ar/O_2, He/O_2, and N_2/O_2 enviroments at ambient temperature, which was assumed to be 300 K. The particles exhibited asymmetric burning in all O_2 dilute envrionments. The effect of the asymmetry varied based on diluent and O_2 concentration. Dissolved oxygen and oxide caps were found on all quenched particles; however, the size of the cap differed depending on the environment.

2.1.2 Aluminized Explosives

The detonation properties of explosives are inherently non-ideal. A study by Orth and Krier[38] investigated the non-ideal detonation of HMX and 5 percent aluminum by using a one dimensional, unsteady model. By adding non-inert aluminum reacting at the same rate as the HMX in the model, the detonation pressure and velocity were increased as a

result of the large energy release of the aluminum particles. When an ignition delay for the aluminum was added to the model, a secondary shock wave formed, and the addition of endothermic reactions behind the initial shock wave decreased the pressure behind the initial shock front. Thus, experimentally observed reduced detonation velocities and pressure come from extended reaction zones, which lead to secondary shocks and late energy release. The extended reaction zones may also lead to additional combustion of the aluminum with the detonation products.

Several studies have measured these lower detonation velocities and pressures. Brousseau et al.[39] found that the addition of aluminum decreases the detonation velocity, but increases the heat of detonation. Gogulya et al.[40] determined that for HMX and BTNEN using micron sized aluminum particles, the detonation velocity was decreased similar to the addition of LiF—an inert material—in the same quantity as the aluminum; and smaller aluminum particles decreased the detonation velocity more than larger particles. Trzcinski et al.[41] also found that the detonation velocity of RDX and 30 percent Al was lower than when using 30 percent LiF. In another study, Trzcinski et al.[42] observed a lower overpressure peak for Al/RDX versus pure RDX, but that the impulse increased for the aluminized explosive. In general, the quasi-static pressure was higher for the aluminized charges indicating that reactions of aluminum with the O_2 in air and the detonation products occurs. The measured heat of explosion—measured using a steel bomb that heavily confines the charges in an inert gas—was higher for the aluminized charges than the total energy of detonation calculated using CHEETAH code for inert Al, but lower than the total energy calculated for reactive aluminum, further indicating that part of the Al reacts with the detonation products in the steel chamber[42]. Therefore, while aluminum additives to explosives reduce the detonation velocity, the explosive energy is increased as a result of the reactions with the detonation products.

In explosive fireballs, aluminum particle combustion is not only a function of particle size—as in quiescent aluminum particle combustion—but also is a function of the amount

of aluminum loading, as expected. Grishkin et al.[43] found that the detonation velocity depends on the size and type of aluminum powder. Spherical particles reduced the detonation velocity more than platelet shaped particles, and the reduction was greater for smaller aluminum particles—sizes 15 μm to less than 1 μm—using 15 to 20 percent aluminum added to RDX and HMX charges. While for charges containing 20 percent aluminum, courser particles resulted in a greater detonation velocity reduction. From thermo-gravimetric analysis of the residue from tests with 60/40 HMX/Al and 60/40 RDX/Al charges, Gilev and Anishichkin[10] found that a decrease in aluminum particle size increased the fraction of reacted aluminum; and an increase in the amount of aluminum increased the total yield of oxide. Similarly, Trzciski et al.[9] found that charges having small aluminum particles (5 μm) have an increase in Al reactivity versus 75–90 μm particles, and the quasi-static pressure was larger for the small aluminum particles. The smaller particles have a higher specific surface area, which leads to a higher heat exchange and reactivity in explosives, and should show more complete combustion compared to larger particles.

A study by Carney and Lightstone[3] dealt with the effect of particle size on AlO emission. Using a HMX based charge having 35 percent aluminum particles and sizes varying from 1 μm to 120 μm, they measured more light emission for the charges having smaller aluminum partices, and the smaller particles followed the shock expansion more closely. The AlO emission peak had a slower onset and decay for larger particles, while the Al emission peak increased with particle size. Pyrometry measurements showed more emission as particle size decreased, although the calculated temperatures did not vary with particle size. It was concluded that the trend of integrated intensity and particle size agreed with current explanations of particle burning behavior, and it is expected that particles smaller than 10 μm would burn in the kinetic limited region, while particles larger than 20 μm burn in the diffusion limited region. Burning in the kinetic regime means lower temperatures and thus dimmer emission. Therefore, smaller particles should show less emission, which could indicate less oxidation than for the larger particles. However, it was found in the

other studies that the smaller particles had more oxidation, indicating that the correlation between light emission and oxidiation is not well understood.

Aluminum can react not only with oxygen, but also with CO_2 and H_2O—common combustion products—which is an important aspect since many explosive compositions are oxygen deficient[1], and the aluminum continues to burn after the oxygen is consumed by the other energetic materials. Some studies have shown that little oxidation occurs when the oxygen is removed from the environment even though the explosive formulas contain oxygen and oxidizers are in the detonation products[44, 45]. In a study comparing aluminized oxygen-rich (PBXN-111) and oxygen-deficient (PBXIH-135) charges, a second combustion phase was observed when hot aluminum particles survive the initial combustion and mix with the ambient air[46]. The initial AlO peak was higher for the oxygen-rich charge caused by the additional oxidizer in the detonation products. The oxygen-deficient charge had a more pronounced second combustion phase because the higher temperature impeded an oxide layer from forming on the aluminum particles and supported the secondary combustion. Understanding the role of the ambient environment on the energy release rate can give insight to the relative significance of the detonation products.

The effect of oxidizer and atmosphere was investigated in three studies by Carney et al.[44, 47, 48] An aluminized PBXIH-135 charge was tested in air and in N_2, by Carney et al.[44] In N_2, the AlO emission was less than in air, and spread out over the blast duration without a prominent peak. Other peaks were also observed, e.g., CN at 387 nm and 418 nm, and a strong AlN feature at 508 nm. The AlN emission in N_2 followed the same trend as the AlO emission for the tests in air. It was concluded that the Al is consumed quicker in an environment with oxygen, since the light emission from AlO is reduced, and has a longer time scale in an environment without oxygen. Similarly, Carney and Wilkinson[47] studied an aluminized PBXN-113 charge tested in air, N_2, a one to one ratio of air to N_2, and in vacuum. In vacuum, the Al emission signal was observed for a longer time during the blast time, and the AlO emission signal was delayed compared to the cases in air (30 μs

later), and in N_2 (20 μs later). Carbon, C_2 and AlN peaks were seen in vacuum as in the N_2 atmosphere. In [48], Carney et al. investigated the oxidizer concentration dependence using fuel rich Al/HMX charge having 35 percent aluminum by mass. It was found that as the oxygen concentration increased, the aluminum burn time decreased, and the temperature and impulse increased. The light breakout observed was approximately 22 μs long and the peak AlO emission delay increased as the O_2 concentration decreased. The luminosity was visible at the fireball perimeter, and was concluded to be from AlO emission from aluminum reactions with the ambient environment or shocked O_2 (aerobic reactions). It was also concluded that the early time reactions with oxygen heat the particles and cause pressure enhancement.

In another study, Trzcinski et al.[9] also studied the effect of the environment using an RDX based charge having 30 percent aluminum. From thermo-gravimetric analsyis of recovered solid products it was determined that in air all the aluminum oxidizes to Al_2O_3 indicating post detonation burning. In N_2 and Ar environments AlN, Al_2O_3, and C products were found in the products. Pure Al was found only in residue from the N_2 environment tests. A key conclusion is that the external atmosphere of gas is critical to the mixing process of detonation products leading to aluminum oxidation, and confirms that the detonation products are essential for aluminum combustion in explosive fireballs. The evidence of a prompt AlO signal and/or a later AlO signal can give us insight to chemical mechanisms, such as, reactions with the ambient gas or the detonation products. From post-detonation burning a larger amount of aluminum oxide can be expected.

Experiments at the University of Illinois by Chesterfield[45], working with Professors Glumac and Krier, investigated relative AlO intensities in different environments using 20 percent aluminum loaded RDX charges. It was found that the AlO signal was greatest in air, but in N_2, the AlO intensity was about half as it was in air, further indicating that the detonation products play a key role in aluminum combustion. The least AlO signal was in a CO_2 environment. Recovered residue analysis showed a direct correlation between

the amount of AlO signal seen and the amount of particle oxidation for the air and N_2 environments only. In air, a thin epoxy layer across the front face of the charge decreased the AlO signal, indicating that a material on a charge tip affects AlO emission measurements. Further study must be done to verify and quantify how the amount of aluminum loading affects the AlO signal measured.

Recent experimental and modeling results indicate when and where the aluminum is burning in the explosive fireball. Granholm et al.[49] saw a delayed reaction of the aluminum powder initiated using HMX, and saw reaction enhancement from pressure measurements. It was also determined that the heating, heat capacity and mixing of the ambient environment are important, and a reduction in overpressure could occur from incomplete mixing. Frost et al.[50] investigated open (unconfined) experiments using C4 and Al H-50. It was found that the shock may be sustained by the shock-particle interactions if the interactions lead to particle fragmentation, and could lead to enhanced burning rates, if mixing at the shock wave interface increases the local after burning. Therefore, evidence exists that some of the aluminum particles burn at or near the shock wave interface. Modeling results of a TNT charge detonated into a dilute distribution of aluminum particles by Balakrishnan and Menon[51] confirm the importance of the detonation products and the ambient environment mixing. It was found that the aluminum particles create instabilities at the shock and detonation products interface, which creates a mixing layer between the detonation products and the ambient air leading to after burn. The after burn energy release affects the flow fields behind the blast wave, and after 2 ms, the energy release occurs at outer regions of the mixing layer. Modeling by Baudin et at.[52] using the CHEETAH code determined the metal combustion must occur in the release wave in order to completely describe the detonation propagation and the expansion wave. Finally, Brown et al.[53] modeled aluminized explosive fireballs using the SHAMRC code and proposed that the aluminum particles do not contribute positive energy at the detonation front, but may contribute to the energy release behind the detonation front in the detonation products.

Work by a group at US Army ARDEC determined a model which explains the aluminized explosives they developed that are capable of good metal pushing—which refers to the early volume expansion work[5]—and high blast energies[4, 5]. In the model, the explosive expands through the reaction zone at a constant detonation velocity until 100 percent aluminum reaction is attained, and reacted and unreacted aluminum are assumed to be in equilibrium with the C-H-N-H products[54, 55]. In addition, it was determined from the model that the alumina layer on the aluminum particles initially prohibits the reactive participation of the aluminum in the initial H-C-N-O reaction zone, resulting in the higher detonation velocities and pressures which were experimentally measured[56]. The aluminum initially behaves as an inert, but in the expansion from an unreactive state the aluminum is freed of the alumina and reacts with CO_2 and H_2O—the oxygen was used up to form the CO_2 and H_2O before the aluminum has time to react—and it is these reactions that are the cause of the early blast energy release from the aluminum[56]. However, the model only works to explain the blast performance for explosives containing micron sized aluminum particles, and the amount of aluminum percent loading, particle size and the percent oxygen balance influence the onset of the aluminum reactions[56].

Thus, evidence exists that the aluminum burns with the detonation products behind the detonation front, based on an increase in pressure impulse when aluminum particles are added to the explosive, and a higher heat of explosion. From optical diagnostics of the explosive fireball, it has been observed that the majority of visible light is from the region behind the shock, indicating the burning aluminum region. Spectroscopy measurements of the fireball, in the 400 nm to 600 nm range, show an early AlO signal in environments containing oxygen and later—by 20 μs—an AlO signal in environments having no oxygen, suggesting that the early AlO is from aluminum burning with the oxygen and the later AlO is from aluminum burning with the detonation products[44]. Additionally, the AlO/light emission is affected by particle size and environment, and the light emission peaks correlate to the time of blast wave reflections[49]. Therefore, there is a need to relate the AlO intensity

to the amount of aluminum combustion. Experiments also indicate that the placement of the aluminum particles with respect to the explosive material affects the AlO emission, and therefore differences in the AlO signal based on the external characteristics of the charge are expected.

2.1.3 Explosive Optical Depth

Most documented studies implicitly assume optically thin conditions—which assumes light measured comes from all regions of the fireball—while some past experiments indicate that a fireball from an explosive may indeed be optically thick at some times during the lifetime of the fireball. Persson et al.[57] indicated that the observations of light emitted from explosive disks made of 60%/40% RDX/TNT, may suggest that the reaction products are absorbent and the emission comes from a thin layer—5 or 10 μm—near the front of the explosive disk. In another study of explosions of RDX, tritanol and H6 (45% RDX, 29.2% TNT, 21% aluminum, 4.7% wax) in air, the fireball was determined to be optically thick at infrared wavelengths (1800 to 6000 cm^{-1}) during the 3 second data collection time[58]. Carney and Wilkinson[47] observed Al and AlO features for 25 μs after detonation from streak spectroscopy that were significantly broadened by optical depth for explosions of PBXN-113—a fuel rich aluminized explosive—in air at atmospheric pressure. The authors also concluded that experiments in vacuum reduced the optical thickness of the fireball and allowed identification of detonation transients such as C_2. In another study from the same group, Carney et al.[59] concluded that fireball imaging under appropriate conditions may be used to determine the optical depth of an advancing fireball. Bouyer, Baudin and Le Gallic[60] examined optical density of nitromethane detonation products, and found that the reaction products are optically thick in the spectral range of 600 to 850 nm and are optically thin within the range of 400 to 600 nm, and the detonation products are optically thick in the visible range for the time frame of 5 μs after the formation of the super detonation,

which occured 1.65 μs from initiation. Thus, while there is ample evidence that optical density is significant under some circumstances, little work has been completed on precise quantification of optical depth of explosive fireballs for common energetic materials as a function of time, location, and wavelength.

2.2 Plan of Study

As suggested by previous work in the area of aluminum combustion—specifically aluminum combustion in explosive fireballs—several conclusions can be made. The explosive energy of the explosive is increased as a result of the reactions of aluminum with the detonation products. Aluminum reacts not only with oxygen, but also with CO_2 and H_2O—common combustion products—as well as N_2, and the aluminum continues to burn after the oxygen is consumed by the other energetic materials. The external atmosphere of gas is critical to the mixing process of detonation products which leads to aluminum oxidation, and understanding the role of the ambient environment on the energy release rate can give insight to the relative significance of the detonation products. The evidence of a prompt AlO signal and/or a later AlO signal can give insight to chemical mechanisms, such as, reactions with the ambient gas or the detonation products.

While these conclusions are useful in understanding aluminum combustion in explosive fireballs, questions remain as to the accurate interpretation of the optical measurements, and understanding when, where and with what aluminum burns inside the fireball. To accomplish the study objectives described in Section 1.5, the following tasks were completed.

The first step in characterizing optical measurements was to measure the optical thickness of an aluminized explosive. As the results show, the optical thickness is significant during the times when key species for characterizing the combustion of aluminized explosives—Al and AlO—have been seen. The optical depth study further motivates the remaining work, and must be considered during analysis of the data from aluminum burning in explosives.

To investigate when aluminum particles burn in an explosive fireball, time resolved pressure measurements were made. Peak pressure and initial blast impulse give information about blast wave enhancement from aluminum additives, and pressure measurements on the millisecond time scale give information about the overpressure enhancement. To determine with what the aluminum particles burn in an explosive fireball, experiments were conducted in different ambient environments—air, N_2, 20%/80% CO_2/N_2 and 40%/60% O_2/N_2. By comparing the pressure impulses in the different environments, aerobic and anaerobic effects on blast enhancement from the aluminum particles can be isolated. Non-aluminized charges were used a baseline to which the aluminized charges were compared to establish any blast enhancement. To establish where the aluminum particles burn, pressure measurements from pre-loaded aluminized charges are compared to aluminum particles attached to the tip of non-aluminized charges, which deposits the aluminum particles primarily in the fireball mixing layer rather than spread throughout the fireball. The effect of particle size on the blast wave enhancement was investigated using 3, 10 and 40 micron aluminum particles. In addition, the effect of the amount of additive loading on blast wave enhancement was studied using aluminized charges containing 20 percent and 50 percent aluminum particles by mass, and by varying the amount of aluminum attached to a non-aluminized charge tip.

Using a series of different sizes of a gap between an aluminum pellet and a non-aluminized charge, the effect of aluminum particle location was further investigated by studying the blast enhancement at the different gap distances and comparing the results to inert SiO_2 pellets. As the gap between the aluminum pellet and the non-aluminized charge increases, presumably the level of blast enhancement decreases and, hence, aluminum particle activation decreases. Thus the air-gap experiments are also used to quantify the aluminum particle activation process, and determine at what distance from the explosive charge an aluminum pellet no longer contributes to blast enhancement. The aluminum pellet gap experiments were also conducted in a N_2 ambient environment to isolate anaerobic and aerobic reactions.

In order to evaluate AlO emission measurements in an explosive fireball, AlO emission

measurements were made during the experiments described above. The AlO emission measurements are compared to the pressure measurements to determine if the AlO emission time can be correlated to blast enhancement. To determine if a correlation between the integrated AlO emission and total particle oxidation could be made, experiments were conducted in four environments—air, N_2, CO_2, and O_2—in which the AlO emission was measured, and the residue was collected and analyzed. The effects of a confined versus a weakly confined fireball, and the effects of the optical collection and collection volume were investigated by comparing AlO emission measurements made from fireballs in two chambers—inside a 4 inch ID tube and a semi-spherical 3 foot diameter enclosure. Time-resolved pyrometry measurements were made, and—together with experiments using alumina (Al_2O_3) loaded charges—are used to investigate the effect of high (greater than 4000 K) condensed phase temperatures on the AlO emission measured. The effects of the amount of aluminum and the aluminum particle location in the fireball were studied using comparisons of the AlO emission from the pre-loaded aluminized charges, the end-loaded non-aluminized charges, and the air-gap experiments. Finally, there is the question of what effect a material or substance directly in front of an aluminized charge has not only on the amount of AlO emission measured, but also if—and how—that material affects the activation of the aluminum and hence the blast enhancement. To test this effect, a layer of silicone grease was placed on the tip of an aluminized charge, and compared to the same charge without the silicon layer.

CHAPTER 3

OPTICAL DEPTH OF ALUMINIZED FIREBALLS

Knowledge of the optical thickness of an explosive fireball is critical for interpreting optical measurements such as pyrometry or emission spectroscopy. Of primary importance is the spatial region over which the measurement provides useful information. For optically thin fireballs, a path-averaged or volume averaged interpretation is valid. However, as opacity increases, measurements become more indicative of conditions at or near the surface of the expanding fireball. Furthermore, the effect on processing pyrometry signals can be less accurate since variation of emissivity with wavelength must be assumed in processing, and this function depends strongly on optical depth.Higher optical depths lead to grey body behavior, while thin clouds can have markedly non-grey distributions.

This part of the study's results are quantitative, spatially-resolved and temporally-resolved data on optical depth using several methods in fireballs from small scale aluminized RDX-based high explosives (HEs) at 532 nm. The 532 nm wavelength is simple to generate in the lab, and it is also near (but not overlapping) the AlO features often studied in emission spectroscopy of aluminized explosives. Thus, these results will be useful in evaluating optical strategies to monitor fireballs of aluminized HE.

3.1 Light Transmission through Media

Attenuation of an electromagnetic wave as it travels through a particulate medium is called extinction and includes two parts—scattering and absorption. For a dispersion of aluminum particles, the dominate feature of extinction is absorption because of the free-election con-

tribution to absorption in metals and extends from radio to far-ultraviolet frequencies[61]. Therefore the attenuation of light through an aluminized explosive fireball is dominated by absorption and the absorbance may be measured as described below.

The absorbance of incident light by a medium can be described by the natural log of the fraction of transmitted light, I/I_o:

$$A = -ln\,(I/I_o) = \kappa L \tag{3.1}$$

In equation 3.1 A is the absorbance, I_o is the incident light intensity, I is the transmitted light intensity, κ is the absorbance coefficient in 1/cm, and L is the light path length in cm through the medium. If the product of κL is much less than unity, then the medium is said to be optically thin[62]. The characteristic length or attenduation length is defined as the length at which the absorbance is equal to 1. At this length the absorbance decreases by 1/e or by approximately 1/3. Therefore, the absorbance can be seen as a measurement of the optical thickness of an explosive fireball. The following section descibes the measurements for the optical thickness or optical depth of the explosive fireballs.

3.2 Optical Depth Measurement Techniques

The charges used in these experiments were based on a modified RP-2 exploding bridgewire detonator from Teledyne RISI. An exploding bridgewire initiates a 32 mg PETN booster, which then ignites an 18 mg output pellet of 80% PBX-9407/20% Al (by mass) produced by RISI. The charges were securely mounted to explode horizontally in the open air experiments. The blast produces a conical fireball—shown in Figure 3.5—that shows a brief ($\sim$30 μs) burst of intense light which includes strong molecular AlO emission, after which the intensity decays rapidly though luminosity is observed out to at least 200 μs. The fireball length and diameter are of the same order, and grow from approximately 4 cm at 10 μs after detonation

to more than 10 cm at 100 μs. The optical thickness of the fireball as a function of time and location is estimated by four different strategies described below. The experimental technique employed in this study is based on a typical method of measuring laser beam attenuation through a medium. The use of the framing cameras and notch and interference filters to simultaneously image the laser attenuation and fireball luminosity for a transient event in a time-resolved fashion, as described below, is, to the author's knowledge, a novel approach to characterizing temporal and spatial variations of optical attenuation in single shot experiments.

3.2.1 Beam Splitter Tests

In these tests a 100 mW Nd:YAG CW laser beam was split into five separate beams using beam splitters. The five beams were aligned parallel to each other and perpendicular to the blast area in order to transverse the blast flame ball centerline. The laser beam intensity was measured using Thorlabs photo diodes having a time response of less than 14 ns. A mask having holes was positioned between the blast and the photo diode detectors to reduce the possibility of stray light from the blast being measured by the photo diode. The laser beams were set at 1.8, 5.4, 7.8, 11.8, and 13.9 cm from the front surface of the charge to allow for spatial resolution of the flame ball optical thickness. The schematic in Figure 3.1a shows the location of the beams with respect to the charge location. The incident light intensity, I_o, was calculated by averaging the intensity signal approximately 50 μs before the charge was triggered at t = 0 s.

To address the possibility of beam steering and/or fireball luminosity affecting the results, a second test was performed with the photodiodes replaced by a diffuser screen onto which each beam impinged. The beams were visualized from behind the diffuser by a Phantom V7.0 CMOS high speed camera (HSC). The images were taken at 80,000 frames per second with a 7 μs exposure. A diagram of the setup for the HSC images is shown in Figure 3.1b.

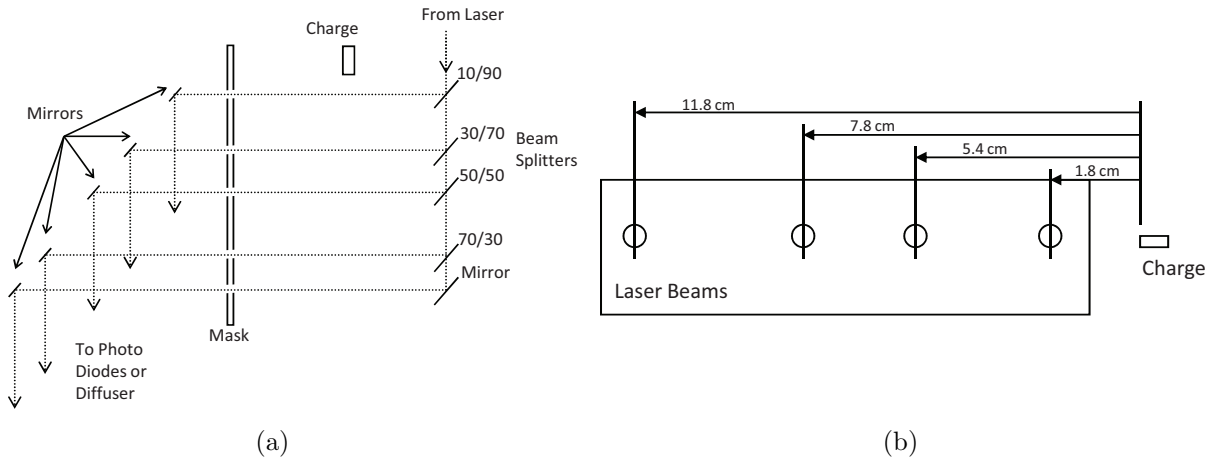

(a) (b)

Figure 3.1: (a) Schematic of the set up of the photo diode measurements of the laser beams intensities and High Speed Camera images, (b) Side view of first four beams through the mask with the distance from the charge for each laser beam denoted.

The beam locations with the distances from the charge are denoted, and the box outline represents the edge of the images.

To compensate for any steering effects and background luminosity, the core of each laser beam was located in each image, and the background intensity around the core was averaged and subtracted from the core region. The initial intensity for the HSC images is the average beam intensity prior to the detonation for each beam. The ratio of transmitted to incident light, I/I_o, is reported for all tests.

3.2.2 HSFC Tests

In order to simultaneously image the fireball and measure local optical depth, two Cooke Corporation High Speed Framing Cameras (HSFCs) were used in separate experiments. Each HSFC has four high resolution CCD image sensors ($1280x1024$ pixel resolution) that can record up to two images each with a minimum delay time of 500 ns between the images on the same CCD[63]. Each frame can be assigned an independent delay and exposure time.

A schematic of the HSFC test set up is shown in Figure 3.2. A diffuser screen was placed just behind the fireball such that the fireball was between the screen and the cameras, and

cylindrical optics were used to generate a laser line on the diffuser roughly parallel to the axis of propagation of the fireball. In a second experiment, diffractive optics were used to generate a 7 x 7 grid on the diffuser instead of a line. For both laser configurations, a 532 nm interference filter with a narrow 1 nm (FWHM) bandpass was used in front of one HSFC to image the laser pattern on the diffuser, and a holographic notch filter was placed in front of the second camera to image the fireball while rejecting all laser light. For the tests, eight images were taken by each set of framing cameras, and both cameras used the same delay and exposure for each image. The delay times after the charge was triggered were 5, 10, 15, 40, 60, 80, 120, and 160 μs with increasing exposure times for the later images, 500 ns for the first three images, 10,000 ns for the next two delay times and 20,000 ns exposure for the last three images. The delay times are listed in Table 3.1, as well as the exposure time for each image.

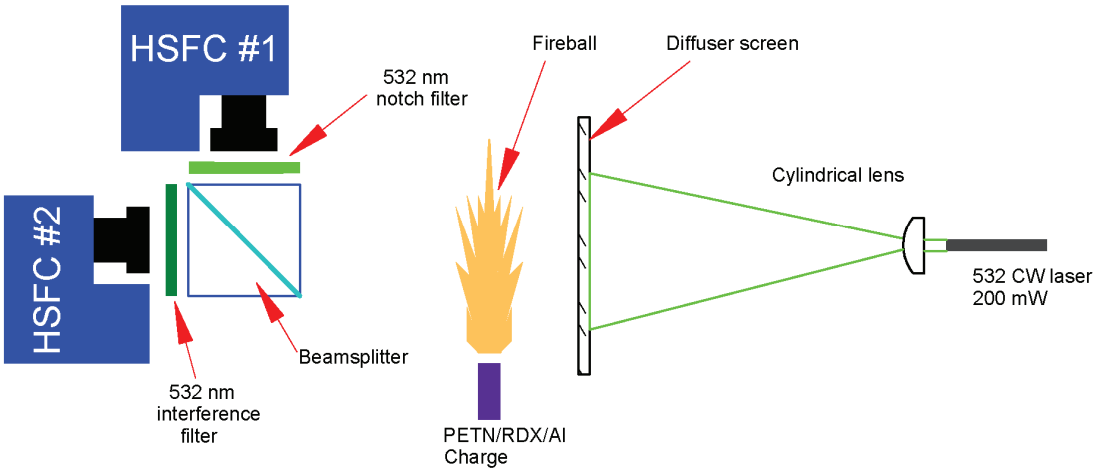

Figure 3.2: Schematic of HSFC test setup. Camera 1 images the laser pattern only, while camera 2 images the fireball and rejects the laser light.

For both laser line and laser grid imaging, the reference intensities were determined using frames taken immediately prior to the test at identical settings. Background intensity taken in the vicinity of the laser pattern was subtracted from each image separately. Therefore, a local value of I/I_o could be determined and compared to the location in the fireball as shown by the second (notch-filtered) camera.

Table 3.1: Delay and exposure times for images taken using the High Speed Framing Cameras (HSFC).

Image	Delay [μs]	Exposure [μs]
1	5	0.5
2	10	0.5
3	15	0.5
4	40	10
5	60	10
6	80	20
7	120	20
8	160	20

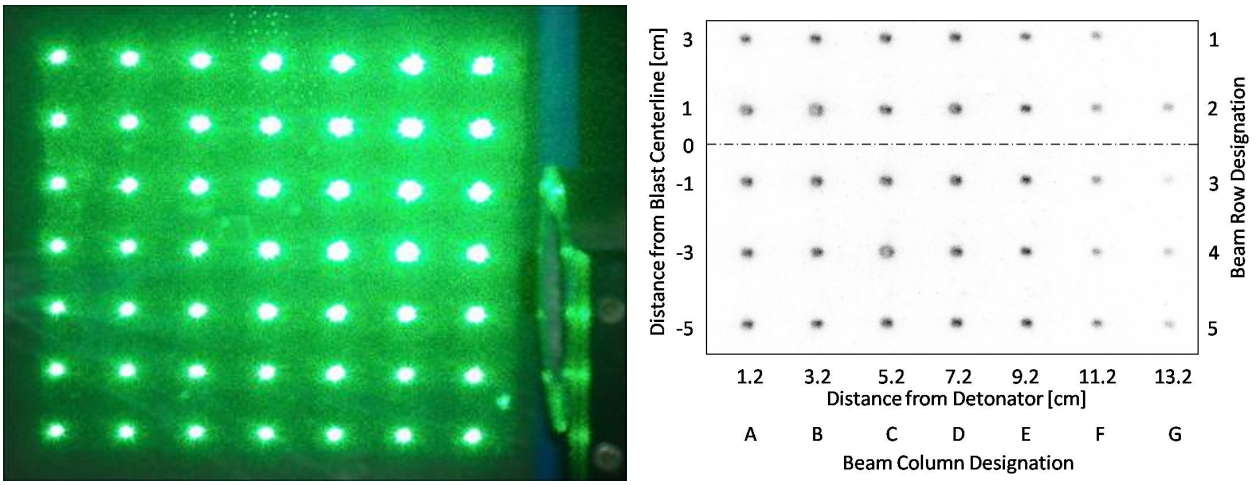

(a) 7x7 dot matrix

(b) Beam locations with respect to the charge location and individual beam designation

Figure 3.3: Dot matrix setup.

From the images of the fireball (imaged with the laser line), a three dimensional estimate of the fireball geometry was made assuming axisymmetry along the horizontal axis in the images. The axisymmetry assumption of the fireball images works best for the images in which the entire fireball can be viewed (horizontally top and bottom) and appears symmetrical in the 2-D image, i.e., those images having the laser line 10 to 120 μs. From the reconstruction of the fireball, a local path length for each location at which the laser pattern is seen can be estimated. In this fashion, the absorbance—$ln(I_o/I)$—versus path length can be plotted, allowing the estimation of the characteristic attenuation length of the fireball as a function

of time and spatial location. For this analysis only beams or portions of the laser line inside the luminous fireball were analyzed.

To process the laser line data, the images were first aligned and cropped using the program ImageJ[64]. The average beam intensity was found along the line as a function of the x-location along the laser. The background intensity was defined as the average intensity above and below the laser line and was subtracted from the laser line intensity. The background intensity was subtracted from the laser line intensity for laser line images with and without the blast. The images taken without the blast used the same camera settings as with the blast and are designated as the baseline or I_o intensity values. The laser line intensity data was smoothed using Savitzky-Golay Filtering in Matlab. Third order smoothing was used with a frame size of 41 for all images except the images at 10 and 15 μs in which a frame size of 101 was used because the data had more noise at the first two times.

The dot matrix images were aligned and cropped in ImageJ, similar to the laser line images. The location of the beams with respect to the location of the charge is shown in Figure 3.3. In the images the blast direction is right to left. For each beam the integrated intensity was calculated in Matlab. The background intensity, defined as average intensity surrounding the beam, was subtracted from the integrated intensity. Images taken of the dot matrix without the blast, designated as calibration images, were used to determine the relationship of beam intensity with respect to a reference beam. Reference beams are beams that are unobstructed by the blast in the blast images. The calibration relationship was used to then construct I_o values for the beam images showing the blast. Using the average and standard deviation for I/I_o values for each beam, a set of appropriate references were determined for each image. Each image has five to ten reference points and all I/I_o values reported have a standard deviation of less than 0.20. For each image, certain points are excluded from the subsequent analysis because the I/I_o values are greater than 1.0 or the standard deviation is greater than 0.20.

3.3 Results and Analysis

Absorbance data for the multiple laser beams are shown in Figure 3.4 for four axial locations from 1.8 cm to 11.8 cm. At each axial location, absorbance rapidly rises from zero to ∼3 (5% transmission) as the fireball reaches each laser beam. At all locations except the one closest to the charge, the absorbance peak lasts 30 to 40 μs before beginning an equally rapid decay. However, the decay is not to zero but rather in the 0.5 to 1 range (37-61% transmission) out to 200 μs. In general, there is good agreement between the two measurement methods, suggesting good test repeatability, as well as minimal effects of beam steering and fireball luminosity on the measurements. The one case in which there is a noticeable difference is in the HSC data at 1.8 cm, which shows as second late time attenuation peak not seen in the photodiode experiment. This late resurgence of attenuation is only observed very near the charge surface and is not observed in all shots. It is suspected that it is a result of shot to shot variation in the complex recirculating flow near the holder, perhaps drawing debris from the casing rupture into the first beam path.

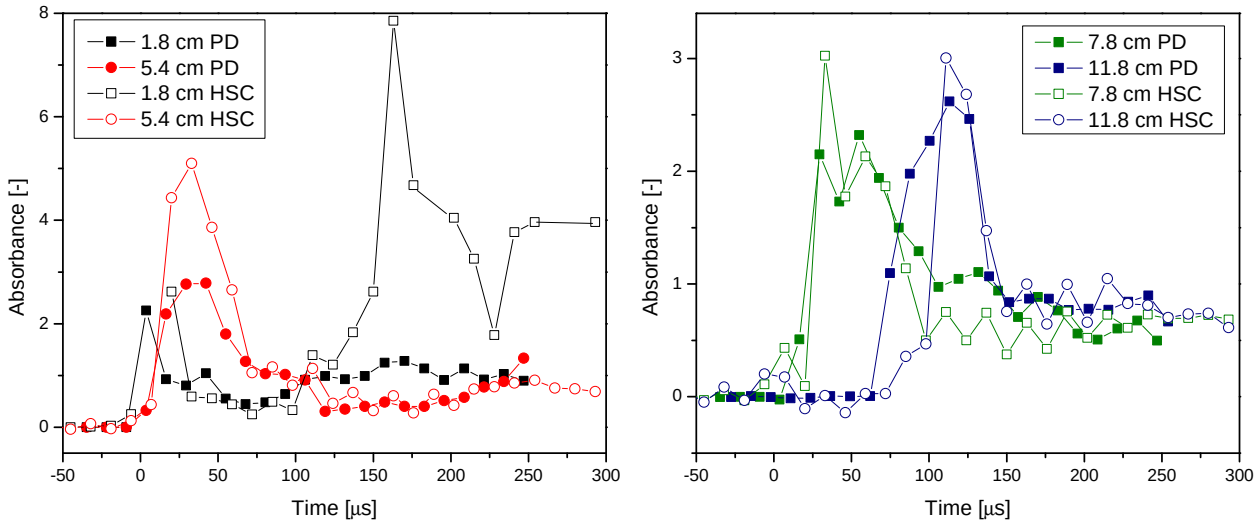

(a) (b)

Figure 3.4: Absorbance of laser beam as measured by the photo diodes (PD) and high speed camera (HSC) images for the beams located at (a) 1.8 cm and 5.4 cm (b) 7.8 cm and 11.8 cm from the charge.

The beam data provide several useful insights into the attenuation of 532 nm light by aluminized fireballs. For fireballs with length scales on the order of a few centimeters, peak attenuation is 95% or greater. There is a period and location of maximum opacity which appears to correspond to the front of the fireball. For charges of this size, the duration of maximum opacity is less than 50 μs. However, these early times represent a critical period in the fireball as it is when key combustion intermediates Al, AlO, AlN, and CN have been observed[45, 59], indicating a rapidly reacting gas mixture. Thus, at the time in which emission spectroscopy measurements show the most prominent signals is when fireball opacity is maximum. After this initial burst of gas radical emission, the gas shows no molecular signatures, only a strong continuum indicating persistent high temperatures, suggesting that the reactivity has decreased, and the gas perhaps reaching at least partial equilibrium. For this mixture of weakly reacting fireball gases, there remains significant attenuation out to 200 μs, but it is an order of magnitude less than the peak opacity.

The laser beam set experiments provide high signal to noise attenuation data at fixed locations as a function of time. Unfortunately, where the fireball is located with respect to these locations cannot definitively be established. For those measurements, the HSFC image sets are used, with the trade-off of having a lower signal to noise ratio as a result of a lower absolute signal level.

Figure 3.5 shows the results of the HSFC images using a single laser line imaged through the fireball. The two sets of images are superimposed and the laser line data are processed to show a shaded strip at the location of the laser line, and the colors correspond to the transmission. The laser line was positioned to be slightly off-axis in the experiment as shown in Figure 3.5. Figure 3.6 shows the data from the images in Figure 3.5 processed to yield the quantitative transmission along the laser line. The image at 10 μs shows attenuation ahead of the luminous fireball and inside it. Ahead of the fireball, the attenuation is small but significant, probably caused by in part to distortion of the imaging in the region behind the blast wave and ahead of the fireball. Such distortion would have a stronger effect on

these imaging measurements as opposed to the beam measurements described above. At the edge of the luminous fireball, there is a significant increase in attenuation that persists through the entire luminous region, with a recovery of transmittance only at the very back end of the fireball. The images taken at 15 and 40 μs show similar behavior with strong attenuation within the bright parts of the fireball, especially where the path length is longest. Between 60 and 120 μs, the fireball continues to expand and dim—noting that exposures are 40 times longer than the 10 and 15 μs shots in order to maintain sufficient signal. Despite the reduction in luminosity, the attenuation remains strong through at least 120 μs. At 160 μs, the beginnings of recovery of transmission are starting to appear, consistent with the photodiode/HSC measurements.

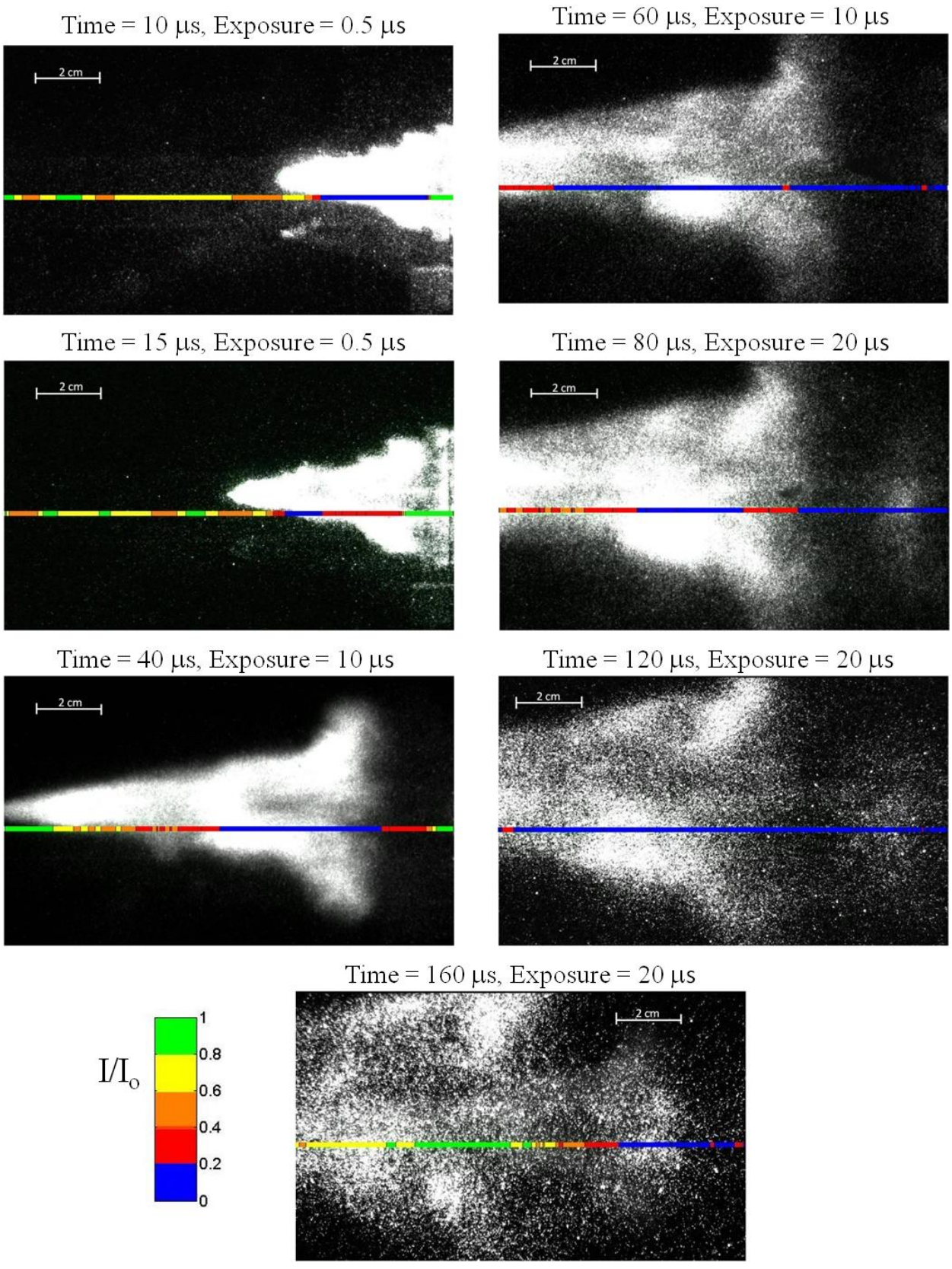

Figure 3.5: Transmission of the laser line through fireball at seven different time intervals. The colored line represents the region in which the attenuation at 532 nm was measured.

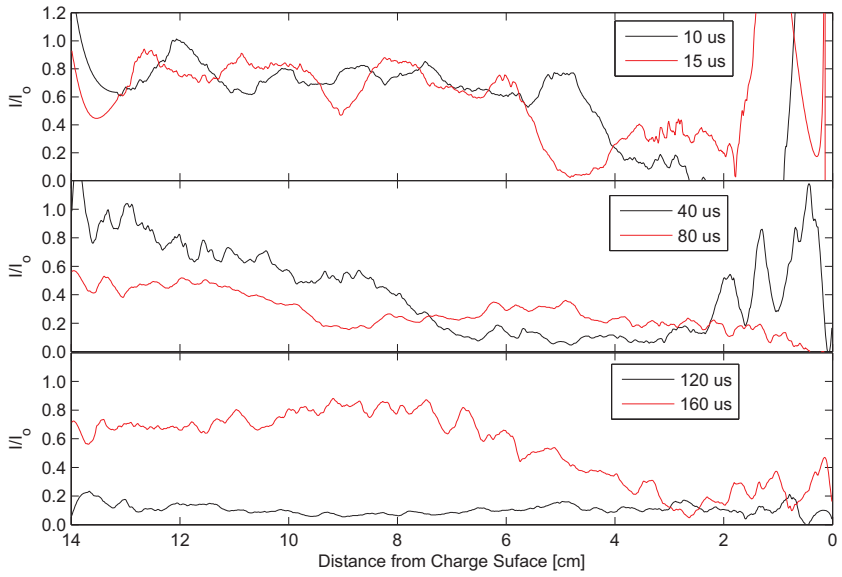

Figure 3.6: Transmission of the laser line for all delay times as a function of position from the initial charge surface. These data are taken from the images shown in Figure 3.5.

The 7 x 7 laser grid approach gave some additional two-dimensional information not possible with the laser line approach. Similar phenomena were seen with the strongest attenuation in the fireball core (longest path lengths), weaker attenuation at the edges, and non-negligible attenuation in front of and behind the luminous fireball. Figure 3.7 shows the images of the 7 x 7 laser grid.

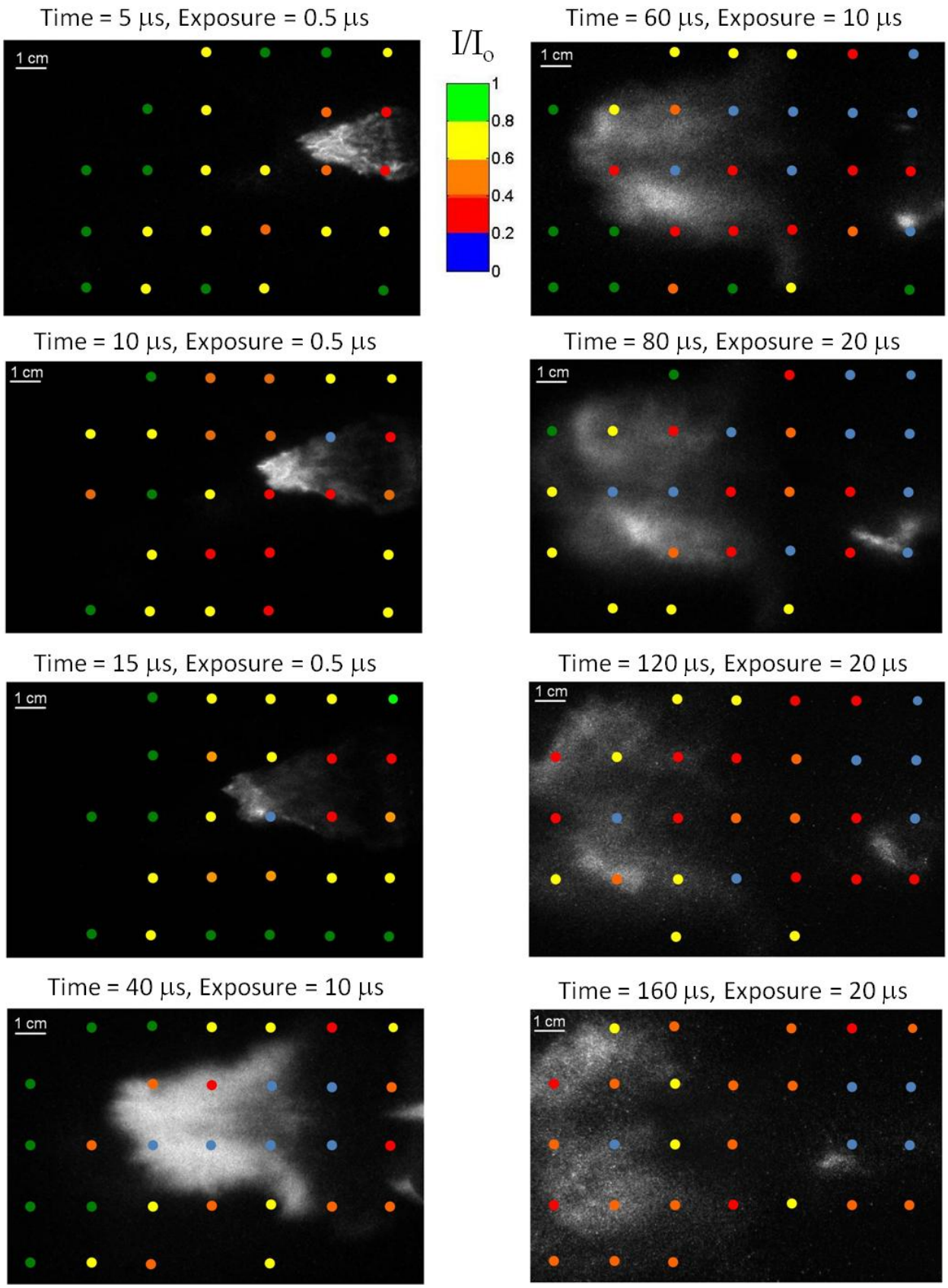

Figure 3.7: Transmission of dot matrix beams through the fireball.

To quantify the attenuation as a function of path length and time, the laser line data is used, and an estimate of the path length at each point in the luminous fireball zone is made. The result is plot of absorbance versus path length. These data are shown in Figure 3.8. Though there is significant scatter, the monotonic increase in absorbance with path length is apparent. Each set of data (i.e. each delay time) can be fit to a line passing through the origin, assuming:

$$ln(I_O/I) = -ln(I/I_O) = -ln(e^{-\kappa L}) = \kappa L \tag{3.2}$$

where $1/\kappa$ is a characteristic length scale for attenuation. The fits are shown as the dashed lines in Figure 3.8. The attenuation lengths and associated uncertainties are given in Table 3.2. The attenuation lengths vary from a fraction of a cm at 10 μs and remain at the few cm scale until around 160 μs, when the fireball begins to clear. Though the uncertainty in these measurements remains significant, the critical result is the order of the attenuation length and its dependence on time. For similar mixtures at similar temperatures and pressures, it is thus reasonable to expect attenuation lengths to be of the centimeter scale as well.

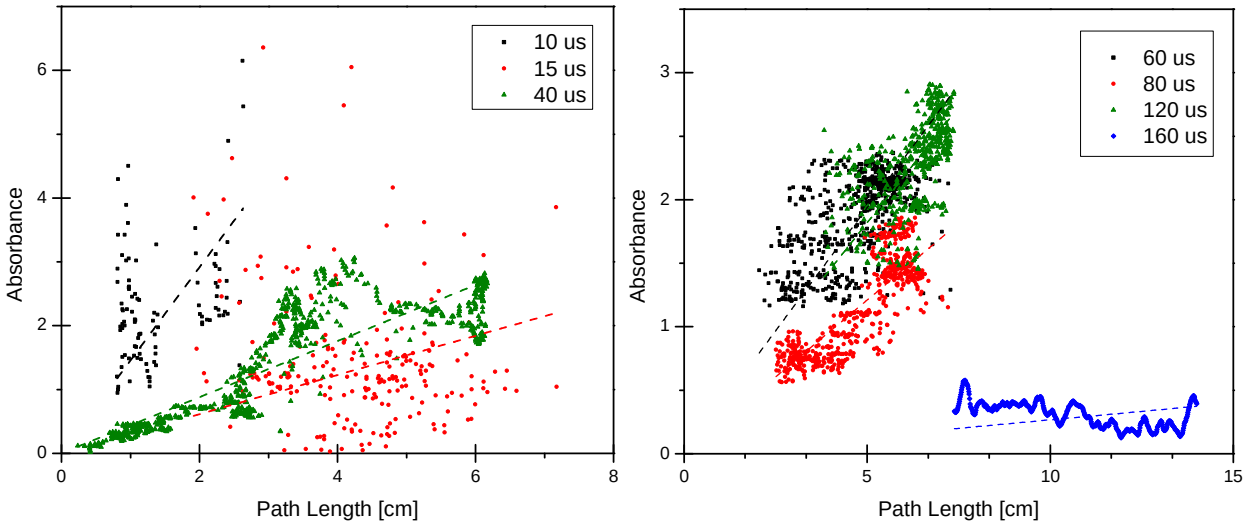

Figure 3.8: Absorbance within fireball as a function of the estimated path length through the fireball. Linear fits passing through the origin are shown as dashed lines for each time.

Table 3.2: Attenuation length for each delay time and associated uncertainties.

Time [μs]	Attenuation Length [cm]	2σ Uncertainty
10	0.7	0.2
15	3.3	2.9
40	2.3	0.2
60	2.6	0.2
80	4.1	0.2
120	2.7	0.3
160	37.5	13.3

It is also possible that the optically thick fireball is partly caused by the addition of the aluminum which under oxidizes the RDX. The oxygen balance of an explosive is defined as the amount of oxygen liberated as a result of the complete conversion of the explosive material to carbon dioxide, water, aluminum oxide, and is expressed in weight percent. A large, negative oxygen balance indicates that there is not enough oxygen for carbon dioxide to be formed, which can then result in solid carbon to remain in the combustion products[1]. RDX (and by extension PBX-9407) by itself has an oxygen balance of -21.6%, and PBX-9407 (RDX plus binder) has an oxygen balance of -29.2%, which already implies an under oxidized reaction. With the addition of 20% by mass of Al to the PBX-9407, the oxygen balance is lowered to -41%, further under oxidizing the reaction based on the liberated oxygen from the explosive material. The lower oxygen balance points toward solid carbon being in the fireball contributing to the optical depth.

Since the charges in this laboratory study are significantly smaller than those used in practical applications, scaling of the results is important. As charge mass is increased, energy release increases, but detonation pressure and temperature will not vary significantly, and so the composition of fireball gases will not be expected to vary as well. The fireball from a larger charge will take longer to expand to its final radius, and it will stay hot longer, as a result of a lower surface to volume ratio. Thus, the time dependence of attenuation observed in this study is not expected to be valid for larger charges, though it is possible that it could be scaled with appropriate modeling. However, since the composition, pressure,

and temperature of the fireball are expected to be similar, the attenuation lengths during the luminous period of the fireball should be of the same order for (i) similar explosives - 20% Al in RDX, and (ii) similar wavelengths, around 532 nm. For the 18 mg charges, the attenuation length is already of the order of the fireball dimensions. Since fireball radius scales as charge mass to the 1/3 power, charges at the scale of a few grams will already have attenuation lengths much smaller than the fireball radius, and the optical depth will be even stronger for practical charges. Further work is warranted to examine the effects of Al loading and wavelength in order to extend and generalize the results presented here.

3.4 Optical Measurement Implications

These results give important information about the optical thickness of an aluminized explosive fireball. The absorbance plots show that the absorbance is well above the optically thin assumption for the entire fireball and during the entire time that the fireball was imaged. The laser line images and data give information about the optical thickness near the centerline of the fireball and the laser dot matrix images show that the edges of the visible fireball are also optically thick. As the fireball disperses it remains optically thick. The fireball is optically thick at times when key species for characterizing the combustion of aluminized explosives, such as Al and AlO, have been seen. If the optical thickness of the fireball is not taken into account, the interpretation of spectroscopy measurements will likely be inaccurate, for accounting of the AlO emission at the flame front. At later times, if there is post-combustion detonation of aluminum, the AlO emission may be hidden because the fireball remains optically thick.

CHAPTER 4

EXPERIMENTAL METHODS TO EVALUATE ALUMINUM COMBUSTION IN EXPLOSIVE FIREBALLS

As shown in the previous chapter, the fireball optical depth is significant and can influence the interpretation of optical measurements. This chapter details the experimental techniques used to evaluate the aluminum combustion in explosive fireballs: optical methods—spectrometry, pyrometry, and high speed photography—and non-optical methods to record pressure and the product residue. The results between techniques are compared in the subsequent chapter in order to determine a meaningful interpretation of the AlO emission. In this chapter, first the charges used to produce the fireball are described, and next details of each of the diagnostic tools used are given. The third section describes the testing chambers used—denoted as the tube chamber and the blast chamber. The final section describes the different tests completed and includes lists of all tests completed. The motivation for these tests is described in Chapter 2.2.

4.1 Charge Descriptions

In these experiments, charges based on the RP80 explosive bridge wire (EBW) detonators manufactured by Teledyne RISI were used. The original or bare RP80 contains 123 mg of PBX-9407 (RDX+binder) ignited by 80 mg of low density PETN, and initiated by an exploding bridgewire[65]. The binder in PBX-9704 is Exon 461—$[(CF_2CFCl)_{0.64}/(CH_2CHCl)_{0.36}]_n$—and is 6 percent by weight of the PBX-9407[6]. A schematic of the RP80 is shown in Figure 4.1[65]. The RP80s used did not have the aluminum cup that is shown in the schematic. The RP80 has a threshold burst current of 180 amps and threshold voltage of approximately 500

volts[65]. The function time to fire is 2.65 μs. Appropriate safety procedures, as described in Appendix A, were followed during all tests.

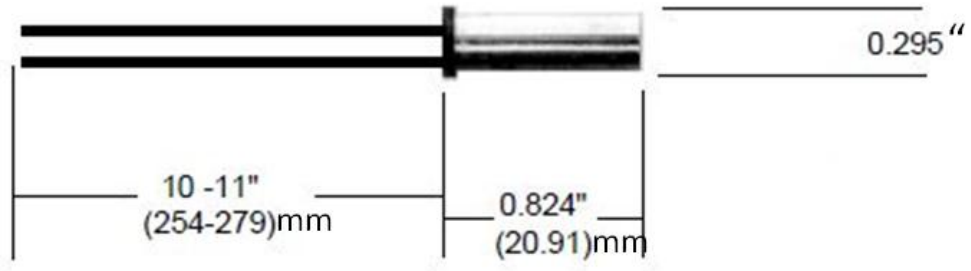

(a) Schematic

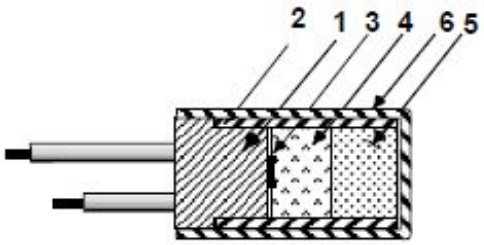

(b) Explosive Train

Figure 4.1: Schematic of original RP80 detonator adapted from [65] a) size of detonator in inches (mm), b)Explosive train 1. Plastic molded head, 2. Brass sleeve, 3. Bridgewire (Gold), 4. Initiating explosive: 80 mg PETN, 5. Output explosive: 123 mg PBX-9407 (RDX), 6. Aluminum cup 0.007" thick (removed for all experiments).

Aluminum particles were added to the RP80 in order to create the aluminized fireballs, and test the effect of aluminum particle size and loading. The variations of the RP80 charge used are summarized in the Table 4.1 and shown schematically in Figure 4.2. The bare RP80 is used as a baseline case. Aluminum powder was mixed by RISI to the PBX-9407 (RDX) section for four of the charges—designated as pre-loaded—and were used to test the effect of aluminum particle size and percent loading. The 20%-3-μm-Al loaded charge serves as a baseline for the aluminized charges. For the other three aluminumized charges, one parameter—aluminum particle size or percent loading—was varied to study the effects of each parameter separately. Two sets of charges have 3-μm aluminum powder added to make 20/80 and 50/50 Al/PBX-9407 (RDX) combinations by mass, and are designated

as '20A' and '50', respectively. Two more combinations used 10-μm or 40-μm aluminum powder in a 20/80 Al/PBX-9407 (RDX) mixture by mass, and are designated as '20B' and '20C', respectively. Another charge type was the addition of inert Al_2O_3 in a 20/80 by mass combination to the PBX-9407 (RDX) section, and was used an inert comparison to the 20 percent loaded aluminum charges.

The bare RP80's were used in two capacities in combination with aluminum powder to test the effect of aluminum additive enhancment when the aluminum is not embedded in the high explosive (HE) material. The end loaded charges consisted of a bare RP80 with 3-μm aluminum powder attached to the end of the charge by silicon grease. The amount of aluminum powder on the bare RP80 varied between 7 and 18 mg for the tests. The gap tests, to be described in detail in Section 4.4.5, used a bare RP80 and a 24.6 $\pm$ 1 mg Al pellet (the same amount of Al in the pre-loaded charges), shown in Figure 4.2d, suspended above the charge on a 2.5 μm thick sheet of Mylar.

Table 4.1: Charges used in the study.

Loading	Charge Designation	Particle Size	Al/RDX (by mass)	Loading Amount
-	Bare	-	-	-
Aluminum	20A	3 μm	20/80	24.6 mg
Aluminum	20B	10 μm	20/80	24.6 mg
Aluminum	20C	40 μm	20/80	24.6 mg
Aluminum	50	3 μm	50/50	24.6 mg
Alumina (Al_2O_3)	alumina	3 μm	20/80	24.6 mg
Aluminum	End	3 μm	-	7–18 mg
Aluminum	Gap	3 μm	-	24.6 mg

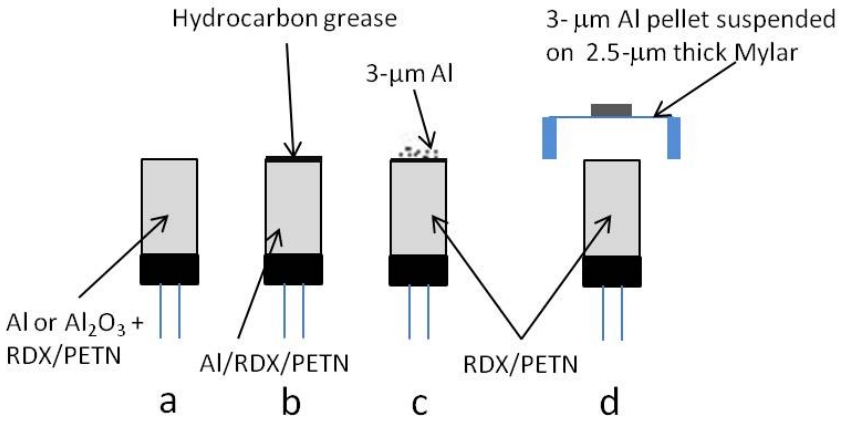

Figure 4.2: Schematic of charges used a) preloaded aluminized or alumina-ized b) aluminized with grease layer, c) end-loaded d) air gap with Al pellet.

4.2 Diagnostics

This section details the diagnostic tools used. Further details of exact equipment settings for each experiment can be found in the test description section, Section 4.4, and in Appendix A.

4.2.1 Emission Spectroscopy

The spectroscopy measurements were made in the spectral range of 450–650 nm using a custom 50 mm focal length f/1.4 spectrometer, which uses a 1800 groove/mm equivalent volumetric phase grating, has a 2:1 inlet to exit focal length ratio, and a spectral resolution of 5 Å. The CCD detector is an Andor model DV420-FK. The CCD detector was used in 'fast kinetics' mode, in which a single line of pixels is used at each exposure resulting in time resolved spectra, and has a minimum exposure/shift speed of 1 μs. The spectrometer and detector are shown in Figure 4.3. The CCD detector has the capacity to have up to a 1 μs time resolution in the fast kinetics mode. Typically 100 spectra were taken per test (128 spectra is the maximum for the CCD detector in fast kinetics mode used). Intensity and wave length calibration spectra were also taken for data analysis calibrations, using a tungsten halogen lamp calibrated at 3100 K (intensity), and a mercury lamp (wavelength).

To separate the AlO emission from the grey-body thermal background, a polynomial curve was fit to the background intensity, and then subtracted from the spectra to isolate the AlO emission intensity.

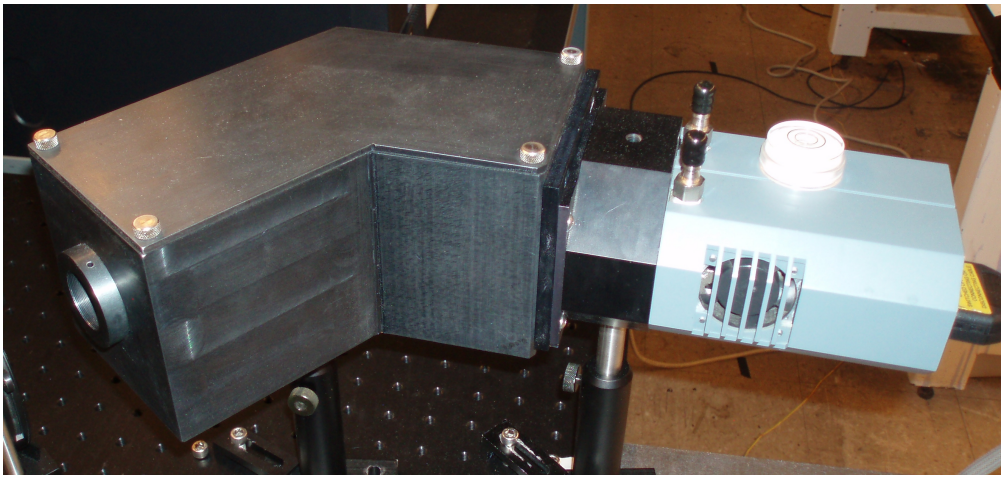

Figure 4.3: Custom built spectrometer (left) and CCD detector (right).

4.2.2 Pyrometry

Pyrometry measures the temperature by detecting radiation emitted from surfaces. According to the Stefan-Boltzmann law, the black body radiant emittance in units of power per unit area is $W = \sigma T^4$. Actual body emission is only fraction of black body emission and the ratio gives the emissivity. Planck's equation for a real body, which includes the emissivity is:

$$L_\lambda = \frac{\epsilon_\lambda C_1}{\lambda^5[exp(C_2/\lambda T) - 1]} \tag{4.1}$$

where L is the radiance or radiant emittance per solid angle, $C_1 = 2\pi hc^2 = 3.742 \times 10^8\ W\mu m^4/m^2$ and $C_2 = \frac{hc}{k} = 1.439 \times 10^4\ \mu mK$. An approximation of the Planck relation is the Wien radiation relation, which gives a deviation of less than 1% from Planck law if $\lambda T < 3125\ \mu mK$[66].

$$L_\lambda = \frac{\epsilon_\lambda C_1}{\lambda^5 exp(C_2/\lambda T)} \tag{4.2}$$

A two-color pyrometer was used for the temperature measurements. The temperature can be calculated from the Wien relation using the measured intensities (radiance) at two wavelengths:

$$T = \frac{C_2(\lambda_2 - \lambda_1)}{\lambda_1\lambda_2[5ln(\lambda_2/\lambda_1) - ln(L_1/L_2) + ln(\epsilon_1/\epsilon_2)]} \tag{4.3}$$

For two-color pyrometry, the wavelengths are chosen such that a grey body can be assumed—therefore $\epsilon_1 = \epsilon_2$—and the temperature calculation using Equation (4.3) becomes straightforward. However, it is impossible to verify the assumption that the emissivity is independent of the wavelength using 2-color pyrometry. Indeed, recent work measuring the emissivity of aluminum oxide particle clouds concluded that the grey-particle emissivity assumption is only valid for temperatures from 3000 K to 3300 K[67], which indicates that temperatures measured outside this range will have uncertainty as a result of the less valid grey-particle emissivity assumption.

Temperature measurements made using pyrometry are often interpreted as the peak temperature, which is most likely not the case, as the temperature will have averaging effects. The temperatures will be a spatially weighed average of the temperature, though strongly weighed to high temperature regions[68]. It is also worth noting that the emission measured from the fireball is primarily from the condensed phase species.

The pyrometer, shown schematically in Figure 4.4, uses interference filters to isolate the 730 nm and 940 nm ±2 nm wavelengths—outside the wavelength region containing AlO emission—using approximately 10 nm FWHM bandpasses. A bifurcated fiber optic was used to transmit light to each photodiode. The wavelengths were monitored with photodiodes—Thor Labs PDA 100, which have a nominal rise time of 233.3 ns—and the output recorded by a digital oscilloscope, Picoscope 3424. The sampling increment of the pyrometer measurements is 0.4 μs. The photodiodes were used at the maximum gain setting—70 dB—to maximize the output voltage. At the 70 dB setting, the gain is 4.75×10^6 V/A ± 5%, the bandwidth is 2 kHz, the noise (RMS) is 740 μV, the noise equivalent power (NEP) at the

peak wavelength is $2.1 \times 10^{-12}\ W/\sqrt{HZ}$[69].

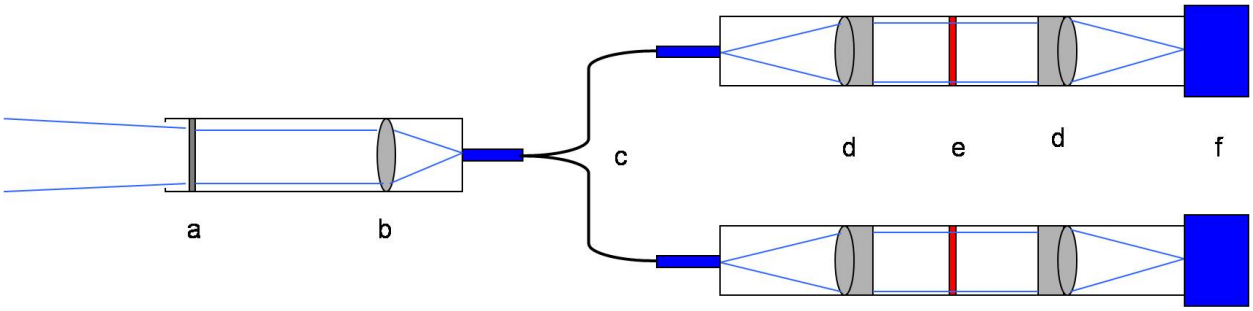

Figure 4.4: Pyrometer schematic: a) diffuser, b) f = 25 mm lens, c) bifurcated fiber optic cable, d) NIR achromatic lens f=50mm, e) notch interference filter, f) photodiode.

4.2.3 Pressure

Transient pressure measurements were made using piezoelectric pressure transducers, model Kistler 603B1—having a rise time of 1 μs—and 5000 series amplifiers—having a DC frequency responce of 200 kHz. The output had a resolution of 10 psi/Volt, and a range of 100 psi (689 kPa) was used. The data were recorded using a Picoscope, model 3424, and a sampling increment of 0.2 μs. The pressure transducers were mounted in a lollipop style in two orientations—side-on, 21.3 cm from the charge, and end-on, 21.3 cm and 32.1 cm (8.4 in and 12.65 in, respectively) from the charge. The piezoelectric pressure transducers exhibited significant noise and drift, especially after the first pressure impulse wave, as shown in Figure 4.5. In Figure 4.5 distinct reflections of the blast wave are measured using the piezoresistive pressure transducers that are not measured using the piezoelectric transducers. The data is from 20%-3-μm-Al charges in air at 32.1 cm (12.65 in) from the charge. Therefore the three piezoelectric pressure transducers were switched out for two piezoresistive pressure transducers, which were used for all tests starting May 2010.

The piezoresistive pressure transducers used were Endevco model 8530C-50 absolute pressure transducers, have a range of 50 psi (344.7 kPa) and an inherent rise time of 7.8 μs (320 kHz resonance frequency). The two transducers were mounted 21.3 cm and 32.1 cm

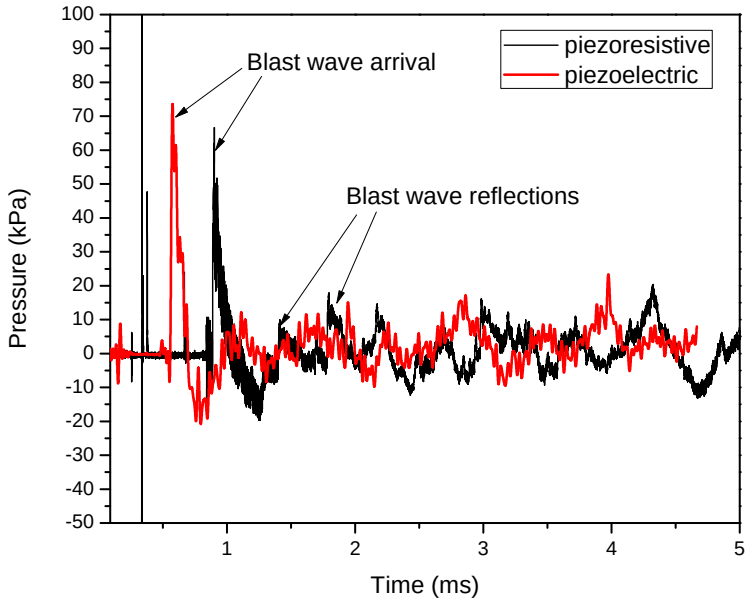

Figure 4.5: Comparison of pressure traces from the two pressure transducers.

(8.4 in and 12.65 in, respectively) from the charge to steel disks that has a knife edge, and oriented such that the transducer surface was in the same plane as the detonation wave. Ten milliseconds of data were recorded using the digital oscilloscope, Picoscope model 3424, using a sampling increment of 0.2 μs. An Endevco model 136 DC Differential Voltage Amplifier—having a broadband requency responce of DC to 200 kHz—was used to condition and amplify the signal which was recorded by the digital oscilloscope. Exact settings for the digital oscilloscope and amplifiers, as well as photographs of the mounted pressure transducers can be found in Appendix A.

All pressure data were processed using Matlab. The pressure impulse was determined by numerically integrating the positive phase pressure from the initial spike until the pressure decayed to zero gage pressure. The peak pressure was calculated by finding the intersection between a linear fit to the initial spike and an exponential fit to the pressure decay, as shown in Figure 4.6. This method of determining the peak pressures—based on [70]—takes into account any noise in the pressure signal and eliminates false peaks caused by electrical noise. The arrival time of the pressure wave to the pressure transducer was found by calculating the time at which the pressure reached 5% of the peak.

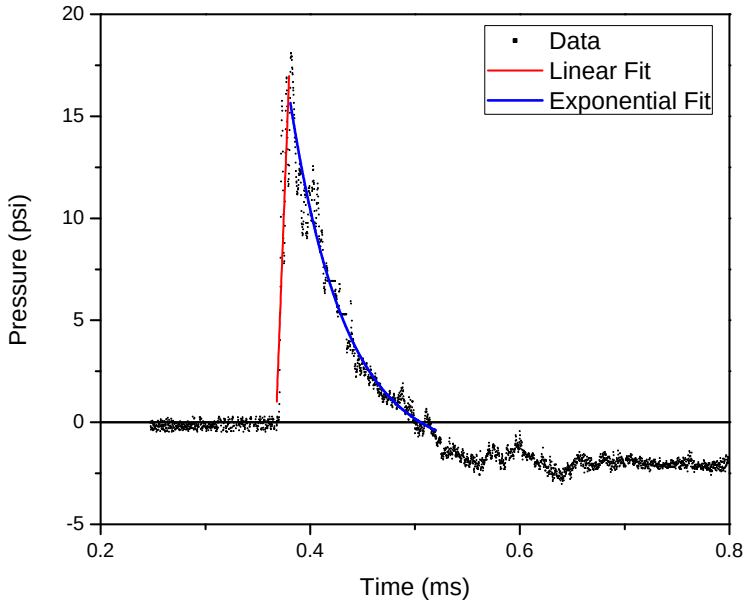

Figure 4.6: Example of linear and exponential fits to the pressure wave data to determine the peak pressure.

4.2.4 Residue Collection and Analysis

Collected residue was analyzed using a scanning electron microscope (SEM) and X-ray spectrometer to determine the percent oxidation of the aluminum particles. The particles were viewed using the JEOL 6060LV scanning electron microscope at the Center for Microanalysis of Materials at the University of Illinois Urbana-Champaign. For each test sample, a minimum of twenty particles were analyzed. SEM images were primarily viewed with an accelerating voltage of 20 kV.

The SEM used is equipped with an Oxford Instruments Energy Dispersive X-ray Spectrometry (EDS) system and corresponding Oxford Link ISIS software. In an area of residue, individual aluminum particles were identified with the SpeedMap function at a resolution of 500-2000x. The identified particles were then zoomed in on such that only the particle surface was visible in the SEM/EDS detectors. Using the SEMQUANT function available with the EDS software, the relative concentrations of aluminum and oxygen were determined.

The EDS system identifies elements based on the energy of the reflected electron beam

that is initially shot at the sample. Each element has a signature reflected energy that can be used to it. The X-ray identification is biased to the surface of the sample and the penetration scattering volume of the X-ray is pear shaped[71]. A basic assumption of the method is that the sample is homogeneous and may have additional bias for non-flat samples. The actual amount of oxidation or oxygen in a sample is difficult to quantify using the EDS method because the reflected X-ray from oxygen is at low energy since the outer shell of the oxygen self absorbs the reflected X-ray and electron emission. The oxygen X-ray measurement is also sensitive to the surface conditions and is chemical state dependent[71]. The EDS measurement of oxygen is semi-quantitative because the detector sensitivity is not constant, and large correction factors are needed in order to make it a true quantitative measurement[72]. However, relative comparisons between pure Al, pure Al_2O_3, and the combusted Al particles are valid[71].

To determine the percent oxidation that occured, the measured percent oxygen of the residue particles from the tests are compared to the measured amount of relative percent oxygen of reference samples of Al_2O_3 and 3 μm Al particles, and partially oxidized 3 μm Al particles. To partially oxidize 3 μm aluminum particles, aluminum particles were heated in an oven at 650°C, and the change in mass of the aluminum particles was measured. At 650°C, the aluminum particles remained solid during the entire heating, since the melting temperature of aluminum is 660°C. The results of the mass measurements are summarized in Table 4.2.

Table 4.2: Mass measurements for heated aluminum particles.

Aluminum Particle	Mass Measurements	
Al Starting Amount	107.7 mg	0.003989 mole Al
Al Ending Amount	128.5 mg	
Change in Weight	20.8 mg	0.0013 mole O

The resulting mass balance for the heated particles is $0.003989Al + 0.0013O \rightarrow 0.000433Al_2O_3 + 0.003122Al$, which gives 0.08429 g Al and 0.044166 g Al_2O_3. The fraction of oxidation of

the aluminum is

$$\%\text{oxidation} = \frac{2n_{Al_2O_3}}{n_A l} = \frac{2(0.000433)}{0.003989} \times 100 = 21.71\% \tag{4.4}$$

The untreated aluminum particles, heat-treated aluminum particles, and alumina particles were examined using the SEM/EDS analysis to correlate an O:Al ratio to percent oxidation. The SEM/EDS analysis showed an average percent oxygen of 22.88%, having a standard deviation of 2.39% for eight measurements of the heated aluminium particles. The percent oxidation is plotted in Figure 4.7 as a function of the measured percent oxygen for three Al particle data points—pure aluminum, pure alumina, and the heated particles to 22 percent oxidation. The linear fit is good, having an R-squared value of 0.97, where 1.0 is a perfect fit. Based on the plot, it was concluded that the relationship between the particle

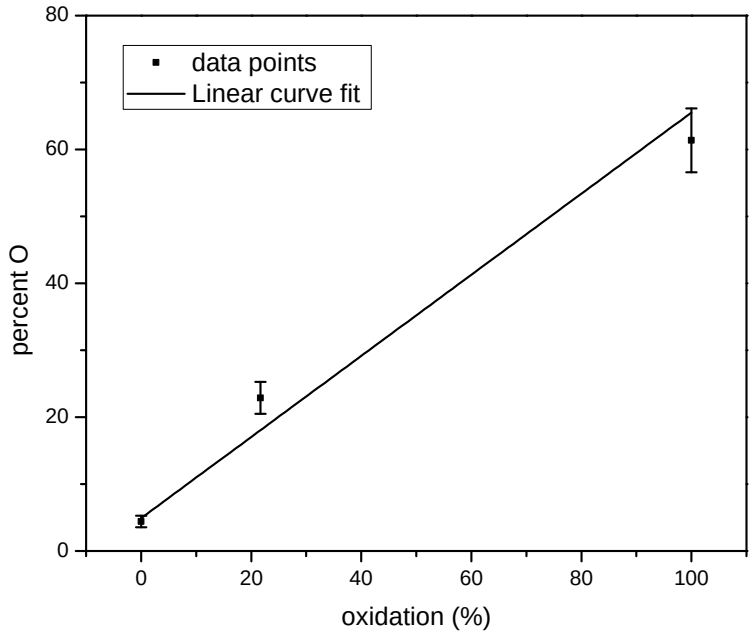

Figure 4.7: Aluminum particle oxidation as a function of measured oxygen using the SEM/EDS.

oxidation and the measured percent O by EDS is approximately linear. The resulting linear fit equation: $\%\text{oxidation} = 1.798265(\%O) - 12.583050$ was used to detemine the fraction of complete oxidation for each set of data presented in the results.

For the tests in the tube chamber, a plastic sheet was inserted into the tube, which covered the entire inside surface. After each test, the sheet was removed and cleaned using distilled water to collect the particle residue in petri dishes. The collected residue was then allowed to dry. Large plastic and brass pieces from the charge casing were separated from the debris before attaching the fine powder residue to aluminum cylinders via double sided carbon tape. All the residue was collected from each test and combined together, and therefore the particles tested from the charge tests can be assumed to come from every part of the tube.

4.2.5 Shadowgraph and High-Speed Images

Using a shadowgraph technique, the shock (blast) wave was imaged with a Phantom V5.2 CMOS high speed camera. A standard camera flash, modified to allow only a 3.8 mm pinhole of light, was used to illuminate the blast area and form a shadow of the shock wave on retroreflective material positioned behind the fireball as described in Coverdill[73]. The experimental schematic is shown in Figure 4.8. The different image sizes, frames per second (fps) and frame interval used are listed in Table 4.3

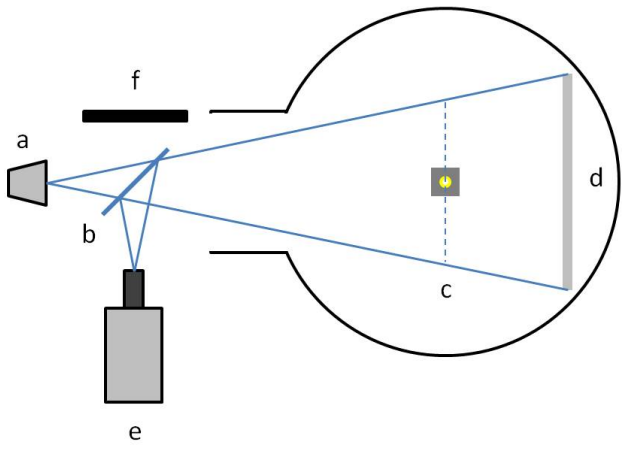

Figure 4.8: Schematic of shadowgraph a) light source, b) beam splitter, c) image plane, d) retroreflective screen, e) camera, f) beam stop, adapted from [73].

Table 4.3: Typical size, frames per second and frame interval used for high speed camera images.

Size	FPS	Frame Interval
192 x 64	43010	22.75 μs
256 x 96	25316	39.5 μs
288 x 64	35714	28 μs
208 x 64	35714	28 μs

Using Matlab and ImageJ, the images were processed to identify the shock wave and determine the shock wave velocity. The shock wave tip locations with respect to the charge block were determined manually in ImageJ, and the location data were processed using Matlab to calculate the shock wave velocity. For all tests, the shock wave was clearly visible in most images. The top edge of the shock wave, was used to determine the shock wave position and velocity. For the images in which the shock wave was not clearly distinguishable, the tip of the fireball was used as the shock wave location.

4.3 Test Chambers Descriptions

Two experimental setups were used in this study: a setup which confined the fireball diameter to 10.2 cm called the tube chamber, and a larger enclosed setup called the blast chamber which is semispherical having a diamter of 0.91 m. Each setup used a Teledyne RISI FS-43 firing system using a 4000 volt pulse and 1500 amp peak current to initiate the charges. The firing system and all diagnostics timing were controlled by a Stanford Research System DG 535 pulse generator. The settings used for the pulse generator are listed in Appendix A, as are additional pictures of the experimental setups.

4.3.1 Tube Chamber

The tube chamber has a 10.2 cm (4 inch) inner diameter and is 0.91 m (3 ft) long, and is shown in Figure 4.9. Tube chamber construction details can be found in Chesterfield[45].

An adjustable chuck was used to hold the charge at the plastic head ('1' in Figure 4.1b). The mount for the chuck fit into the chamber such that the charge fired toward a glass window and was centered radially in the tube chamber and fired horizontally. A steel ring behind the mount ensured that it did not move axially in the chamber during the firing. Aluminum bridgewires were exploded to check alignment and settings before each test.

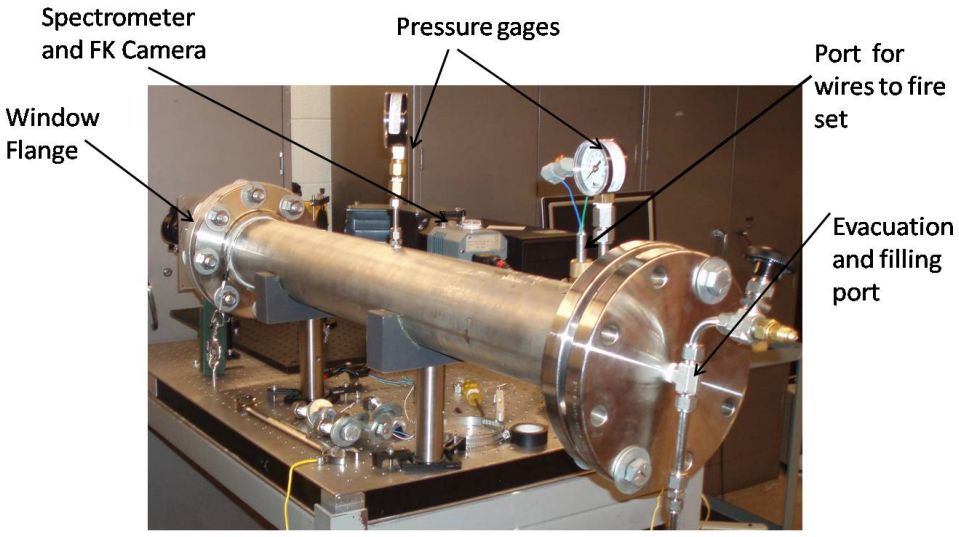

Figure 4.9: Tube chamber experiment setup.

Each charge tested in the tube chamber was fired in four ambient environments: air, N_2, O_2, and CO_2. Except for air, the chamber was flushed four times with each gas before filling the chamber for firing to ensure a pure environment. The chamber was evacuated to -96 kPa gage for each flushing, resulting in a 99.99% pure environment. The starting pressure was 0 gage pressure for the air tests and 4 kPa gage for all other tests to ensure no air leaking into the chamber. In addition, the chamber was leak tested before the tests began.

A 8.9 cm diameter glass window in the flange at the far end from the firing allowed for spectroscopy measurements from the leading front of the fireball, as shown in Figure 4.10. The charge was checked during and after the flushing/filling with a mirror through the window to ensure the Al/RDX charge was in place before firing.

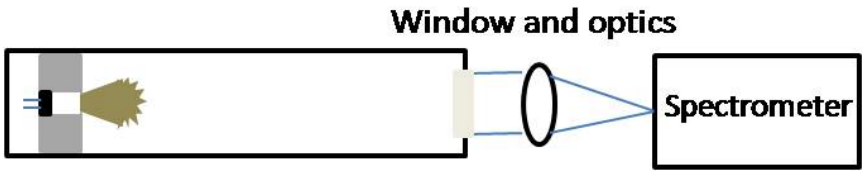

Figure 4.10: Schematic of spectroscopy measurements for tube chamber.

4.3.2 Blast Chamber

The blast chamber is shown in Figure 4.11, and it was designed by Professor Nick Glumac and Andrew Coverdill[74]. It is a fully enclosed 470 liter environmental hemispherical chamber having a diameter of 0.91 m (3 ft). The blast chamber weakly confines the fireball development, since the walls are at approximately 70 charge diameters from the charge, and the chamber volume is 10,000 times the volume of gas released by the charge. The charges were fired vertically toward an upper window from which spectroscopy and pyrometry measurements were made using fiber optics, shown in Figure 4.12. Pressure transducers mounted inside the chamber allowed for pressure wave and impulse measurements. The front port window allowed for shadowgraph and high speed photography of the fireball and the shock wave as described in section 4.2.5 and shown schematically in Figure 4.8. The charge was mounted—fully confined in a brass sheath—in a 6.35 cm x 6.35 cm x 5.1 cm (2.5 in x 2.5 in x 2 in) steel block. The tests were conducted in the ambient environments of air, 99.99% pure nitrogen, 20%/80% CO_2/N_2, and 40%/80% O_2/N_2. The same procedure as for the confined chamber was used to flush and fill the chamber with N_2. The 20/80 CO_2/N_2 and 40/80 O_2/N_2 environments were made by flushing the chamber three times with N_2, then filling to 0.2 atm (or 0.4 atm for the O_2/N_2 environment) and topping off to 1 atm with N_2.

Figure 4.11: Pressure vessel used as the blast chamber.

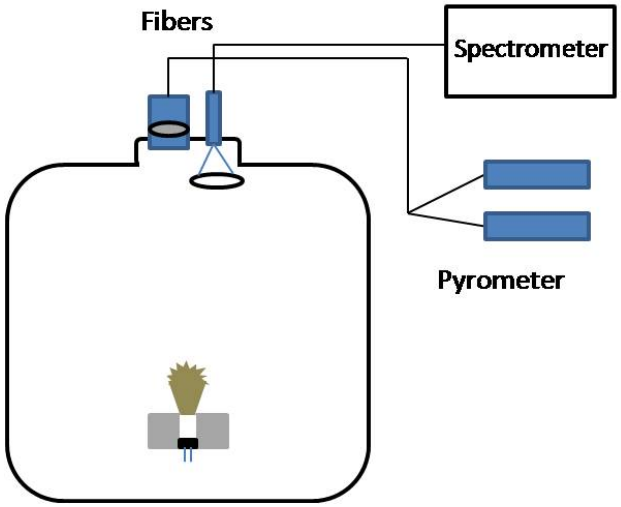

Figure 4.12: Spectroscopy and pyrometry setup schematic for the blast chamber.

4.4 Test Descriptions

This section gives a brief description of the types of experiments completed for this study. Each set of tests used a variety of aluminum loaded charges and diagnostic techniques as described below. In the tables of completed tests, each test is distinguished by a title which

details the test date, charge designation, and environment. These designations are used in some of the plot legends.

4.4.1 Confined Tests—Environment and Residue Collection

In the tube chamber—which confines the fireball development—the three types of Al-loaded (20A, 20C, 50) and end-loaded charges were fired in four distinct ambient environments: air, O_2, N_2, and CO_2. Diagnostics used were emission spectroscopy, and residue collection and analysis. Spectra were taken with 2 μs exposure every 2 μs during the first 200 μs of each firing. The purpose of these tests is to compare the AlO emission signal to the aluminum particle oxidation in order to determine if there is a correlation between AlO emission measurements and the percent oxidation. These tests are also compared to similar Al-loaded charge tests in the blast chamber. The tests completed in the tube chamber are listed in Table 4.4.

Table 4.4: Summary of tests completed in the tube chamber for the confined fireball experiments and designations.

Test	Environment	Loading	Test Date	Designation
1.	Air	Bare	1/28/2009	0128_bare_air
2.	Air	Bare + 11.7 mg 3-μm Al	2/9/2009	0209_end_air
3.	Air	20% 40 μm Al	2/17/2009	0217_20C_air
4.	Air	20% 40 μm Al	3/17/2009	0317_20C_air
5.	Air	20% 40 μm Al	4/3/2009	0403_20C_air
6.	Air	20% 3 μm Al	2/17/2009	0217_ 0A_ air
7.	Air	20% 3 μm Al	3/16/2009	0316_20A_air
8.	Air	20% 3 μm Al	4/7/2009	0407_20A_ air
9.	Air	50% 3 μm Al	3/13/2009	0313_50_air
10.	Air	50% 3 μm Al	3/18/2009	0318_50_air
11.	N_2	Bare + 13.7 mg 3-μm Al	3/12/2009	0312_end_N2
12.	N_2	20% 40 μm Al	3/11/2009	0311_20C_N2
13.	N_2	20% 3 μm Al	3/11/2009	0311_20A_N2
14.	N_2	50% 3 μm Al	3/12/2009	0312_50_N2
15.	CO_2	Bare + 11.3 mg 3-μm Al	3/4/2009	0304_end_CO2
16.	CO_2	20% 40 μm Al	3/6/2009	0306_20C_CO2
17.	CO_2	20% 3 μm Al	3/4/2009	0304_20A_CO2
18.	CO_2	50% 3 μm Al	3/4/2009	0304_50_CO2
19.	O_2	Bare + 7.3 mg 3-μm Al	3/16/2009	0316_end_O2
20.	O_2	Bare + 14.2 mg 3-μm Al	3/18/2009	0318_end_O2
21.	O_2	20% 40 μm Al	3/13/2009	0313_20C_O2
22.	O_2	20% 40 μm Al	3/17/2009	0317_20C_O2
23.	O_2	20% 40 μm Al	4/8/2009	0408_20C_O2
24.	O_2	20% 40 μm Al	4/27/2009	0427_20C_O2
25.	O_2	20% 3 μm Al	3/13/2009	0313_20A_O2
26.	O_2	20% 3 μm Al	3/16/2009	0316_20A_O2
27.	O_2	50% 3 μm Al	3/13/2009	0313_50_O2
28.	O_2	50% 3 μm Al	4/27/2009	0427_50_O2

4.4.2 Weakly Confined Fireball Tests

The Al-loaded charges were tested in air in the blast chamber for comparisons between confined and weakly confined fireball AlO emission measurements. In addition to spectroscopy, diagnostic techniques included pyrometry, pressure measurements, and high speed images. Spectra were taken using 16 μs exposure every 16 μs. For the shockwave images, the bare

charge tests used a 25,316 fps frame rate, 2 μs exposure and 256 x 96 pixel frame, while the aluminized charge tests used a 35,714 fps frame rate, 2 μs exposure and 288 x 64 pixel frame. The Kistler piezoelectric transducers were used—end on gages located 21.3 cm (8.4 in) and 32.1 cm (12.65 in) from the charge and the side on gage 21.3 cm from the charge. Table 4.5 lists the tests completed.

Table 4.5: Tests completed for the weakly confined fireball comparison and test designations.

Test	Environment	Loading	Test Date	Designation
1.	Air	Bare	4/27/2009	Bare Test 1
2.	Air	Bare	4/27/2009	Bare Test 2
3.	Air	20% 3 μm Al	6/29/2009	0629_20A
4.	Air	20% 40 μm Al	6/29/2009	0629_20C
5.	Air	50% 3 μm Al	6/26/2009	0626_50 or Test 1
6.	Air	50% 3 μm Al	6/30/2009	0630_50 or Test 2
7.	Air	50% 3 μm Al	7/16/2009	0716_50 or Test 3

4.4.3 Al_2O_3-, Al-, Al+Grease-Loaded Charge Tests

The effects of the fireball optical depth and temperatures on the AlO emission measurement were explored using these tests. To determine the effect of the alumina layer on the aluminum particles, the amount of AlO emission from Al_2O_3-loaded charges is compared to Al-loaded charges. The effect of an Al-loaded charge having a grease layer on the charge tip, which could buffer the Al from ambient oxidizers and add to the optical depth, were also tested. These tests were completed in the blast chamber and diagnostic techniques included spectroscopy, pyrometry, pressure, and high speed images. Spectra were taken with 16 μs exposure every 16 μs. For the shockwave images, a 35,714 fps frame rate, 2 μs exposure, and 208 x 64 or 288 x 64 pixel frame was used. The Kistler piezoelectric transducers were used in order to measure pressure—end on gages located 21.3 cm (8.4 in) and 32.1 cm (12.65 in) from the charge and the side on gage 21.3 cm from the charge. Table 4.6 listed the tests completed.

Table 4.6: Tests completed for the Al_2O_3-, Al-, Al+grease-loaded charge tests and designations.

Test	Environment	Loading	Test Date	Designation
1.	Air	20% 3 μm Al	10/23/2009	1023_Al_air
2.	Air	20% 3 μm Al_2O_3	10/23/2009	1023_Alumina_air
3.	Air	20% 3 μm Al + grease	10/23/2009	1023_grease
4.	Air	20% 3 μm Al	11/12/2009	1112_Al_air
5.	Air	20% 3 μm Al_2O_3	11/12/2009	1112_Alumina_air
6.	Air	20% 3 μm Al + grease	11/12/2009	1112_grease
7.	N_2	20% 3 μm Al	11/17/2009	1117_Al_N2-1
8.	N_2	20% 3 μm Al	11/17/2009	1117_Al_N2-2
9.	N_2	20% 3 μm Al	11/25/2009	1125_Al_N2
10.	N_2	20% 3 μm Al_2O_3	11/25/2009	1125_Alumina_N2
11.	Air	20% 3 μm Al	11/25/2009	1125_Al_air

4.4.4 Weakly Confined Fireball Environment Tests

This set of tests used the three 20% aluminized charges—20A, 20B, and 20C—and end-loaded bare charges, as well as the bare and Al_2O_3-loaded charges. The charges were fired in air, N_2, 20%/80% CO_2/N_2, and 40%/80% O_2/N_2 in the blast chamber. Diagnostics include spectroscopy, pyrometry, pressure, and high speed images. Spectra were taken using 16 μs exposures every 16 μs. The high speed 192 x 64 pixel images were taken using a 43,010 fps rate and a 2 μs exposure. The pressure was measured for 10 ms using a 2 μs sampling increment by the Endevco piezoresistive pressure transducers, oriented side-on and located 21.3 cm (8.4 in) and 32.1 cm (12.65 in) from the charge.

Table 4.7: Tests completed for end-loaded and environments tests in the blast chamber and designations.

Test	Environment	Loading	Test Date	Designation
1.	Air	bare	5/3/2010	bare_air1
2.	Air	bare	5/14/2010	bare_air2
3.	Air	20% 3 μm Al	5/4/2010	20A_air1
4.	Air	20% 3 μm Al	5/14/2010	20A_air2
5.	Air	20% 3 μm Al	5/24/2010	20A_air3
6.	Air	20% 3 μm Al_2O_3	5/6/2010	alumina_air
7.	Air	20% 3 μm Al_2O_3	5/14/2010	alumina_air
8.	Air	20% 10 μm Al	5/21/2010	20B_air1
9.	Air	20% 10 μm Al	5/21/2010	20B_air2
10.	Air	20% 40 μm Al	5/21/2010	20C_air1
11.	Air	20% 40 μm Al	5/24/2010	20C_air2
12.	N_2	bare	5/17/2010	bare_N2
13.	N_2	20% 3 μm Al	5/18/2010	20A_N2
14.	N_2	20% 10 μm Al	5/20/2010	20B_N2
15.	N_2	20% 40 μm Al	5/24/2010	20C_N2-1
16.	N_2	20% 40 μm Al	5/24/2010	20C_N2-2
17.	20/80 CO_2/N_2	20% 3 μm Al	5/18/2010	20A_CO2
18.	20/80 CO_2/N_2	20% 10 μm Al	5/20/2010	20B_CO2
19.	20/80 CO_2/N_2	20% 40 μm Al	5/24/2010	20C_CO2
20.	40/80 O_2/N_2	bare	5/18/2010	bare_O2
21.	40/80 O_2/N_2	20% 3 μm Al	5/18/2010	20A_O2
22.	40/80 O_2/N_2	20% 10 μm Al	5/20/2010	20B_O2
23.	40/80 O_2/N_2	20% 40 μm Al	5/24/2010	20C_O2
24.	Air	bare + 8.3 mg 3-μm-Al	5/19/2010	end_8.3air
25.	Air	bare + 17.6 mg 3-μm-Al	5/19/2010	end_17.6air
26.	N2	bare + 8.1 mg 3-μm-Al	7/2/2010	end_8.1N2
27.	N2	bare + 17.3 mg 3-μm-Al	7/2/2010	end_17.3N2

4.4.5 Air Gap Tests

Expanding on the aluminum powder end-loaded tests, experiments were conducted in which the gap between a fixed bare charge and an aluminum output pellet was varied, as shown in the schematic in Figure 4.13. By varying the distance between the aluminum pellet and the initiating charge, the role of the location of the aluminum with respect to the charge can be determined. By comparing inert pellets to aluminum pellets, the amount of energy released

as a result of the aluminum pellets burning can be determined. Testing in air and nitrogen environment tests will separate the contribution of aerobic and anaerobic reactions to the aluminum burning enhancement.

The aluminum pellets—24.6 ± 1 mg 3-μm-Al—were placed on a 2.5 μm thick sheet of Mylar suspended across a steel shim, shown in Figure 4.14. In addition to the aluminum pellets, inert pellets made of silicon dioxide (SiO_2) powder were tested. The Mylar was attached to the shim using silicon grease. The addition of the grease and Mylar on the shim did not change the shim thickness within measurement ability (0.00005 in). The shims were stacked—using grease to hold the shims together—to produce all gap distances. The deflection of the Mylar as a result of the aluminum pellet was calculated to be negligible. The amount of energy output from the Mylar burning is approximately 31.5 J, or 2.25% of the energy output from the PBX-9407/PETN in the charge. The energy calculation is based on the 7/8 inch diameter (ID of steel shim) of Mylar which appeared to burn during the test, and the heat of combustion for Mylar—23.5 MJ/kg[75]. Diagnostics include emission spectroscopy, pyrometry, pressure measurements, and high speed images.

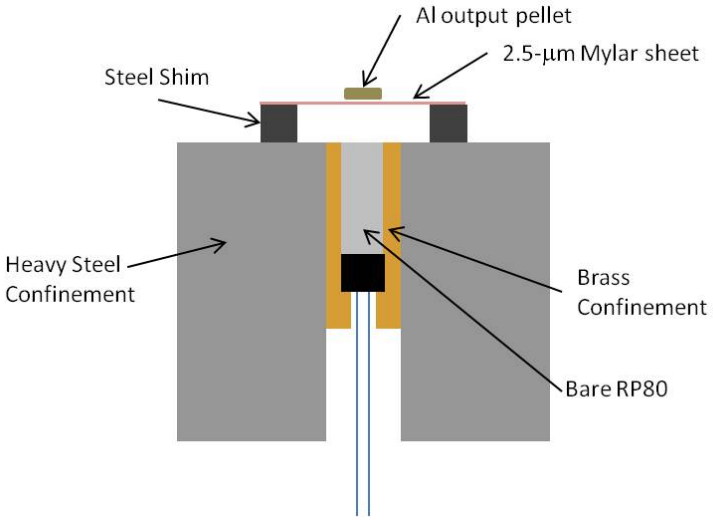

Figure 4.13: Schematic of air gap experiment charge and Al (or SiO_2) pellet setup.

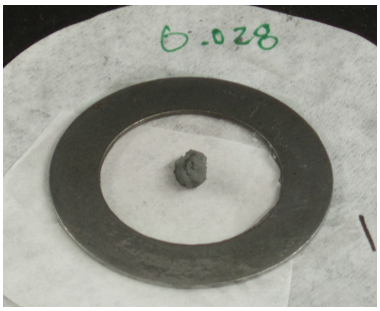

(a) 0.028 inch thick shim

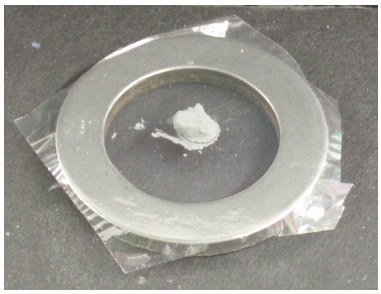

(b) 0.059 inch thick shim

Figure 4.14: Examples of an aluminum pellet suspended on 2.5-μm thick Mylar attached to a steel shim.

Table 4.8: Tests completed for the gap tests and designations.

Test	Environment	Gap (inch)	Al Amount	Test Date	Designation
1.	Air	0	24.4 mg	5/22/2010	Air 0
2.	Air	0.005	24.5 mg	7/1/2010	Air 005
3.	Air	0.015	25.3 mg	5/19/2010	Air 015
4.	Air	0.017	24.9 mg	5/27/2010	Air 017
5.	Air	0.02	23.6 mg	7/1/2010	Air 020-1
6.	Air	0.02	25.5 mg	7/1/2010	Air 020-2
7.	Air	0.028	25.6 mg	5/28/2010	Air 028-1
8.	Air	0.028	23.6 mg	7/1/2010	Air 028-2
9.	Air	0.059	24.3 mg	5/22/2010	Air 059
10.	Air	0.141	24.9 mg	5/22/2010	Air 141
11.	Air	0.245	24.6 mg	5/31/2010	Air 245
12.	Air	0.562	25.5 mg	5/31/2010	Air 562
13.	N_2	0.014	25.6 mg	5/27/2010	N2 010
14.	N_2	0.035	25.6 mg	5/27/2010	N2 028
15.	N_2	0.059	25.8 mg	5/28/2010	N2 059-1
16.	N_2	0.059	24.7 mg	7/1/2010	N2 059-2
17.	N_2	0.121	24.5 mg	5/28/2010	N2 121
18.	N_2	0.245	24.2 mg	5/27/2010	N2 245
19.	N_2	0.562	25.8 mg	5/28/2010	N2 562
20.	Air	0.021	24.7 mg SiO_2	7/21/2010	021 SiO2
21.	Air	0.028	24.6 mg SiO_2	7/21/2010	028 SiO2
22.	Air	0.059	24.0 mg SiO_2	7/21/2010	059 SiO2
23.	Air	0.124	24.4 mg SiO_2	7/21/2010	124 SiO2
24.	Air	0.242	24.5 mg SiO_2	7/21/2010	242 SiO2
25.	Air	0.563	25.3 mg SiO_2	7/21/2010	563 SiO2

CHAPTER 5

RESULTS FROM ALUMINUM COMBUSTION IN EXPLOSIVE FIREBALLS EXPERIMENTS

5.1 Energy Release Measurements

In the Taylor similarity solution to the blast equations for a spherically symmetric blast wave (weak assumption for current study), the pressure, P, at the shock front at R meters from the blast location is proportional to the energy released, E: $P = 0.155R^{-3}E$[76]. Therefore, the pressure is one measure of the energy released by an explosive. The energy output can also be quantified by determining the the initial blast wave impulse—integrated from the pressure-history measurements. The terms pressure, energy and impluse are therefore interchanged when discussing the energy output of the charges in this study. Any energy released as a result of the addition of aluminum to an explosive can be determined by comparing aluminized charges to charges not having aluminum. The additional energy released as a result of the addition of aluminum to a charge in this study is denoted 'enhancement'.

The initial blast wave impulses are shown in Figure 5.1 for three Al-loaded charges and a bare charge. For these experiments the piezoelectric pressure transducers were used to measure the pressure. The aluminized charges have a higher positive initial blast wave impulse for the closer end-on pressure transducer than for the bare charge by 60 percent, and similar positive initial blast wave impulses further away at the second end-on pressure transducer, within 15 percent of each other. More differences between the initial blast wave impulses are expected closer to the charge than further away because the pressure wave decays as $1/r^3$ according to the Taylor similarity solution to the blast equations for spherical blasts[76], where r is the distance from the blast site. Similarly, the side-on positive

initial blast wave impulses are higher by 40 percent for the aluminized charge than the bare charge. Based on the repeated experiments using the 50 percent aluminum charges (3 experiments) and bare charges (2 experiments), the uncertainty using the piezoelectric pressure transducers is 10 percent. The aluminized charges pressure-time data are within 10 percent of each other for all the initial blast wave positive impulses, and therefore there is no significant difference between the different Al/HE combinations in terms of uncertainty initial blast wave impulse strength. From the pressure measurements, we can *conclude that the aluminum clearly adds to the energy of the explosive.*

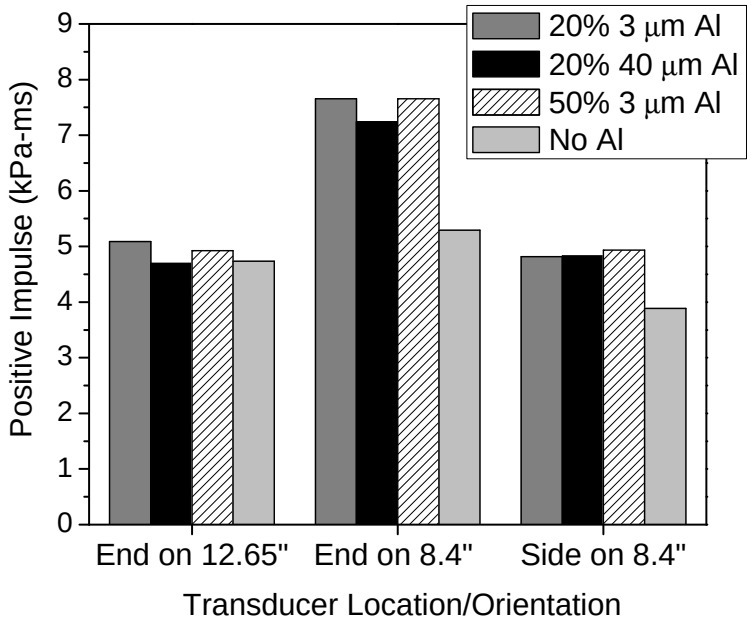

Figure 5.1: Comparison of the positive impulse from the initial blast wave (approximately first 0.5 ms after the time of arrival at the pressure transducers) from charges in air.

The pressure results shown demonstrate that pressure is a useful meausurement in determining the energy enhancement from burning aluminum. Another method to determining the amount of aluminum burned is to measure the oxidation of the aluminum particles using an X-ray technique to identify elements. Results from using this method are discussed in the next section.

5.2 AlO Emission and Al Particle Oxidation

5.2.1 AlO Emission as Function of Loading, Particle Size, Ambient Environment

The AlO intensity signals from tests in the tube chamber in the four ambient gas environments differ as expected because of the different oxidizers available in the ambient gas, as shown in Figure 5.2a–c. The 20%-3-μm-Al charge tests have an AlO emission signal within the first 40 μs, which is typically measured from aluminized explosive fireballs[45, 59]. The 50%-3-μm- and 20%-40-μm-Al charge tests, however, have AlO emission signal throughout the data collection in O_2 and air. The "tail" AlO emission signal seen in air and O_2 is most likely only a result of aerobic reactions since it is not seen in experiments which contain no O_2 in the environment. The AlO emission peak in N_2 is delayed compared to the the AlO emission peaks in air and O_2 for the 3-μm aluminum charges. The shift in time may be a result of delayed reactions in the detonation products compared to the aerobic reactions that occur because of fast mixing with the ambient environment.

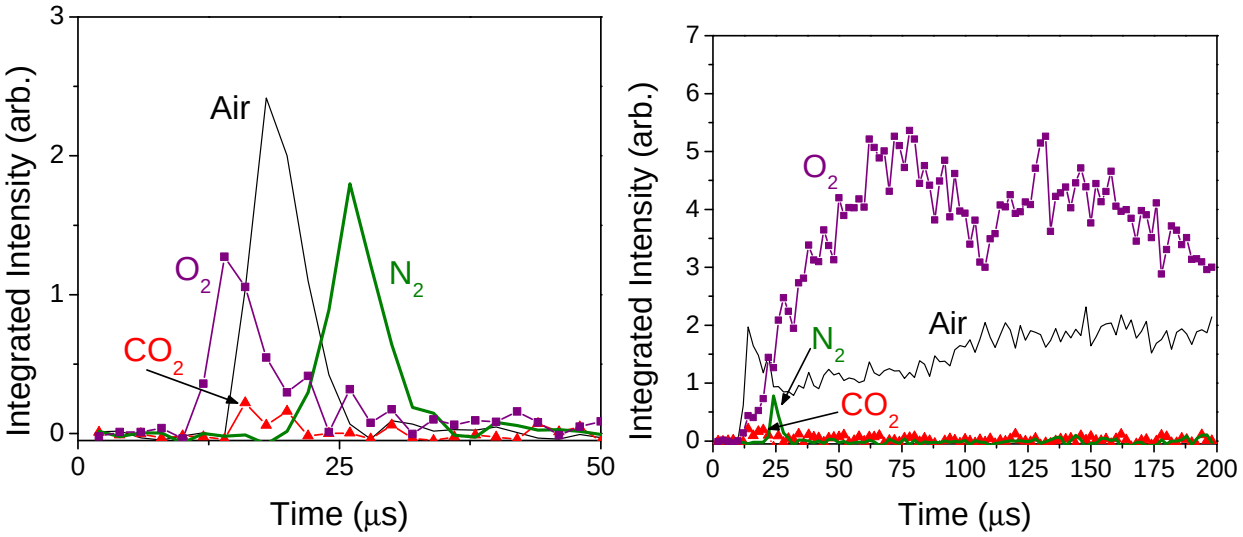

(a) 20%-3-μm-Al

(b) 50%-3-μm-Al

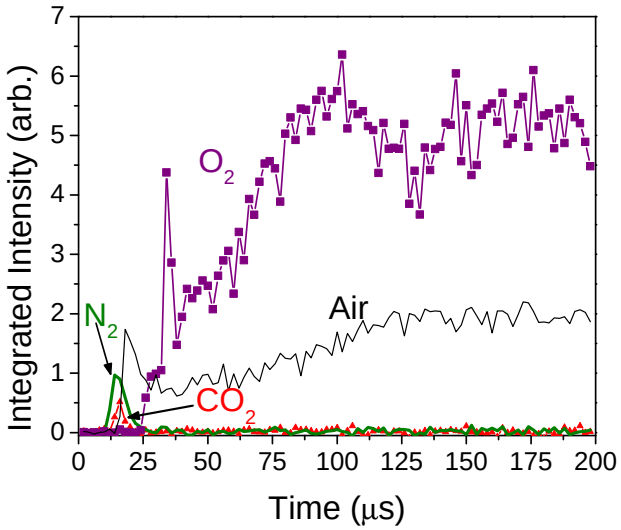

(c) 20%-40-μm-Al

Figure 5.2: AlO emission intensities from the confined fireball tests for each aluminized charge in four environments.

Repeatability of AlO Emission Measurements

The next four plots demonstrate the repeatability of the tube chamber AlO intensity measurements. Figure 5.3 and Figure 5.4 show tests using the 20%-3-μm-Al charges in air and O_2, respectively. These tests in air and in O_2 have a sharp peak in AlO signal within the

first 25 μs. The peak intensities vary between repeated tests but are within 20 percent of each other for each environment. For the tests in O_2, the time for the peak varies by one frame or 2 μs. All 20%-3-μm-Al charges in air and O_2 imply the same result: that the aluminum combustion is complete within 40 μs, (provided AlO emission is a necessary marker for combustion).

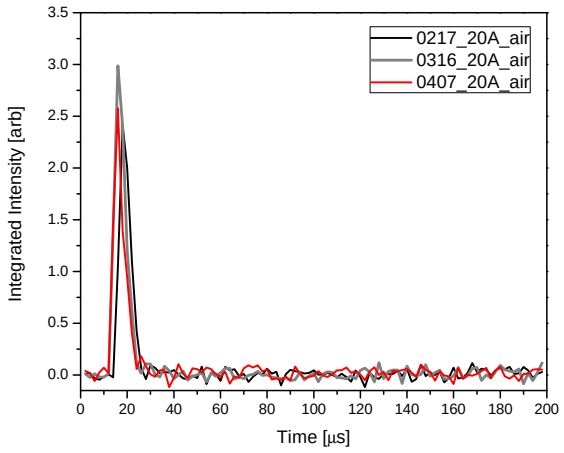

Figure 5.3: 20%-3-μm-Al charge in air repeated tests in the tube chamber.

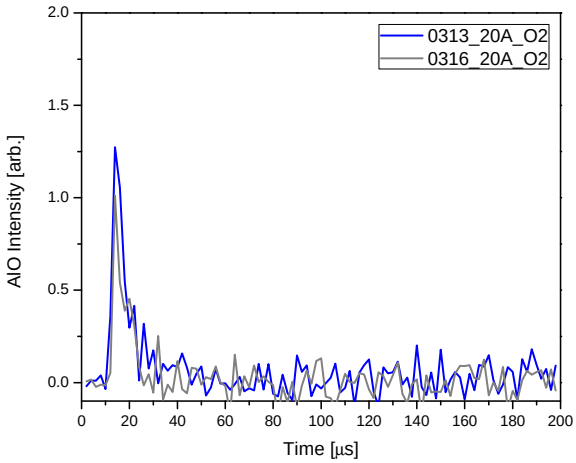

Figure 5.4: 20%-3-μm-Al charge in O_2 repeated tests in the tube chamber.

Repeated tests using the 20%-40-μm-Al charges in air are shown in Figure 5.5. All tests have a distinct AlO intensity peak within the first 25 μs; having an offset of one frame or 2 μs. For the 20%-40-μm-Al in air tests, the peak AlO intensity values are within 14 percent of each other. One test—denoted "0317_20C_air" in the figure—drops off to zero intensity with the same development as the 20%-3-μm-Al charge tests. The AlO emission signal from the other tests drops off initially, indicating a sharp peak intensity, but does not drop off to zero. Instead, after 30 μs, the AlO signal increases again, more slowly this time before leveling off. The amount of noise (scatter) in the tails is similar to the noise seen in the 0317 test at zero intensity. For the 20%-40-μm-Al in air tests, the peak AlO intensity values are within 14 percent of each other. The results from four tests using the 20%-40-μm-Al charge in O_2 in the tube chamber are shown in Figure 5.6. Unlike the 20%-3-μm-Al charge or the 20%-40-μm-Al charges in air, the 20%-40-μm-Al tests in O_2 do not exhibit a repeatable peak. Of the four tests, three have a long AlO emission signal, similar to two of the 20%-40-μm-Al

in air tests.

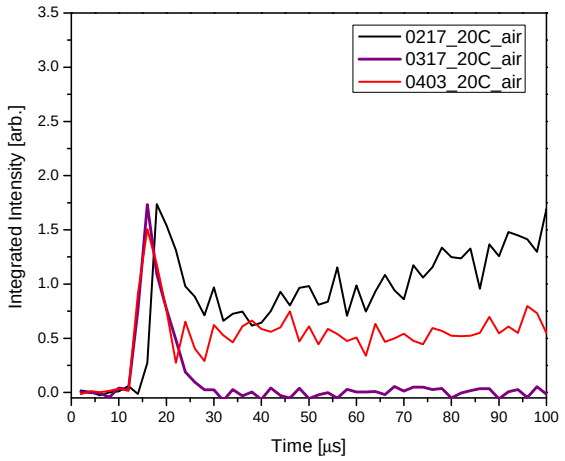

Figure 5.5: 20%-40-μm-Al charge in air repeated tests in the tube chamber.

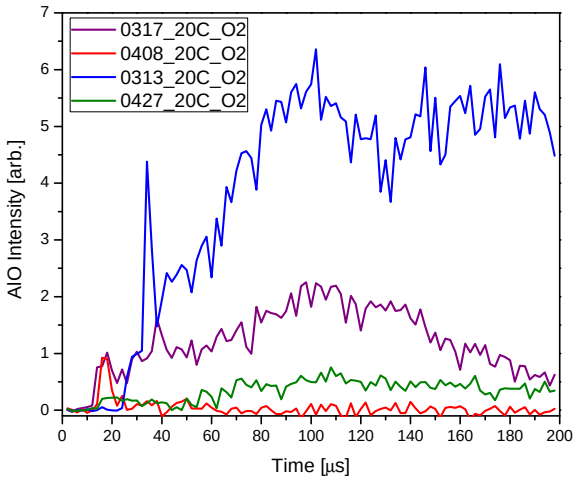

Figure 5.6: 20%-40-μm-Al charge in O_2 repeated tests in the tube chamber.

The 50%-3-μm-Al tests in air and O_2 show repeatability, as shown in Figure 5.7 and Figure 5.8. In air, both tests have a sharp peak within the first 25 μs, and then have AlO intensity throughout the entire time recorded. The tail AlO intensity appears to increase with time and the noise is on the same order seen with previously shown test results. The initial peak AlO intensities are within 6 percent of each other. From the repeated tests using the 20%-40-μm-Al and 50%-3-μm-Al charges, there is repeatability of aluminum after-burning in air and O_2. Out of eleven tests, eight show evidence of after-burn via the tail AlO signal as seen in Figures 5.5, 5.7, 5.6, and 5.8. It is also clear that the entire AlO emission signal was not collected in the tube chamber tests with a long AlO emission tail that does not return to zero within the date collection time frame.

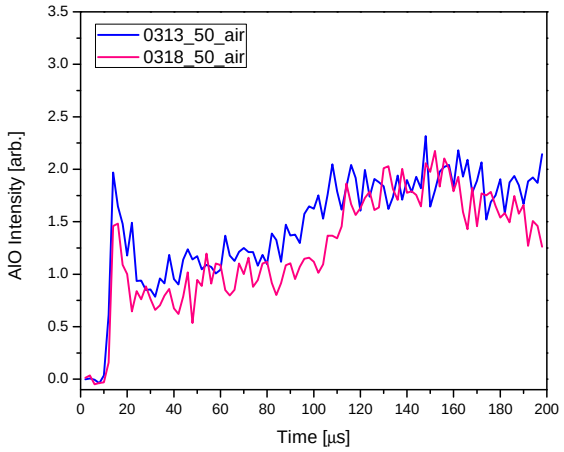

Figure 5.7: 50%-3-μm-Al charge in air repeated tests.

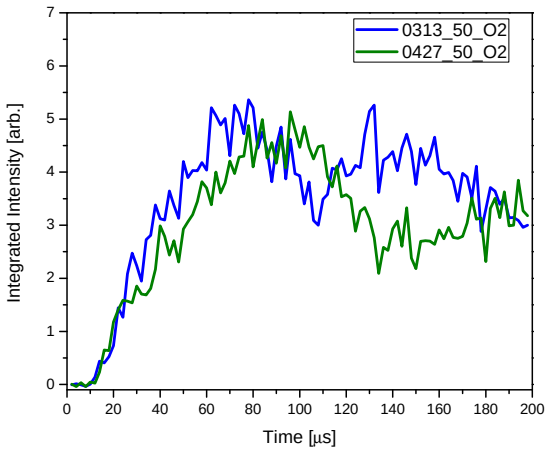

Figure 5.8: 50%-3-μm-Al charge in O_2 repeated tests.

5.2.2 X-ray Analysis of Al Particles

The results from the SEM/X-ray analysis of the aluminum particle oxidation are presented in Table 5.1, organized by charge type and the ambient environment of the test. The percent oxidation of the aluminum particles varied from 57 percent to 69 percent in the nitrogen ambient environment, and the aluminum particles are 67 percent to 71 percent oxidized in the carbon dioxide ambient environment. The residue percent oxidized in N_2 is less than in CO_2, but within the standard deviation for the same charges, indicating that there is not much more aluminum oxidizing with the extra CO_2 in the environment than with the detonation products only in the N_2 environment. The 57 to 69 percent oxidation that occurred when using pure N_2 is the result of anaerobic reactions, and therefore part of the oxidation in the air and O_2 environments will also be from anaerobic reactions. The particles tested in air were oxidized 75 to 92 percent, while in the pure oxygen evironment, the particles were oxidized 78 to 86 percent. Within the standard deviation of the measured oxidation, the particles were oxidized the same amount in both air and oxygen. Therefore the extra oxygen in the pure O_2 ambient environment did not enhance the total amount of aluminum burned.

Table 5.1: Aluminum particle percent oxidation and standard deviation (std dev.) determined from SEM/EDS analysis.

Loading &	CO_2		N_2		O_2		Air	
Al size	% oxidation	std dev.	% oxidation	std dev.	% oxidation	std dev.	% oxidation	std dev.
20%-3-μm	69.4	20.6	56.7	15.5	84.5 84.5	9.76 9.52	83.5 76.8 81.3	20.1 10.5 7.63
20%-40-μm	67.7	17.9	57.5	17.7	78.9 86.4	19.3 8.77	92.2 75.4 82.3	11.1 15.2 8.63
50%-3-μm	70.9	17.9	69.0	14.6	82.4	15.2	83.4 86.5	9.21 12.7

5.2.3 AlO Emission Compared to the Amount of Particle Oxidation

The residue percent oxidation is independent of the total integrated AlO signal measured, as shown in Figure 5.9. Almost constant percent oxidation exists for each environment, independent of the charge type. Based on the amount of oxidizer present in the environment, it is expected that the aluminum particles in the N_2 environment would have the lowest oxidation, as was previously shown in similar experiments using smaller charges[45]. This lower oxidation is present for the 20 percent aluminum loaded charges in N_2, but not for the 50 percent aluminum loading.

Environments containing oxygen have more aluminum oxidation than the environments without O_2, viz., N_2 and CO_2, but not as much as is expected based on the total integrated AlO emission intensity measurements if AlO intensity were proportional to the amount of aluminum combustion. The CO_2 and N_2 environments had a fraction of the AlO emission signal that was measured in air and O_2 environments for the 20%-40-μm-AL and 50%-3-μm-Al charges. However, more than 50 percent oxidation was found for these cases from the residue X-ray analysis—indicating significant combustion occurred. A pure O_2 environment does not contribute to more aluminum oxidation—in air and O_2 the aluminized charges have the same percent oxidation within standard deviations.

The amount of the AlO emission measured *does not correlate* to the aluminum particle oxidation determined by the X-ray analysis. This lack of correlation questions the inter-

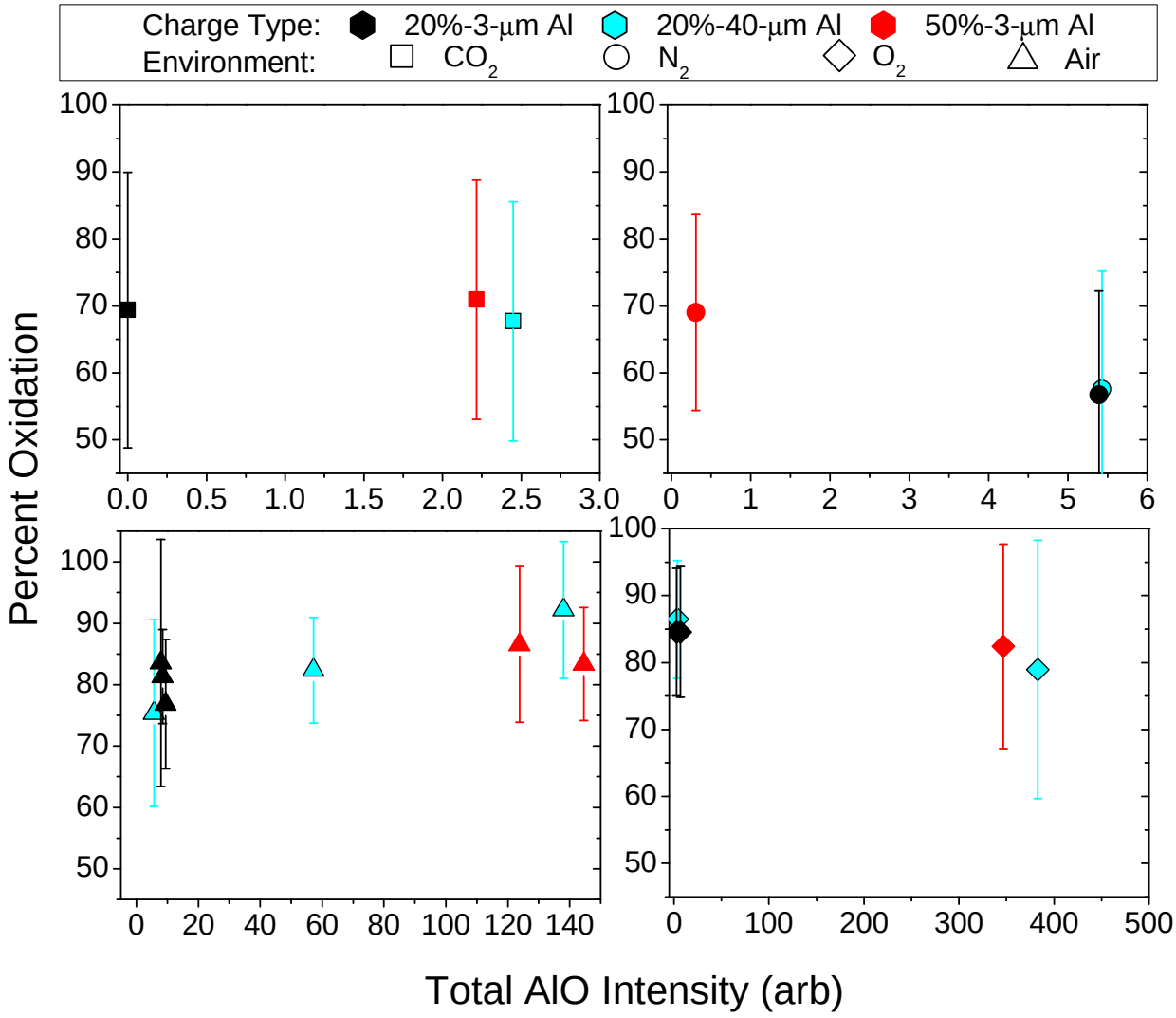

Figure 5.9: The residue percent oxidation from SEM/X-ray analysis is within the standard deviation—based on the average measured oxidation of 20 particles from individual tests (each data point)—for different charges in the same environment.

pretation of an integrated AlO emission signal as a measure of the amount of oxidation. It is clear if an AlO signature is not seen, it does not necessarily indicate the aluminum is not burning. *The particle oxidation amounts from tests in CO_2 and N_2 indicate aluminum combustion with the detonation products is occuring, at least in some cases.*

5.2.4 Gordon-McBride Equilibrium Calculations

Chemical equilibrium calculations were done for 20 percent and 50 percent aluminum RP80 charges, in each environment and no explicit environment using Gordon-McBride software[77]. The assigned pressure, enthalpy problem was used. The pressure was set to 1 bar for the air and no environment cases, and to 1.05 bar for O_2, N_2, CO_2 environments to account for 4 kPa pressure in chamber tube during experiments. PETN, and PBX-9407 (94 percent RDX and 6 percent binder by weight) were entered as reactants along with the amount of aluminum for the two cases. The binder in PBX-9407 is Exon 461, a chlorotrifluoroethylene/tetrafluoroethylene/vinylidene fluoride copolymer, and has a chemical formula of $[(CF_2CFCl)_{0.64}/(CH_2CHCl)_{0.36}]$[6]. The number of moles of reactants used in the calculations was based on the amount of PETN/PBX-9407/Al in the RP80, and environment gas inside the tube chamber.

The results of the equilibrium calculations without an explicit environment are shown in Table 5.2. Both aluminized RP80's have unreacted Al in the vapor phase, more for the charge containing 50 percent aluminum. There are also significant amounts of liquid Al_2O_3. Products having significant amounts also include CO, and N_2. Even without an environment, the majority of the Al, by mass, is oxidized to Al_2O_3, is partially oxidized to Al_2O and Al_2O_2 in the vapor phase, or reacts with the hydrogen to form AlOH. The Al also reacts with the Cl and Fl in the binder. The Cl and Fl in the binder represent less than 4 percent by mole of the total elements/molecules available for reactions. AlCl is formed at high temperatures, such as those in the explosive fireball, but is unstable.

If chemical equilibrium can occur, these calculations indicate sufficient oxidizer is available to support the amount of oxidation found from the Al particles detonated in the N_2 environment, 65 percent to 75 percent oxidation, compared to the nearly complete combustion, 80 percent to 95 percent oxidation, in the air and O_2 environment. There is also the possibility of additional oxidizer in the detonation zone from the thin layer of alumina on the surface of the aluminum particles, which was proposed by Schlöffel et al.[78] as a reason to why AlO emission was measured during aluminum burning in Ar. Assuming a 3-μm diameter spherical aluminum particle having an oxide layer of 3 nm, the mass of the oxide layer is less than 0.09 percent of the total mass, and the oxygen mass is less than 0.04 percent of the total mass. Therefore, the oxide layer was not taken into account in any calculation.

Table 5.2: Results from Gordon-McBride equilibrium calculations of the aluminized RP80s.

20% Al RP80				50% Al RP80			
Product	Mass Fraction	Product	Mass Fraction	Product	Mass Fraction	Product	Mass Fraction
Al	0.17%	CO_2	5.01%	Al	4.49%	CO_2	1.17%
AlCl	0.15%	Cl	0.46%	AlCl	1.00%	Cl	0.31%
AlF	0.52%	H	0.51%	AlF	1.54%	H	0.72%
		HCl	0.60%	AlH	0.08%	HCl	0.23%
AlO	0.76%	HF	0.49%	AlO	5.72%	HF	0.09%
AlOCl	0.03%	H_2	0.86%	AlOCl	0.05%	H_2	0.67%
AlOF	0.71%	H_2O	5.91%	AlOF	0.53%	H_2O	1.29%
AlOH	1.98%	NO	0.85%	AlOH	7.63%	NO	0.41%
AlO_2	0.02%	N_2	23.83%	AlO_2	0.07%	N_2	17.37%
$Al(OH)_2$	0.02%	O	1.79%	$Al(OH)_2$	0.02%	O	1.42%
Al_2O	0.14%	OH	2.94%	Al_2O	9.42%	OH	1.31%
Al_2O_2	0.11%	O_2	1.07%	Al_2O_2	2.04%	O_2	0.23%
CO	33.34%	Al_2O_3(L)	17.70%	CO	28.99%	Al_2O_3(L)	13.16%

Other studies have investigated the location of the Al oxide reactions. Gilev[10] investigated 60/40 RDX/Al and HMX/Al combinations and found from SEM analysis that the aluminum oxide reaction is on the surface and the inner part does not react. Additionally, smaller aluminum particles had an increased fraction of reacted aluminum. The rate of the aluminum sub-oxides condensing to Al_2O_3 is faster than the kinetic step of Al_2O_3 dissociation, therefore the liquid phase Al_2O_3 produced in the flame zone diffuses to the particle surface and deposits on the particle surface[13]. The SEM/X-ray analysis only looks at the

surface of the particles and therefore could be overestimating the actual oxidation of the particle. If the liquid Al_2O_3 is indeed deposited on the surface of the particle and the inner part of the particle does not react—more likely for the larger 40 μm particles—then a relatively high percent oxygen would be expected as found in the residue based on X-ray analysis. A thick layer of Al_2O_3 on the particle surface may partially explain why high oxygen percents were seen with the X-ray analysis of the aluminum particles.

The results from equilibrium calculations having an explicit environment showed that for both 20 percent and 50 percent Al charges in air and O_2, the products are mainly those that are expected for complete combustion—CO_2, H_2O, N_2, O_2, and Al_2O_3—plus an almost insignificant amount of Cl_2, HCl, HF and AlF_3; thus implying complete combustion as previous calculations predicted, and other studies confirm for detonations in air[9]. Only the F interfers with the oxidation of Al to Al_2O_3, shown by the formation of AlF_3—F is strongly bonded to Al, which prevents further oxidation[79]. However, the amount of F available for reactions is significantly less than the oxygen available, and the amount of AlF_3 formed is 20–40 times less than the aluminum oxide formed. In the N_2 and CO_2 environments, there are additional products for both amounts of aluminum in the charge: H_2, C and CO, which are the products of aluminum reacting with H_2O, CO and CO_2, respectively, to form Al_2O_3. Most notable in the products is that there is Al_2O_3, but no elemental Al. It appears that in equilibrium, all of the aluminum reacts with the detonation products in the CO_2 and N_2 environments.

Table 5.3: Results from Gordon-McBride equilibrium calculations of the 20 percent Al RP80s, different environments.

Air		O_2		N_2		CO_2	
Product	Mole Fraction	Product	Mole Fraction	Product	Mole Fraction	Product	Mole Fraction
Ar	0.0092	CO_2	0.00831	CH_4	0.00049	CH_4	0.00001
CO_2	0.00895	Cl_2	0.00007	CO_2	0.00328	CO	0.00003
Cl_2	0.00005	HCl	0.00007	HCl	0.00018	CO_2	0.97339
HCl	0.00012	HF	0.00004	H_2	0.00026	HCl	0.00028
HF	0.00007	H_2O	0.00721	H_2O	0.00501	HF	0.00001
H_2O	0.00745	N_2	0.00552	N_2	0.98599	H_2	0.00005
N_2	0.77245	O_2	0.9773	AlF_3(II)	0.00009	H_2O	0.00965
O_2	0.20018	AlF_3(II)	0.00009	Al_2O_3(a)	0.00121	N_2	0.00748
AlF_3(II)	0.00008	Al_2O_3(a)	0.00139	C(gr)	0.00349	AlF_3(II)	0.00013
Al_2O_3(a)	0.00145					Al_2O_3(a)	0.00187
						C(gr)	0.0071

Table 5.4: Results from Gordon-McBride equilibrium calculations of the 50 percent Al RP80s, different environments.

Air		O_2		N_2		CO_2	
Product	Mole Fraction	Product	Mole Fraction	Product	Mole Fraction	Product	Mole Fraction
Ar	0.00924	CO_2	0.00687	CH_4	0.00069	CH_4	0.00001
CO_2	0.00745	Cl_2	0.00003	CO	0.00001	CO	0.00082
Cl_2	0.00002	HCl	0.00014	CO_2	0.00066	CO_2	0.97068
HCl	0.00018	HF	0.0003	HCl	0.00018	HCl	0.00028
HF	0.00031	H_2O	0.00559	HF	0.00003	HF	0.00009
H_2O	0.00579	N_2	0.00406	H_2	0.00154	H_2	0.00022
N_2	0.77467	O_2	0.9794	H_2O	0.00204	H_2O	0.00746
O_2	0.19859	Al_2O_3(a)	0.00359	NH_3	0.00001	N_2	0.0055
Al_2O_3(a)	0.00373			N_2	0.98705	AlF_3(II)	0.00011
				AlF_3(II)	0.00008	Al_2O_3(a)	0.00481
				Al_2O_3(a)	0.00309	C(gr)	0.01002
				C(gr)	0.00463		

5.3 Effect of Fireball Confinement

Repeatability of AlO Emission Measurements in Blast Chamber

The AlO intensity from all 50 percent Al charges is shown in Figure 5.10. All three tests show the same the same trend: the AlO emission immediatly peaks within the first 50 μs, then decreases slower back to zero AlO emission, and the AlO emission was measured through 416 μs. The average FWHM is 104.8 μs and the standard deviation is 16.7 μs of the AlO

emission. The average peak AlO emission counts (in the thousands) is 6.37 and the standard deviation is 1.5.

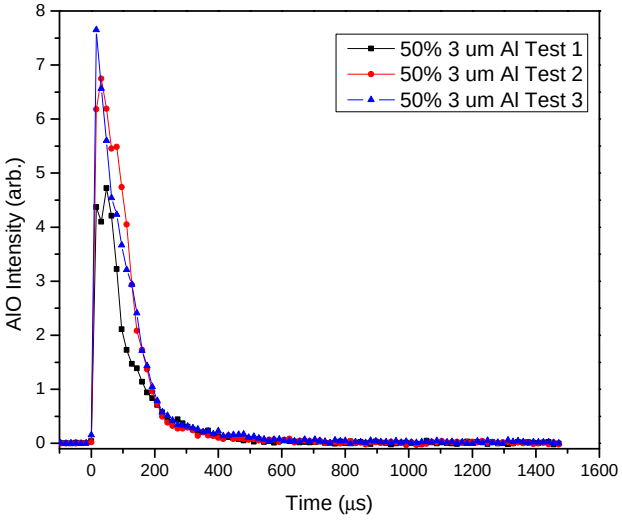

Figure 5.10: AlO Intensities from three tests using 50%-3-μm-Al charges.

5.3.1 Tube Chamber Compared to Blast Chamber—AlO Emission

Confinement of the fireball affects the emission measurements, as shown in Figure 5.11a–c. For the charges having 50 percent aluminum, both experimental setups show late AlO emission (after 40 μs) but having different histories. For the confined fireball, the AlO emission increases with time after the peak AlO, and in the unconfined case the AlO emission decreases with time. High speed images of the fireball from tests in the unconfined setup showed the fireball expanded to have a diameter greater than 10 cm—the diameter of the tube—within the first 56 μs. The optical collections are different for the confined and unconfined setup, as shown in Figure 5.12. In the confined setup, Figure 5.12a, all the light reaches the detector. In the unconfined setup, Figure 5.12b, the amount of the fireball gas in the collection volume decreases with time. As the fireball spreads the measured emission must decrease, even if the particles emit the same power.

The confinement of the fireball has less mixing within the fireball than the unconfined

fireball because in the tube there is less ambient oxidizer and a smaller area of the fireball is exposed to the ambient environment. This mixing influences where the aluminum particles are burning. The location of the particles may not consistently be near the fireball surface, from test to test, where most of the measured AlO emission signal originates. The shockwave reflections on the end wall of the confined setup also influence the development of the fireball, and the location of the aluminum particles. The fireballs may cool at different rates in each set up—as a result of the fireball expanding in the unconfined setup, and cooling as a result of the hot gases meeting a cold wall in the tube—and can also influence AlO emission measurements. All these differences between the two fireball expansions contribute to optical measurement differences, and subsequently can influence how the measurements are interpreted.

The aluminum particle burn-time calculations based on the AlO emission intensities will yield different results from the two setups for all charge types, affecting the interpretation of these results. Typical burn time calculations include the methods of constant intensity cutoff, which determines the time it takes to reach a common level of intensity; percent peak height, such as full-width at half-maximum (FWHM); and percent total area, which assumes the area under the intensity curve is proportional to the rate of energy release[28]. Using these methods to calculate the burn time of the aluminum based on the AlO emission will likely yield different results from the two set ups for all charge types, which would then affect the interpretation of these results when comparing to other studies.

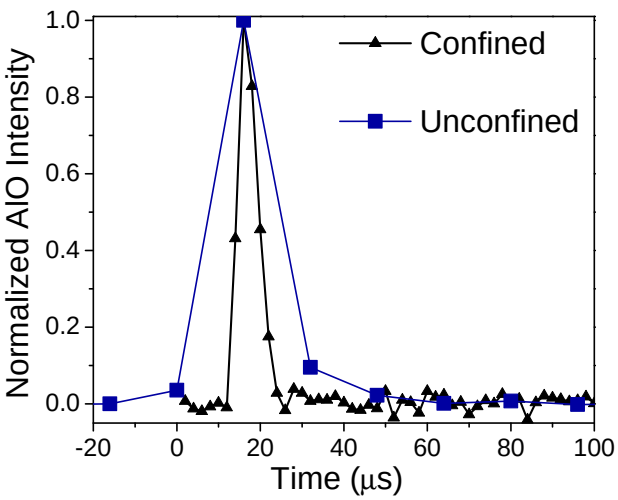

(a) 20%-3-μm aluminum

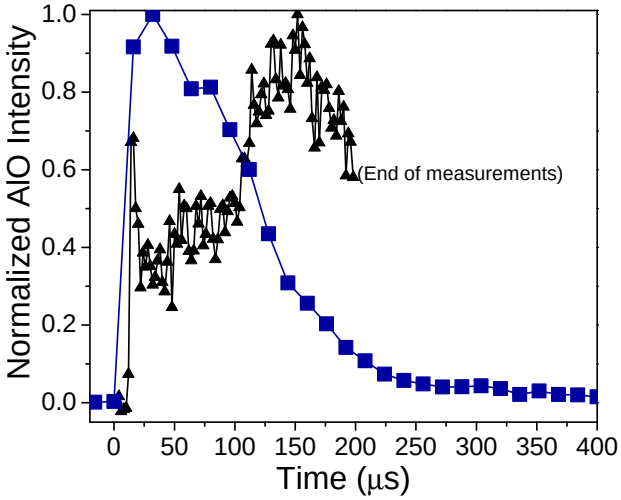

(b) 50%-3-μm aluminum

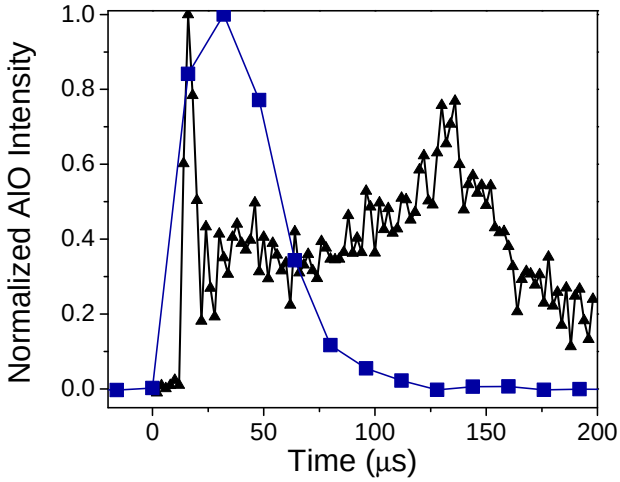

(c) 20%-40-μm aluminum

Figure 5.11: The normalized AlO emission intensities from both experiment setups for each aluminized charge show different histories, which can affect measurement interpretation. The time resolutions for the confined (triangles) and unconfined (squares) setups are 2 μs, and 16 μs, respectively.

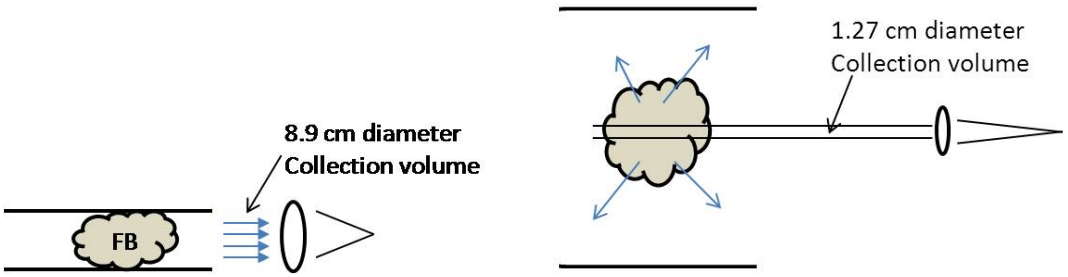

(a) Confined (b) Unconfined

Figure 5.12: Schematic showing the difference in optical collection for the confined and unconfined setups, FB: fireball.

5.4 Effect of Temperature

AlO emission is proportional to the number density of gaseous AlO in the B state, which is proportional to the total concentration of AlO, and dependent on temperature. The AlO emission increases exponentially with temperature, and differences in measured AlO emission will also be the result of those different temperatures. The population ratio n_1/n_2 for the same energy level of ϵ, but at different temperature, can be determined by:

$$\frac{n_1}{n_2} = \frac{Z_2}{Z_1} exp\left(\frac{\epsilon(T_1 - T_2)}{kT_1T_2}\right) \tag{5.1}$$

where Z is the partition function, and the subscripts denote values at the two temperatures T_1 and T_2. If the concentration is assumed to be constant, then the ratio of the population in the B state population at $T_1 = 4000\ K$ to $T_2 = 3000\ K$ is 9.6, i.e., the population in the B state at 4000 K is almost 10 times the population at 3000 K, an order of magnitude difference. Details of the population ratio calculation can be found in Appendix C.1. Therefore, comparing absolute the AlO emission intensity values alone may not be sufficient to indicate which test has more aluminum combustion for higher temperatures.

5.4.1 Temperature Measurement Results

Pyrometry Measurments Results

The temperatures from the pyrometer measurements from the blast chamber for three aluminized charges and the bare charge are shown in Figure 5.13. The temperature measureed is a result of the condensed phase emission and is generated from a spatial average of the luminosity. The reasons for the extreme temperatures (greater than 5000K) during the first 20 μs are discussed in Section 5.4.2.

The aluminized charges have higher temperatures than the bare charge, as expected, indicating that the addition of aluminum increases the temperature. Prior to 200 μs, the temperatures between the aluminized charges differ. After the peak temperatures, the 20%-40-μm-Al charge temperaure begins as the highest, then has the steepest decline until it becomes the same temperature, within the error, as the 20%-3-μm-Al charge. The temperature of the 20%-40-μm-Al charge starts 3000 K above the 20%-3-μm-Al charge. Both fine aluminum (3-μm) charges have a similar decrease in temperature with time and consistantly differ by over 1000 K. The temperatures from the two 20 percent aluminum charges are very similar after 200 μs and the average temperatures after 230 μs are within 1 percent of each other. The average temperatures based on the time frames given in Table 5.5 show the differences between the aluminized charges and the repeatabilty using the 50 percent aluminum charges. The average temperature of the 50 percent aluminum charge is higher by almost 1000 K than the 20 percent aluminum charges. The 50 percent Al charge average temperaures are within 2 percent of each other.

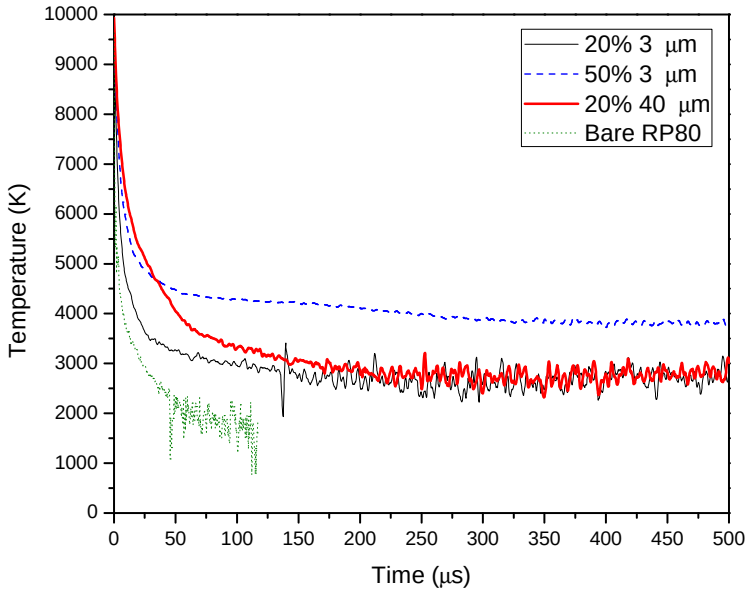

Figure 5.13: Comparison of temperatures from all charges.

Table 5.5: Average temperatures for blast chamber experiements.

Test	Al Composition	Average Temperature (K)	Error (K)	Time Range (μs)
0629 20A	20%-3-μm	2784	184	200-1800
0629 20C	20%-40-μm	2770	212	200-1800
0626 50	50%-3-μm	3613	193	400-1800
0630 50	50%-3-μm	3697	202	400-1800
0716 50	50%-3-μm	3608	285	400-1800

The temperature from the pyrometry measurements is subject to uncertainty caused by a non-constant emissivity of aluminum oxide particles as a function of wavelength in the range of temperatures measured[67]. Specifically, Lynch et al.[67] found for Al_2O_3 particle clouds that the error in the measured temperature—when assuming gray body emitters—is low in the range of 3000–3300 K, but for higher temperatures the temperature can be under predicted by up to 10 percent, and for temperatures lower than 2500 K the temperature can be over predicted by up to 20 percent in optically thin conditions; however the error in temperature outside the range of 3000–3300 K would be less for optically thick conditions, including the fireball from the charges used in the current study. Limitations to assumption

of a gray body temperature measurement include the optical depth of the cloud (or fireball) of emitters, the presence of other emitters besides Al_2O_3, and the size distribution of the particles, such that as the size of the particles increases, the gray assumption is better[67]. The key finding from Lynch et al.[67] related to the current work is that the gray body assumption for alumina particles is good for micron sized particles between 3000–3300 K, and is okay for optically thick conditions outside this range. Therefore, outside this range, the measured temperatures are apparent temperatures and have an uncertainty of up to 20 percent for the lower temperatures. The uncertainty is less for the higher temperatures; however, the temperatures still represent an apparent temperature of the fireball.

Temperature Measurements from AlO Emission Spectra

The condensed phases in the fireball emit radiation, which shows up as background emission under the AlO emission. Planck's black body equation—Equation (5.2), where C_1 and C_2 are the Planck constants—can be fit to the background emission for regions in which the spectra are free of distinguishable features such as AlO. Using this curve fitting, it is possible to estimate the condensed phase temperature.

$$L_\lambda = \frac{C_1}{\lambda^5[exp(C_2/\lambda T) - 1]} \tag{5.2}$$

The condensed phase temperature plot fits from the chamber tests are presented in Figure 5.14. The temperature is greater during the tests in which the tail AlO emission was measured than those without it for the same charge. In Figure 5.14, the temperatures are compared in the different environments, by charge type. For the 20%-3-μm-Al charge, Figure 5.14a, the temperatures are comparable among the different environments. The 50%-3-μm-Al and 20%-40-μm-Al charges have the same temperature pattern: the air and O_2 tests—which have the tail AlO—have higher temperatures (see Figures 5.14b and 5.14c), and the higher temperatures are maintained longer. The CO_2 tests start at temperatures

comparable to the air tests, but quickly decrease. The N_2 tests have lower temperatures, but the same decreasing temperature as a function of time as the CO_2 tests. The temperatures are approximately the same for each charge fired in CO_2 and N_2, with respect to the environment.

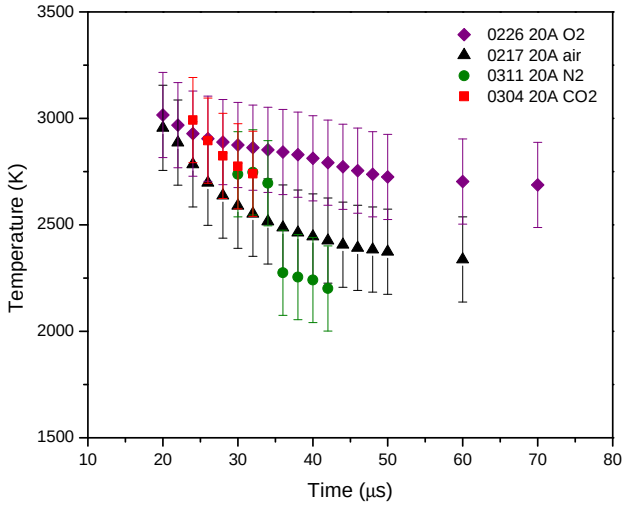

(a) 20%-3-μm-Al

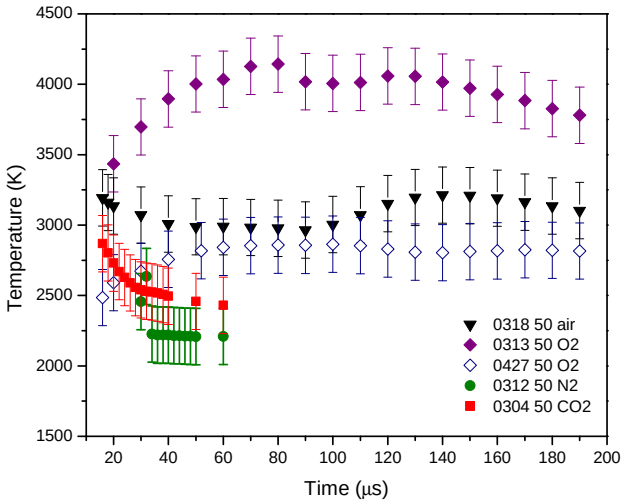

(b) 50%-3-μm-Al

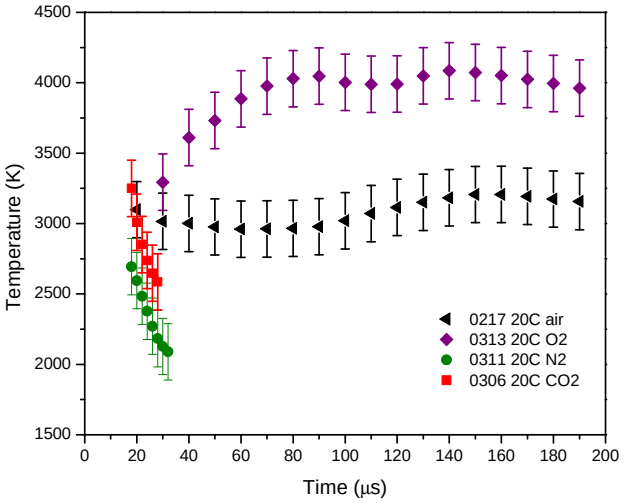

(c) 20%-40-μm-Al

Figure 5.14: Condensed phase temperature measurements from tube chamber tests for each aluminized charge in each environment (temperatures determined from spectrometer measurements).

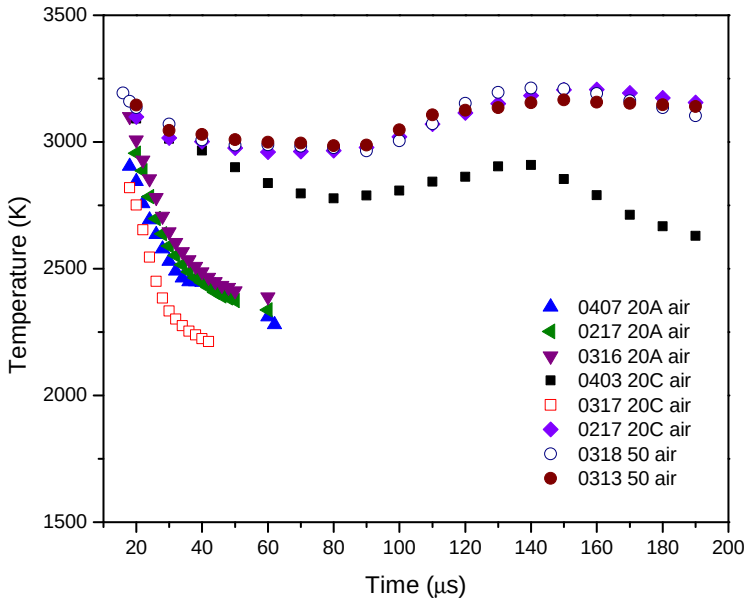

Figure 5.15: Condensed phase temperatures each charge tests in air (temperatures determined from spectrometer measurements).

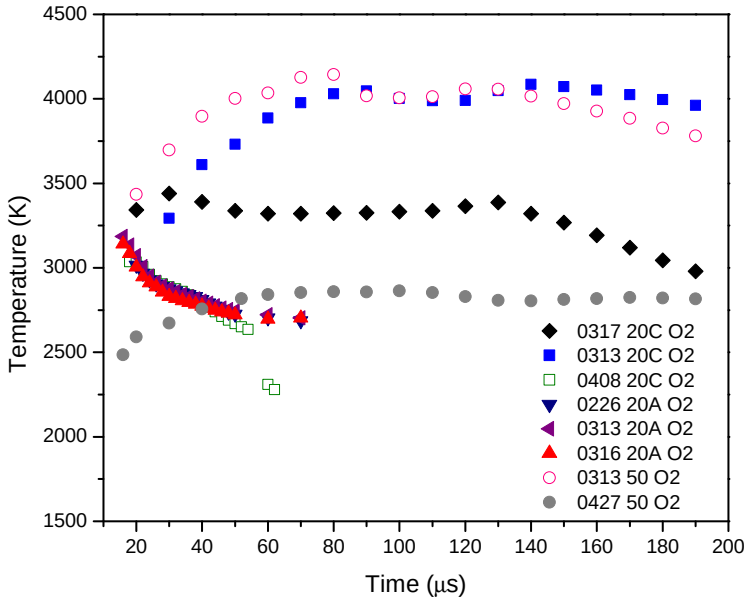

Figure 5.16: Condensed phase temperatures each charge tests in O_2 (temperatures determined from spectrometer measurements).

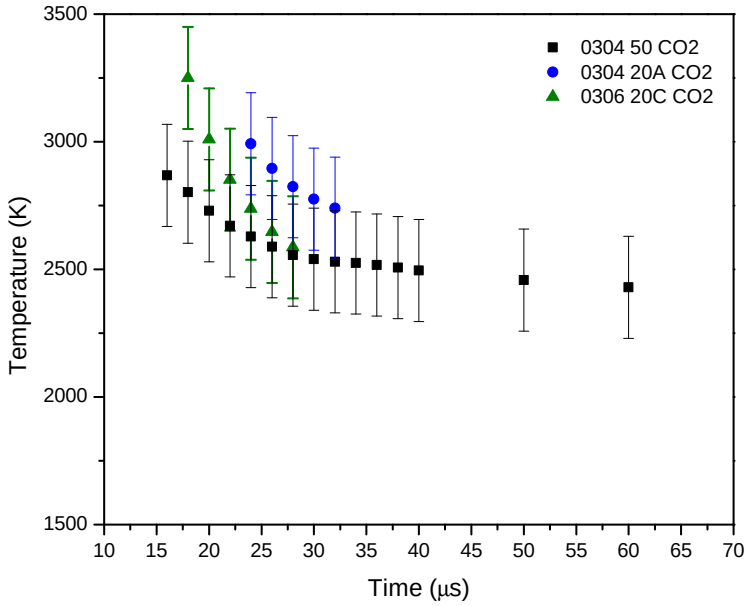

Figure 5.17: Condensed phase temperatures each charge tests in CO_2 (temperatures determined from spectrometer measurements).

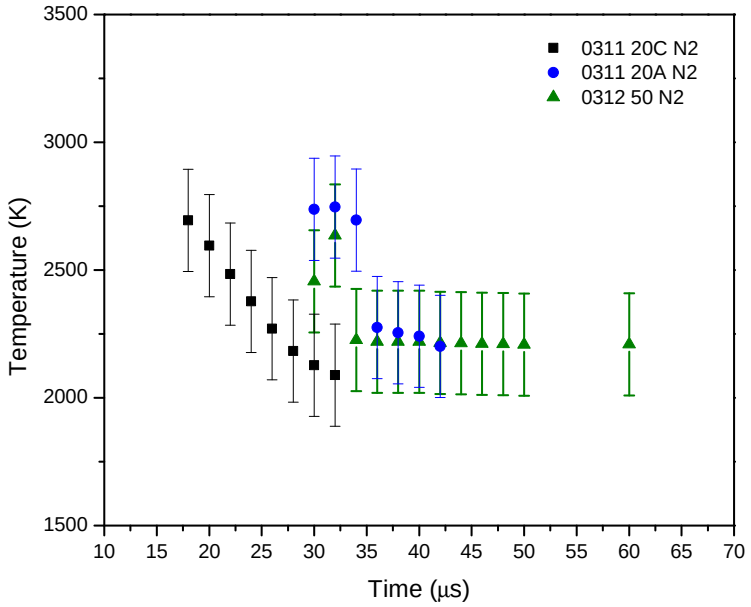

Figure 5.18: Condensed phase temperatures each charge tests in N_2 (temperatures determined from spectrometer measurements).

5.4.2 Discussion of High Early Temperatures

The extreme temperatures—greater than 5000 K—during the first 20 μs may not be physical and may be representative of non-equilibrium conditions. However, some evidence does exist for very high temperatures immediately after breakout. At the shock wave interface—to maintain continuity—the initial temperature jump across the jump must be very large—estimated to 10,000 to 15,000 K[80]. Recent experiments at the University of Illinois by the Energetics Research Group show that at breakout plasma effects exist during at least the first 10 μs[80]. The resulting temperatures have been measured to be 13,100 K from 0–1 μs, 10,700 K from 2–3 μs, and 7,000 K from 4–5 μs. These experiments indicate that the breakout temperatures of 10,000 K measured using the pyrometer are of the correct order, although short lived. The breakout work suggests that temperatures stabilize to approximately 3000 K before 20 μs after breakout. Emission measurements before the stabilization are likely affected by the high transient temperatures.

5.4.3 AlO Emission Compared to Temperature as a Function of Time

The temperatures determined from the pyrometer measurements compared to the normalized AlO emission intensity for the Al-loaded charge are shown in Figure 5.19. The temperature measured assumes a greybody thermal distribution and is a spatial average of the luminosity.

The AlO emission is greatest near the peak temperature, and peaks during the period in which the temperature decreases most rapidly. Emission from the hottest regions is more intense than other regions, but the emission measurements are a spatially weighed average measurement. If some particles are burning at a higher temperature, and therefore have more emission, then it is possible the AlO emission measurement is disproportionally weighed to higher temperature regions. The actual concentration of burning aluminum particles is unknown because hot particles emit most intensely when the temperatures are the highest because the intensity is proportional to the fourth power of temperature, i.e., $I \propto T^4$, and

hotter particles will outshine cooler ones. As the fireball cools, the amount of measured AlO emission also decreases. The decrease in AlO signal with time can result from either a reduction in AlO concentration, a decrease in AlO temperature, a change in optical depth, or fireball expansion. In these experiments, as well as those of most other investigations, it is difficult or impossible to distinguish between these effects.

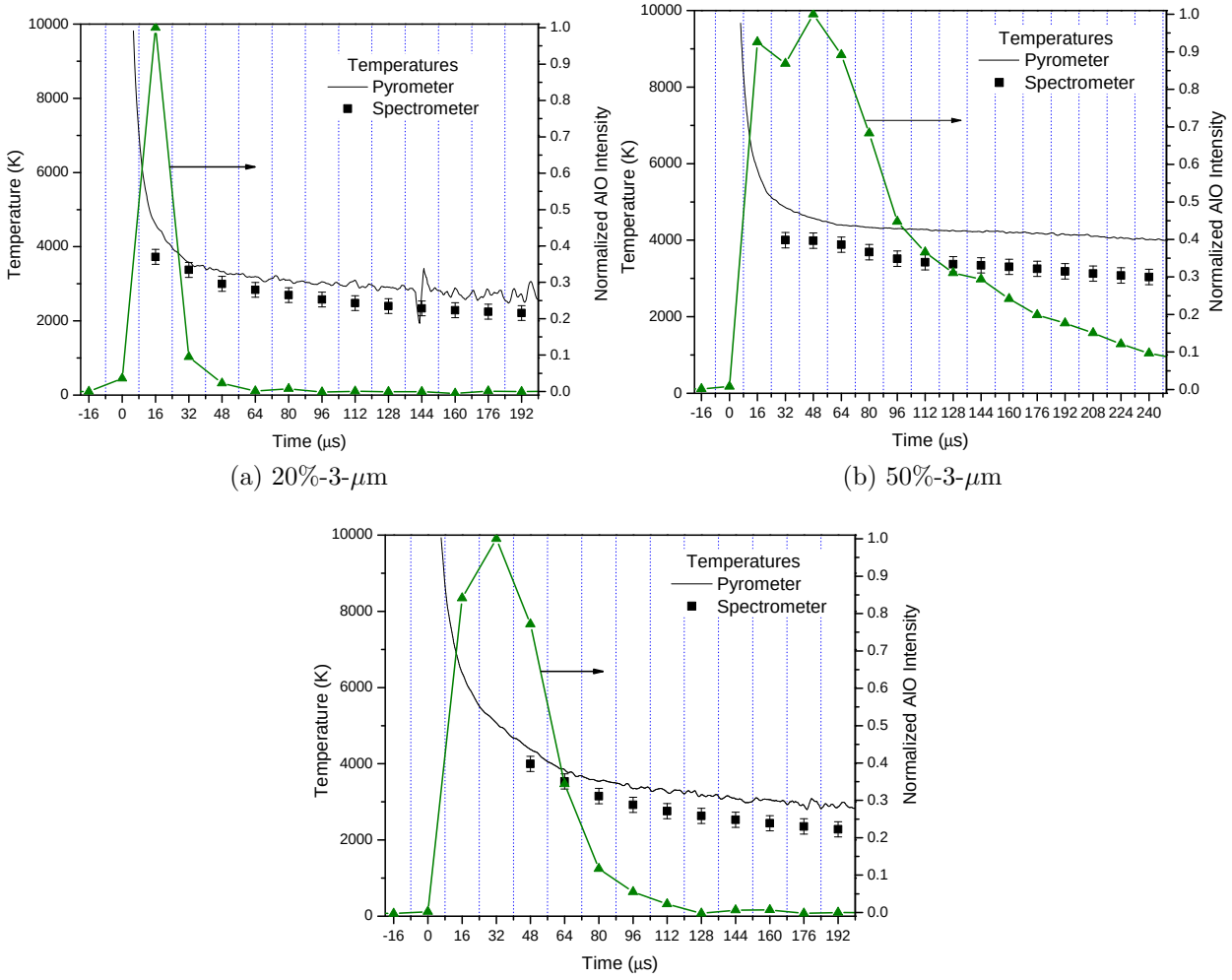

(a) 20%-3-μm

(b) 50%-3-μm

(c) 20%-40-μm

Figure 5.19: Condensed phase temperatures from two measurement techniques compared to normalized AlO emission for each aluminized charge. Data is from tests in the blast chamber.

For the spectrometer determined temperatures, temperatures could not be fit to the spectra at the peak AlO emission and just before the peak. The grid lines show the time

resolution of the spectrometer data points. The temperatures determined from the spectrometer are always lower than the pyrometer temperatures at the same time, but both techniques show the same development with time. The peak temperature is approximately the same for all charges, around 4000 K, slightly lower for the 20%-3-μm-Al charge, based on the spectrometer measured temperatures. For the 20%-3-μm-Al charge, Figure 5.19, the difference between the two techniques is less around the peak and approximately 500 K at the later times. For the 20%-40-μm-Al charge, Figure 5.14c, the difference between the two temperatures is approximately 800 K and less at earlier times around the peak AlO intensity. The biggest difference between the two temperature techniques is for the 50%-3-μm-Al charge, Figure 5.19b—after 100 μs, the difference is 1000 K.

Both the spectrometer and the pyrometer determined temperatures are apparent temperatures of the fireball, rather than the true temperature. Differences in how the radiation is measured—i.e., broadband radiation at all wavelengths (450–650 nm) as for the spectrometer, or at two particular wavelengths as for the pyrometer—will contribute to different apparent temperatures and thus, the temperatures from the two techniques will be different. The major source in the differences is from changes in emissivity of the fireball. Both techniques assume gray body; however, as discussed above, the gray body assumption is best for an optically thick explosive fireball in the temperature range of 3000–3300 K at the pyrometer wavelengths[67], which is near the temperatures measured, but outside that temperature range the gray body assumption becomes less valid. In addition, the validity of the gray body assumption at the spectrometer wavelengths is unknown, and it is likely that the emissivity is not constant with respect to wavelength across the entire wavelength range of the spectrometer and the pyrometer; and thus would contribute to different measured temperatures as seen.

The temperatures compared to the AlO emission intensity for the 20%-3-μm-Al charge from tests in the tube chamber are shown in Figure 5.20. The CO_2 temperature is comparable to the O_2 and air temperatures, even though the AlO emission signal is not significant. The

temperature in N_2 drops most rapidly.

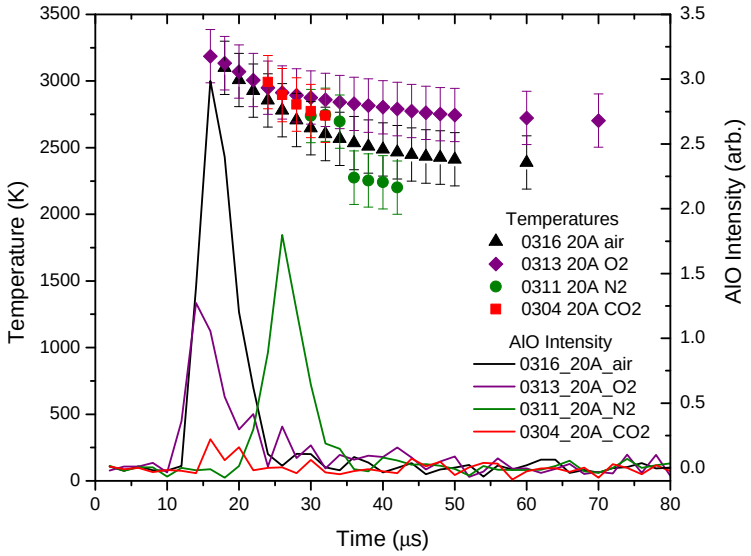

Figure 5.20: Comparision of temperatures to the AlO intensity for 20%-3-μm Al charge tests in each environment, (temperatures determined from spectrometer measurements). Data is from tests in the tube chamber.

In Figures 5.21 through 5.24, the temperature and AlO emission intensity are compared for the air and O_2 environments for the 20%-40-μm-Al and 50%-3-μm-Al charges from tests in the tube chamber. The temperatures show the same development as the AlO emission signal, except for the 50%-3-μm-Al charges in O_2, in which the temperatures do not correspond, but the AlO emission signals are similar.

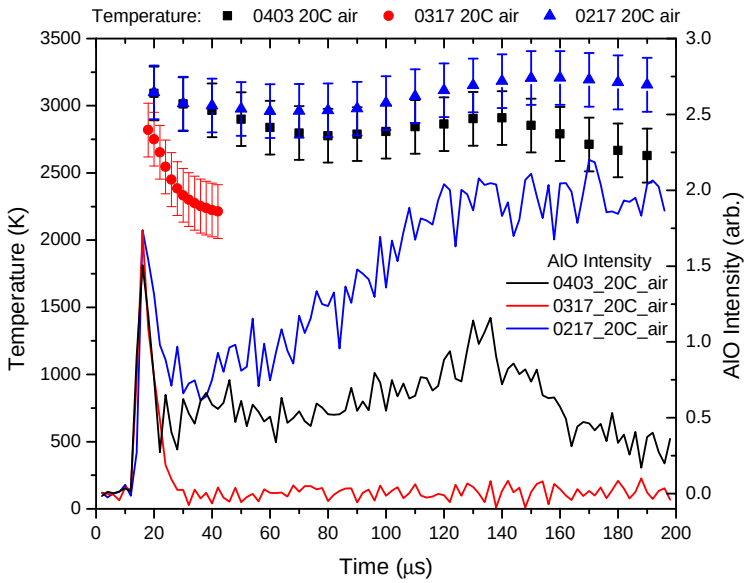

Figure 5.21: Comparision of temperatures to the AlO intensity for 20%-40-μm Al charge in air, (temperatures determined from spectrometer measurements).

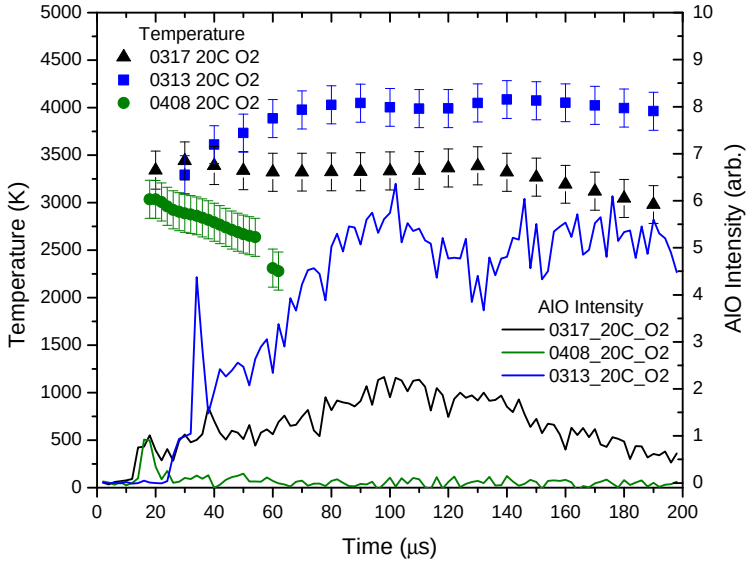

Figure 5.22: Comparision of temperatures to the AlO intensity for 20%-40-μm Al charge in O_2, (temperatures determined from spectrometer measurements).

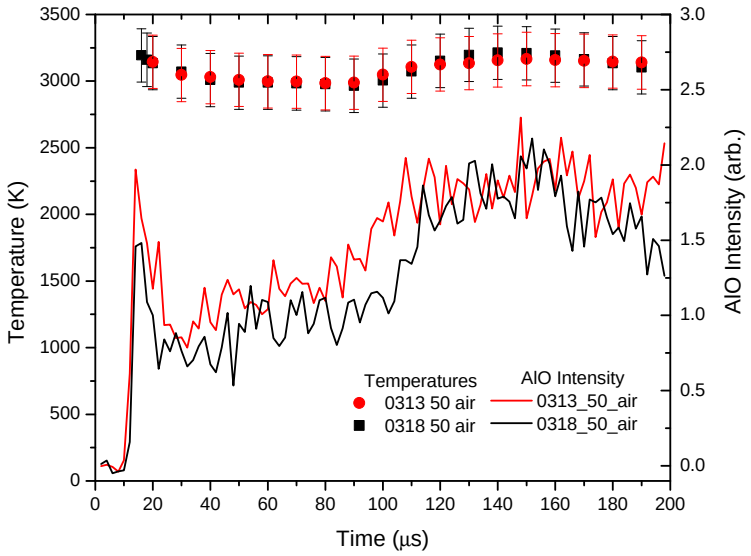

Figure 5.23: Comparision of temperatures to the AlO intensity for 50%-3-μm Al charge in air, (temperatures determined from spectrometer measurements).

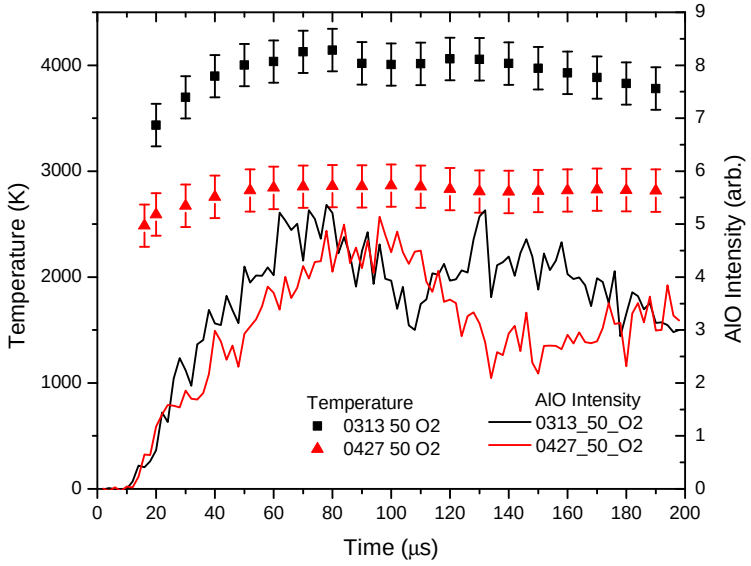

Figure 5.24: Comparision of temperatures to the AlO intensity for 50%-3-μm Al charge in O_2, (temperatures determined from spectrometer measurements).

For the tests in air and O_2, the no tail AlO emission tests have quick temperature drops, and those tests having an AlO emission tail, the temperature is maintained throughout the time frame. The maintained temperatures that were measured may be partial caused by data collection settings. The short exposure time (2 μs) used for the tube chamber tests

may not be able to tell the whole story of luminosity from the condensed phase, if not enough light was collected to enable a temperature fit. After the initial high temperature peak, the temperature rapidly decays to an almost constant temperature that lasts for 100s of microseconds, as shown by the blast chamber pyrometry data measurements in Figures 5.19, 5.56.

5.5 Effect of Hot Al_2O_3

The AlO emission signals in both air and pure O_2—for the tube chamber tests when comparing the AlO emission to the X-ray analysis results—beg the question of what role the thin layer of alumina (Al_2O_3) on the surface of the Al particles plays. At the temperature of the condensed phase species in the fireball, the alumina layer on the aluminum particles is in the liquid phase on the aluminum particle surface. The alumina may dissociate and recombine, emitting AlO in the process. Schlöffel et al.[78] speculated that this layer of alumina was a reason as to why AlO emission was measured during shock wave experiments of aluminum particles in Ar.

Figure 5.25 shows the average and standard deviation for the AlO emission peak value—a single 16 μs exposure which dominated the total AlO emission—for each type of charge test. The alumina loaded charge average includes the AlO emission intensity measurement from both environments because the AlO emission signal was the same for the alumina loaded charges in air and N_2. The AlO emission for the alumina charges was 46 percent the strength of the aluminum charges AlO emission signal in air. The AlO emission signal was reduced by 33 percent for the aluminum charge in N_2 compared to the charge in air.

The initial blast wave impulse from the Al_2O_3-loaded charge was reduced by 20 percent—shown in Figure 5.26—supporting the assumption that the alumina is inert with respect to the output energy.

The amount of AlO emission from the oxidation layer on the aluminum particles is not a

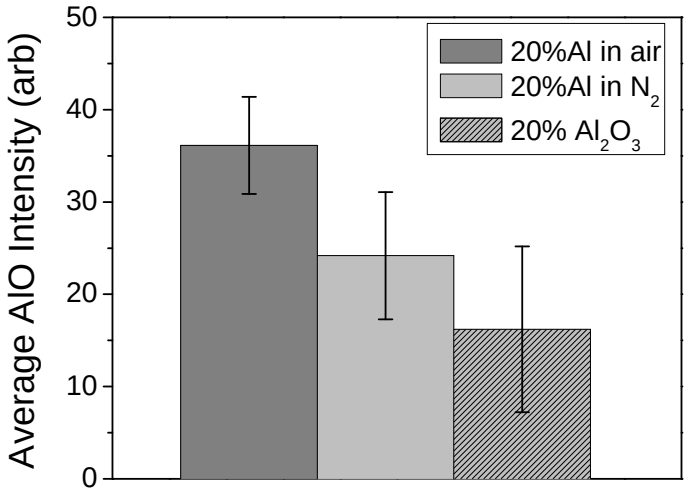

Figure 5.25: Average integrated AlO values at peak AlO emission, one 16 μs exposure frame, for each type of charge.

function of the environment since the alumina charges have the same intensity in air and N_2. The difference between the AlO intensity for the Al-loaded charges in air and N_2 may give a measure of the additional oxidation from reactions with the oxygen in the air; however it is not a straight forward calculation. While the amount of AlO emission from different reactions cannot be determined, these different charge tests show that the amount of AlO from hot alumina is significant and cannot be ignored in the AlO emission measurement interpretation.

5.6 Effect of Al Particle Location

The location of the aluminum particles within the fireball affects whether or not AlO emission can/will measured or not. The optical thickness of the fireball biases the measurements to the outer surface of the fireball. As shown and discussed below, when a layer of grease is put on the tip of an aluminized charge—reducing the amount of aluminum on the outer edge of the fireball—a smaller AlO emission signal is measured. Alternatively, if the aluminum powder is attached to the end of a bare charge, a significant AlO emission signal is measured. When a gap exists between a bare charge and the aluminum powder, the amount activiation

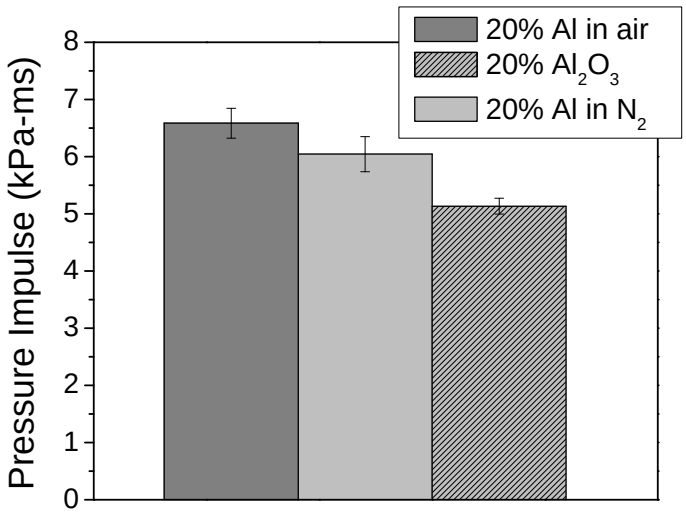

Figure 5.26: Average initial blast wave impulse for Al- and Al_2O_3-loaded charges.

of the aluminum decreases as the gap distance increases, as described in Section 5.6.3.

5.6.1 Al-Loaded Charge Having Grease Layer

The pressure impulses—from the initial blast wave and shown in Figure 5.27—were within 5 percent for the Al-loaded charge and the Al+grease charge, indicating that the same amount of blast driving as a result of aluminum combustion occurred.

The AlO signal from the charge having a grease layer was only 11 percent of the AlO signal from the unmodified aluminum charge in air, as shown in Figure 5.28. The results from the different loaded charges further indicate that the AlO emission measurements cannot be necessarily interpreted as proportional to aluminum combustion.

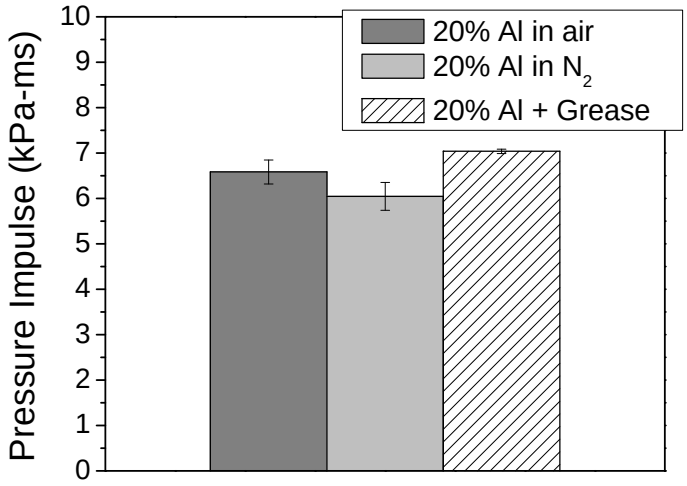

Figure 5.27: Initial blast wave positive impulse for Al-loaded charges with and without a grease layer. The grease layered Al-loaded charge was tested in air.

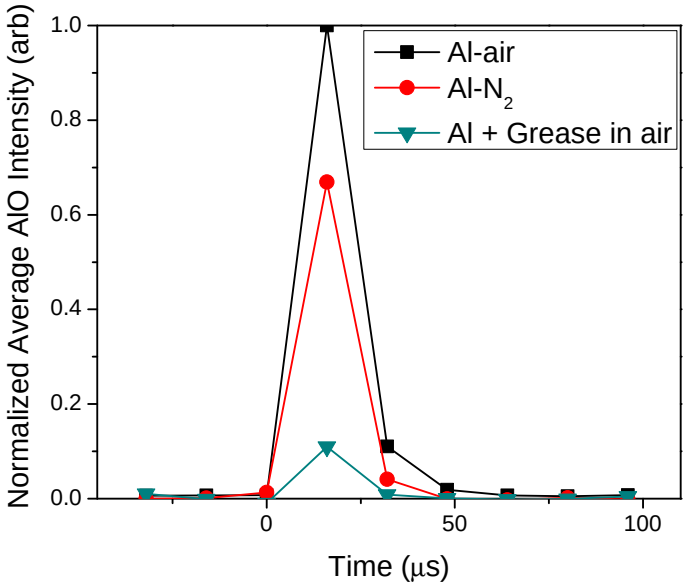

Figure 5.28: Normalized AlO emission signal for Al-loaded charges with and without a grease layer.

The results from the grease-layered charge confirms that the spatial distribution of the burning Al within the fireball affects the amount of measured AlO emission. The same amount of aluminum burns in both the Al-air, and Al+grease cases, but the latter case has significantly less AlO emission measured. The initial blast wave pressure impulses were within 5 percent for the Al and the Al+grease cases, but lower by 20 percent for the Al_2O_3

charge. The pressure measurements support the assumption that the same amount of aluminum burns for the two aluminum loaded charges, with and without a grease layer.

5.6.2 End Loaded—Al Particles Attached to a Bare Charge

A larger AlO emission intensity was measured for the end-loaded bare charge compared to the Al-loaded charge, shown in Figure 5.29. For these tests, the time resolution of spectroscopy measurements was 2 μs. A bare charge with aluminum powder attached to the charge tip ensured the aluminum particles burned on the outer surface of the fireball. The Al-loaded charge contained 24.6 mg of aluminum, while the end-loaded charge contained 11.7 mg of aluminum particles. The end-loaded charge had less than half the number of aluminum particles, but had more than twice the temporally integrated AlO emission. Pressure measurements were not taken for these tests; however, X-ray analysis of the residue particles from each test show near complete oxidation of the aluminum particles. Therefore, it can be assumed that the aluminum particles burned completely in both cases, whether or not the AlO emission measurement indicates it occurred.

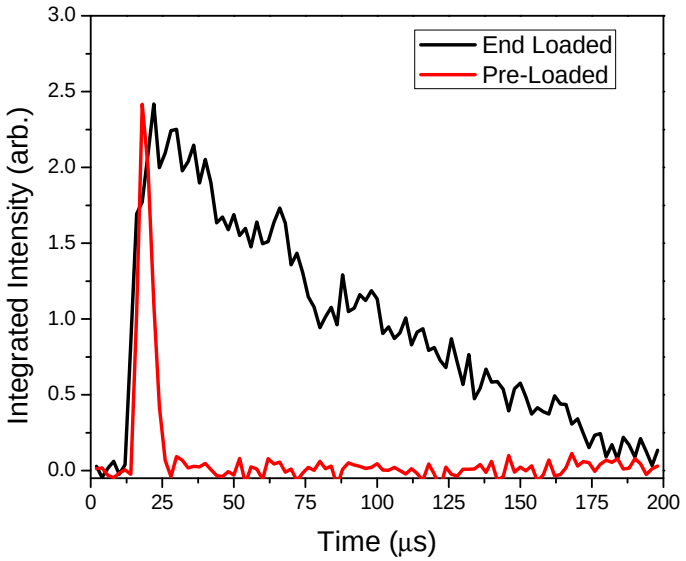

Figure 5.29: When the Al burns on the outer surface of the fireball, the AlO emission intensity is greater than when most of the Al burns inside the fireball.

For the end loaded bare charges in the tube chamber—shown in Figure 5.30—the amount of aluminum on the charges was 11.7 mg, 11.3 mg, 13.7 mg, and 14.2 mg for the tests in air, CO_2, N_2 and O_2, respectively. In air, the AlO emission peaks quickly, but then has a slow decline as time increases. Tests in CO_2 and O_2 show similar developments: a gradual increase and decrease in AlO emission signal and both are delayed. The end-loaded test shows the greatest AlO emission signal of all the tests in CO_2 in the tube chamber, and is similar in shape to the O_2 test—a delayed peak and slow increase and decrease in intensity to/from the peak. The peak intensity of the end-loaded tests match the intensity from the 50%-3-μm-Al and 20%-40-μm-Al charges for the tests in O_2.

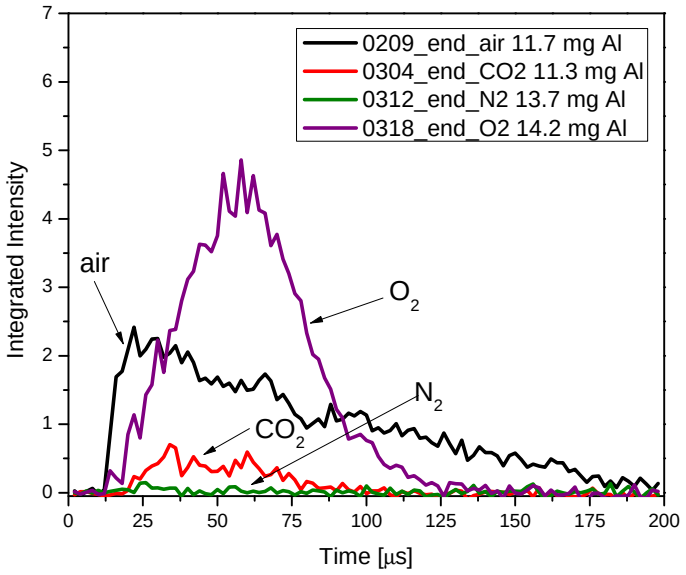

Figure 5.30: End-loaded test results from the tube chamber using different ambient environments.

Two end-loaded tests were completed in the tube chamber in an ambient environment of O_2, and the results are shown in Figure 5.31. Two different amounts of Al powder were used—7.3 mg and 14.2 mg—as denoted in the plot legend. Despite the difference in initial aluminum powder loading between the tests, the tests have similar AlO emission intensity trends—both tests show a slow increase in intensity to a peak, and a slow decrease back to zero AlO emission signal. The test having less aluminum powder peaks earlier and has a

lower peak intensity which occurs at approximately 25 μs. The test having more aluminum peaks later and the entire AlO emission signal last approximately 100 μs compared to 50 μs for the first test. The results show that when more aluminum particles are on the outer edges of the fireball, more AlO emission is measured.

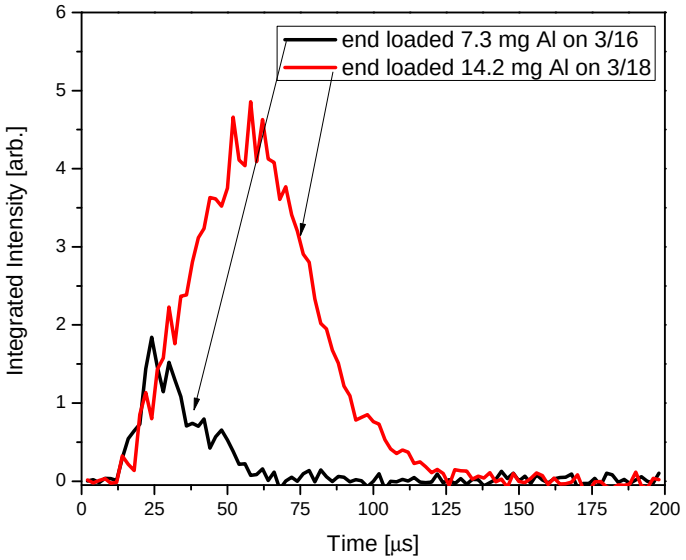

Figure 5.31: End-loaded bare charge in O_2 repeated tests.

The residue particles collected from the end-loaded experiments performed in the tube chamber were also analysed using the SEM/EDS. The results comparing the residue oxidation to the total AlO emission are shown in Figure 5.32. Similar to the Al-loaded charges, all particles showed significant oxidation. The lowest oxidation was from the tests in CO_2 and N_2 at 67 to 75 percent oxidized. The two tests in O_2 had the same oxidation. For aluminum particles on the outer edge of the fireball, the AlO emission measured does not correlate to the oxidation amount measured using X-ray analysis.

Similar end-loaded experiments were completed in the blast chamber in air and N_2, and used two different amounts of aluminum powder. The results from the AlO emission measurements are shown in Figure 5.33. For the tests in air, a larger amount of Al powder resulted in more AlO emission signal, as was seen in the tube chamber tests. The AlO signal was weaker in the N_2 environment compared to in air, although the charge having a

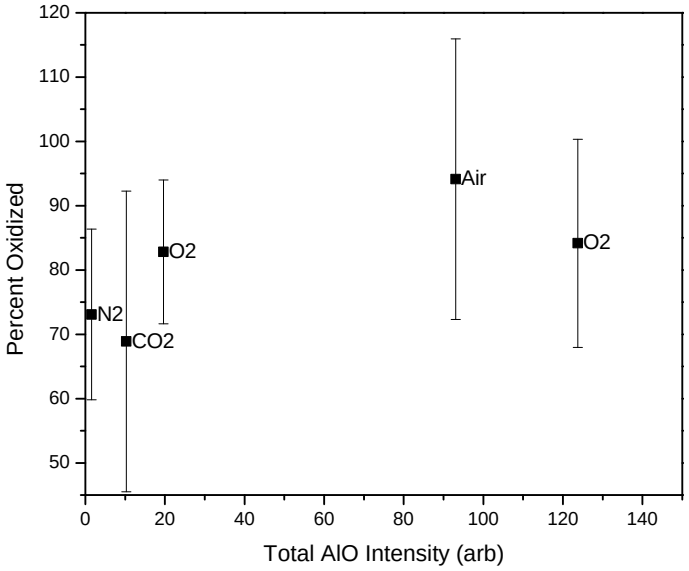

Figure 5.32: Residue oxidation for the end-loaded tests in the tube chamber.

larger amount of aluminum powder had a lower AlO emission signal. For the tests in air, the AlO emission signal lasts longer than the 20%-3-μm-Al charges—as was seen in Figure 5.11(a)—such that it is not dominated by one frame of AlO emission.

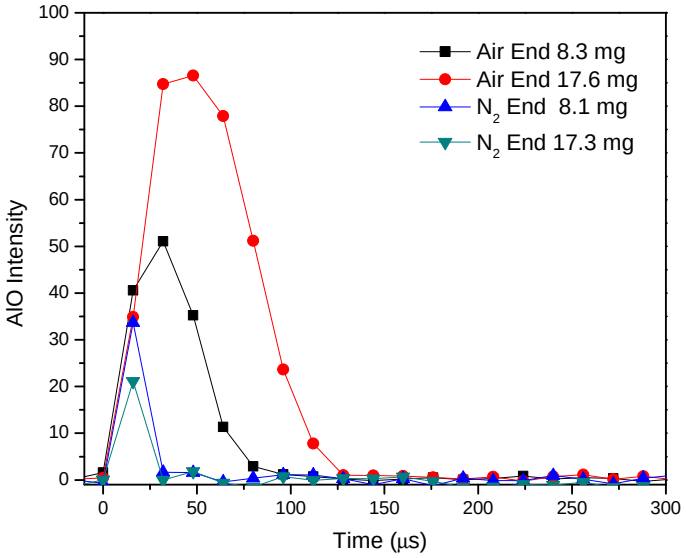

Figure 5.33: Blast chamber tests' AlO emission for end-loaded charges.

The initial blast wave impulse and peak pressures for the four end-loaded tests in the blast chamber are presented in Table 5.6. At the close pressure transducer (21.3 cm), the

impulse is smaller for the end-loaded charges having a larger amount of aluminum powder. The lower impulse for a larger amount of aluminum indicates that the aluminum powder on the outer edge of the fireball contributes less to the energy output than aluminum burning on the inside of the fireball. However, the peak pressures were higher for the charges having more aluminum powder. At the outer pressure transducer (32.1 cm), the impluse increased for a larger amount of aluminum powder, and the peak pressures increased. As expected, the impluse and peak pressures were higher for the tests in air compared to N_2 for each of the similar amounts of aluminum powder.

Table 5.6: Initial blast wave impulse and peak pressures for the end-loaded charges.

		21.3 cm (8.4 in)		32.1 cm (12.65 in)	
Environment	Al amount (mg)	First Impluse (kPa-ms)	Peak Pressure (kPa)	First Impluse (kPa-ms)	Peak Pressure (kPa)
Air	8.3	5.17	106.4	2.79	39.9
Air	17.6	5.04	111.3	2.96	46.6
N_2	8.1	3.98	98.79	2.17	36.0
N_2	17.3	3.65	113.7	2.39	38.4

The impulse—measured at the outer (32.1 cm) transducer—as a function of time for the end-loaded charges in the blast chamber—is shown in Figure 5.34. The arrows denote the increasing gap between the impulses from the air and N_2 tests for each of the similar amounts of aluminum powder. The amounts of aluminum powder between the tests are not identical, so it would not be appropriate to subtract the N_2 tests from the air tests; however, the increasing gap between the impulses indicates that as time progresses the aerobic (air minus N_2) component of the reactions occurring becomes increasingly important to the overall aluminum burning.

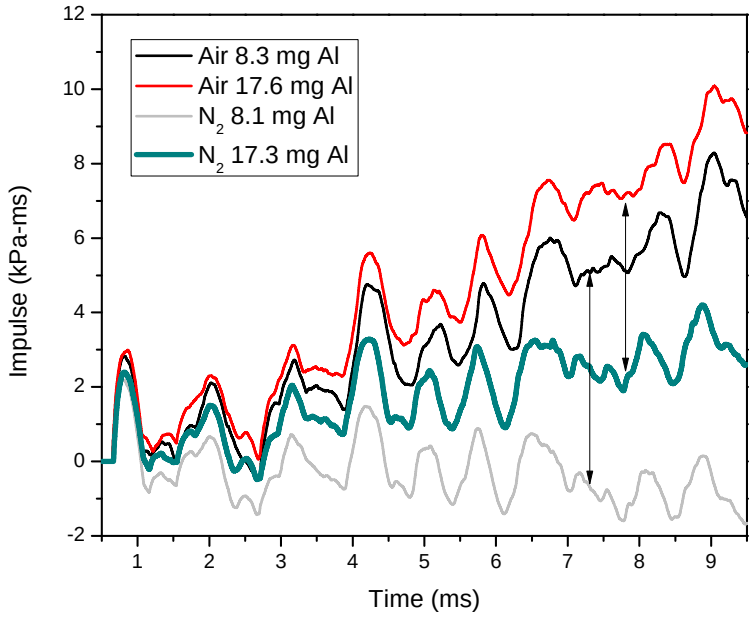

Figure 5.34: Impulse as a function of time for the end loaded charges.

5.6.3 Effect of a Gap between the Al Powder and the Detonator

By varying the distance between the aluminum particles and the initiating charge, the role of the detonation wave on the activation of aluminum can be determined, as well as using the pellet location to control the location of the aluminum in the fireball. The inert pellet comparion to the aluminum pellets determines the amount of energy released as a result of the aluminum pellets in air. The air and nitrogen environment tests separate the contribution of aerobic and anaerobic reactions.

Experiments were conducted in which the gap between a fixed bare charge and an aluminum output pellet was varied, as discussed in Section 4.4.5 The aluminum pellets—24.6 $\pm$ 1 mg 3-μm-Al—were placed on a 2.5 μm thick sheet of Mylar suspended across a steel shim, and in addition to the aluminum pellets, inert pellets made of silicon dioxide (SiO_2) powder were tested. The Mylar was attached to the shims using silicon grease.

Energy Output (Pressure)

The initial blast wave impulse of the bare charge plus aluminum pellet as a function of the gap is plotted in Figure 5.35 for both pressure transducer locations—21.3 cm and 32.1 cm—and for the aluminum pellets in air and nitrogen. The initial blast wave impulse from the SiO_2 pellets is also plotted, and the average of the initial blast wave impulses from these experiments is plotted as a line. Since the SiO_2 is an inert material, the initial blast wave impulse was expected to be constant—independent of the gap distance between the pellets and the Mylar/pellet—which is generally the case as shown in Figure 5.35. The charge diameter (0.295 in) and two times the charge diameter (0.59 in) are also denoted in the plot. The initial blast wave impulse data show that there are no anaerobic effects—the experiments in nitrogen are basically the same as the SiO_2 experiments.

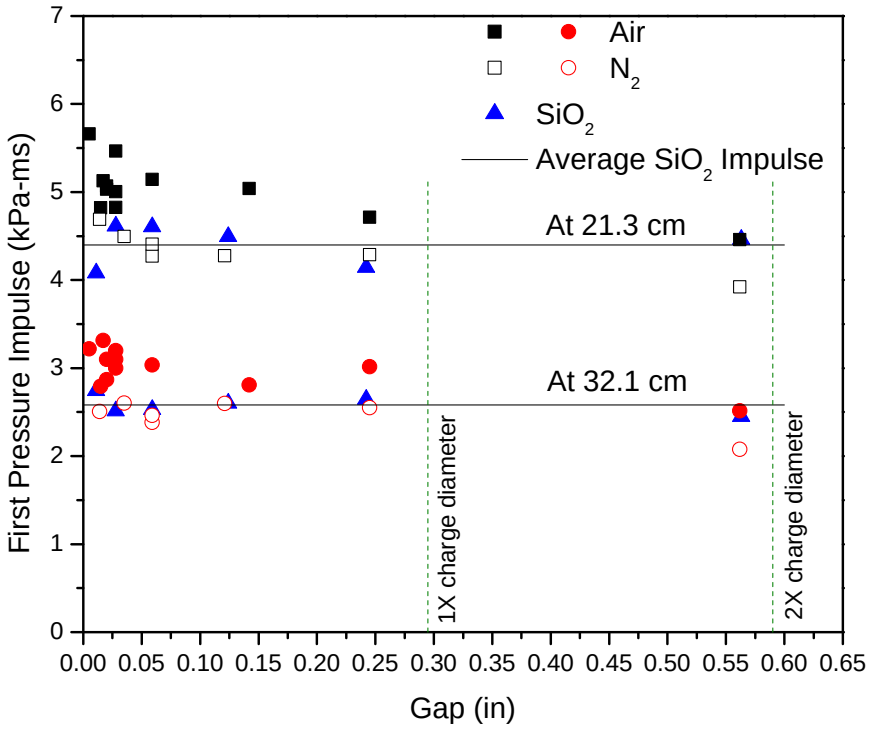

Figure 5.35: Initial blast wave impulse comparison for gap tests—Al in air and N_2, and SiO_2 in air.

As a result of the gap between the charge and the Mylar/pellet, the additional energy

released as a result of the aluminum decreases at both distances from the charge location. The energy released decreasing is also evident in Figure 5.36, which shows the difference in impulse between the aluminum pellet experiments and the SiO_2 pellet experiments from both pressure transducer measurements. To determine the net enhancement of the Al pellet-charge combination, a linear curve was fit to the SiO_2 data which was then subtracted from the Al pellet in air data. While the data at small gaps ($< 0.1\ in$) has significant scatter—most likely a result of measurement uncertainty of the gap distance, variation in the aluminum powder amount, and alignment of the aluminum pellet on top of the charge—the overall conclusion is clear: the enhancement caused by the aluminum burning decreases as the gap increases. The enhancement is effectively zero just before the gap distance is twice the charge diameter, confirming the hypothesis that the aluminum will only be activated close to the charge, and there is no activation at a distance of two times the charge diameter. However, as is discussed below, the aluminum pellets furthest from the charge had measurable amounts of AlO emission, indicating that the aluminum burned even though it did not contribute to the initial blast wave energy release. Understanding that there is decreased blast enhancement from the aluminum further from the charge is important for explosive design in order be able to maximize the initial blast wave energy output, and/or to be able to control the post-detonation burning and temperature by controlling the location of the aluminum particles with respect to the charge.

AlO Emission (Gap Tests)

The time integrated AlO emission is shown in Figure 5.37 for the experiments in air and in Figure 5.38 for the experiments in N_2. Compared to the aluminized charges, which will be discussed later and shown in Figure 5.54, the AlO emission from the Al pellets have a longer duration of the measured AlO emission signal for experiments in air, similar to the end-loaded charge tests. In N_2, there is little to no AlO compared to experiments in air, which shows the AlO emission is dependent on the ambient environment. The longer duration of

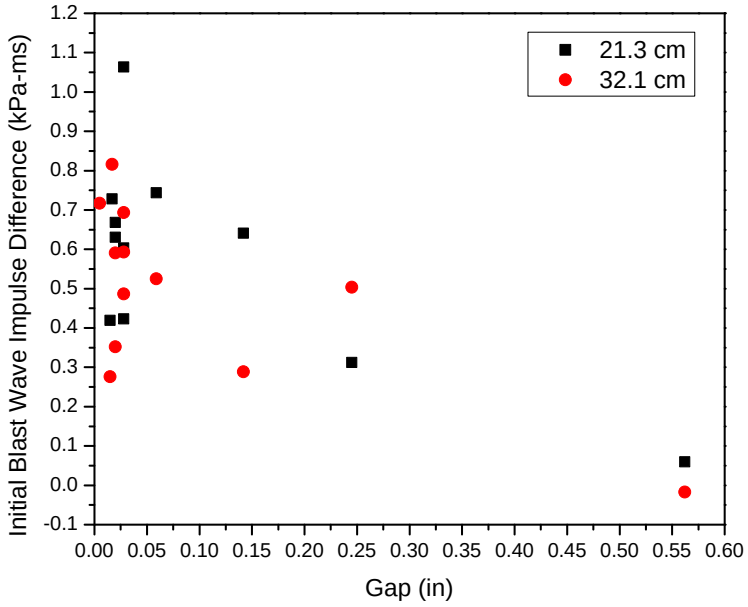

Figure 5.36: Net enhancement from the Al pellets—Al pellet impulse minus SiO_2 pellet impulse, (initial blast wave impulses).

AlO emission measured in air shows the dependence of the aluminum particle location in the fireball on the measured AlO emission. This dependence on particle location was shown to be significant by comparing an aluminized charge to a bare charge having a thin layer of aluminum particle attached to it in Section 5.6.2, and these experiments—using a gap to control the location of the aluminum—confirm the earlier results.

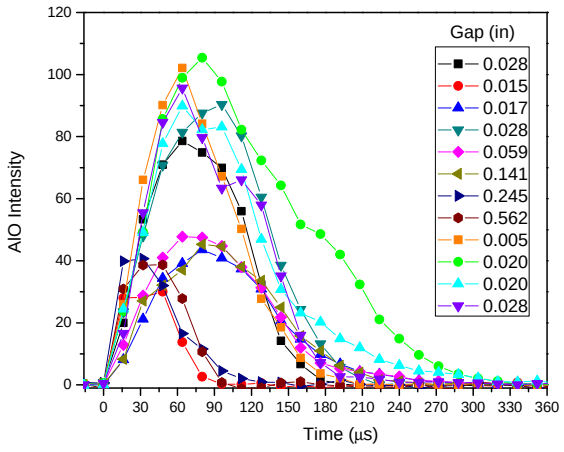

Figure 5.37: AlO emission from experiments in air.

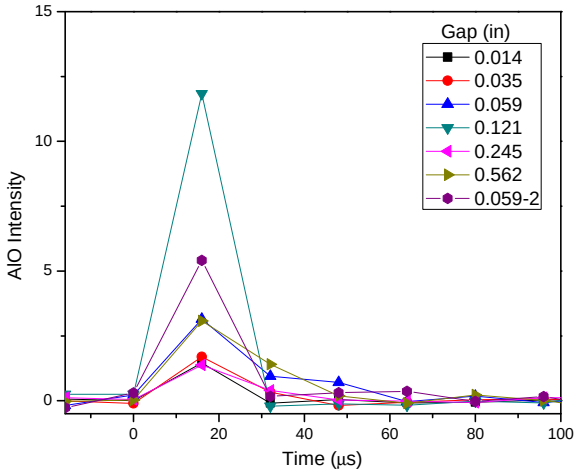

Figure 5.38: AlO emission from experiments in N_2.

From Figure 5.37 a relationship between the gap distance and the peak AlO emission

or AlO emission duration is not evident. The total integrated AlO emission plotted as a function of the gap distance is shown in Figure 5.39. The data plotted in Figure 5.39 implies there may be an exponential dependence for total AlO emission as a function of gap; however, significant scatter exists, because, as suggested earlier there is measurement uncertainty of the gap distance.

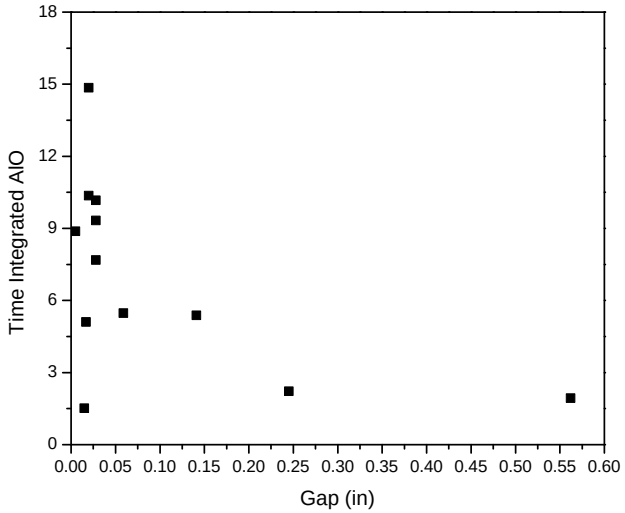

Figure 5.39: Total time integrated AlO emission as a function of gap distance.

AlO Emission vs. Initial Blast Wave Impulse (Gap Tests)

To investigate if AlO emission could be used as an indicator of increased enhancement or not, the total integrated AlO was plotted against the initial blast wave impulse difference—impulse of the aluminum pellet minus the impulse from the SiO_2 pellet—for both pressure transducer locations. As a result of the significant scatter, no clear relationship between initial blast wave impulse and AlO emission exists.

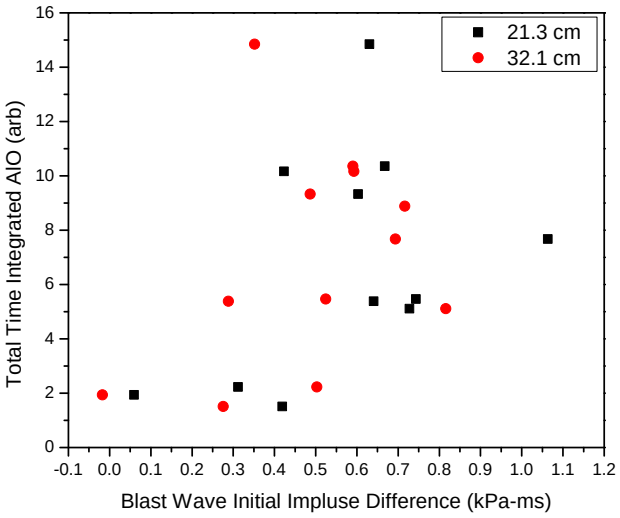

Figure 5.40: Total AlO emission as a function of the initial blast wave impulse difference—Al minus SiO_2.

Temperature Measurements (Gap Tests)

The temperatures measured using the pyrometer for all the aluminum pellet experiments in air are shown in Figure 5.41. The luminosity measured for the experiments in N_2 and using the SiO_2 was too small to be able to accurately determine the temperature . For the experiments in air, the luminosity was not recorded after 2 ms. The minimum and maximum durations of the AlO emission measurements are also denoted in Figure 5.41. The time of the AlO emission measurements corresponds to the higher temperatures and the minimum duration time of AlO emission coincides with the "extremely" high temperatures. Since AlO emission is exponentially dependent on temperature, the higher AlO emission corresponding to the higher temperatures is expected, as discussed previously.

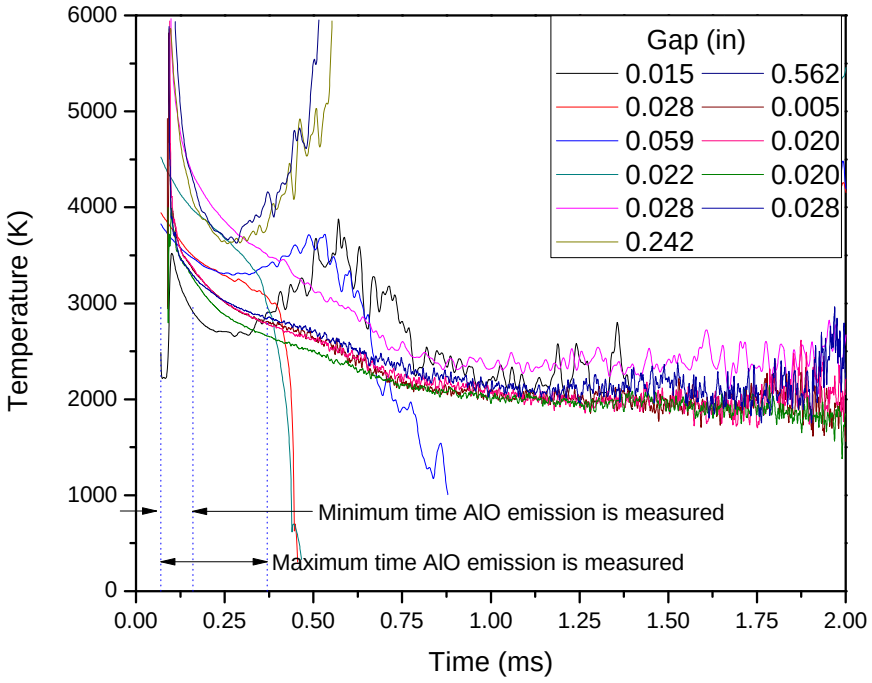

Figure 5.41: Temperature from gap tests in air. (Temperatures measured using the pyrometer.)

5.7 Effect of Al Particle Size and Ambient Environment

While the previous results point out the difficulties in using AlO emission as an aluminum combustion indicator and indicate many that factors can affect AlO emission measurements, a fundamental question of when, where and with what aluminum burns in explosive fireballs still remains to be answered.

The following set of results investigate the effect of the aluminum particle size on the energy output and when and with what the aluminum burns. The experiments were completed using three 20 percent by mass aluminum-loaded charges and using different sized aluminum particles—3-μm, 10-μm, and 40-μm. These aluminum-loaded charges are also compared to a bare charge—no aluminum-loading—and an alumina-loaded charge—20 percent by mass of 3-μm Al_2O_3 particles. In addition to the pressure measurements, temperature via pyrometry and emission spectroscopy measurements were also made. Experiments were conducted in

the ambient environments of air, 40%/60% O_2/N_2, 20%/60% CO_2/N_2, and pure N_2. More experimental details can be found in Section 4.4.4.

5.7.1 Energy Output (Pressure)

Early Time Combustion (<1 ms)

The first set of plots and figures—Figures 5.42–5.45—show the initial blast wave positive impulse, peak pressure, and blast wave time of arrival (TOA). The pressure traces were analyzed to determine the initial blast wave positive impulse and peak pressure. The comparison of the pressure trace to the impulse as a function of time is shown in Figure 5.42 for one case—a 20%-40-μm Al charge in air. The data is from the pressure transducer located 32.1 cm from the charge location. Since impulse is an integration of several data points, and peak pressure is an extrapolation of a fit, it is likely that the impulse data are more reliable for assessing relative blast contributions.

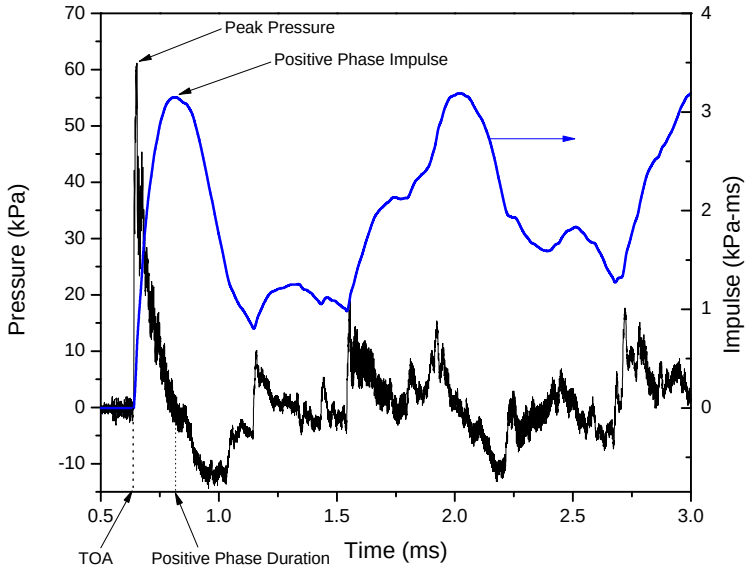

Figure 5.42: Pressure trace analysis.

The peak pressures, initial blast wave impulse, and blast wave time of arrival are shown in Figures 5.43, 5.44, and 5.45, respectively. For these experiments, the Al_2O_3 is assumed to be

inert with respect to the energy output. This assumption is supported by the peak pressure and initial blast wave impulse measurements which show that the initial blast wave impulse from the Al_2O_3-loaded charge is 14 percent lower than the initial blast wave impulse from the bare charge—both in air—at the pressure transducer 21.3 cm from the charge location. The peak pressure for the Al_2O_3-loaded charge is 24 percent lower that the bare charge at the 21.3 cm transducer. Further from the charge location—at 32.1 cm—the difference between the alumina and bare charges is less but still significant—5 percent and 7.4 percent decrease for the initial blast wave impulse and peak pressure, respectively. The Al_2O_3-loaded charge is a good baseline to compare to the Al-loaded charges because the charges have the same amount of explosive and additive—20 percent by mass.

Both the peak pressure and initial blast wave impulse are enhanced by the addition of aluminum to the charge compared to the bare and alumina-loaded charges. Focusing on the experiments in air, the aluminized charges have a higher peak pressure—at the 21.3 cm transducer—than the bare charges by 7 to 18 percent, and higher than the alumina charges by 41 to 56 percent, depending on the aluminum particle size. At the 32.1 cm transducer, the peak pressure from the aluminized charges is 5 to 13 percent higher than the peak pressure from the bare charge, and 13 to 22 percent higher than the alumina charge peak pressure. The initial blast wave impulse is higher from the aluminized charges than the bare and alumina-loaded charges by 19 to 28 percent, and 38 to 48 percent, respectively, for the 21.3 cm transducer. At the 32.1 cm transducer, the initial blast wave impulse from the aluminized charges was higher than the initial blast wave impulse from the bare and alumina-loaded charges by 14 to 20 percent and 19 to 29 percent, respectively.

While the aluminized charges enhanced the energy output, the early time ($t < 1\ ms$) energy output and enhancement weakly depends on the aluminum particle size. The peak pressure at 21.3 cm changes (decreases) by 1 percent for the aluminum particle size increasing from 3 μm to 10 μm, and increases 12 percent as the aluminum particle size increases to 40 μm for the experiments in air. At 32.1 cm the peak pressure increases by less than 2

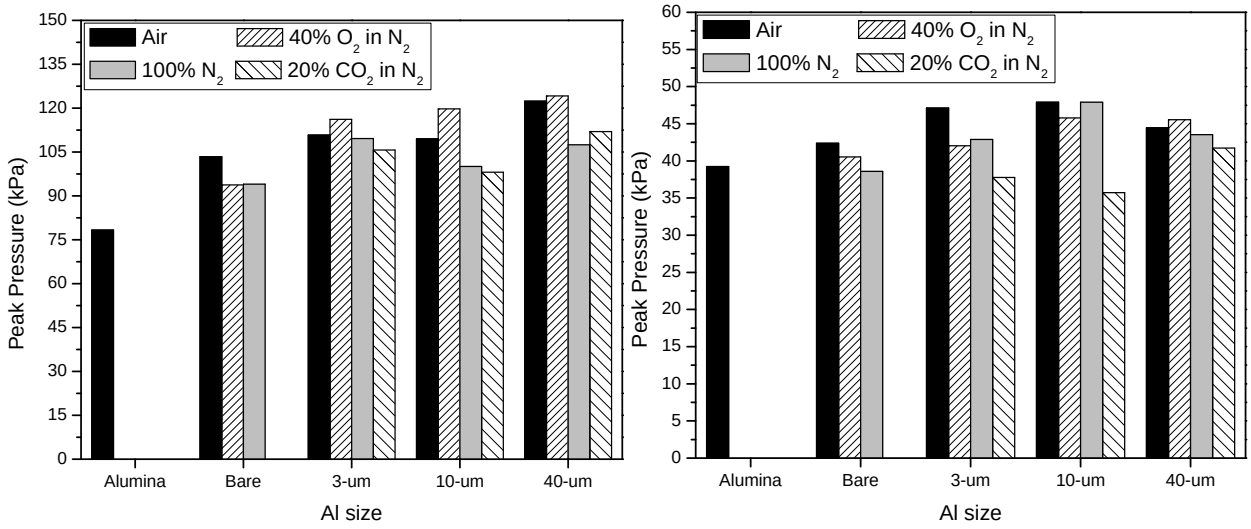

(a) At 21.3 cm from charge

(b) At 32.1 cm from charge

Figure 5.43: Peak pressures for 20 percent aluminized charges in four environments.

percent as the aluminum particle size increases from 3 μm to 10 μm, and the peak pressure decreases by 7 percent for the 40 μm particles compared to the 3 μm particles for the experiments in air. The pressure wave decreases approximately as $1/r^3$ (see discussion in the next paragraph), and therefore the differences between tests for the peak pressure and initial blast wave impulse are not expected to be as significant further from the charge (32.1 cm transducer data) compared to closer to the charge (21.3 cm). In the other environments, the trend in peak pressures is similar as that in air. The largest peak pressure increase is a result of the addition of the aluminum (from the bare to addition of 3-μm aluminum particles), and the change in peak pressure is less when comparing the small to the large particles, and in some cases—such as in CO_2 or N_2—the peak pressure decreases by 5 to 9 percent as the particle size increases from 3-μm to 10-μm. The difference between the peak pressure measurements from the same charge is within 9 percent for all repeated tests—two of each charge type were repeated in air, except for the 20%-3-μm-Al charge in which three charges were tested in air. Therefore, the differences between the peak pressures from the different charges is within the measurement uncertainty, and the variations between the peak pressures are not as significant as may be expected.

The peak pressures scale close to $1/r^3$ for the two transducers. The ratio $(r_2/r_1)^3$ is equal to 3.42 for $r_1 = 21.3\ cm$ and $r_2 = 32.1\ cm$. The average P_1/P_2 ratio is 2.56 and the standard deviation is 0.25, which is within 30 percent of the radius ratio. A ideal blast wave scales as $1/r^3$[76], and therefore some difference between the ratios is expected. The pressure ratios suggest that the pressure wave decays similarly to what would be expected for the ideal case. A more detailed discussion of the pressure ratio can be found in Appendix B.2.

Besides the peak pressure, the initial blast wave impulse has a weak dependence on the aluminum particle size. The uncertainty for the initial blast wave impulses is 5 percent based on the repeated tests of each charge in air. For all environments—at both distances from the charge location—the initial blast wave impulse decreased 1 to 6 percent, which is within the measurement uncertainty, as the particle size is increased from 3 μm to 10 μm. The initial blast wave impulse increased—independent of ambient environment—when the particle sized increased from 10 μm to 40 μm: the initial blast wave impulse increased further from the charge location—7 to 10 percent—compared to closer to the charge location—3 to 8 percent. The largest particles tested have the largest initial blast wave impulse at 32.1 cm from the charge location—2 to 10 percent higher than the initial blast wave impulse for the 3-μm-Al charge. The enhancment resulting from larger aluminum particles compared to the smaller particles is smaller than the enhancement resulting from replacing 20 percent of the HE with aluminum particles. The bare charge had a 20 percent lower initial blast wave impulse in air than the 20%3-μm-Al charge. Closer to the charge location, initial blast wave impulse depended less on the size of the particles. Comparing initial blast wave impulse from the charges having the 3-μm particles to charges having 40-μm particles at 21.3 cm from the charge location, the initial blast wave impulse changed only by 1 to 4 percent. It decreased in air (1 percent) and N_2 (4 percent) and slightly increased in CO_2 (by 3 percent) and O_2 (by 2 percent), which are all within the measurement uncertainty. Overall, the size of the particles weakly influenced the initial blast wave impulse, independent of the ambient atmosphere and distance from charge. Similar to the peak pressure, the largest enhancement

comes from replacing 20 percent of the HE with aluminum particles.

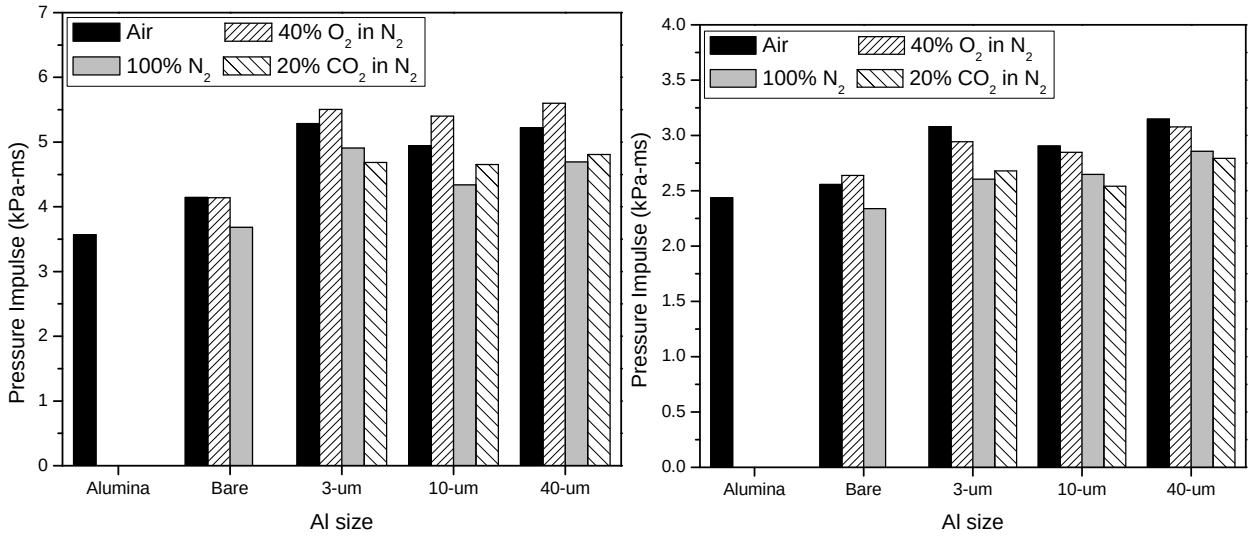

(a) At 21.3 cm from charge

(b) At 32.1 cm from charge

Figure 5.44: Initial blast wave impulse for 20 percent aluminized charges in four environments.

The peak pressure and initial blast wave impulse both have aerobic and anaerobic effects—charges in air or O_2 have higher peak pressures and initial blast wave impulses than the charges in N_2 and CO_2. On average—at 21.3 cm from the charge location—the peak pressure from the experiments in air and O_2 was 10 percent higher than the peak pressure in N_2 or CO_2, and the separation between the oxygen and no oxygen environments was higher for the charges having larger aluminum particles. Further from the charge location at 32.1 cm, the largest difference between the environments was in the CO_2 ambient environment, which on average had a peak pressure 15 percent lower than in the other environments. The difference between the oxygen/no oxygen environments is also evident from the initial blast wave impulses, plotted in Figure 5.44. At 23.1 cm from the charge location, the initial blast wave impulse in the air and O_2 environments is 7 to 20 percent higher than in the N_2 and CO_2 environments. Therefore, early time reactions of the aluminum with detonation products and the ambient environment occur. However, no explicit distinction between aluminum/detonation product reactions and Al/N_2 reactions can be made, since

aluminum will react with N_2 in oxygen deficient environments[33, 34]. Further away from the charge location the differences are smaller but still significant—the initial blast wave impulse is seven to 15 percent lower in N_2 and CO_2 than in air and O_2.

Results from tests with enhanced oxygen provide interesting insight. If aerobic components are significant in blast enhancement, then adding additional oxygen should provide stronger blast since the increased concentration should lead to an increased aerobic oxidation rate, and this available channel may replace some reaction through the less energetic anaerobic and nitridation channels. Data from the 21.3 cm pressure transducer support this assessment by having small ($\sim$5 percent) increases in blast when the ambient O_2 content is doubled. However, the 32.1 cm transducer shows negligible differences between the two environments in terms of blast—the added-O_2 cases actually underperforms the air cases, though the difference is within experimental uncertainty. The results are consistent across several tests and the three particle sizes. It is clear that doubling the O_2 concentration does not double the enhancement, suggesting that the aerobic channel may be saturated or nearly saturated. One possible explanation could be that only a certain fraction of particles are mixed enough with ambient air at early times to oxidize aerobically and that they are mostly reacted in the 20 percent O_2 case. In that situation, adding additional O_2 would not significantly influence blast—though it may still influence overall energy release and overpressure.

Carbon dioxide as a detonation product is an oxidizer for aluminum fuel, especially in the absence of O_2 in the ambient environment. However, cold (relative to the detonation gases) CO_2 in the environment appears to have little effect to provide additional enhancement from the aluminum compared to the pure N_2 environment. There was no statistically significant difference between pure N_2 and 20/80 CO_2/N_2 cases. The difference between the initial blast wave impulses in CO_2 and N_2 varied between 2 and 7 percent. The difference is greatest closer to the charge location and smaller aluminum particles. Further from the charge location the difference is less than 5 percent.

The blast wave arrives at the pressure transducers earlier for all the aluminized charges compared to the bare and alumina charges except in CO_2, as shown in Figure 5.45. The earlier time of arrival indicates that the blast wave is faster and is, therefore, enhanced. The peak pressures at 21.3 cm in CO_2 and N_2 were similar, yet the blast wave was significantly slower—the blast wave time of arrival was later by 5 to 9 percent in CO_2 compared to in N_2. At 32.1 cm from the charge location, the peak pressures were lower in CO_2 than in N_2 and the blast wave was slower. The decay of the blast wave further from the charge explains the difference between the two peak pressures.

The specific heat ratio ($\gamma = c_p/c_v$) and the speed of sound of the different atmospheres are tabulated in Table 5.7. The air, 40%/60% O_2/N_2 mixture and pure N_2 have a specific heat ratio of 1.4, while the specific heat ratio of the 20%/80% CO_2/N_2 mixture is slightly less at 1.381, though still within 2 percent of 1.4. The air, pure N_2 and 40%/60% O_2/N_2 mixture have sound speeds within 2.8 percent of each other, while the speed of sound in the 20%/80% CO_2/N_2 mixture is lower than the pure N_2 environment by 6 percent, and lower than in the 40%/60% O_2/N_2 mixture by 3.2 percent. The lower specific heat ratio and speed of sound can explain the difference between CO_2 and the other ambient environments for the time of arrival. Note that the 20%/80% CO_2/N_2 atmosphere results in a better comparison than pure CO_2 would, as the specific heat ratio is much closer to 1.4 than the specific heat ratio of CO_2, which is 1.292, and the speed of sound in pure CO_2 is much lower at 267 m/s. The same is true for the 40%/60% O_2/N_2 mixture versus comparing to a pure O_2 atmosphere which has a specific heat ratio of 1.398, and a speed of sound of 326 m/s. The time of arrival is weakly dependent on aluminum particle size, independent of ambient environment, and is weakly dependent on ambient environment except for CO_2.

Table 5.7: Specific heat ratio and speed of sound for different ambient environments, at 20°C, assuming ideal gas.

Ideal Gas	Specific Heat Ratio	speed of sound
Air	1.400	343 m/s
40%/60% O_2/N_2	1.400	339 m/s
20%/80% CO_2/N_2	1.381	328 m/s
N_2	1.401	349 m/s

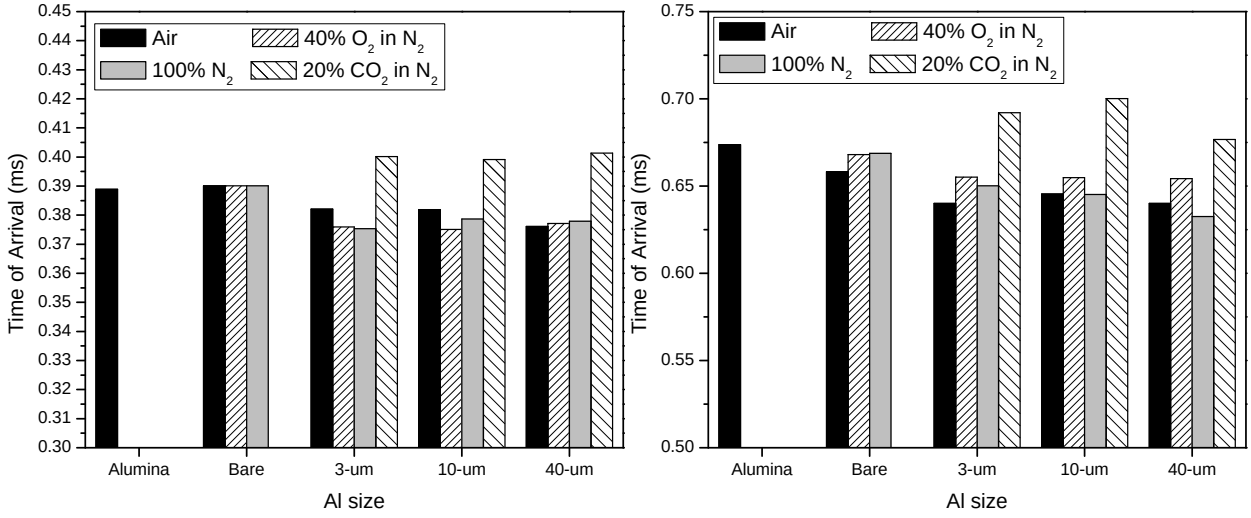

(a) At 21.3 cm from charge

(b) At 32.1 cm from charge

Figure 5.45: Time of arrival of the pressure wave for 20 percent aluminized charges in four environments.

From these results, and utilizing simple scaling, the amount of aluminum reaction that drives the blast can be estimated. For ideal explosives, impulse should scale as charge energy to the one-third power. Assuming a detonation energy of 6.2 kJ/kg for the PBX9407, and heat release of 31 kJ/g for the Al (the upper limit), replacing 20 percent of the HE with aluminum in the charge that reacts completely would yield a blast enhancement of 21 percent in the far field of a spherical blast. The fact that this geometry is not entirely spherically symmetric—there is a directional effect that drives the flow preferentially upward—and that neither PBX9407 nor the aluminized versions are ideal explosives makes this calculation imperfect. However, it does suggest that an appreciable amount of the metal, quite possibly

most of it, does react to drive the blast, and the fraction reacted is fairly independent of particle size in the 3–40 micron range.

Later Time Combustion ($> 1ms$)

This section investigates the effect of size and environment on the later combustion—$t > 1\ ms$. The effect of environment focuses on separating the aerobic (air minus N_2) and the anaerobic (N_2) components of the blast enhancement. Impulse versus time plots are from both the 21.3 cm and the 32.1 cm pressure transducer measurements. The measurements from the 21.3 cm pressure transducer for some of the experiments—Al_2O_3-loaded in air, the 3-μm-Al-loaded in CO_2 and O_2, the 10-μm- and 40-μm-Al-loaded in CO_2, and the bare charge in air—are not acurate, such that the impulse is negative indicating a vacuum atmosphere at the pressure transducer, which is not phyically possible, though there is a negative portion of the pressure curve that is real. The cause of the negative impulse curves for these particular cases is unknown, since they occured on different days, for different charges, and in different atmospheres. The impulse curves are plotted to show the complete data set, but are not used in any comparisons or calculations to determine the effect of the particle size and environment on the later combustion.

The aerobic and anaerobic components for $1\ ms < t < 5\ ms$ are shown in Figures 5.46 and 5.47 for each aluminum particle size. The plotted impulses as a function of time from the 32.1 cm transducer measurements are the enhancement compared to the alumina charges, i.e., the impulse from the alumina case was subtracted from the each of the plotted cases. (For the impulses at 21.3 cm from the blast site, the Al_2O_3-loaded charge impulse was negative, therefore the impulses do not represent the enhancement.) The plots indicate that the effects are mostly aerobic, but the anaerobic component is not negligible at both pressure transducer locations, especially at 21.3 cm for the 20%-3-μm-Al charge in which the impulse in N_2 is actually greater than the impulse in air. The significant aerobic component shows that mixing with the air can enhance the combustion. From 1 ms to 5 ms the

fraction that the aerobic component is of the total impulse is roughly constant, that is, it is not a function of time, as shown in Figure 5.48 for the 32.1 cm pressure transducer. The breakdown of the anaerobic/aerobic components of the enhancement at 32.1 cm—based on the average impulses from 1–5 ms—are 47 percent anaerobic, 53 percent aerobic for the 3-μm aluminum; 24 percent anaerobic, 76 percent aerobic for the 10-μm aluminum; and 40 percent anaerobic, 60 percent aerobic for the 40-μm aluminum. Therefore the aerobic reactions are more important for the larger particles. During the time frame $1\ ms < t < 5\ ms$, the aerobic component is most important for the mid-sized aluminum particles.

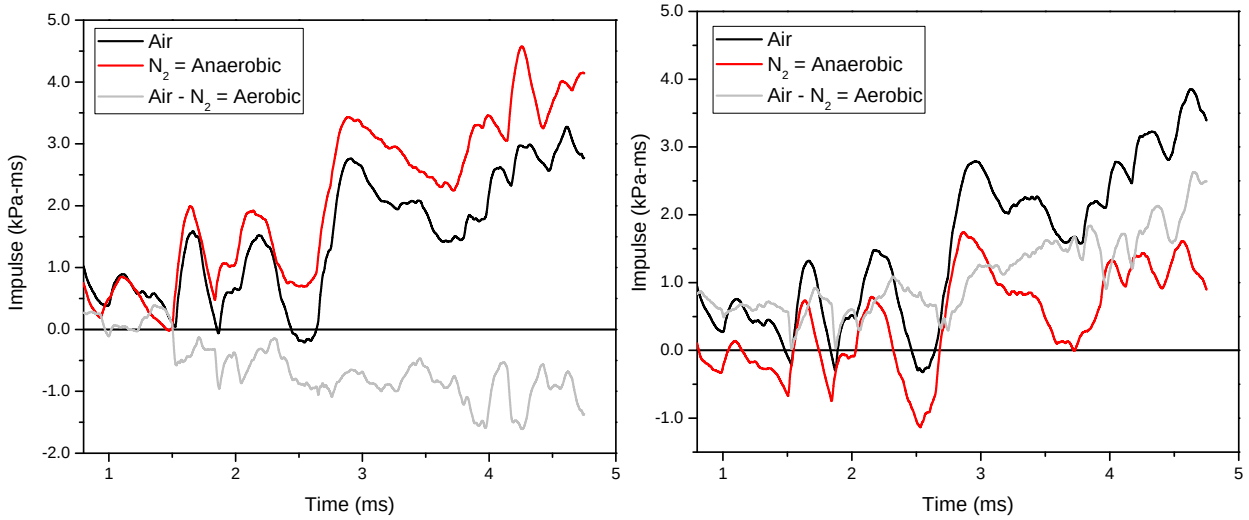

(a) 20%-3-μm-Al

(b) 20%-10-μm-Al

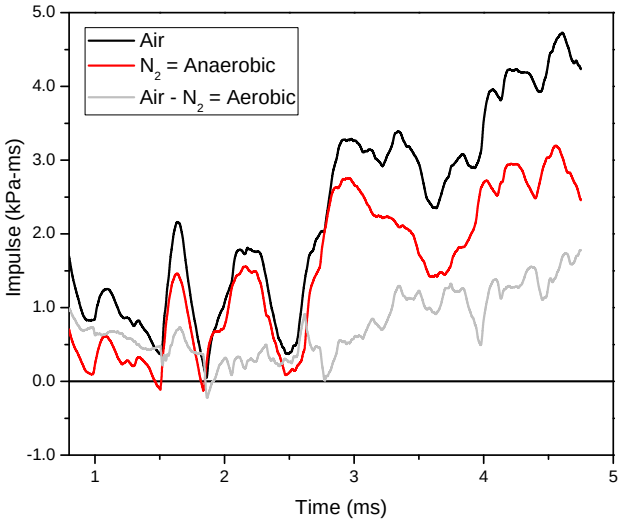

(c) 20%-40-μm-Al

Figure 5.46: Aerobic vs. anaerobic components from the 20 percent aluminized charges at 21.3 cm from the blast site; comparison for $t < 5$ ms.

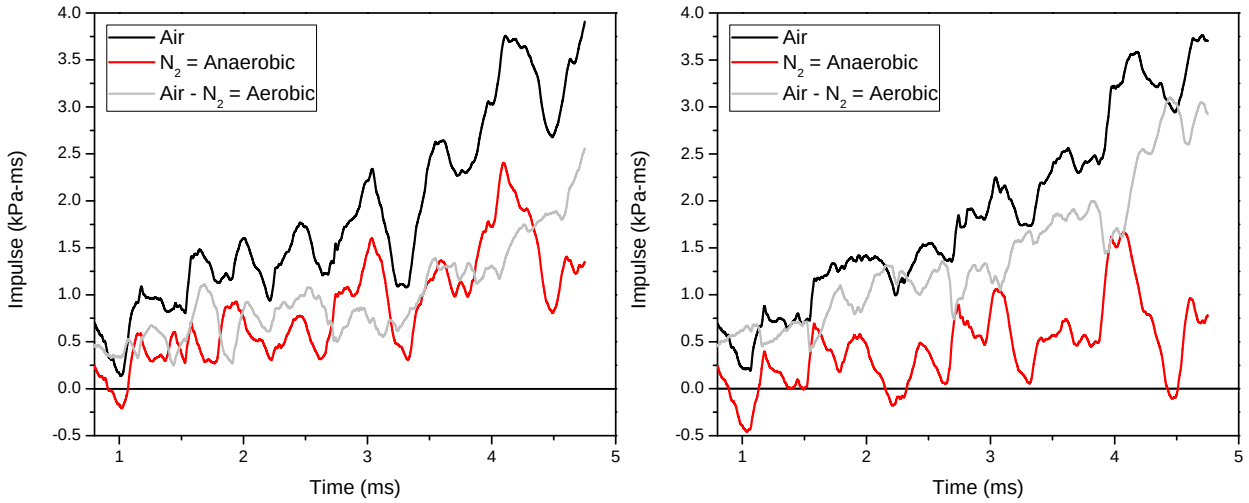

(a) 20%-3-μm-Al

(b) 20%-10-μm-Al

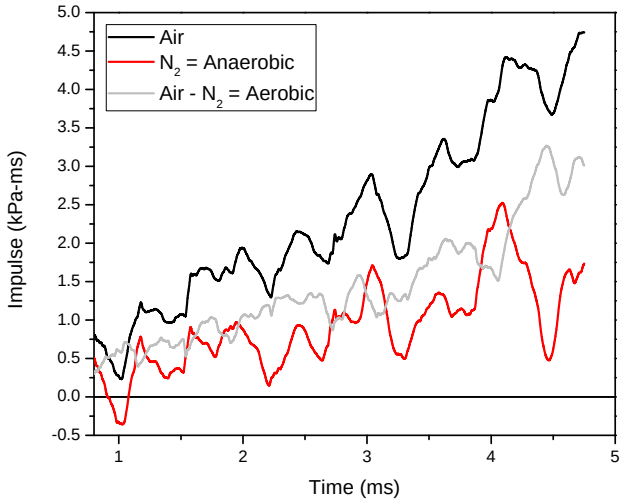

(c) 20%-40-μm-Al

Figure 5.47: Aerobic vs. anaerobic components of the enhancement from the 20 percent aluminized charges at 32.1 cm from the blast site; comparison for $t < 5$ ms.

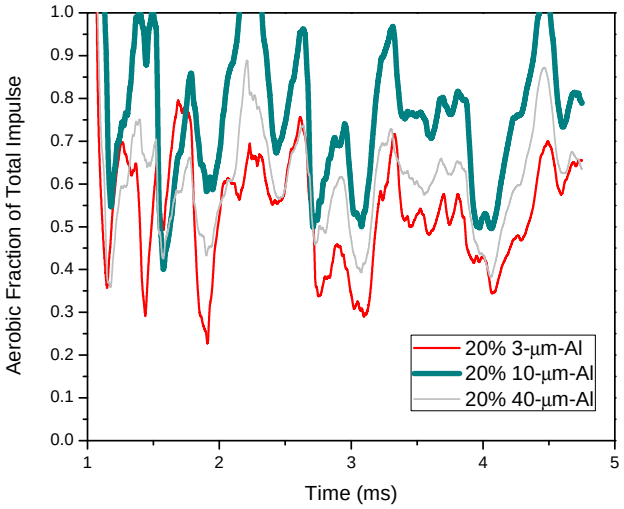

Figure 5.48: The aerobic fraction of the total impulse, i.e., $\mathbf{Impulse_{air-N_2}/Impulse_{air}}$ at 32.1 cm from the blast site.

The effect of aluminum particle size on the aerobic and anaerobic features is further explored in Figures 5.49 and 5.50. As Figures 5.49a and 5.50a show, the aerobic reactions are more important for larger aluminum particles—10 μm and 40 μm—than the smaller aluminum particles—3 μm. The anaerobic combustion—shown in Figures 5.49c and 5.50c—is weakly dependent on aluminum particle size up to approximately 3 ms. After 7 ms, the anaerobic component is more important for the 3 and 40 μm particles at both pressure transducer locations.

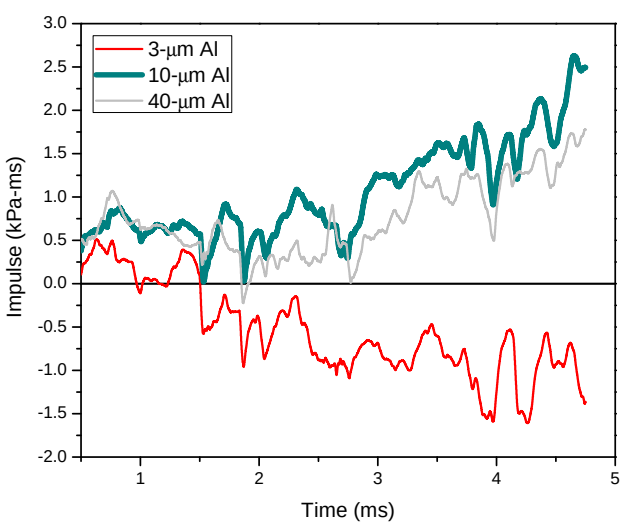

(a) Aerobic (Air − N_2)

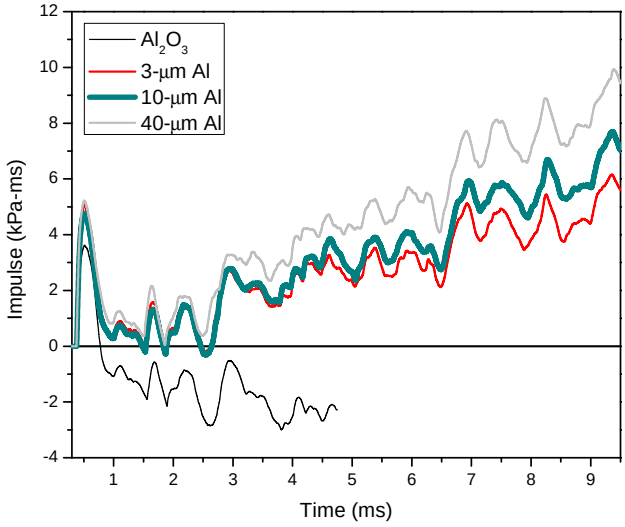

(b) In Air

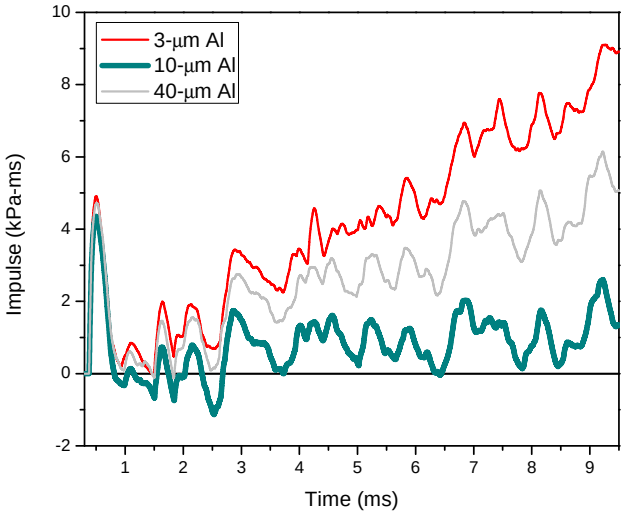

(c) In N_2

Figure 5.49: Impulses in air, N_2, and aerobic (air-N_2) component plotted to show aluminum particle size comparisons, at 21.3 cm from the blast site.

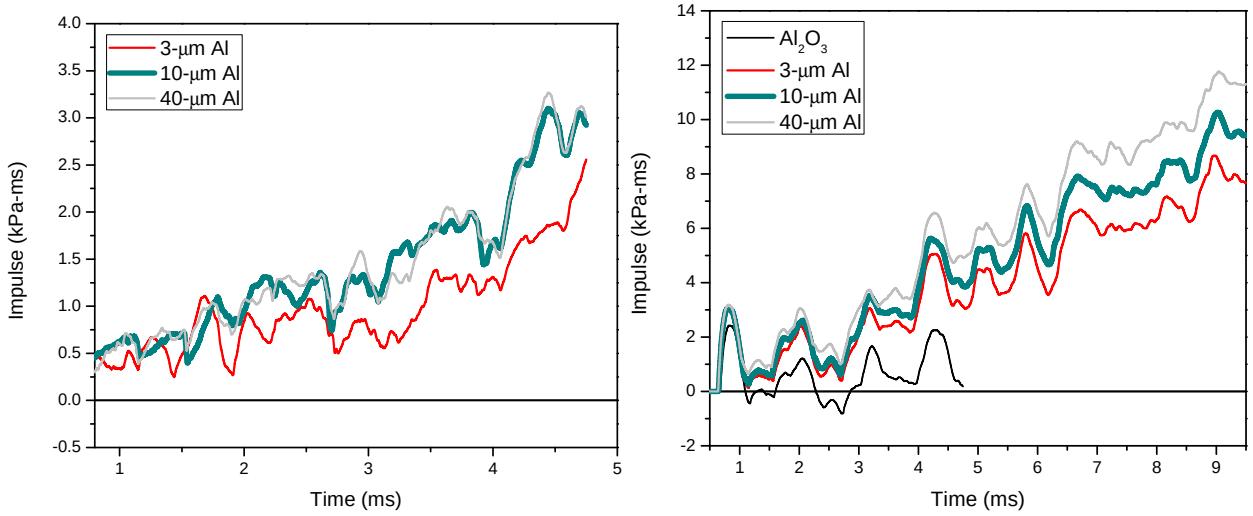

(a) Aerobic (Air − N_2)

(b) In Air

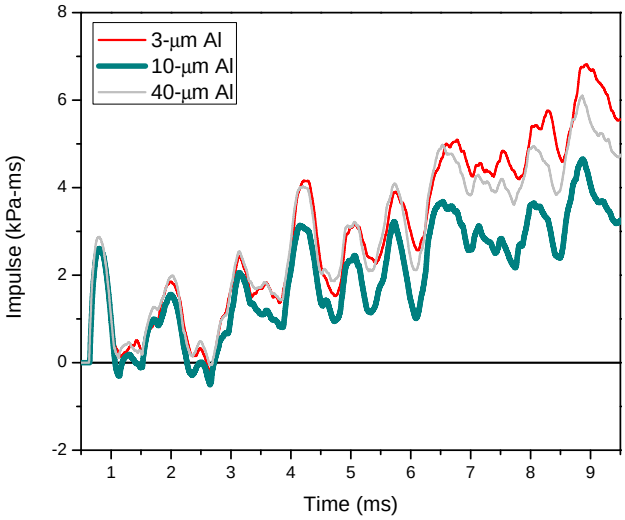

(c) In N_2

Figure 5.50: Impulses in air, N_2, and aerobic (air-N_2) component plotted to show aluminum particle size comparisons, at 32.1 cm from the blast site.

In air, the aluminum particle size has a larger effect and the larger particles have more enhancement at the later times. The larger particles having a bigger impact on the enhancement at later times is expected because larger particles take longer to burn than smaller particles. The later enhancement from the larger aluminum particles can be contrasted against the initial blast wave impulse enhancement which had only a weak dependence on

size, though the largest particles did have the most enhancement. Enhancement as a result of the larger particles is at both early—evidenced by the initial blast wave positive impluse results discussed above—and later times—as shown by the impulse-time curves from 1–9.5 ms.

The effect of the environment is further investigated in Figures 5.51 and 5.52, which show the impulse as a function of time—1 to 9 ms—for each aluminum particle size. The later combustion enhancement is affected by both the ambient environment and the aluminum particle size. Ignoring the tests in which the impulse is negative, in general, the enhancement from the charges in Air/O_2 compared to in CO_2/N_2 is greater, using the Al_2O_3-loaded charge in air as the baseline. The difference between the environments becomes more significant as the aluminum particle size increases, especially at $t > 5\ ms$. More energy is released from aerobic reactions for larger aluminum particles at the later times, and the smaller aluminum particles have more anaerobic oxidation/nitridation.

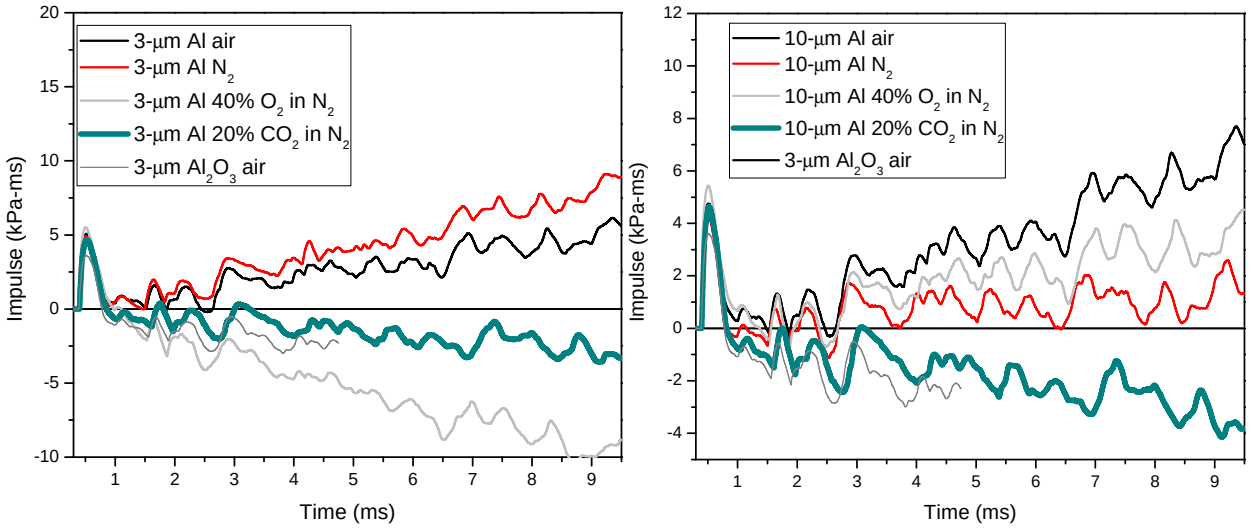

(a) 20%-3-μm Al

(b) 20%-10-μm Al

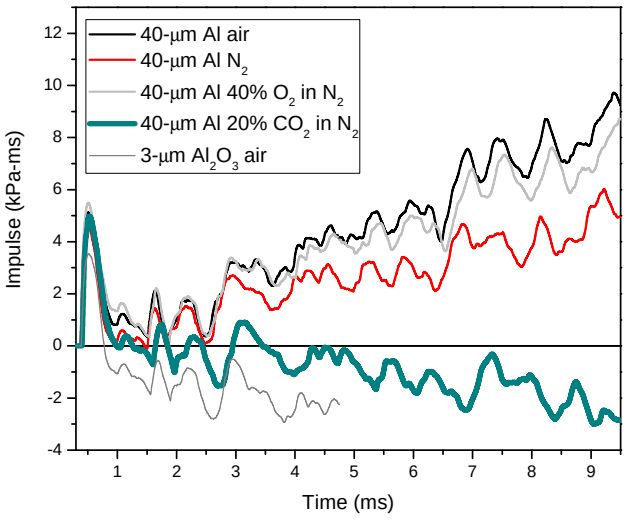

(c) 20%-40-μm Al

Figure 5.51: Impulse vs. time for 20 percent aluminized charges in four environments,at 21.3 cm from the blast site.

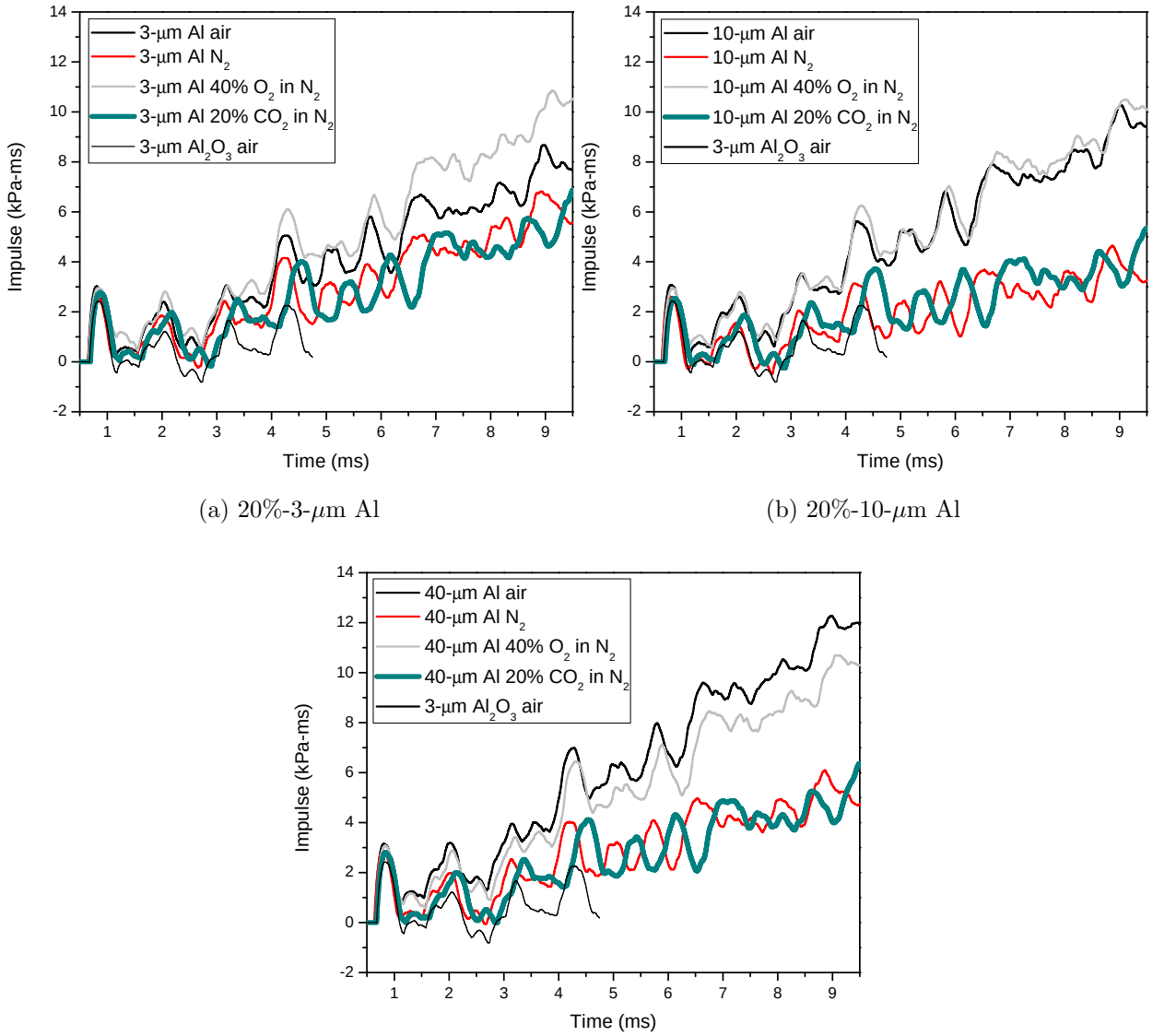

(a) 20%-3-μm Al

(b) 20%-10-μm Al

(c) 20%-40-μm Al

Figure 5.52: Impulse vs. time for 20 percent aluminized charges in four environments, at 32.1 cm from the blast site.

The bare charge (only HE) is compared to the 20%-3-μm-Al- and 20%-Al_2O_3-loaded charges in Figure 5.53. The Al_2O_3-loaded charge is used as the baseline for comparisons for the data from the 32.1 cm transducer. An aluminized charge provides a net yield in the primary blast and ms-scale impulse, even in the absence of aerobic effects, evident by the enhancement seen at the 32.1 cm transducer in Figure 5.53b, and especially demonstrated

at the 21.3 cm transducer in Figure 5.53a, in which the impluse in air is lower than the impulse in N_2. After 1 ms, the 20%-3-μm-Al-loaded charge in N_2 (anaerobic reactions) has 1–2 times more explosive enhancement compared to the bare charge's enhancement at 32.1 cm. The aluminized charge in air has 3–5 times more explosive enhancement than the bare charge after 2.7 ms at 32.1 cm. The enhancement from the aluminized charge can be up to approximately 10 times more than the enhancement from the bare charge, and the aerobic effects on the enhancement are 2–3 times more than the anaerobic effects when compared to the bare charge at the 32.1 cm transducer.

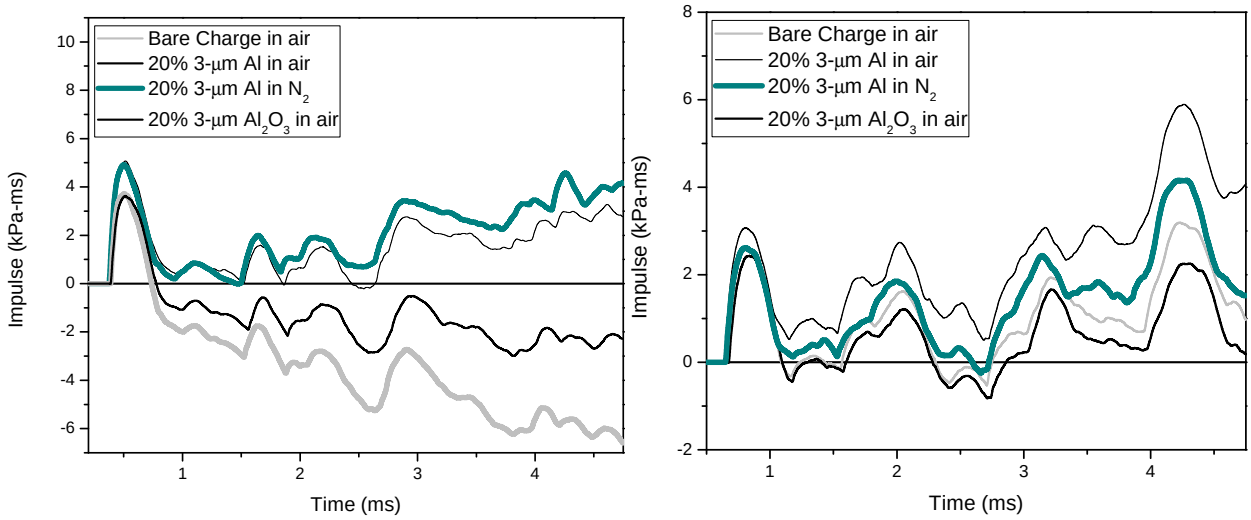

(a) At 21.3 cm

(b) At 32.1 cm

Figure 5.53: Impulse vs. time for 20 percent aluminized charges in four environments.

5.7.2 AlO Emission

In addition to the pressure/impulse measurements, the AlO emission was measured for each experiment and integrated for each time step. The results are presented in Figure 5.54, organized by aluminum particle size. Each experiment—except for one 3-μm-Al test in air and all 40-μm-Al tests in air—the AlO emission was dominated by a single 16 μs exposure. The few experiments which had more than one 16 μs collection of AlO indicate late time

combustion.

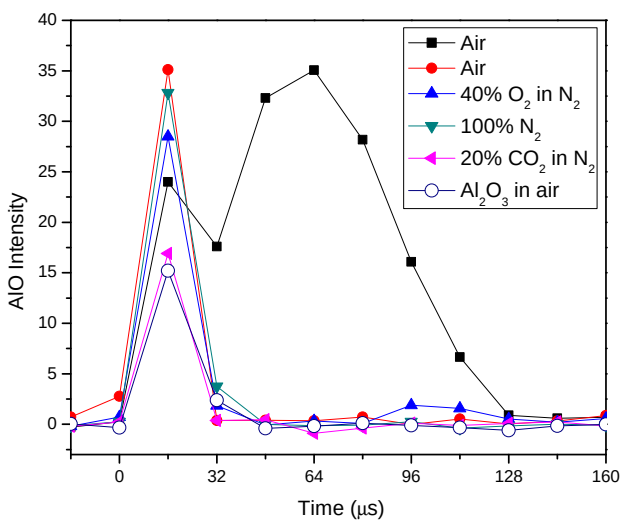

(a) 20%-3-μm Al

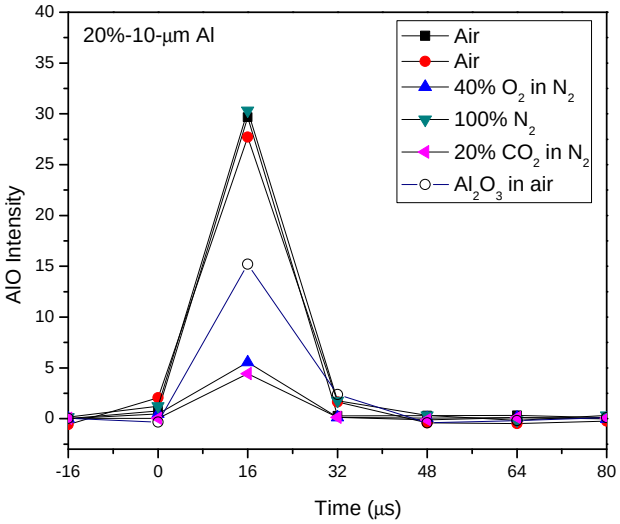

(b) 20%-10-μm Al

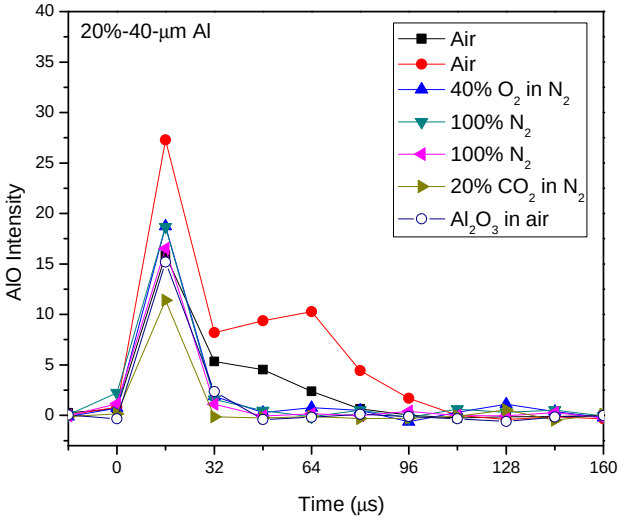

(c) 20%-40-μm Al

Figure 5.54: AlO for 20 percent aluminized charges in four environments.

For the 20%-3-μm Al charge the order of magnitude of the AlO emission is air, N_2, O_2, CO_2. For the 20%-10-μm Al charge the order of magnitude of the AlO emission is air/N_2, O_2/CO_2. And for the 20%-40-μm Al charge the order of magnitude is air, N_2/O_2, CO_2. Except for the lowest signal measured in CO_2, no clear atmosphere or size dependence on the AlO emission exists from these experiments.

As discussed in Section 5.4.3, high temperatures influence the AlO measurements. The collection of the AlO emission is spatially biased to the brightest area of the explosive fireball. It is biased by the set-up of the AlO emission collection in which the fiber optic cable optics are directed toward the middle of the fireball, as shown in Figure 5.55. The collection volume is biased toward the brightest areas of the fireball during the first 50 μs.

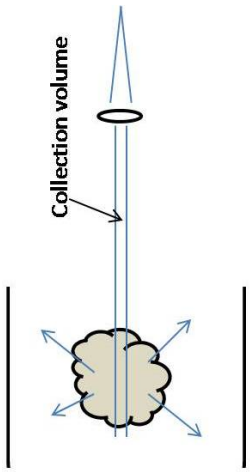

Figure 5.55: Schematic of AlO emission collection.

5.7.3 Temperature

The temperature from the pyrometer measurements is shown in Figure 5.56, organized by aluminum particle size. Similar to previous experiments, the temperature starts extremely high ($> 4000\ K$) and decreases exponentially. Marked in Figure 5.56a is the time that the majority of the AlO emission is measured and the maximum time (for the air experiments) AlO emission that was measured for these experiments. The AlO emission measurement coinciding with the peak temperature measurements is in agreement with the other results.

Observations about the effect of atmosphere on the temperature can be made. The 3-μm-Al charge has higher temperatures in O_2 than in air. For larger particles, the temperatures are about the same for experiments in air and O_2. For all the tests in CO_2 and N_2, very little light was measured, and it is probably not enough to have an accurate temperature

calculation. The luminosity was highest for experiments in air/O_2. The 10-μm-Al and the 40-μm-Al charge experiments in air have "increase/decrease" in temperature between 0.25 ms and 0.75–1.0 ms, and is more pronounced for 10-μm-Al charge experiments. These large temperatures after 0.25 ms are most likely a result of a too small intensity ratio of the two measured wavelengths, mathematically resulting in a large 'temperature' and is not a true representation of the actual temperature.

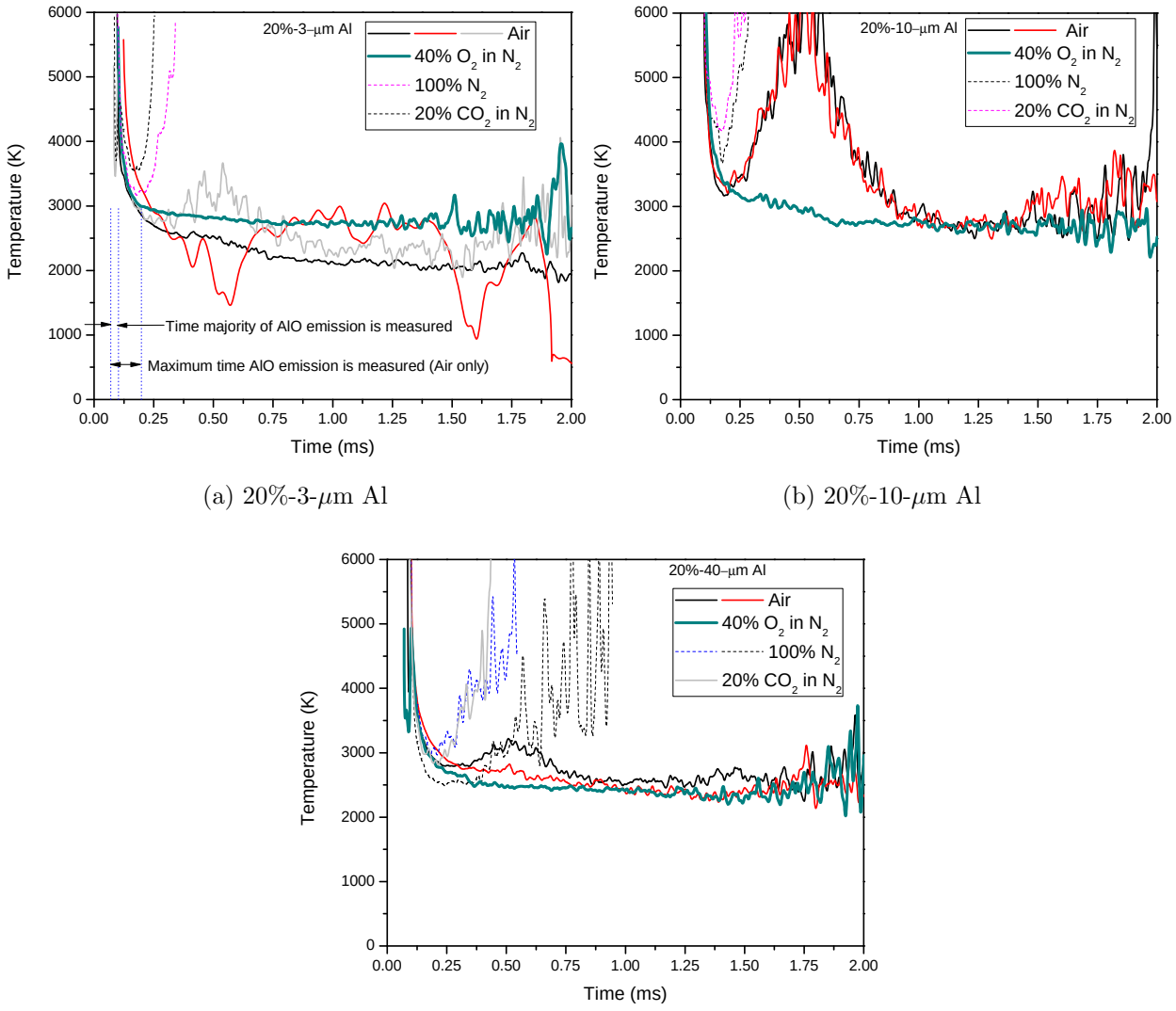

(a) 20%-3-μm Al

(b) 20%-10-μm Al

(c) 20%-40-μm Al

Figure 5.56: Temperature for 20 percent aluminized charges in four environments, (temperatures measured using the pyrometer).

5.8 High Speed Camera Visualization of the Fireball and Shock Wave Velocity Measurements

In this section selected fireball and shock wave images are shown and discussed. The images selected are representative images of the fireball and show some similarities and differences between different types of experiments, e.g., air gap or aluminized charges. Typically 13 to 16 frames were captured per test. The two circular spots of light in the same location in each frame come from reflections of the flash through the chamber window, and can be ignored. The time resolution of all the images is 22.75 μs unless otherwise noted.

5.8.1 Bare and Alumina-loaded Charges

The first two sets of images—Figures 5.57 and 5.58—are from a bare charge and from an alumina-loaded charge, both tests in air. The HSC images from the bare charge test are shown in Figure 5.57. All the frames, except the first one are dark and without much visible luminocity. The first frame showing a bright break out of light is typical of most tests performed. The shock wave is also slower for the bare charge compared to the aluminized charges. The peak speed was approximately 1500 m/s compared to 2000 m/s to 3000 m/s for the 20 percent aluminized charges.

The HSC images from an alumina-loaded charge are shown in Figure 5.58. One frame of bright luminicity can be seen in the first frame, and only eight frames were able to be captured in which the shock wave was visible. The one bright frame most likely corresponds to the single frame of AlO emission measured at the beginning of the AlO emission collection time. Both the bare and alumina-loaded charge fireballs exhibit a round or spherically shaped shock wave and fireball.

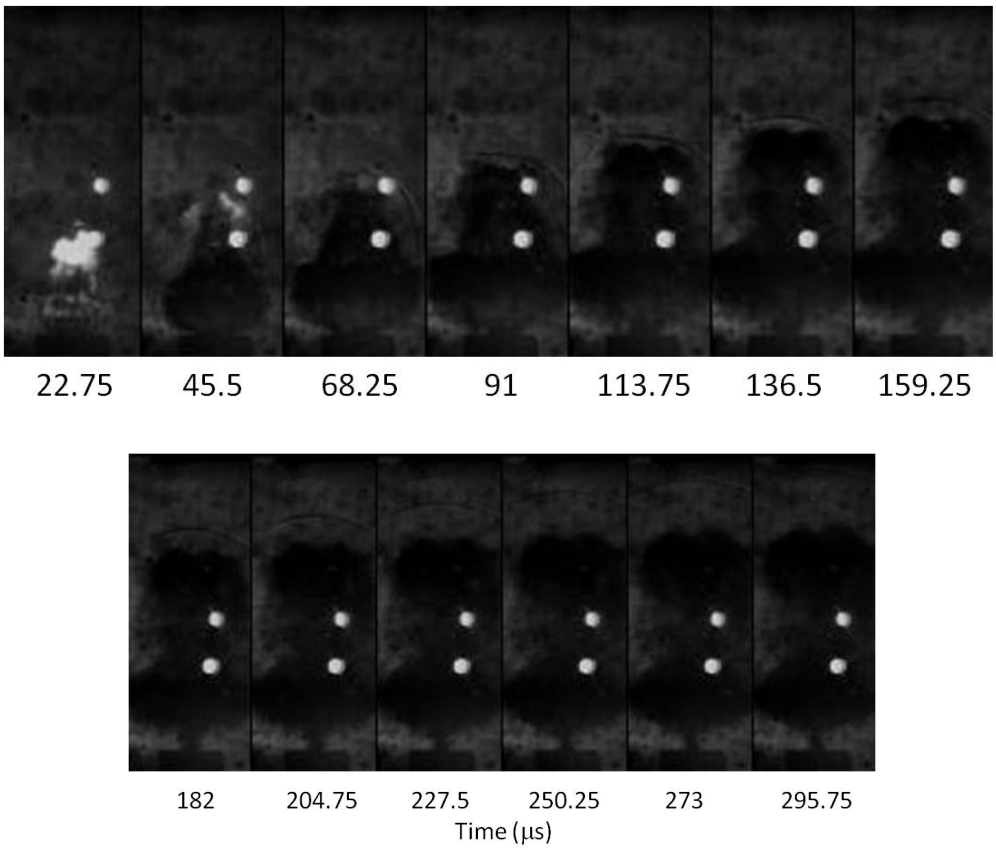

Figure 5.57: Images from 0514-bare-air test.

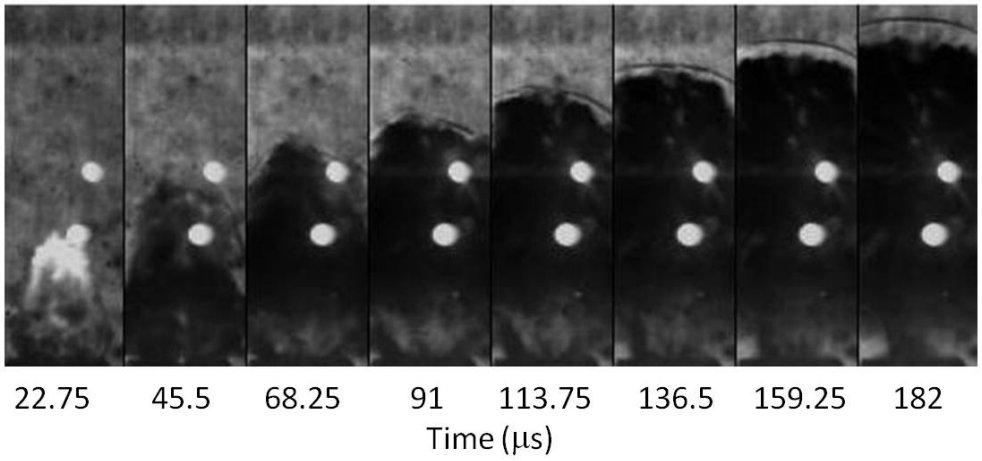

Figure 5.58: Images from the 0506-alumina-air test.

5.8.2 As a Function of Size, Loading Amount, and Environment

The HSC images from a 20%-3-μm-Al loaded charge in air are shown in Figure 5.59. After the initial bright breakout, three more more frames also show additional brightness (until $t = 91.0\ \mu s$), and most likely show the aluminum burning or alumina radiating, since the bare charge images only showed the initial bright breakout in the first frame. As shown earlier, only one frame of AlO emission was measured for the 20%-3-μm-Al charges, except for one test. The bright frames also exhibit an upward directional fireball shape. The shape becomes more spherical starting at the sixth frame (at $t = 136.5\ \mu s$). Some light can also been seen later (after the sixth frame) on the side of the fireball.

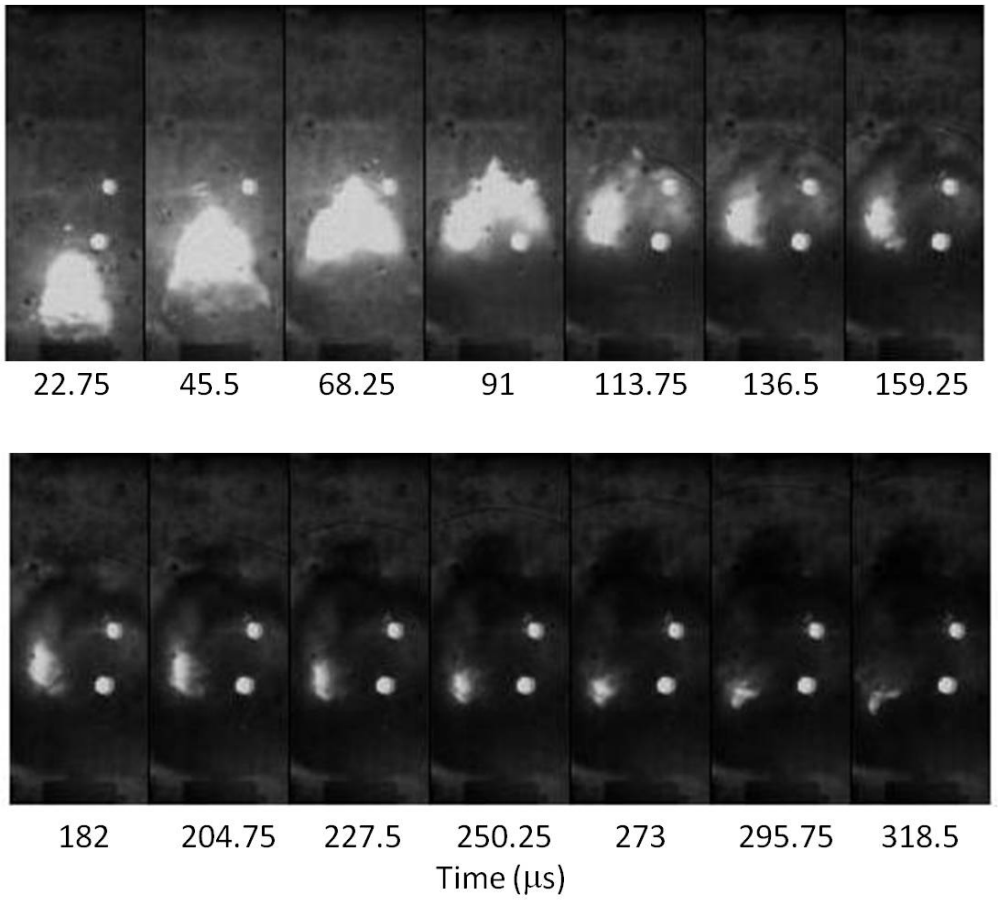

Figure 5.59: Images from 20%-3-μm-Al loaded charge tested in air.

The 20%-10-μm-Al loaded charge images are shown in Figure 5.60 for a test in air. These

images have less light than the images from the 20%-3-μm-Al loaded charge. Only one frame of AlO emission was measured from this test, and is most likely from the bright breakout seen in the first two frames. The shock wave and fireball are spherically shaped.

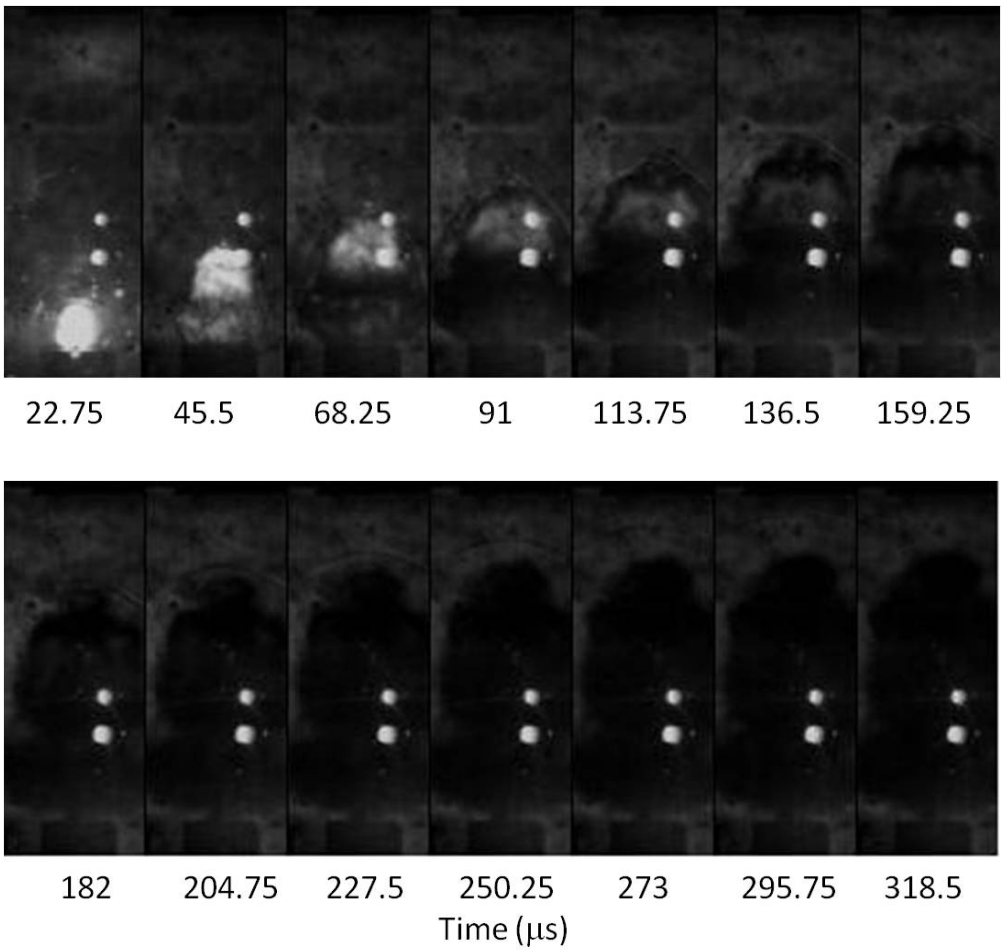

Figure 5.60: Images from 20%-10-μm-Al loaded charge tested in air.

Images from a 20%-40-μm-Al loaded charge tested in air is shown in Figure 5.61. Five frames (until $t = 113.75\ \mu s$) of a bright breakout are seen and correspond to same time frame in which the longest AlO emission was measured. The fireball is jet shaped during the brightest times, up to approximately 136 μs. The fireball then becomes more rounded or spherically shaped and looks similar to the 20%-3-μm-Al and 20%-10-μm-Al tests in air.

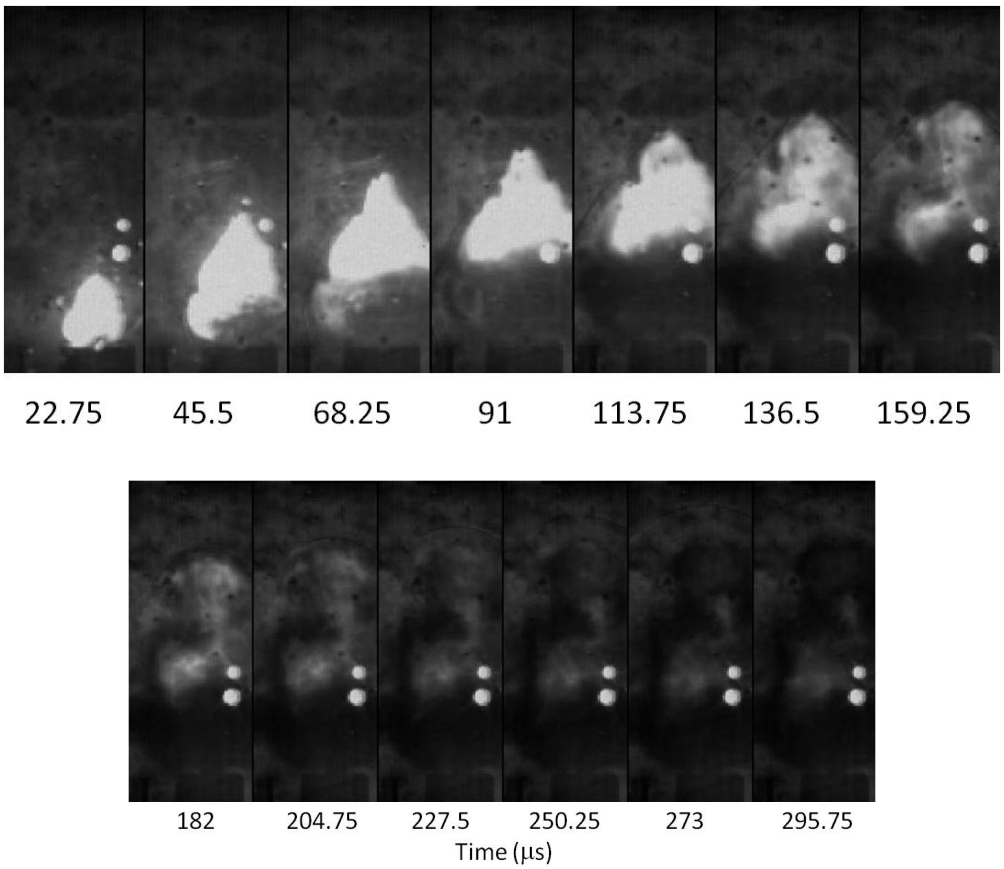

Figure 5.61: Images from 20%-40μm-Al loaded charge tested in air.

The shock wave velocity—determined from the HSC images by manually finding the shock wave tip or leading edge location with respect to the charge mount—is shown in Figure 5.62 for the three 20 percent aluminized charges and the bare charge. The initial velecity increases as the aluminum particle size increases. For all tests, the shock wave velocity drops exponetially from the peak to approximately the same velocity of approximately 500 m/s after 150–175 μs.

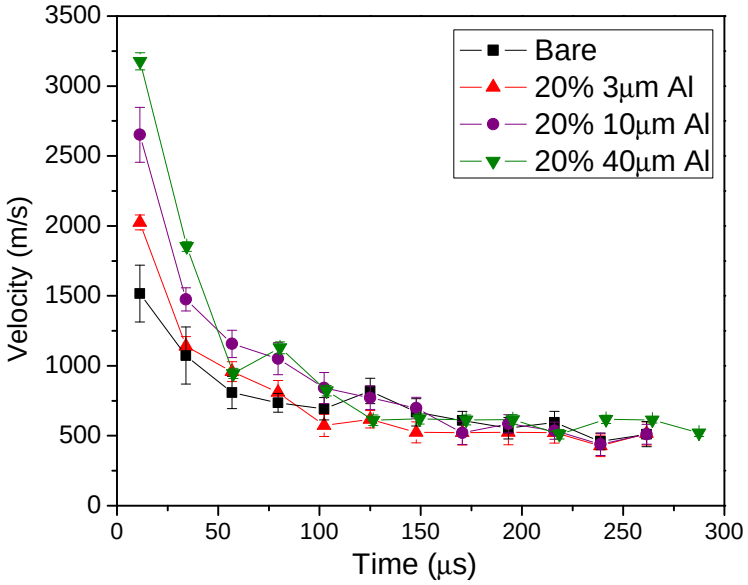

Figure 5.62: Shock wave velocities for bare and aluminized charges in air.

Images from the 50%-3-μm-Al charge are shown in Figure 5.63, tested in air (Test 2), and the shock wave velocities for all three 50%-3-μm-Al tests in air are shown in Figure 5.64. The time resolution of the 50 percent aluminum tests was 28 μs. The bright breakout lasts for approximately 168 μs, and visible light exists during the entire time the shock wave is visible in the images. AlO emission was measured until 400 μs. The fireball is directionally jet-like shaped and the shock wave is not as spherically shaped as the shock wave from the 20%-3-μm-Al charge. The initial shock wave velocity of the images is approximately 2500 m/s and is average for the three tests. While the initial velocity varied from 1250 to 3250 m/s, the three sets of data quickly collapse—after 100 μs—to the same velocity and development with time. Similar to the other aluminized charges, the shock wave velocity at the end of the measurement period is around 500 m/s.

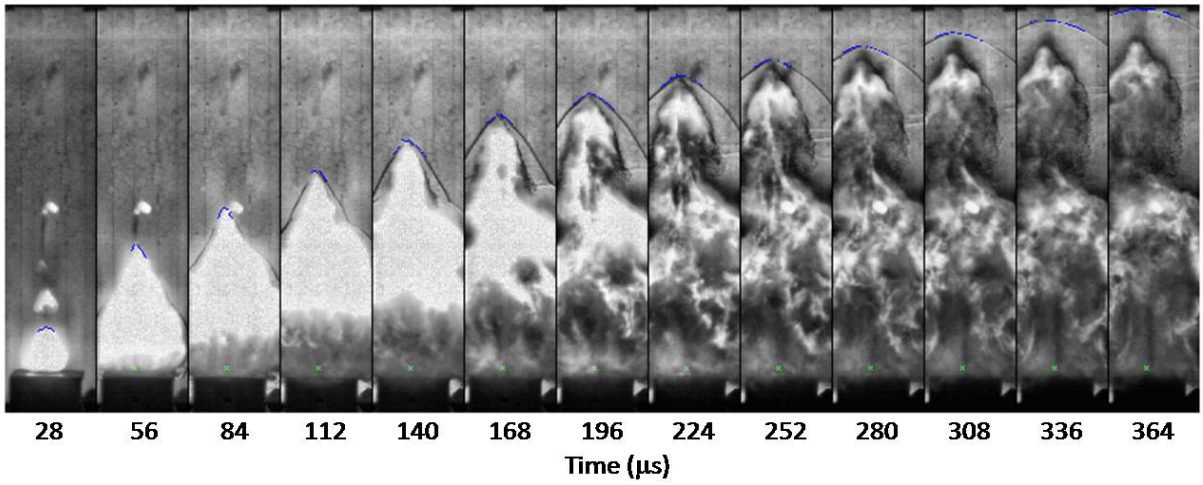

Figure 5.63: Images from 50%-3μm-Al loaded charge tested in air.

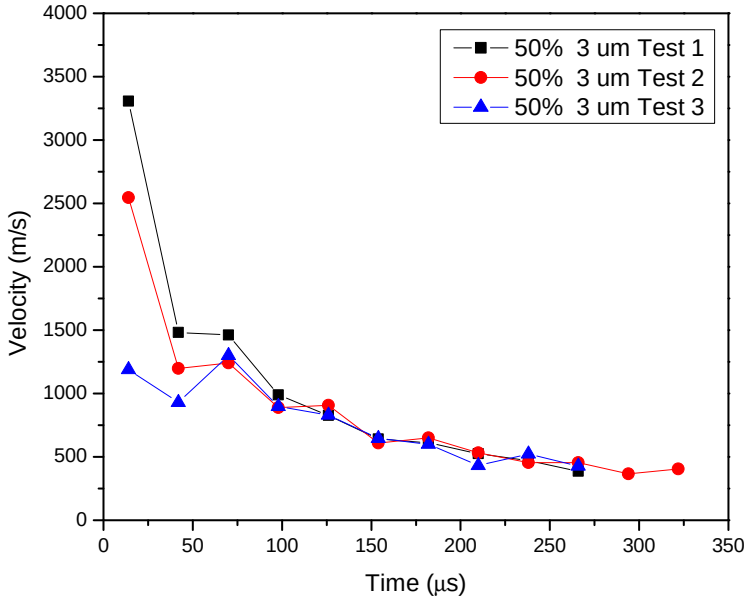

Figure 5.64: Shock wave velocity for the 50%-3-μm-Al tests in air.

The next three figures show differences in the fireball images for the 20%-3-μm-Al charge. The images from the test in 40/60 O_2/N_2 are in Figure 5.65, in N_2 in Figure 5.66, and in 20/80 CO_2/N_2 in Figure 5.67. The test in 40%/60% O_2/N_2 has a longer bright breakout than in air—136.5 μs compared to 91 μs. The fireball is also an upward directional jet longer—until approximately 136 μs—than the fireball in air, and then becomes more spherical in

shape, but still has a directional 'point'. Bright spots can be seen in the fireball throughout the time (295.75 μs) imaged; however, from this test only one frame of AlO emission was measured.

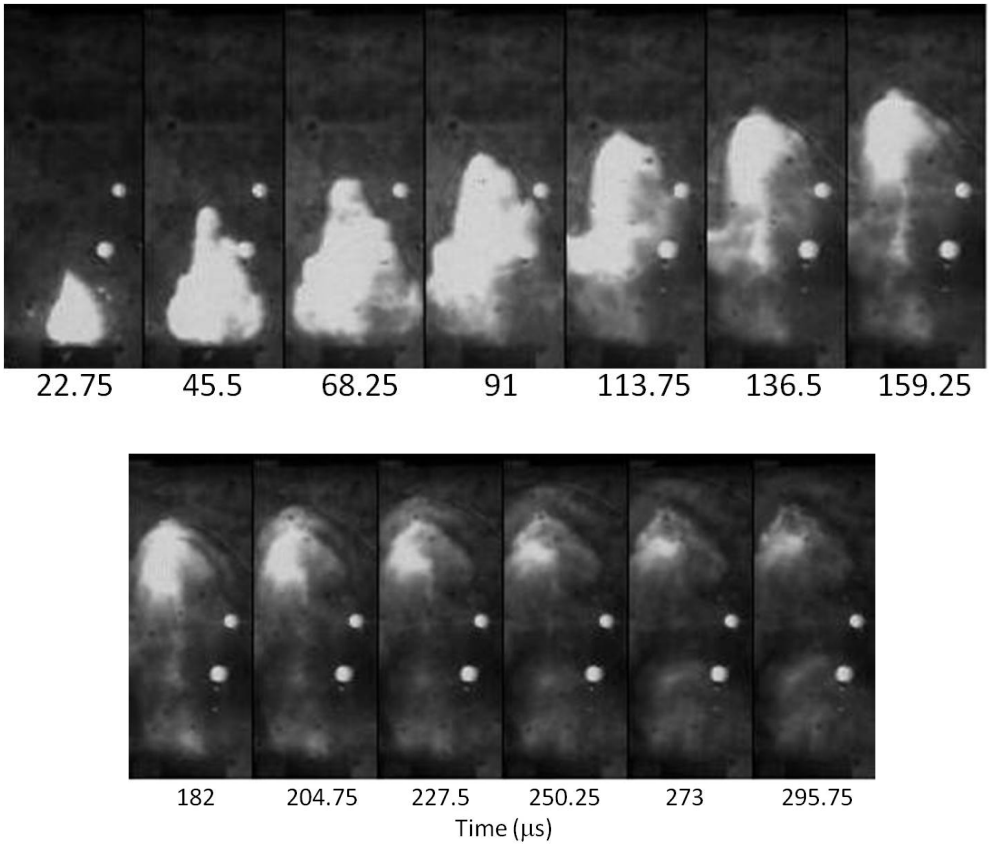

Figure 5.65: Images from 20%-3-μm-Al loaded charge tested in O_2.

The images from the tests in N_2 and 20%/80% CO_2/N_2 are similar. The tests in N_2 have one frame of the bright breakout, plus two additional frames of light visible from the top half to 1/3 of the fireball. The fireball and shock wave are rounded/spherical in shape. The test in CO_2 has the one frame of bright breakout plus one additional frame of visible light. The fireball and shock wave are also rounded/spherical in shape. The images from the tests in N_2 and CO_2 have less visible light than the images from the tests in air or O_2; however the AlO emission measured from the test in N_2 was still significant for the one frame compared to the tests in the other environments (see Figure 5.54a).

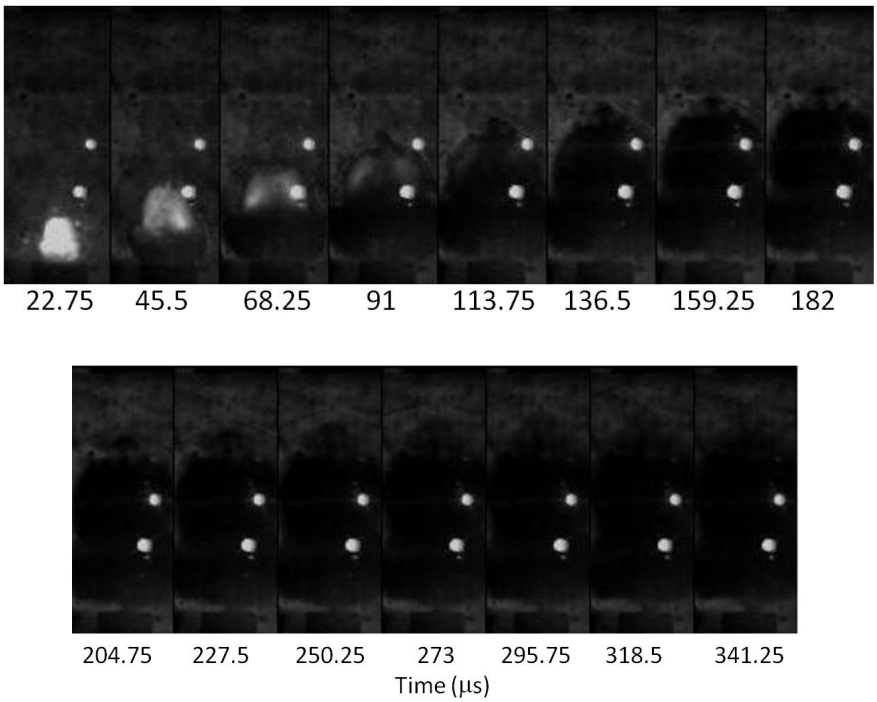

Figure 5.66: Images from 20%-3-μm-Al loaded charge tested in N_2.

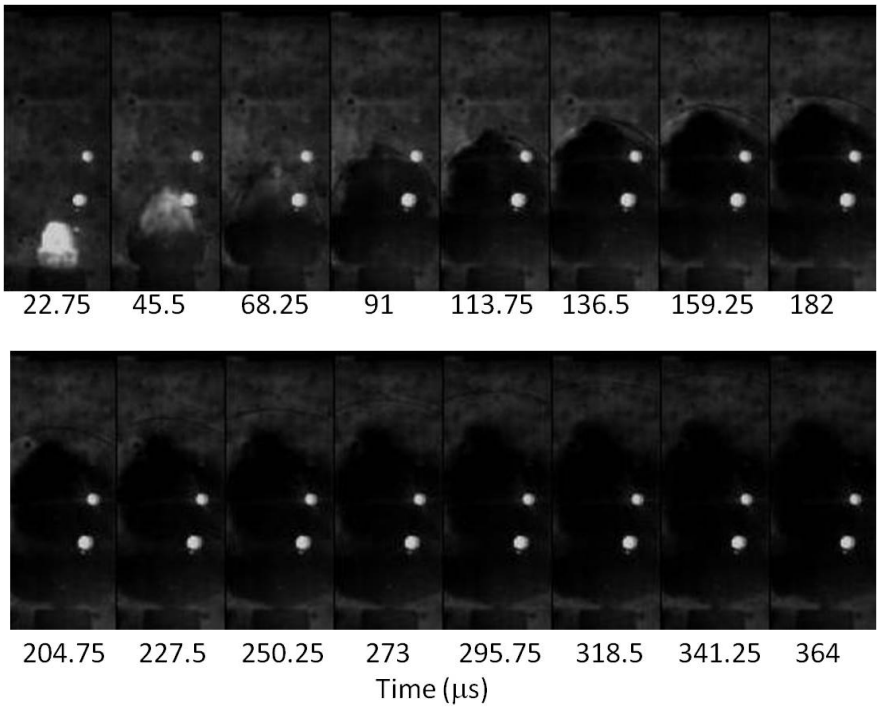

Figure 5.67: Images from 20%-3-μm-Al loaded charge tested in CO_2.

The shock wave velocities from to 20%-3-μm-Al charges in the different environments are plotted in Figure 5.68. The development of the shock wave velocities with respect to time is the same as seen before—after the initial peak, the velocity decreases expontially to approximately 500 m/s after 150 μs. The velocites are similar for each charge after the second data point, independent of the environment. The initial velocities are different, such that the highest velocity was in O_2, then air, CO_2, and N_2.

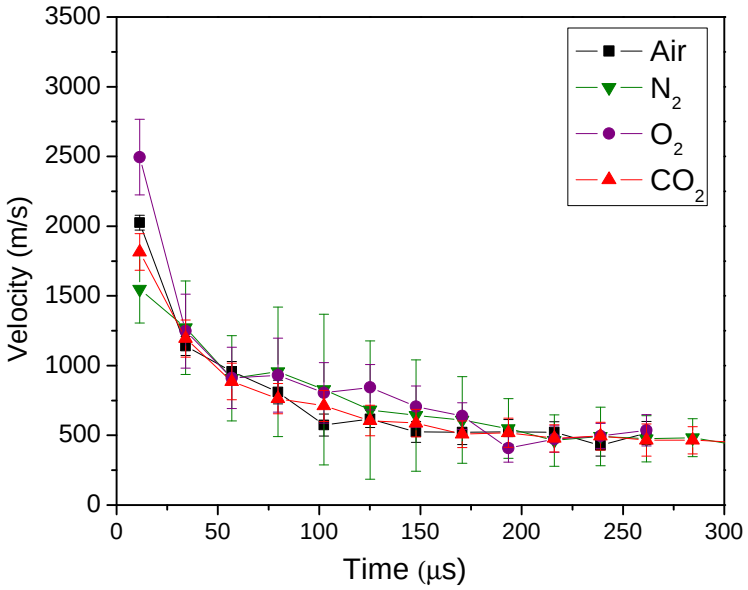

Figure 5.68: Shock wave velocity for the 20%-3-μm-Al loaded charge in each environment.

End-Loaded Charges

The next three HSC images—Figures 5.69–5.71—are from two end-loaded bare charges and the aluminized charge with a layer of grease on the tip. The images from the end-loaded charge tested in air—which used 8.3 mg of aluminum powder—are shown in Figure 5.69. The bright breakout is visible in two frames, and the fireball has a directional jet. The third and forth frames—at 68.25 μs and 91 μs, respectively—also have some brighter visible light on one side of the fireball. AlO emission was measured for 64 μs for this test, which is the same time frame (approximately 68 μs) as the bright spots are seen from the fireball.

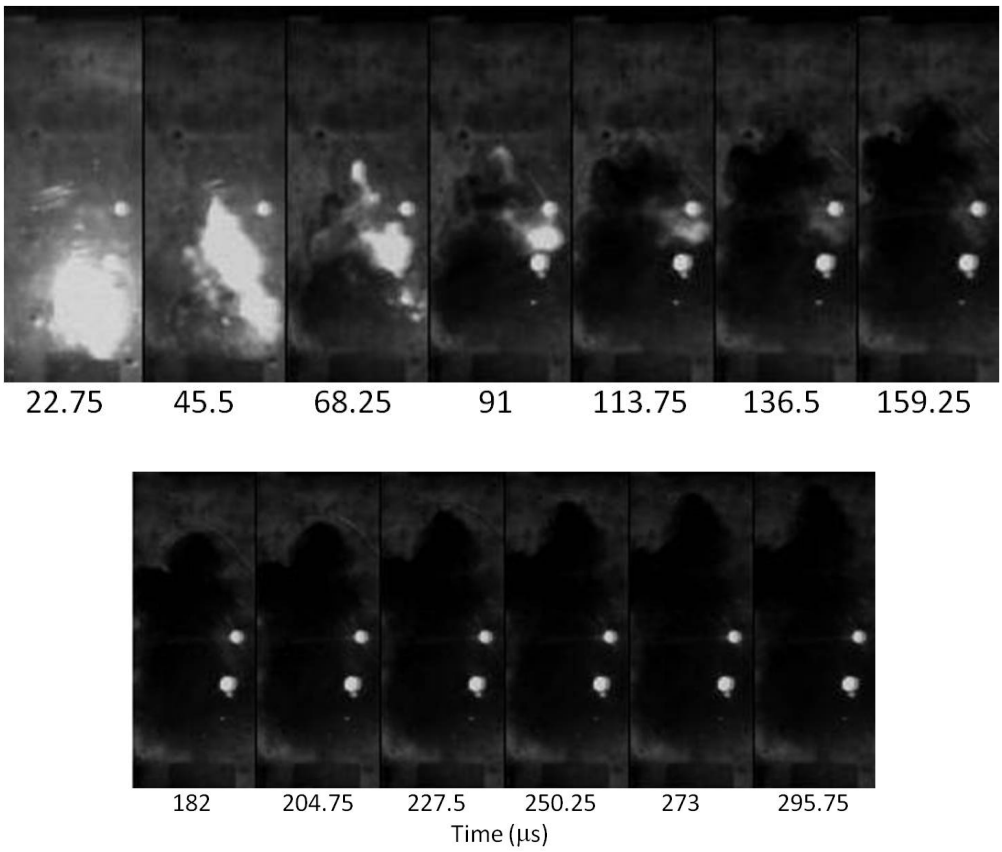

Figure 5.69: Images from the end-loaded charge having 8.3 mg aluminum, tested in air.

The images from the end-loaded charge which used 17.6 mg of aluminum powder, and was tested in air, are shown in Figure 5.70. The charge has more aluminum powder and thus has more bright frames until 113 μs. The bright light seen corresponds to the AlO emission signal measured from this test which lasted 112 μs. The shape of the fireball for the end-loaded charges is more difficult to discern during the bright frames, but is shaped like a jet in some early frames. The shock wave in the later images is rounded or spherical though. The charge having 17.6 mg aluminum powder had a faster shock wave between the first two frames than the charge having 8.3 mg aluminum powder—4200 m/s compared to 2700 m/s. Therefore, the more aluminum powder available to burn, the more visible light seen and the faster the initial shock wave speed.

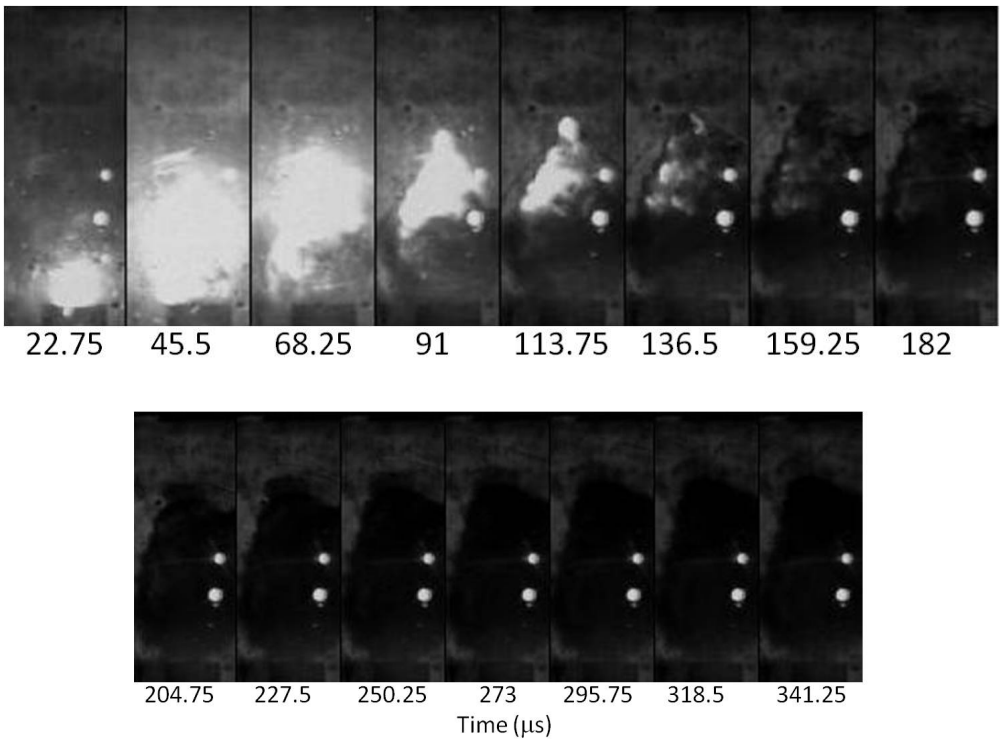

Figure 5.70: Images from the end-loaded charge having 17.6 mg aluminum, tested in air.

The images from the charge having a grease layer are shown in Figure 5.71. The bright breakout of light is present and one additional brighter frame of visible light. The shape of the fireball is similar to the other 20%-3-μm-Al charge, and well as the amount of visible light. Therefore the grease layer does not appear to affect the structure of the fireball after the breakout.

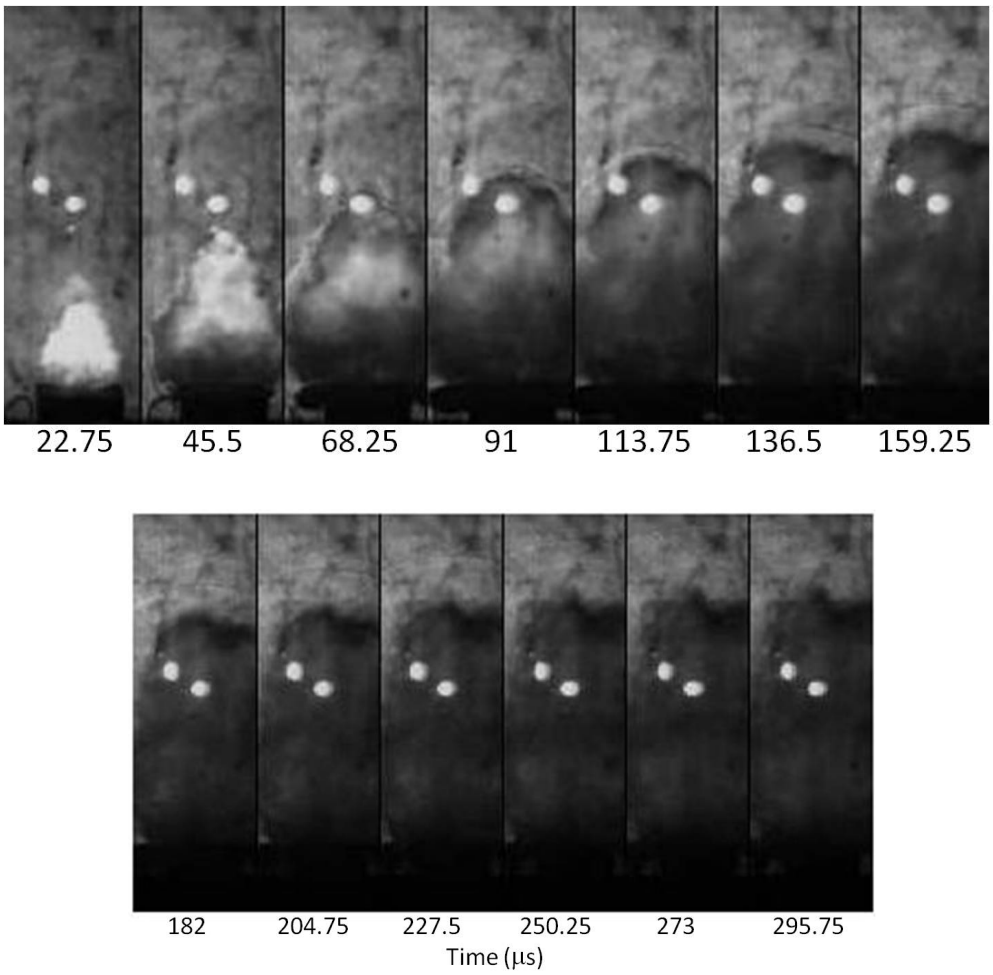

Figure 5.71: Images from a 20%-3-μm-Al charge with a layer of grease on the tip.

5.8.3 Gap Tests

Images from the air gap tests are shown in Figures 5.72 to 5.78. The first set of images is from the test using SiO_2 having a gap of 0.021 inch. Typical of all the tests using a SiO_2 pellets, there is almost no visible luminosity, except a little on the fireball tip in the first frame. Since no aluminum powder is present, the light from the fireball seen in the aluminum pellet tests must be the aluminum burning—as opposed to the mylar or RDX/PETN, which both generate soot and can radiate.

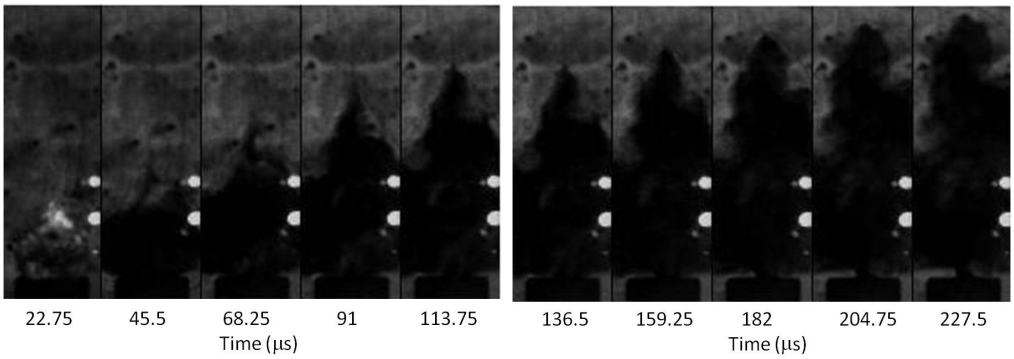

Figure 5.72: Images from the 0.021 inch gap and SiO_2 pellet test.

The next six sets of images are from the aluminum pellet gap tests in air at different gap distances—0.020 in, 0.028 in, 0.059 in, 0.141 in, 0.245 in, and 0.562 in, in Figure 5.73 through Figure 5.78, respectively. The fireball from the smallest gaps—0.02 in and 0.028 in—seems to be brighter than the aluminized charges, especially the first five frames (until $t = 13.75\ \mu s$). The fireball also seems to be more 'consuming' than the aluminized charges, such that the fireball is brighter in general, and the bright light comes from more areas of the fireball. The extra brightness could possibly come from the aluminum powder on the outer surface of the fireball. A directional jet is visible starting in the sixth frame ($t = 136.5\ \mu s$).

The images from the test having a 0.028 in gap (Figure 5.74) have less light in the later frames than the 0.020 in gap, though light is still visible in all the frames captured. As the gap increased, the amount of light visible from the fireball decreased. At a 0.059 in gap, only the top half of the fireball has visible bright light in frames four through seven, when there is also some of the brightest visible light. The directional shape of the fireball is also visible earlier, at $t = 91.0\ \mu s$. At the 0.141 in gap, the brightest visible light is only from the top half of the fireball for all but the first two of the brightest frames, and light is not visible from last few frames, starting at $t = 273\ \mu s$. At the largest gaps—0.245 in and 0.562 in—the amount of visible light is significanly less than at the smaller gaps: only two to three frames. In the few frames that have visible bright light, the light comes from only the top third to quarter of the fireball.

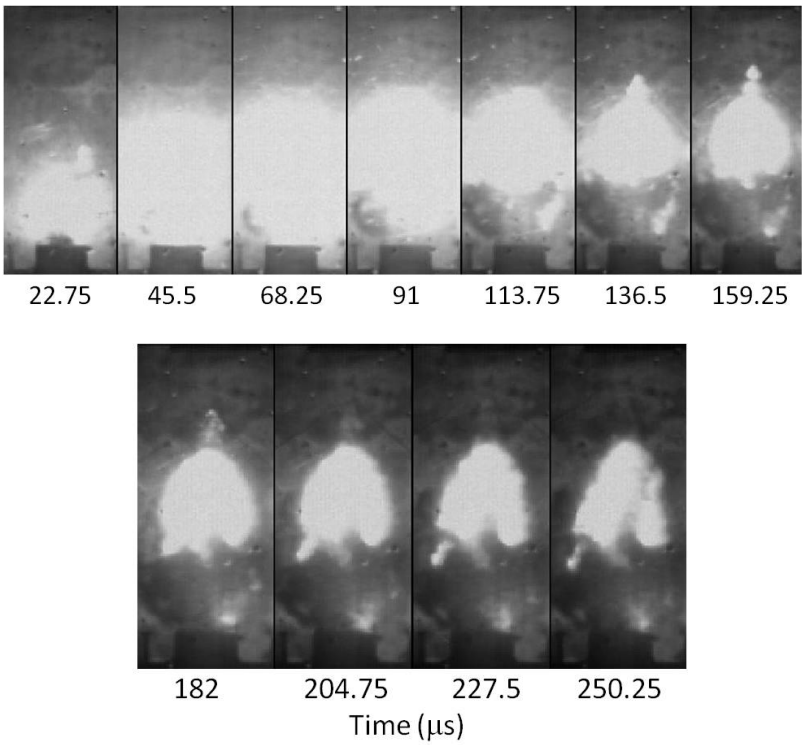

Figure 5.73: Images from the 0.020 in gap, aluminum pellet tested in air.

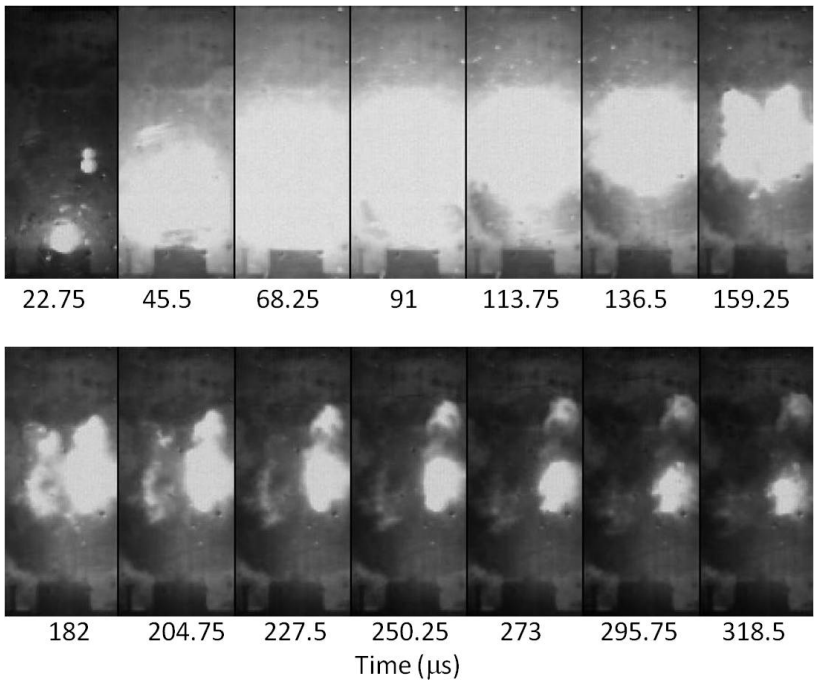

Figure 5.74: Images from the 0.028 in gap, aluminum pellet tested in air.

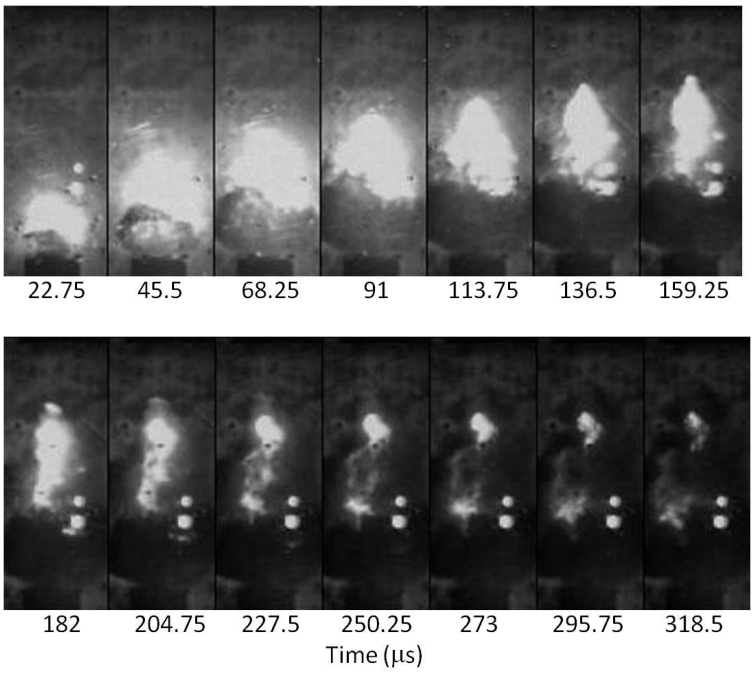

Figure 5.75: Images from the 0.059 in gap, aluminum pellet tested in air.

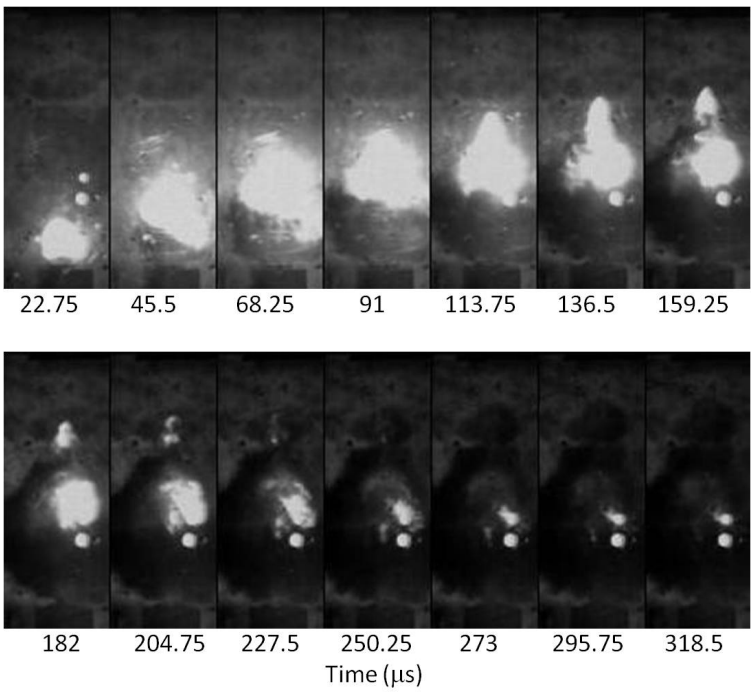

Figure 5.76: Images from the 0.141 in gap, aluminum pellet tested in air.

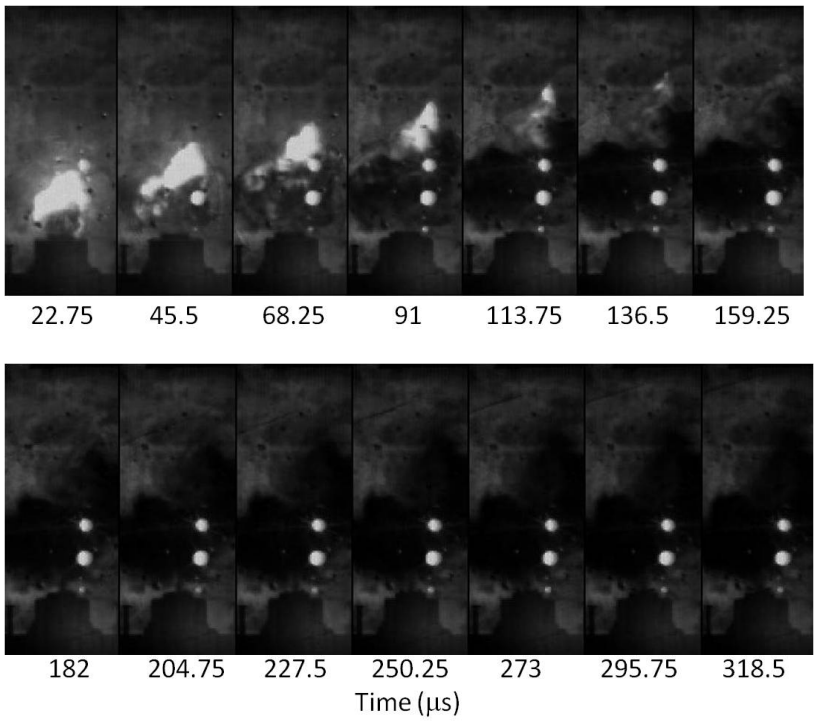

Figure 5.77: Images from the 0.245 in gap, aluminum pellet tested in air.

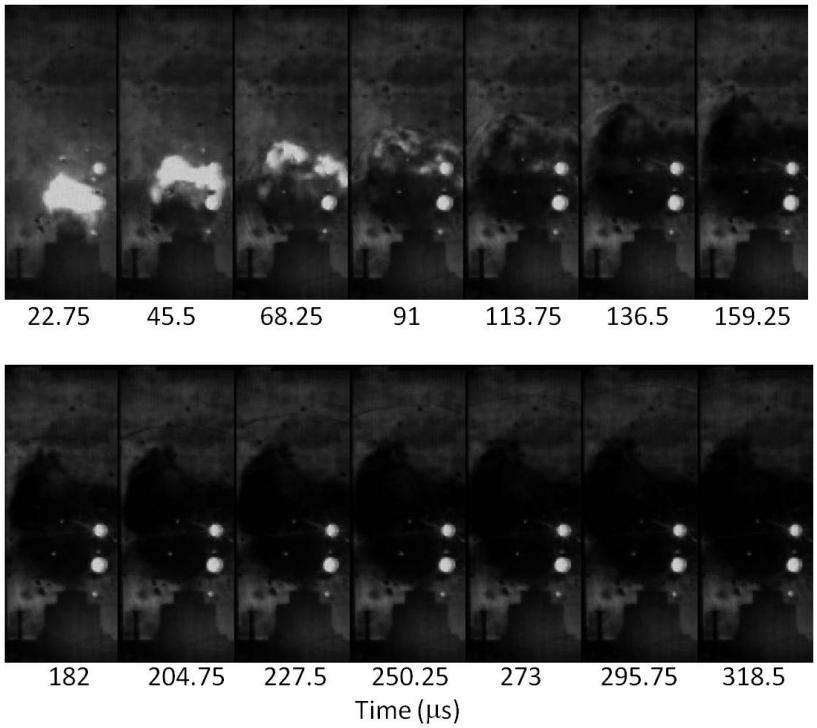

Figure 5.78: Images from the 0.562 in gap, aluminum pellet tested in air.

From the pressure measurements, it was established that the further the aluminum pellet was from the charge, there was less energy released as a result of the aluminum pellet. This is also seen from the amount of bright visible light seen in the HSC images. As the gap increased, the light decreased, indicating that there is less activation of the aluminum powder pellets.

Another effect of the increasing gap is the deceasing initial velocity, shown in Figure 5.79. The development of each test's shock wave was similar to the other tests, such that the velocity decreases exponetially as a function of time to approximately 500 m/s. The initial velocities of each test can give the most information about the shock wave velocity as a funcition of gap distance. As shown in Figure 5.79, the initial velocity decreases exponentially as the gap distance increases. Therefore, as the gap between the aluminum pellet increases, the amount of activation decreases, the amount of visible light from the fireball decreases, and the initial shock wave velocity decreases.

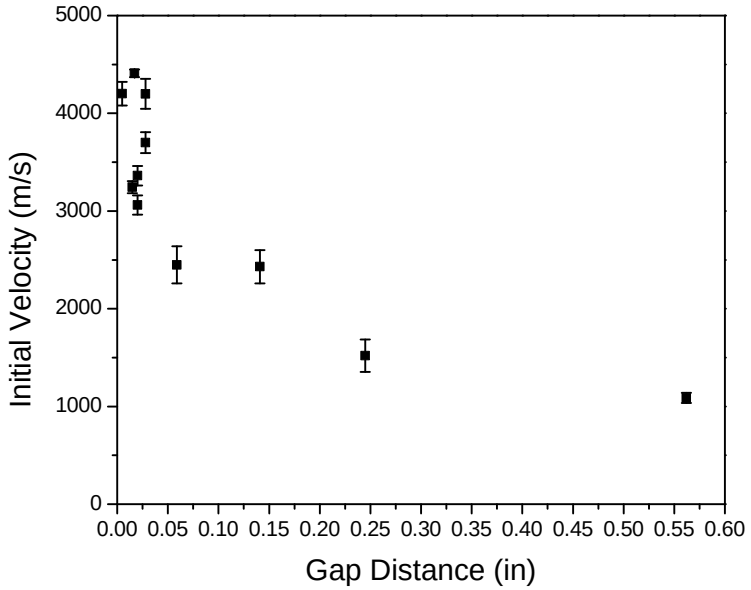

Figure 5.79: Shock wave velocity for the gap test in air using an aluminum pellet.

CHAPTER 6

ANALYSIS OF ALUMINUM BURNING IN AN EXPLOSIVE FIREBALL AND INTERPRETATION OF ALO EMISSION MEASUREMENTS

The work presented has two main objectives: (1) to better understand when, where and with what aluminum burns inside an explosive fireball and (2) to evaluate and characterize AlO emission measurements as an indicator of aluminum burning in the fireball.

In the first section of this chapter, a qualitative description of aluminum burning in an explosive fireball is provided. The model divides the aluminum particle combustion process into four stages. Each stage has its own contributions to the total energy output of the explosive event and implications on the aluminum combustion. The experimental results described in the previous chapter are referenced, and this section brings together the individual sets of data into one cohesive description of aluminum burning in an explosive fireball. The goal is to be able to better answer the question of when, where, and with which oxidizer the aluminum is burning.

The second section focuses on understanding the AlO emission measurement results. Using comparisons to the pressure measurements, this section evaluates the usability and value of an AlO emission measurement in explosives. Nine effects are identified thatwhich influence the AlO emission measurements, and subsequently can influence the interpretation of the AlO emission. The goal is understand what AlO emission measurements can indicate about the aluminum burning in an explosive fireball.

6.1 Understanding Aluminum Burning in an Explosive Fireball

6.1.1 Stage I: Detonation and Aluminum Particle Activation

The first step in the creation of the aluminized explosive fireball is the detonation of the explosive material and the activation of the aluminum particles. McNesby et al.[81] describe this stage as when the detonation wave travels through the solid explosive. Then the shock wave transitions to air, and the dense detonation products start to expand and react anaerobically. McNesby et al. define the end of the first stage as when the detonation products cloud expands to approximately two initial charge diameters, which is when combustion thermochemical calculations indicate that the chemical composition of the detonation products is fixed[81].

During Stage I, the aluminum particles are activated by the detonation wave, and begin to release energy contributing to the initial blast wave velocity. Aluminum combustion behind the detonation wave would contribute to the detonation pressure observed at the edge of the high explosive, causing greater force on the external casing, and higher fragment velocities. Several studies[39, 41, 42] have shown that the detonation velocity of aluminized explosives is not increased significantly over that of the bare explosive—suggesting the aluminum reaction is much slower than reaction occurring in the detonation wave. This observation is consistent with experimental work on aluminum combustion that suggests timescales for oxidation are generally orders of magnitude larger than detonation reaction times, even under extreme conditions[2, 13, 16]. However, in recent work Balas et al.[5] have shown that it is possible for the aluminum to react in the detonation wave in some circumstances, evidenced by high Gurney energies and detonation velocities. The modeling work by Baker et al.[54] confirms that 100 percent aluminum reaction occurs in the detonation wave, and indicates that the activation of the aluminum and the energy release from the aluminum burning is not immediately after the detonation, but is slightly delayed[55]. The enhanced effect from the aluminum combustion appears only in certain formulations, which the authors denote

"combined effects" explosives. The experimental data indicate that there is an aluminum loading limit in order to achieve 100 percent aluminum reaction[5], and other influences to the onset of aluminum reaction include the amount of aluminum, the percent oxygen balance of the explosive, and the aluminum particle size. It is suspected that an energetic binder is needed for the early aluminum reaction[4, 56].

Stage I events occur at near field—at standoff distances of less than or equal to ten charge diameters[82]. Measurements at near-field distance are difficult because of extremely high pressures behind the blast wave, which can be on the order of 100 MPa, and the reflected pressure can be higher than 1000 MPa[83]. Experimental measurements have been completed by [82, 83], and near-field blast modeling has been done by [84–86] to name a few examples of near-field blast investigations. Whether or not the aluminum was activated in the current study was measured by the blast wave enhancement—the air-gap experiments showed that at two charge diameters away from the charge, the aluminum will not be activated since there was no initial blast wave enhancement.

6.1.2 Stage II: Blast Wave Enhancement by Aluminum Combustion

The second stage of aluminum combustion in an explosive fireball is when the aluminum burns to enhance the blast wave, and for the aluminized RP80 charge, this occurs during approximately the first 100 μs after the detonation. The implications of Stage II combustion are a stronger blast wave, and oxidation of the aluminum, increasing the energy output. The stronger blast wave is indicated by higher peak pressures, shown in Figure 5.43, higher initial blast wave impulses, shown in Figure 5.44, and a faster blast wave, shown in Figure 5.45 and as discussed in Section 5.8. Reactions can occur both inside the fireball and on the fireball outer surface.

The available oxidizers for aluminum particles inside the fireball are hot detonation products—CO_2, H_2O, CO, NO, N_2O, and NO_2. As a result, the aluminum reacts with the

hot gaseous detonation products and drives the blast wave, which is indicated by the results from the tests in the N_2, and N_2/CO_2 environments. Independent of the aluminum particle size, in the N_2 environment the peak pressure and initial impulse were increased over the bare and alumina charge cases, as shown in Figures 5.43 and 5.44. Since N_2 is not a purely inert environment and aluminum will react with N_2 in oxygen-deficient environments[33, 34], it is possible that part of the energy released is from the aluminum reacting with the ambient N_2. Similarly, from the end-loaded charges in N_2, the peak pressure is enhanced over the bare charge indicating anaerobic reactions with the surface aluminum. The mixing at the fireball surface exposes the aluminum particles to the inner hot detonation products, enhancing the energy output, as tabulated in Table 5.6. The peak shock wave velocity was higher for the aluminized charges compared to the bare charge, both in N_2, which also indicates early reactions of the aluminum with the detonation products.

On the outer surface layers of the fireball, hot detonation products plus cold atmospheric gasses—O_2, N_2, and/or CO_2—are available oxidizers for the aluminum particles, and mixing of the detonation products and the ambient air occurs. The aluminum particles near the edge of the fireball enhance the mixing by creating instabilities at the shock and detonation products interface, further creating a mixing layer between the detonation products and the ambient air[51]. The mixing of ambient oxidizers (air) and the detonation products heats the ambient environment rapidly locally, and introduces additional oxidizer to the aluminum particles. As a result, the fast aerobic reactions occur near the surface of the fireball in the mixing layers. McNesby et al.[81] also indicate that during the second stage aerobic burning at the fireball-ambient interface may contribute to the thermal emission and enhance the shock velocity.

Reactions from the mixing of the turbulent layers on the outer surface of the fireball are indicated by the further increase of the peak pressure and initial blast wave impulse in the air and O_2 environments as shown in Figures 5.43, 5.43, and 5.44. An effect from the aerobic reactions is seen from the higher shock wave velocities in 40/60 N_2/O_2 and air compared

to N_2 and N_2/CO_2, as shown in Figure 5.68. There is a higher shock wave velocity from end-loaded charges having 17.6 mg aluminum compared to 8.3 mg of aluminum in air, and a higher shock wave velocity for small gaps—less than 0.05 inch.

During Stage II combustion the temperatures are extremely high—3000–4000 K and up to 10,000+ K at breakout—as indicated in Figures 5.13, 5.14, 5.41, and 5.56. The detonation gases are extremely hot and therefore contribute to aluminum combustion. The high temperatures also influence the amount of AlO emission measured because AlO emission is exponentially dependent on temperature.

Additional evidence of aluminum burning during Stage II combustion results from the AlO emission measurements and visible light emission from high speed camera (HSC) images. While the AlO emission measured originates from the outer surface of the fireball, the AlO emission may be evidence of aluminum combustion because it is an intermediate of aluminum reactions with O_2, CO_2 and H_2O. Most of the AlO emission measured was dominated by a single 16 μs frame or was over within 100 μs.

The first of two caveats of using AlO emission as an indication of aluminum combustion during Stage II is the AlO emission from hot dissociated Al_2O_3. While any hot Al_2O_3—from theoxide layer on the particle surface or newly formed—contributes to the AlO emission signal during the first 40 μs, AlO emission from Al particle reactions also exists, as demonstrated in Figure 5.25. The HSC images show only a bright breakout for the alumina (Al_2O_3) charge in Figure 5.58, and less visible light exists than from the aluminized charges, shown in Figures 5.59—5.61 and 5.63, but there is more light emission than from the bare charge in Figure 5.57. Therefore, the light output and AlO emission must be partially from hot dissociated Al_2O_3, and partially from Al particle reactions.

The second caveat for aluminum combustion indicated by AlO emission is the effect of the high temperatures influencing the amount of AlO emission measured. The initial blast wave was enhanced from the aluminum particles at the largest gap, but AlO emission—on the same order as the smaller gaps—was still detected. Therefore, the high temperature of

the fireball induces some Al combustion and/or dissociation of the oxide layer resulting in AlO emission from particles on the outer surface during the first 100 μs, even in the absence of measurable initial blast wave enhancement.

AlO emission measured from tests in N_2—shown in Figure 5.54 and in Figure 5.2—partially comes from anaerobic reactions with the detonation products. The high temperatures caveat applies, and the high temperatures can cause anomalously high AlO emission without a lot of AlO emission being present. The Al_2O_3 test in N_2 did have AlO emission, so some of the AlO emission measured is also from evaporization and dissociation of the oxide layer. The high speed camera images have a bright breakout plus more visible light in one frame—compared to the bare charge—in CO_2 and N_2 as seen in Figure 5.67 and 5.66, respectively. The extra light is most likely from outer particles burning with the detonation products.

Part of the AlO emission is from fast aerobic reactions on the fireball surface after the initial breakout indicated by the significant (meaning more than in CO_2 or N_2) AlO emission measured in O_2 and air environments: one 16 μs frame or more within the first 100 μs as seen in Figures 5.2, 5.31, 5.37, and 5.54. The amount of AlO emission measured very much depends on particle location as exhibited by the end-loaded and gap tests—more AlO emission was measured in the first 100 μs than from most aluminized charges, shown in Figures 5.30 and 5.37. For the end-loaded charges, when more aluminum particles are on the fireball surface, more AlO emission was measured, as shown in Figures 5.31 and 5.33.

The high speed camera images show significantly more light after the initial breakout for the aluminized charges in air—shown in Figures 5.59–5.61, and 5.63—in the first four frames, which is up to 91 μs after detonation, and also in O_2 shown in Figure 5.65. Images from the end-loaded charge tests have more light and aluminum burning on the surface when there is 17.6 mg of Al powder (Figure 5.70), compared to when only 8.3 mg of Al powder is present (Figure 5.69). For the air gap tests there was no light from the SiO_2 pellets, shown in Figure 5.72, therefore the visible light from the Al pellet tests is from aluminum burning

or dissociating on the surface of the fireball, as seen in Figures 5.73–5.78.

To determine whether the energy released from the aluminum is used to drive the blast wave, ideal blast calculations were completed using the Taylor similarity solution to the blast equations[76]. Details of these the calculations can be found in Appendix C.2. The ideal peak blast characteristics—peak pressure, time of arrival at 21.3 cm from the blast site, and the initial blast wave impulse—were calculated for four cases. The cases are a bare charge of PETN/PB-9407(RDX) denoted 'bare', an 'inert Al' case in which none of the aluminum reacts to release energy and is based on 20 percent less explosive material than the bare case. The '20% Al' case assumes 20 percent of the RDX is replaced with aluminum that is fully oxidized in the blast wave and similarly, the '50% Al' case replaces 50 percent of the RDX with aluminum that fully reacts in the blast wave. The energy ratios were determined by comparing a calculated energy of explosion[87] (details in Appendix C.2), assuming none of the Al reacts, i.e., 'inert Al', to the case in which all the aluminum forms Al_2O_3—20 percent and 50 percent Al—in the initial blast wave.

The calculated peak pressures and pressure curve decays at 21.3 cm from the blast site are shown in Figure 6.1, and Table 6.1 lists the peak pressures and initial blast wave impulse values for the different cases. The 'inert Al' actual test is based from the Al_2O_3-loaded charge test. The trend of the peak pressures and impulses is as expected—'inert Al', 'bare', '20% Al', '50% Al', in order of lowest to highest. However, the comparison of the actual tests percent enhancement is different. For example, instead of having a 19.6 percent increase in peak pressure from the 'bare' to the '20% Al' case, the actual increase was less than half, at 7 percent. The discrepancy between the predicted and actual peak pressure enhancement indicates that some, but not all of the aluminum energy release contributes to the blast wave enhancement.

The difference between the ideal and actual comparison between the 'bare' and 'inert Al' cases indicates that energy is required to accelerate and heat up the alumina in the blast wave because the blast equations predict a 8 percent decrease in peak pressure, while in

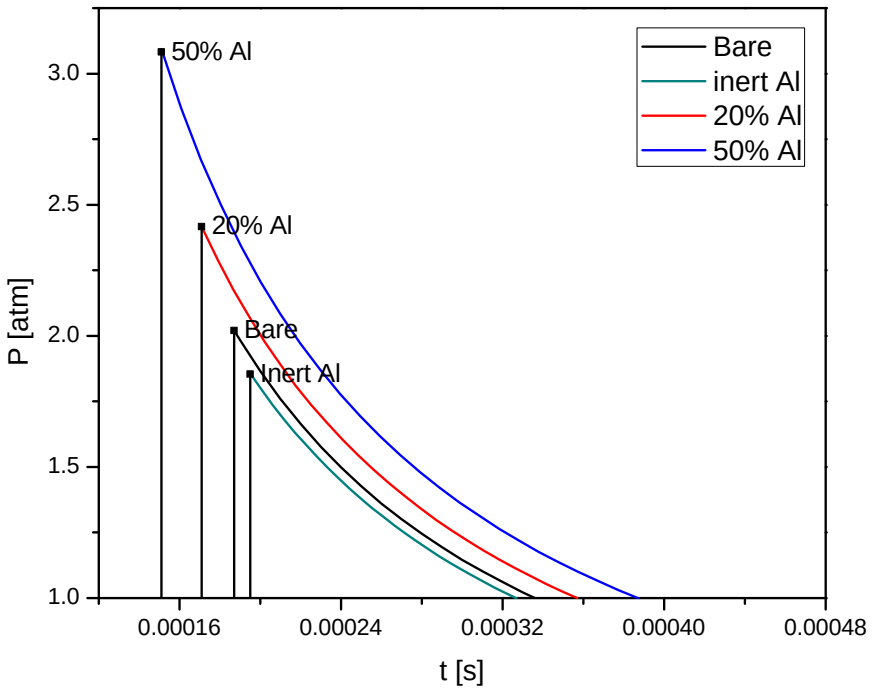

Figure 6.1: Ideal pressure traces for blast driving based on the Taylor blast similarity solution.

the actual tests the peak pressure decreased by 24 percent. Since the peak pressure for the aluminum loaded case is more than the 'bare' case, and peak pressure for the 'inert Al' case is less than the 'bare' case, the aluminum reacts during Stage II combustion to enhance the blast wave.

The differences between the ideal and actual impulse enhancements—which are different than the peak pressure comparisons—indicate that the pressure curve of the actual blast wave is not ideal. The blast wave is expected to be non-ideal because the experimental blast wave does not fit two of the assumptions necessary for the similarity solution—a spherically symmetric blast wave, and an instantaneous energy release which remains constant for a period of time[76]. The blast wave is not spherical in shape as the images from the high speed camera showed, for example in Figure 5.63. In addition, the energy is not released instantaneously, as most real processes require a finite amount of time to take place.

Table 6.1: Comparison of blast driving energy release between the types of charges.

	Bare	Inert Al	20% Al	50% Al
Energy Ratio	1.00	0.917	1.196	1.526
Ideal Peak Pressure (atm)	2.02	1.853	2.416	3.083
Pressure Comparison to Bare (%)		-8.25%	19.6%	52.6%
Actual Peak Pressure Comparison		-24.20%	7.10%	
Ideal Impulse (Pa-s)	21.18	17.91	28.64	40.48
Impulse Comparison to Bare (%)		-15.44%	35.22%	91.12%
Actual Impulse Comparison		-13.80%	24.20%	

A comparison of aluminum loading—20 percent to 50 percent—based on data from piezoelectric pressure transducers—in which only initial blast wave peak and impulse data are available—is presented in Table 6.2. The predicted ideal blast equations for the 50 percent aluminum loading gave the peak pressure to be higher by 27 percent, and the impulse to be higher by 41 percent than the 20 percent aluminum loading if all the aluminum burned in the blast wave. However, the actual data show that (within measurement uncertainty) the initial blast wave has the same performance. In addition, the performances of the 20%-40-μm-Al charge and the 20%-3-μm-Al charge plus a grease layer are the same as the 20%-3-μm-Al charge. These data and comparisons indicate that the same amount of energy (in these cases) is released to enhance the blast wave—approximately 93 percent of the total available for the 20% Al case, and approximately 81 percent of the total available for the 50% Al case—and therefore some energy can still be released to enhance the overpressure. The experimental data indicate some additional enhancement from the 40 μm particles compared to the 3 μm at later times—after 5 ms during Stage III combustion.

Table 6.2: Comparison of peak pressures and initial blast wave impulses of 20 and 50 percent loadings. All percent differences are with respect to the 20%-3-μm-Al charge.

	Percent difference compared to 20%-3-μm		
	50%-3-μm	20%-40-μm	20%-3-μm + grease
Ideal Peak Pressure	27.6%		
Actual Peak Pressure	4.50%	0.30%	3.30%
Ideal Impulse	41.3%		
Actual Impulse	2.40%	1.40%	6.90%

6.1.3 Stage III: Overpressure Enhancement

The time scale for Stage III combustion for the RP80s is on the order of milliseconds. During this time continuous mixing of the detonation products with the ambient environment occurs, and as a result, the aluminum particles inside the fireball are exposed to additional oxidizers. Fast, high energy, hot reactions with O_2, and slower, cooler, less energetic reactions with H_2O and CO_2 and other detonation products happen simultaneously while the aluminum continues to oxidize.

The implications of Stage III combustion are overpressure, an increased impulse—demonstrated by Figure 5.52—and continued high temperatures. The overpressure is a thermobaric overpressure effect and is determined by a sustained pressure in the chamber above 1 atm. Mostly aerobic reactions occur, but the anaerobic component is not negligible—shown in Figure 5.47—because the mixing of the ambient environment and the detonation products enhances energy release. There is a net yield of energy from aluminum particles even without aerobic reactions as seen in Figure 5.53. The overpressure and enhancement is predominantly a function of environment and particle size during this time, such that aerobic reactions are more important for the larger particles, and anaerobic reactions are more important for smaller particles, which is further evident from a quasi-static pressure measurement of the late time combustion and is discussed below. The mixing of the detonation products and ambient environment continues the aerobic reactions, driving the overpressure of end-loaded charges too, which is also indicated by McNesby et al.[81] during this time.

For most test runs, pressure data were taken out to 10 ms. For the region from 5–10 ms, significant ambient fluctuations were still observed, but the fluctuations were dampened and more symmetrical than earlier in the trace. Therefore, by averaging the pressure in the 5–10 ms region, an estimate of quasi-static pressure was obtained. Unlike blast pressure, the quasi-static pressure (QSP) depends linearly on the energy release, and thus provides a more sensitive measure of reactions and reaction channels, e.g. aerobic or anaerobic. Each

run gives two measures of QSP, one from each transducer—21.3 cm and 32.1 cm from the blast site. Unlike the blast data, there is generally good agreement in magnitude of QSP from both sensors. Data from all runs for which late-time pressure traces are available are shown in Figure 6.2.

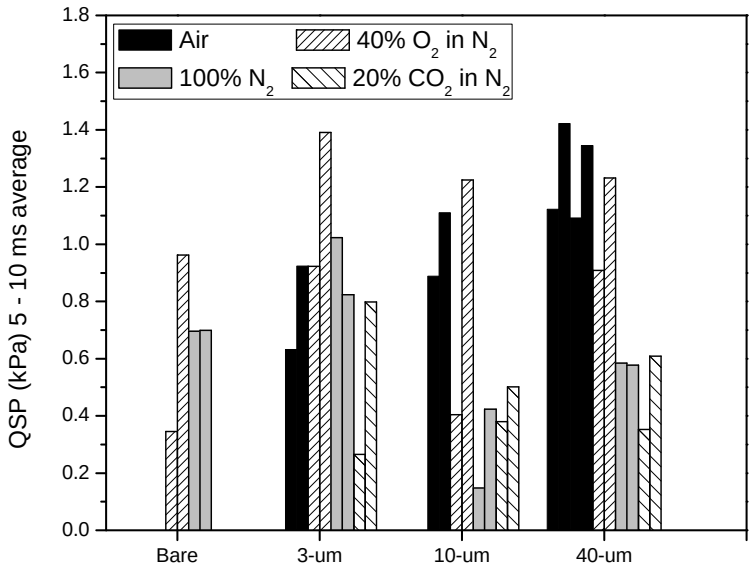

Figure 6.2: Quasi-static Pressure (QSP) for 15 runs. Data is shown from both sensors.

The bare charge data show the expected increase in QSP as a result of the delayed reaction of the fuel-rich detonation products with air. In addition, several trends are apparent. The total energy released from the aluminized charges exceeds that of the bare charge under identical conditions, though the overall effects are less pronounced than those seen in blast. Additional oxygen in the air tends to improve overall heat release by either increasing the total amount of oxidation or by shifting the aerobic/anaerobic fraction. Anaerobic enhancement of the total energy release is small, in agreement with the findings of Carney et al.[48].

To quantify these effects and provide some indication of the total amount of oxidation, the QSP can be compared in a relative sense to the measurements from the bare charge. The bare charge in 40% O_2 is assumed to be fully oxidized by 5 ms after the blast and its

energy release is the sum of the combustion energies of the 80 mg of PETN and 123 mg of PBX-9407. The relative QSP can then be compared to this baseline case in order to estimate the amount of reaction from the aluminum additive by calculating the expected QSP for aerobic and anaerobic environments as a function of the total amount of aluminum reacted for each of the aerobic and anaerobic reactions. The relative QSPs are shown in Figure 6.3.

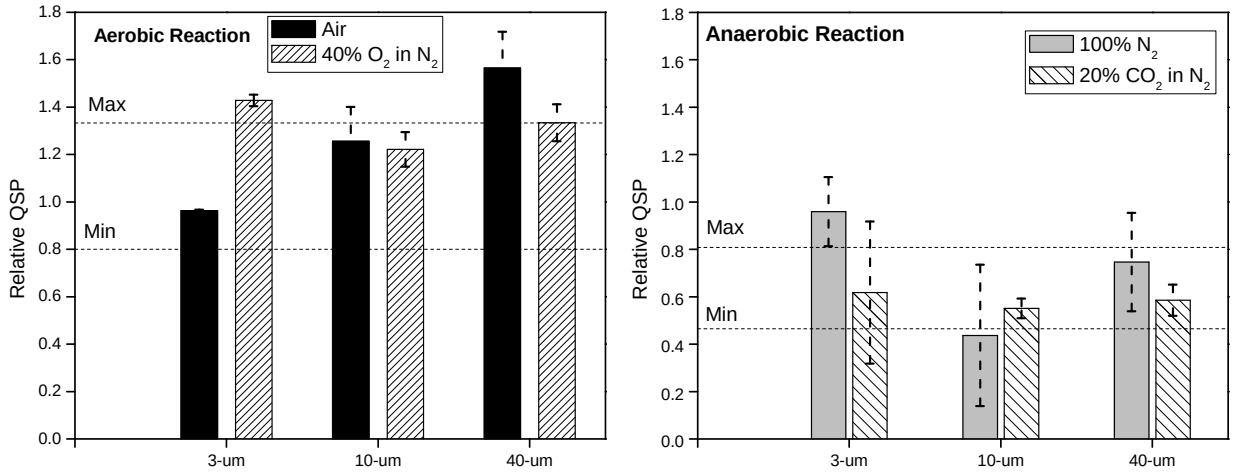

(a) Aerobic Reaction

(b) Anaerobic Reaction

Figure 6.3: QSP scaled to the bare charge in 40% O_2. The minimum corresponds to no aluminum reaction, and the maximum corresponds to complete aluminum reaction.

The assumption that the explosive is fully oxidized in the 40% O_2 case is reasonable considering the relative QSP in the aerobic and anaerobic cases, as well as the absolute value of the QSP. For in the blast chamber, complete oxidation of the bare charge, having no energy go into case fragmentation, mount deformation, or heat losses to the mount yields a QSP of 1.52 kPa, whereas the bare charge provides 1.03 $\pm$ 0.14 kPa experimentally. It is a realistic estimate for a small charge in a large (470 liter) chamber that roughly 25 percent of the energy goes into deformation and heat losses.

For the aluminized charges, the aerobic oxidation channel yields at most 31.0 kJ/g,

while the anaerobic channel is about half that (17.6 kJ/g for reactions with H_2O, 15.3 kJ/g with CO_2, and 11.8 kJ/g for nitridation). The line corresponding to "minimum" for these cases in Figure 6.3 represents no aluminum reaction—i.e. 80% of the bare charge QSP—and "maximum" is the expected QSP for full reaction of aluminum by either aerobic or anaerobic reactions. For the air and 40% O_2 cases, the relevant comparison is shown by the aerobic limits. Note that, within experimental uncertainty, the results are consistent having nearly complete aluminum reaction by aerobic reactions. The nearly complete alumiunm reaction does not mean that all reaction was with O_2, since reaction with CO_2 or H_2O leads to Al_2O_3, and products can be further oxidized to yield identical heat release as direct aerobic oxidation.

The exception in the case of the aerobic system is the 3 micron particles, where the amount of aluminum reaction in the air case is only in the range of 50 percent, though the full release is attained using 40 percent oxygen. Anaerobic measurements in N_2 suggest that around 50 percent of the particles react, again except for the 3 micron case, in which the anaerobic channel is pronounced. It may not be coincidental that the 3 micron particles have anomalously low aerobic oxidation in air. The results taken together suggest that the anaerobic channel for the 3 micron particles is pronounced and/or the aerobic channel suppressed. The blast data in Figures 5.43 and 5.44 show similar results, though the effect is not as apparent. A possible explanation is that smaller particles stop faster and are not thrown out into the mixing layer or even beyond the blast wave—as observed by Carney et al.[48]—and that larger particles have a much greater chance of being propelled into oxygen rich ambient gases, leading to an enhancement of the aerobic channel.

Comparing the 20%/80% CO_2/N_2 cases to the pure N_2 cases, the former cases have lower QSP than the latter for the 3 and 40 micron aluminum cases, though the numbers are typically within the error limits. While air, 40% O_2 in N_2, and 100% N_2 environments generated pressure traces that had peaks and troughs at nearly identical locations, the 20% CO_2 cases were shifted significantly at later times as shown in Figures 5.51 and 5.52; and

are a result of a difference in sound speeds as discussed previously in Section 5.7. Thus, the relative comparison of QSP traces obtained using averages obtained over a prescribed temporal period will be least reliable for this case.

The fireball temperatures shown in Figure 5.56 are still high, approximately 2000–3000 K. Ambient pressures are of order of 1 atm and ambient temperatures are in the vicinity of 1500–2500 K[88, 89]. AlO emission was measured for only two cases—the 50%-3-μm-Al and 20%-40-μm-Al charges in air. The measured AlO emission indicates that the aluminum is burning during Stage III for these two cases. The Stage III or late-time AlO emission measurements are discussed further in Section 6.2.

During Stage III combustion there was no blast wave enhancement. The shock wave velocities quickly decrease—after 150 μs—from the peak velocities to a similar velocity of approximately 500 m/s, regardless of loading, Al particle size, and environment, as shown in Figures 5.62, 5.64, and 5.68.

During Stage III combustion, the energy is released to heat the surrounding environment and to increase the overpressure in the enclosed chamber. To determine when the heat release happens from the aluminum, an ideal impulse curve can be determined for the energy released at a constant rate during different time frames by assuming that all the energy goes to increase the temperature, and therefore, the pressure in an assumed constant volume ideal perfectly stirred reactor. The following unsteady energy equation was used to solve for the reactor temperature:

$$m_{cv}(U - U_o) = \int_{t_1}^{t_2} \frac{Q_{cv}}{\Delta t} dt \tag{6.1}$$

where m_{cv} is the mass in the control volume and is a constant, U and U_o, are the internal energies at the temperature T and the initial temperature, respectively. The heat, Q_{cv}, is released at a constant rate over the time frame $\Delta t = t_2 - t_1$. The resulting pressure was determined using the ideal gas law—$PV = m_{cv}RT$—for the constant volume, mass and calculated temperature, and the impulse is the integral of the pressure with respect to time.

Figure 6.4 shows a comparison of three different time frames in which the energy is released—1–2 ms, 1–3 ms and 1–5 ms—for the 20%-Al case and is compared to experimental data from a 20%-3-μm-Al charge tested in air. After the energy was released in the allotted time frame, the ending pressure was assumed to remain constant—assuming no additional heat loss or gain to the constant volume. The amount of energy released was based on the amount of energy remaining after the initial blast wave expansion, which was shown to be approximately 7 percent based on the ideal blast calculations. In the ideal stirring reactor calculation, 96 J of energy were released, which is 7 percent of the heat of explosion (1376 J) for the 20%-Al charge.

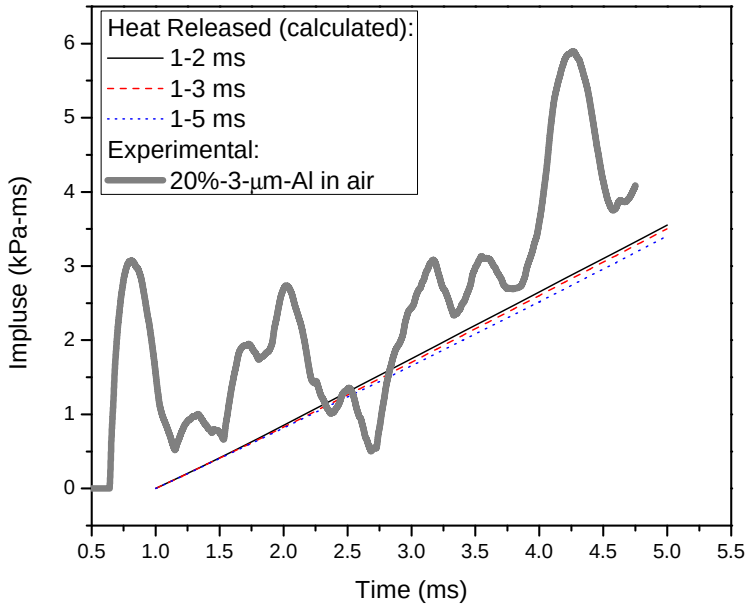

Figure 6.4: Impulses for the energy released in an ideal stirring reactor in three different time frames for 20% aluminum additive and impulse curve from experiemental data.

The calculated impulse curves are similar for each time frame of the heat release. At 5 ms, the difference between the impulse curve of the 1–2 ms and 1–5 ms heat releases is only 4 percent, and the difference between the 1–3 ms and 1–5 ms heat releases is 2.75 percent. In general, there is not much difference in the long-term impulse for the different heat release times, which may be a result of the constant heat released in the calculations. The largest

impulse is for the quickest heat release, so there is some benefit to releasing the energy as quick as possible. The calculated impulse curves are on the same order as the experimental data, and the slope of the calculated curves is also similar to the experimental data. The similarity of the calculated curves makes it difficult to determine the time frame of the actual aluminum energy release.

6.1.4 Stage IV: Cooling and Dispersing Explosive Fireball

Stage IV combustion is on the order of 100s of milliseconds for the RP80 charge. The aluminum particles may continue to oxidize in the cooling detonation products and air, but there was no measured contribution to the energy output from the aluminum particles. The continued aluminum oxidation is indicated by the X-ray analysis of the residue particles, which showed significant aluminum oxidation for all tests, independent of the environment and particle size or loading. However, exactly *when* the particle oxidation occurred cannot be determined, and therefore it is unknown what fraction—if any—actually occurred during the late combustion event. The temperature of the fireball is likely to remain hot—i.e., greater than 1000 K—for at least 1–2 seconds after detonation[88, 89]. At these temperatures, aluminum can continue to oxidize without producing work, such as was observed when aluminum particles were oxidized in the oven at 650°C, (see Chapter 4.2.4). The particles may be quenched early in the cooling fireball, and therefore have only 60–70 percent oxidation in the N_2 and CO_2 environments compared to the initially hotter fireball in air and O_2 environments. Quenching would also eliminate oxidation of the particles during Stage IV. Additionally, equilibrium calculations showed that there is sufficient oxidizer available in the detonation products to fully oxidize the aluminum particles, so it is possible that some oxidation occurs during this stage.

6.1.5 Summary of Combustion Stages

The key characteristics of each stage of combustion are summarized in Table 6.3, and a schematic of the four stages is shown in Figure 6.5 (not to scale). Only Stages I and II contributes to the blast wave enhancement. Aluminum particles in the 3–40 micron range provide primary blast enhancement that is consistent with full reaction of the metal in the period required to drive the blast wave. The blast driving reaction is approximately 50 percent aerobic and 50 percent anaerobic as determined by experiments in nitrogen environments. The blast driving effects are not strongly dependent upon particle size within the 3–40 micron size range. Stage III contributes to millisecond scale impulse enhancement. Quasi-static pressure measurements suggest that the oxygen in air is sufficient to fully oxidize the aluminum within 10 ms.

Table 6.3: Summary of combustion stages.

	Blast Wave Enhancement	ms-Scale Impulse Enhancement	Aluminum Residue Oxidation	AlO Emission Measured	Visible Light Emission	Temperature Ranges (K)
Stage I Reaction in detonation wave	Yes	no	yes	no	no	3000-4000
Stage II Blast wave driving	Yes	no	yes	yes	yes	10000+ (breakout) dec. to 4000
Stage III Reaction in fireball	No	yes	yes	infrequent	infrequent	3000–2000
Stage IV Late time oxidation	No	no	yes	no	no	>1000[88, 89]

AlO emission was measured for the first two stages, as well as visible light emission was seen. The temperature scale of the first stage in the detonation wave is 3000–4000 K. At breakout the temperature starts extremely high—at 10,000 K—and rapidly decreases to 4000–3000 K within the first 20 μs. The temperatures are relatively stable and then decrease during the second stage from 3000 K–4000 K, to 2000–3000 K. During the fourth stage the fireball continues to cool towards the ambient temperature.

As shown from the ideal blast analysis some of the aluminum burns to enhance the blast wave in Stages I and II combustion. However, not all the available energy from the aluminum is released and some of the energy is used in the overpressure enhancement during Stage III

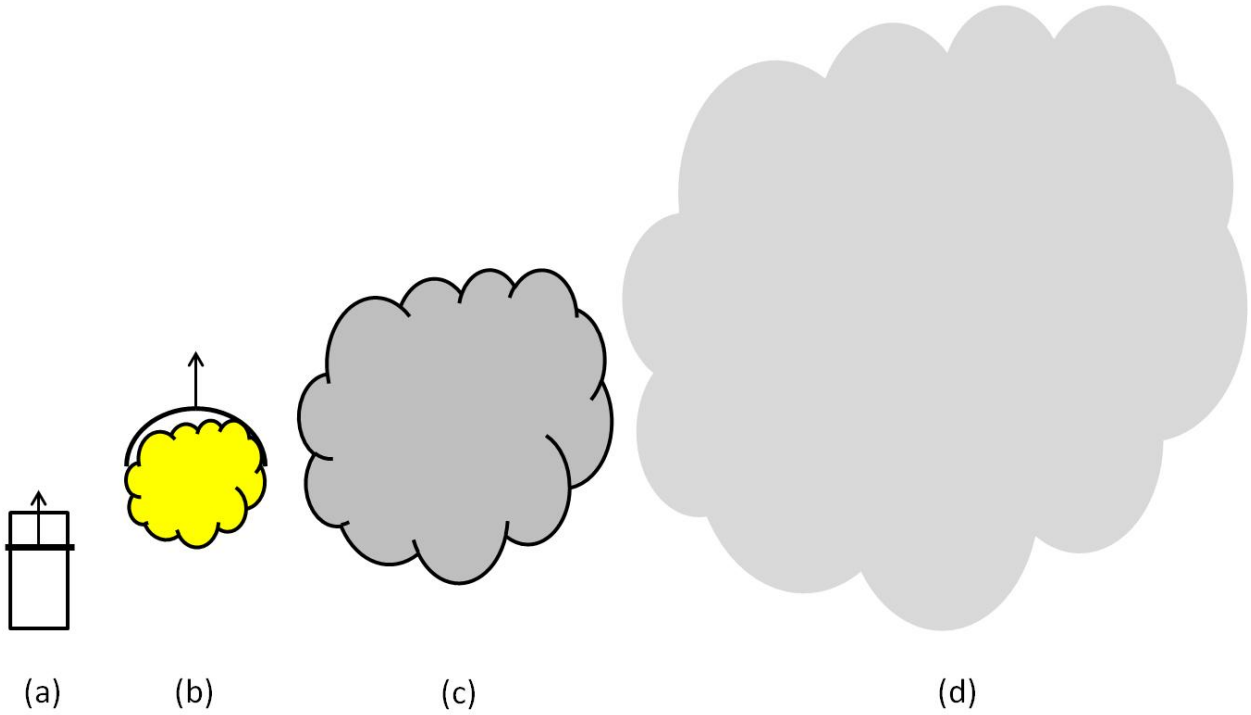

Figure 6.5: Schematic of combustion stages. Not to scale. (a) Stage I: Detonation wave travels through charge, (b) Stage II: Breakout, blast wave travels through ambient and fireball development begins, (c) Stage III: Reactions in growing fireball, (d) Stage IV: Fireball disperses.

combustion, which is confirmed by the blast driving and QSP measurements.

Using some simple scaling, the amount of aluminum reaction that drives the blast can be estimated. For ideal explosives, impulse should scale as charge energy to the one-third power. Assuming a detonation energy of 6.2 kJ/kg for the PBX9407, and heat release of 31 kJ/g for the aluminum—the upper limit—20 percent replacement of aluminum in the charge reacting completely would yield a blast enhancement of 21 percent in the far field of a spherical blast. The fact that this geometry is not entirely spherically symmetric—there is certainly a directional effect that drives the flow preferentially upward— and that neither PBX9407 nor its aluminized variant are ideal explosives makes this calculation imperfect. However, it does suggest that an appreciable amount of the metal, quite possibly most of it, does react to drive the blast, and the fraction reacted is fairly independent of particle size in the 3–40 micron range.

6.2 Influences to AlO Emission Measurement and Its Interpretation

Typical interpretations of AlO emission focus on relating the duration of the AlO emission to the time that the aluminum particles burn. Most burn time measurements of aluminum particles have focused on quiescent burning of individual particles, or a cloud of particles in a shock tube, which can set up a known pressure-temperature condition. The inherently transient conditions of an explosive fireball make it difficult to conduct the same sort of burn time measurements. This section attempts to determine if AlO emission measurements made from an explosive fireball accurately reflect the burn time of the aluminum particles in the fireball.

Shock tube measurements of burn time for 3-μm aluminum at 20 atm and 2650 K (ambient temperature) are approximately 100 μs[19], and burn times for 10-μm particles at 30 atm and 2650 K (ambient temperature) are on the order of 50 μs[16]. The shock tube data suggests that the burn time at higher pressures in the fireball may be on the order of the AlO emission measured for the smaller particles, which other studies have also suggested[48]. However, the AlO emission measured is not on the order of burn times for the 40 μm particles—which weakly depends on pressure—and have a burn time on the order of 4 ms[90], while the fireball AlO emission was measured for approximately 100 μs.

The burn times in the shock tube also depend on oxidizer concentration[2, 16, 19]. Some AlO emission was observed for the tests in N_2 and CO_2, but the duration is much less than the typical reported burn times, which can be on the order of 100s of microseconds for 3 and 10 μm particles in CO_2 at an ambient temperature of 2650 K[2, 16, 19]. The AlO emission is produced by reactions with detonation products; however, since the duration was typically one 16 μs time frame, and was a similar time frame for the experiments in air, the AlO emission duration cannot be considered a burn time in the same meaning as for the shock tube experiments. In addition, pressure measurements show an important anaerobic

component in the overpressure enhancement—more enhancement than may be ascertained from the AlO emission measurement—and therefore the AlO emission time does not correlate to the explosive enhancement of certain conditions. The air-gap experiments showed that hot (but not activated) aluminum particles burn, and can still produce measureable AlO emission.

When comparing the particle size—40 μm vs. 10 μm vs. 3 μm—it is expected that the larger particles will burn longer, because the reported burn times are a function of the particle diameter[13, 19]. The 40 μm particles should have a longer burn time than the 3 μm, which is suggested by the longer AlO emission measurements in air. However, the 10 μm particles had the same amount of AlO emission as the 3 μm, but should burn longer and thus have longer AlO emission, if the AlO emission measurement could be correlated to burn time. It was also shown that the initial blast wave impulse depends weakly on the aluminum particle size, but the late-time enhancement was dependent on the particle size. Therefore, there may be a burn time relationship dependence on the particle size, but it is not correlated by the AlO emission.

Therefore, it is the hypothesis of this work that AlO emission measurement cannot be used as a quantitative burn time measurement in the traditional sense that it is used in the shock tube—such that the time of the optical event does not correlate to the enhancement from aluminum, and cannot entirely predict whether the aluminum is burning to enhance the explosive energy or is oxidizing without any net energy release. The AlO emission measurement cannot always be used as a burn time measurement because of the effects of a combination of the following:

1. High transient temperatures at breakout producing AlO emission from alumina dissociation.
2. The optical collection and collection volume influencing the fraction of the fireball volume that is viewed as a function of time.
3. The fireball optical depth reducing the fireball volume viewed because the AlO emission

measured is only from the fireball outer surface.

4. The confinement of the fireball changing how the fireball expands and develops, thus influencing the optical collection volume.
5. The varying efficiency of the collection of light emitted from different particle locations.
6. A grease layer or material in front of the charge altering the detonation wave progression and reflection through the detonation products and the AlO production.
7. The amount of aluminum powder available for combustion in the fireball and AlO production.
8. A mixing, expanding, and cooling fireball that decreases the temperatures within the fireball, influencing emitted AlO.
9. The quickly changing pressure in the fireball affecting the aluminum particle burn time.

Unfortunately, many of the listed effects are difficult to isolate and can interact with each other to some extent—for example, the confinement of the fireball can influence the optical collection volume, making it difficult to compare data from different experiements; or the fireball optical depth decreasing the optical volume because the AlO emission measured is from the outer surface. In addition, many effects have transient behaviors, therefore, trying to relate an AlO burn time or optical event to an inherently transient event is even more so difficult. The next nine sections identify the key features of each effect, and attempt to describe how the AlO emission event is influenced.

6.2.1 High Transient Temperatures at Breakout

It is known that AlO emission is exponentially dependent on temperature ($\sim e^{-C/T}$) and the higher temperatures—as measured at the initial breakout—will significantly influence the AlO emission measured. As discussed in Section 5.3.1 and shown in Figure 5.19, the AlO emission signal peaks measured were during the time of the highest temperatures, and during periods when the temperature decreases most rapidly. In addition, the AlO emission

is spatially averaged and is disproportionally weighed to higher temperatures in the optical collection volume. Finally, the decrease in AlO emission with respect to time could be from both an actual reduction in AlO production or from the decreasing temperature—the difference in AlO population in the B state is an order of magnitude for a temperature change from 4000 K to 3000 K. The effects cannot be quantitatively separated at this point.

A secondary effect of the high temperatures is the hot Al_2O_3 product, which does not contribute to a net oxidation. Part of the AlO emission measured will come from the dissociated oxide layer on the aluminum particles at the high temperatures[68, 78]. AlO emission was measured in the Al_2O_3-loaded tests during the bright breakout (Figure 5.58). The combustion temperatures in the fireball and, thus, the temperature of the heated aluminum oxide influence how much AlO will be produced as a result of the dissociation of the aluminum oxide. The condensed phase temperatures measured during and just after breakout are well above the volatilization temperature of aluminum oxide—3360±218 K at 10 atm and 4360±214 K at 3 atm[91]. Therefore, AlO emission from the Al_2O_3 influences AlO emission measurements at the breakout.

After the breakout, the fireball ambient temperature will decrease as the combustion begins to complete and fewer reactions are occurring, and therefore the lower temperature will not sustain AlO production from the dissociation of the oxide layer. The local combustion temperature of the aluminum particles could remain higher than the ambient fireball temperature, and therefore it is possible to have AlO emission from the newly formed Al_2O_3. The aluminum particle combustion temperatures—adiabatic flame temperatures on the order of 3200–3800 K depending on the pressure for reactions with oxygen—are below the volatilization temperature, but for liquid alumina, there will be a liquid-vapor equalization which could contribute to AlO production and emission. The AlO emission from Al_2O_3 at the lower aluminum combustion temperatures will be less than at the higher temperatures because of the exponential dependence of AlO emission on temperature. Therefore, AlO emission from Al_2O_3 will likely be less significant after breakout

6.2.2 Optical Collection and Collection Volume

As the fireball expands, the fraction of the fireball volume that the optical collection measures can change—depending on the set-up, which allows the fireball to expand—and therefore the fireball volume that is actually being measured can vary with time. For example, in the blast chamber, the fireball is weakly confined and allowed to expand to a size much larger than the optical collection. In this case, the fraction of the fireball volume that the optical collection measures decreases, and thus the amount of the fireball volume that is actually being measured also decreases. Figure 6.6 shows how the fireball size progresses with respect to time and is compared to the collection volume in the blast chamber. The fireball size and shape were estimated at each time using the high speed camera images from an 20%-3-μm-Al charge test. The collection volume in the figure is approximated as a cylinder having a diameter of 1.27 cm (1/2 inch), which is based on the collection volume of the experiments conducted in the blast chamber. Certainly, different sized optics and configurations of an optical collection are likely, and while the exact dimension would vary, the effects will be similar. As the fireball schematic, Figure 6.6, demonstrates, the optical collection volume is a small proportion of the total fireball volume, even at the early times. Figure 6.7 compares the collection volume to the total fireball volume, assuming no optical depth effects. The typical time that the AlO emission was measured is also shown for comparison.

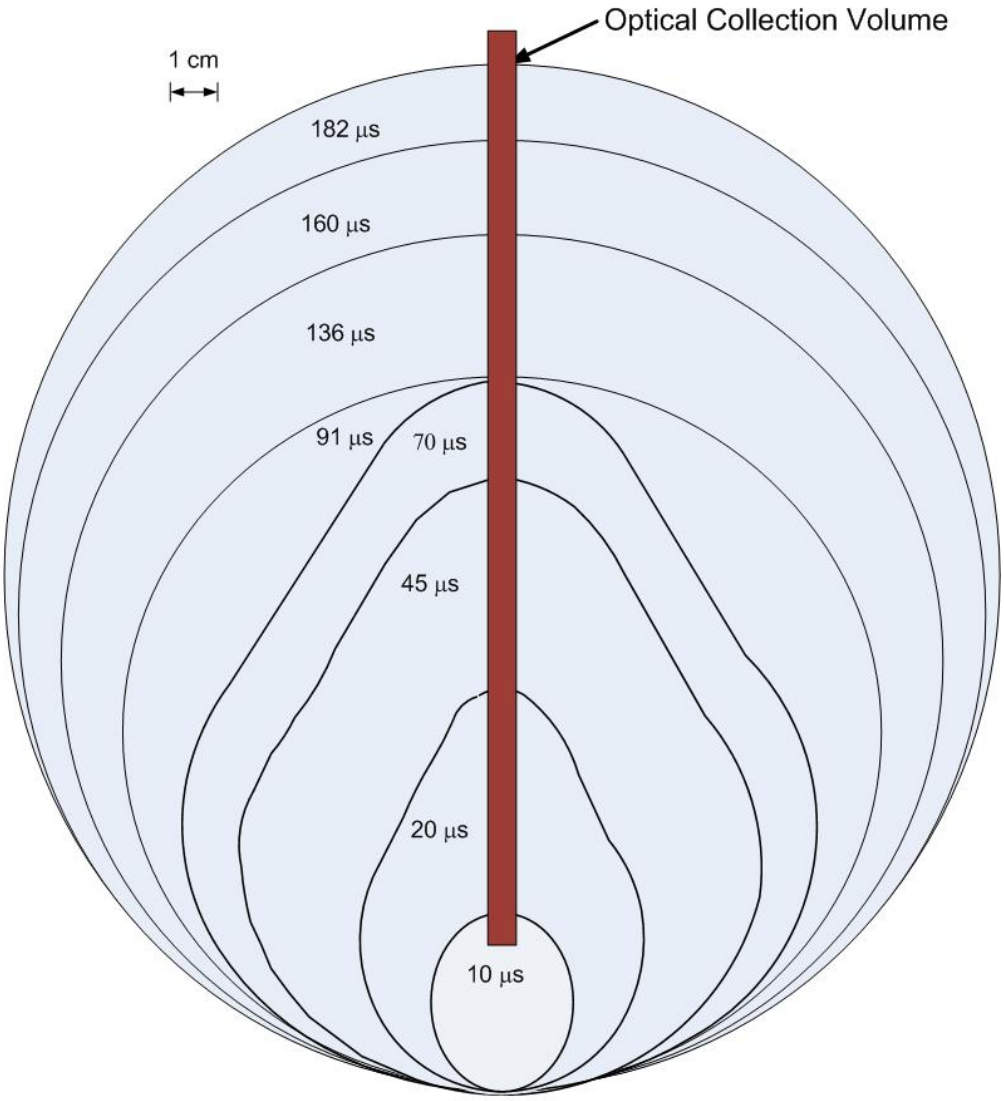

Figure 6.6: Progression of fireball size with respect to time and compared to relative size of optical collection volume.

The peak AlO emission measured occurs at the time of smallest fireball size and when the fractional volume of optical collection is highest. Some late-time AlO emission measurements—e.g., the gap tests, the end-loaded charges, and 20%-40-μm-Al charge in air—occurred until 100 μs, at which point the fraction drops to less than 1 percent.

Depending on how the optical collection is set up, the fireball volume captured will most likely change with respect to time as the fireball expands. Unless the collection optics can capture the entire fireball volume—e.g., by increasing the size of the widow of observa-

tion (optical collection) or by confining the fireball development to the size of the optical collection—as the fireball expands, the fraction of the total fireball captured by the optical collection will decrease for optics focused on the fireball axis. For optics focused off-axis, the fireball fraction collected could increase—at $t = 0$ s, the fraction collected would be zero, then it would increase as the fireball enters the collection volume. The point is that the changing fireball fraction collected will affect the amount of AlO emission measured because the number of burning aluminum particles and amount of the fireball viewed will not remain constant.

The effect of a decreasing fireball fraction collected will, in turn, decrease the amount of AlO emission measured as a function of time. Therefore, it is important to understand how the collection volume size affects the AlO emission measured, especially for any late AlO emission measured. While early in the fireball development, the fireball fraction collected is greater, the fireball is also expanding during this time. The rapidly changing fraction of the fireball collected will influence the AlO emission measured more at the early times than at later times. At the later times, the fireball fraction collected could decrease to less than 1 percent of the total fireball volume—as in the current study—but the fraction collected does not change as drastically as in the beginning fireball development. Therefore, the later AlO emission will not be as influenced by the decreasing fraction of the fireball collected as the early AlO emission.

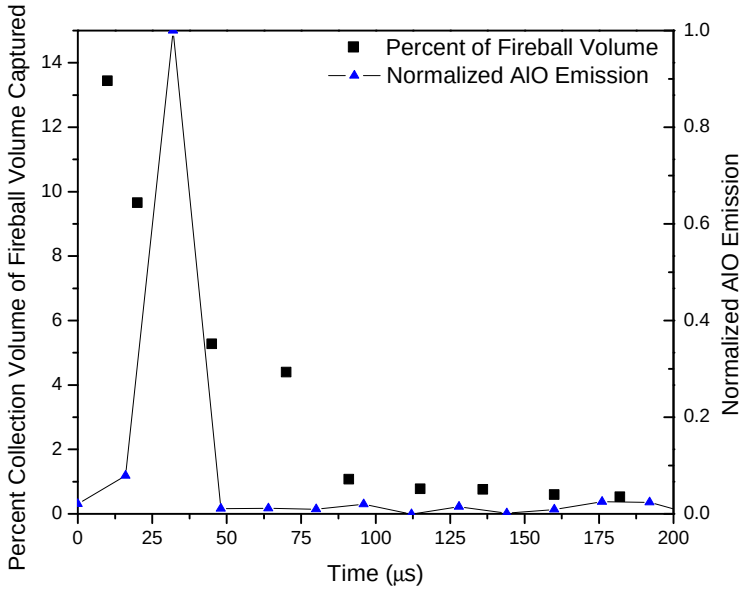

Figure 6.7: Percent collection volume of total fireball volume captured, assuming no optical depth effects, and compared to typical time of AlO emission measurements from the charges in the blast chamber, except the 50%-3-μm-Al and 20%-40-μm-Al charges in air.

One effect of the expanding fireball is the decreasing aluminum particle density in the fireball. Because the fraction of the fireball the optical collection measures decreases, the decreasing aluminum particle density affects the amount of AlO emission measured. The aluminum particle density—the number of particles in themass of the aluminum additive divided by the fireball volume—as a function of time is shown in Figure 6.8 for each of the aluminized charges. The aluminum particle density assumes uniform distribution of the aluminum particles in the fireball volume. There are approximately 40 percent fewer particles for the 20 percent aluminum charge than the 50 percent loaded (same particle size). The difference between particle diameter is more significant—by two orders of magnitude for the 10-μm, and 4 orders of magnitude for the 40-μm compared to the 3-μm particles. Late-time AlO emission was measured for the 50 percent Al charge, which could be partially attributed to the higher particle density.

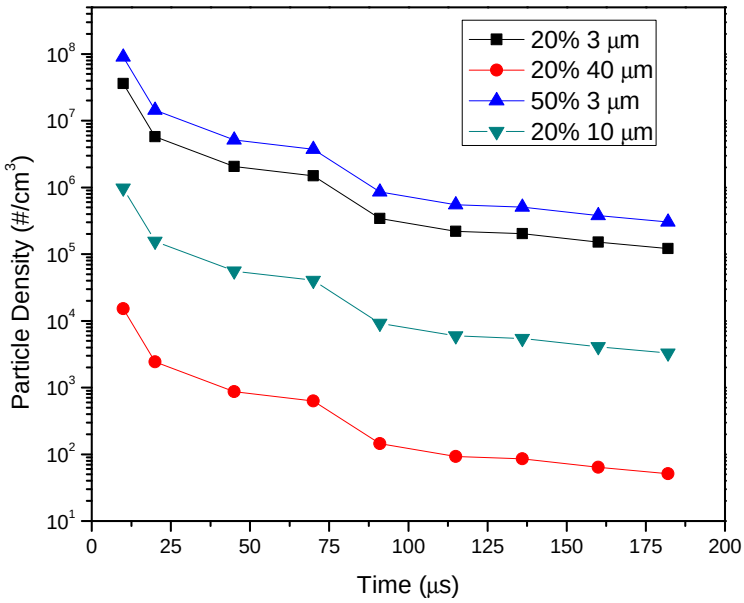

Figure 6.8: Particle density in fireball of each aluminized charge, assuming uniform distribution of Al particles.

A comparison of the calculated aluminum particle density in the fireball (number of Al particles/fireball volume) of the preloaded and end-loaded charges using 3-μm aluminum is shown in Figure 6.9. The 20 percent and 50 percent aluminized charges assume uniform distribution in the full fireball volume.

The aluminum particles in the fireball from the end-loaded charges are on the top surface of the fireball. A first order approximation of the volume the aluminum particles occupy, puts the particles in a thin dome shaped layer on the fireball surface having an approximate height of 2 cm at 10 μs, and the dome expands at an approximately 40 degree angle. The resulting volume the aluminum particles occupy is approximately 10 percent of the total fireball volume up to 70 μs and approximately 2 percent at the later times. The higher density of particles can help explain the longer AlO emission measured for the 50 percent loaded charge, and the end-loaded tests. The aluminum particles on the fireball surface increases the aluminum particle density in the fireball—especially after 70 μs, compared to the pre-loaded charges—increasing the possiblity that any AlO emission could be measured.

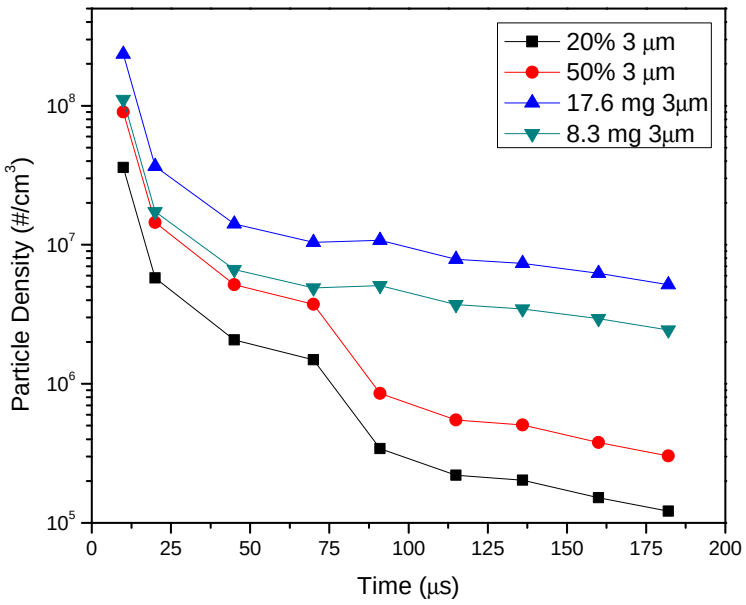

Figure 6.9: Particle density in fireball of 3 μm aluminized charges, assuming uniform distribution of Al particles, and end-loaded charges, assuming particles on leading surface of fireball.

6.2.3 Fireball Optical Depth

From the optical depth study, it was concluded that optical thickness is significant, and that measured AlO emission can be attributed from particles/reactions on the fireball surface or near the fireball surface. Using the attenuation lengths found from the optical depth study and summarized in Table 3.2, the optically thick portion of the fireball was estimated at seven fireball sizes, shown in Figure 6.10. At most time events—up to 160 μs—a significant portion of the fireball is optically thick, reducing the amount of the fireball from which the AlO emission can be measured. Recall that the peak AlO emission for most experiments occurred between 10 μs and 45 μs.

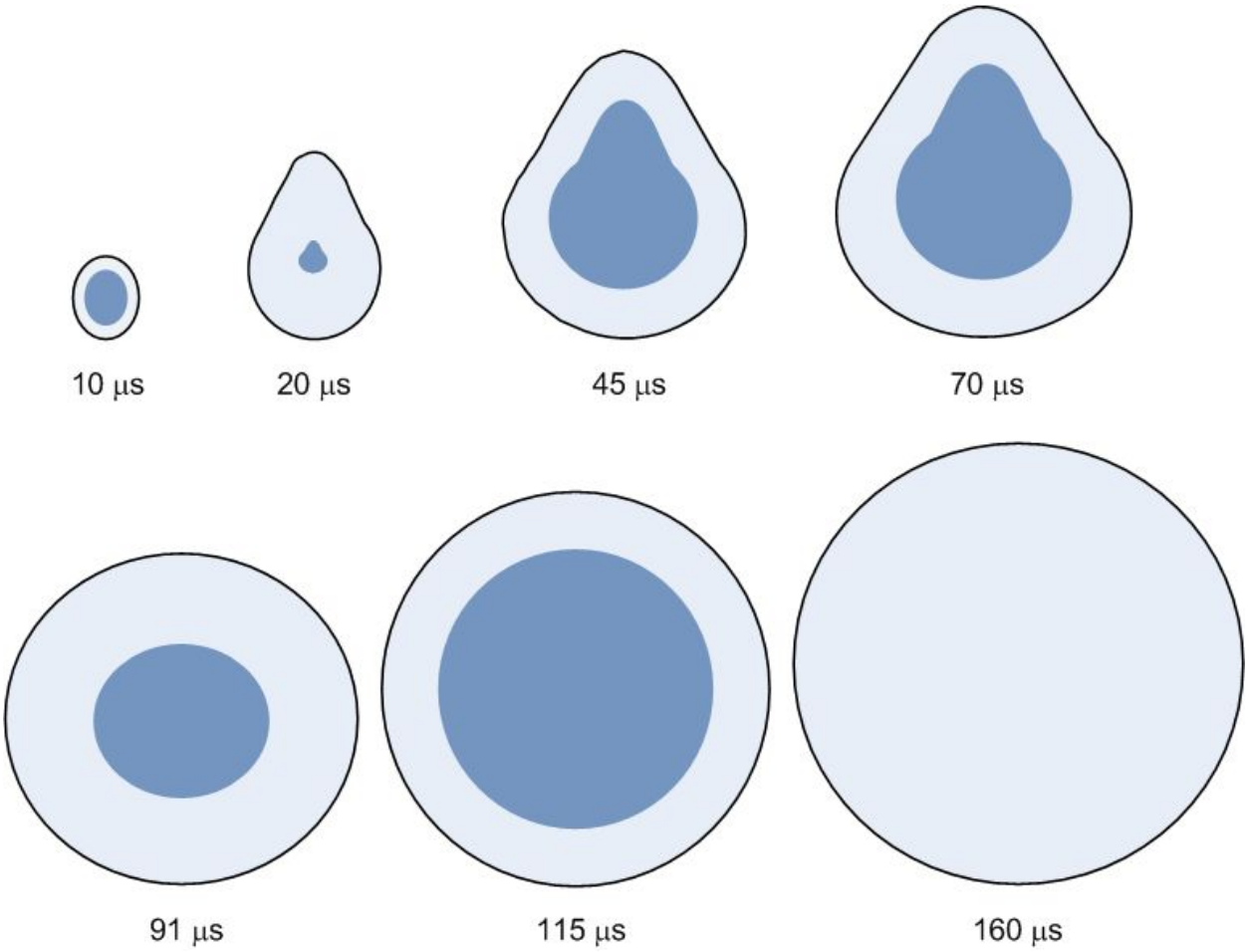

Figure 6.10: Based on measured attenuation length from the optical depth study, the shaded portion of the fireball shown is the approximate portion of the fireball that is less than one attenuation length from the fireball edge. The peak AlO emission for most tests occurred between 10 μs and 45 μs.

From Figure 6.10, it appears that at 20 μs the fireball temporarily clears during the time of peak AlO emission measurements. Figure 6.11 shows the dimensions of the fireball and attenuation length at 10 μs, 20 μs and 45 μs. Usually the attenuation length is much smaller than the fireball vertical length, and therefore only a small portion of the fireball contributes to the optical measurement. But around 20 μs the size of the fireball is nearer the length scale of the attenuation length, and much more of the fireball is viewed by the optical measurements, giving way to a temporary partial clearing at the time of peak AlO emission measurements. The percent of the collection volume in the blast chamber that is

not within one attenuation length of the leading (top) fireball edge is shown in Figure 6.12. The drop in optically thickness is only 10 percent, but could be sufficient to allow more AlO emission to be measured from the front edge of the fireball.

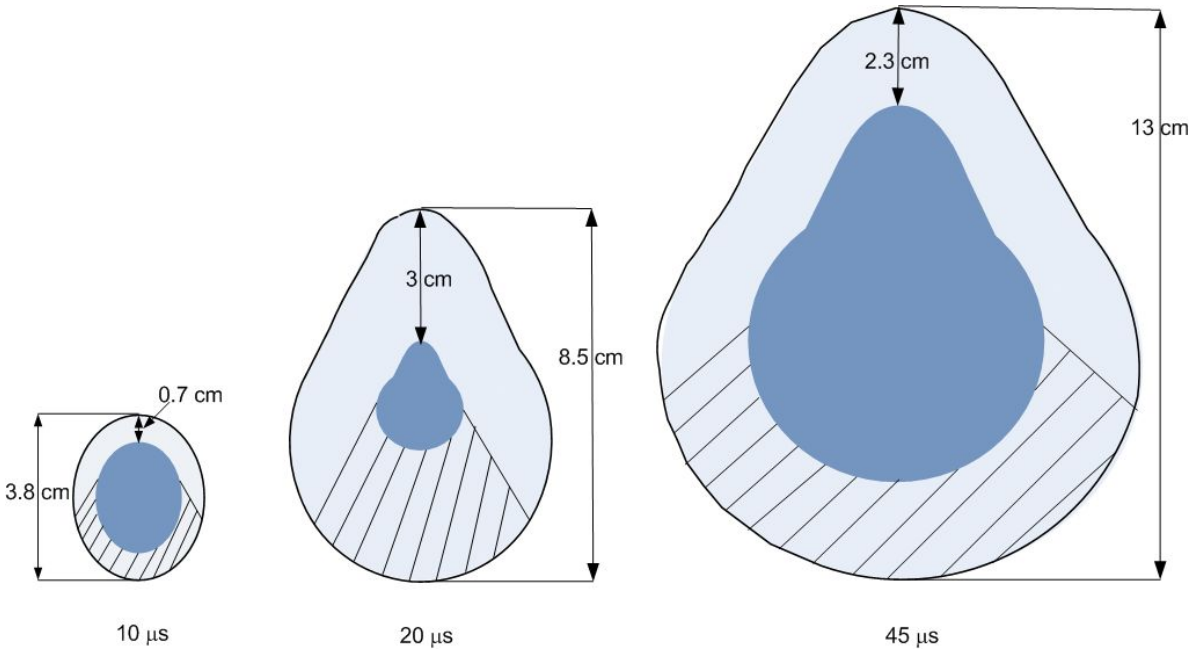

Figure 6.11: Fireball dimensions and attenuation lengths at 10 μs, 20 μs and 45 μs. The shaded area was not considered to be seen by the detector.

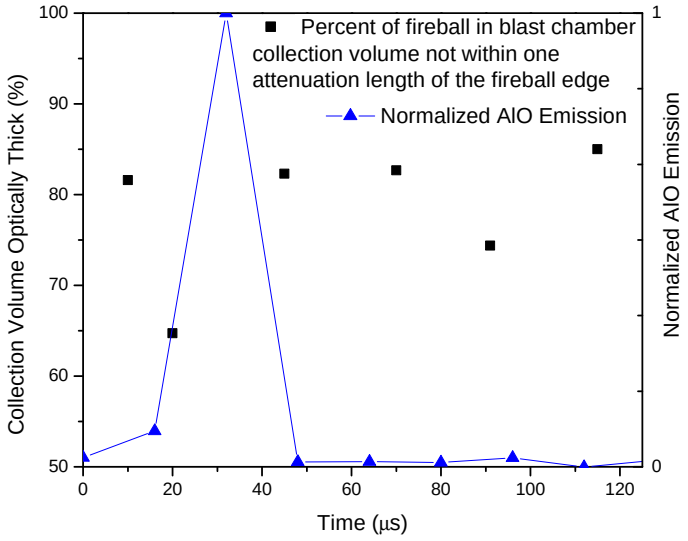

Figure 6.12: Fraction of the fireball captured by the collection volume for blast chamber and not within one attenuation length of the leading (top) fireball edge, and compared to typical peak AlO time. The peak AlO emission occurs at time of temporary 'clearing' of the fireball.

A set of experiments completed by Lynch[91] measured the AlO emission inside the fireball from three of the charges used in the current study—20%-3-μm-Al loaded, 20%-40-μm-Al loaded, and 20%-Al_2O_3 loaded. The experiments used seven fiber optic probes at different distances from the charge, and one external probe to measure the AlO emission at eight time frames, ranging from 6 to 81 μs. The results of the two aluminized charges is summarized in Tables 6.4 and 6.5. A comparison of the fiber probe AlO emission measurement and the current work's AlO emission measurements is provided in Table 6.6.

Table 6.4: Fiber probe AlO measurements for the 20%-3-μm-Al charge. An 'X' denotes AlO was measured. Modified from [91].

Probe distance (cm)/Time (μs)	7–10	10–12	12–15	15–18	36–39	39–49	49–51	51–81
1.3		X	Peak					
3.8			X					
5.1								
6.4								
8.9								
11.4								
14								

Table 6.5: Fiber probe AlO measurements for the 20%-40-μm-Al charge. An 'X' denotes AlO was measured. Modified from [91].

Probe distance (cm)/Time (μs)	6–9	9–12	12–15	15–18	36–39	39–49	49–51	51–81
1.3	Peak	X	X	X	X	X		
3.8			X	X	X	X	X	X
5.1				X	X	X	X	X
6.4					X	X	X	X
8.9				X		X	X	X
11.4				X		X	X	X
14				X				

The peak AlO intensities for both charges and all of the AlO emission measured for the 3-μm-Al charge occured during the bright breakout. The AlO emission time scale for both charges is similar for both the internal probes and the external measurements, which is the time of the highest temperatures and steepest temperature decline. Therefore, more

Table 6.6: Comparison of external AlO emission measurements to inside fireball measurements.

Study	Lynch[91]		Current Work	
Al loading & size	20% 3 μm	20% 40 μm	20% 3 μm	20% 40 μm
Time AlO is measured	10-15 μs	6-81 μs	up to 30-40 μs	up to 100 μs
Relative Intensity of Peak	3 μm is 3 orders of magnitude brighter than 40 μm		about the same peak intensity	
External Probe AlO	None	1 frame at 15-18 μs	one 16 μs frame	Six 16-μs frames
Peak AlO Time	12-15 μs, at closest probe	6-9 μs at closest probe	16 μs	16 μs

AlO emission is expected to be measured during this time, regardless of the measurement technique, as a result of the high temperatures. The external probe measurements differ compared to external only measurements, which is possibly caused by collection volume differences between the two methods. After the initial breakout—for the 40-μm case—the AlO emission measured from the internal probes is diminishing in intensity[91], which is similar to the external only measurements.

It is difficult to assign a burn time to the fiber probe measurements, but similar to the external measurements, the 40-μm aluminum has a longer AlO emission signal than the 3-μm aluminum, and indicates that the aluminum is burning longer. Both measurement techniques—Lynch[91] and the current study—show similar AlO emission times for the two charges, and do not contradict each other. While the optical thickness of the fireball affects the external AlO emission measurements as discussed, the AlO emission that is measured externally appears to be qualitatively representative of the aluminum burning in the fireball in this case. Since the external measurements are representative of the aluminum burning inside the fireball, the effect of the fireball optical depth is not as critical to the interpretation of AlO emission measurements as it would appear from the optical depth study.

6.2.4 Fireball Confinement

The results showed differences between the AlO emission measured from each chamber, as shown in Figure 5.11, and is partially the result of the different optical collection volumes, demonstrated in Figure 5.12. It can be summarized for the three aluminized charges tested

in both chambers—for the 20%-3-μm-Al charge: AlO emission is not measured longer than the first 30-40 μs, regardless of chamber or environment. For the 20%-40-μm-Al charge: AlO emission was measured for longer than 40 μs in air in both chambers—for 200 μs in the tube chamber and 100 μs in the blast chamber. For the 50%-3-μm-Al charge: AlO emission was also measured for longer than 40 μs in air in both chambers—for 200 μs in the tube chamber and for 400 μs in the blast chamber. Restricting the fireball development in the tube chamber introduced more shock wave reflections, whereas in the blast chamber the fireball is allowed to expand radially (rather than only axially as in the tube chamber), and has more surface area for mixing with the ambient than in the tube chamber.

As a result of the differences in how the fireball expands—axially in the tube chamber, and radially in the blast chamber—the particle density is different for each chamber. The aluminum particle density in the fireball in each chamber is compared in Figure 6.13. After the fireball expands radially to fill the tube chamber, it then only expands axially and the particle density decreases more slowly in the tube chamber than in the blast chamber. The relatively constant particle density in the tube chamber occurs after 50 μs, which is after the initial AlO emission peaks were measured.

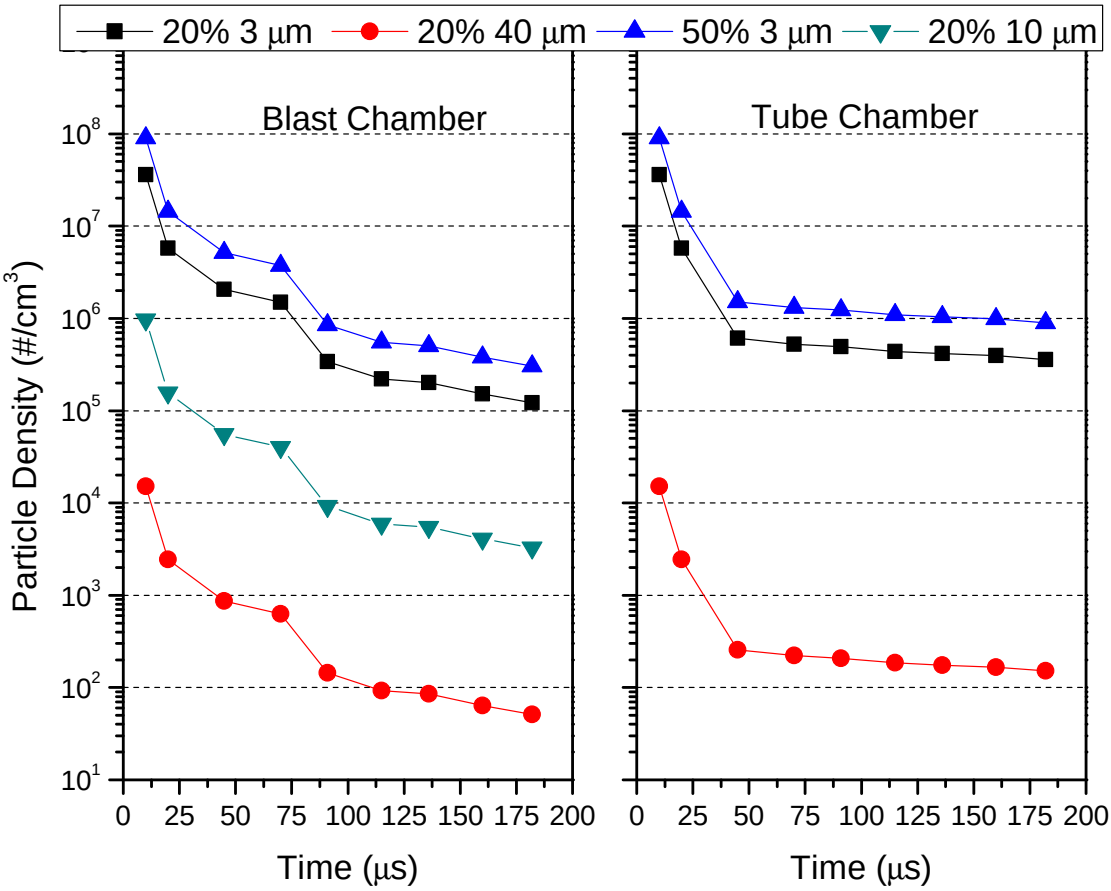

Figure 6.13: Particle density in each test chamber.

The optical collection volumes were also different for each chamber, and along with the different expansion volumes of the fireball, the result is that the optical measurements measure different fractions of the fireball volume. The fraction that the optical collection volume is of the total fireball volume as a function of time—ignoring optical depth effects—is shown in Figure 6.14. The biggest difference between the two chambers is that the tube chamber optics can capture 75 percent of the fireball volume after 40 μs and up to 100 percent of the fireball volume earlier. The blast chamber optics are never able to capture more than 15 percent of the fireball volume.

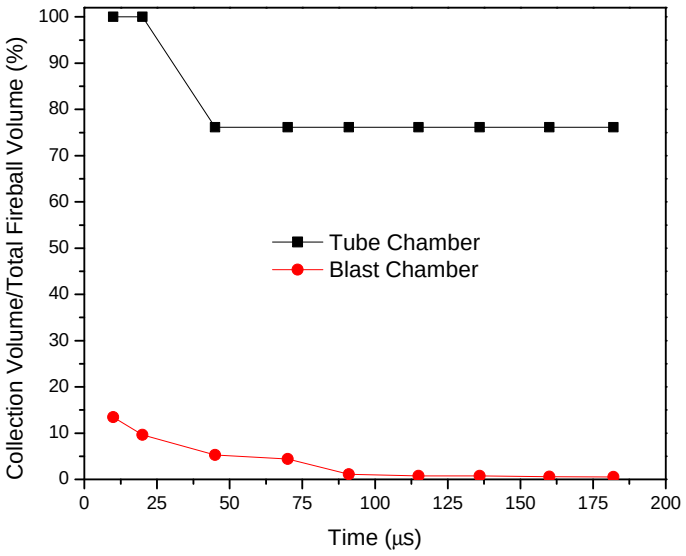

Figure 6.14: Comparision of optical collection volume fractions of the tube chamber and the blast chamber.

The degree to which the fireball development is restricted and the size of the optical collection volume impact the fraction of the fireball that is collected by optics, and can affect the duration that AlO emission is measured. For the 20%-40-μm-Al charge, the AlO emission in the tube chamber was measured until 200 μs, while only until 100 μs in the blast chamber. For the 50 percent aluminum case, after the initial peak, the AlO emission increased in the tube chamber, but decreased in the blast chamber. For the 20%-3-μm-Al charge, AlO emission was measured during the first 30 μs for both chambers. Therefore, the effects of particle density and collection volume ratio have a larger influence on the duration and the time evolution of the later AlO emission than on the early peak.

When the fireball size is restricted, the surface area available for mixing changes, and can subsequently change the amount of AlO produced and thus the AlO emission measurement. A comparison between two tube-style chambers could isolate the effect of the detonation products and air mixing from the fireball confinement effect has on the AlO emission measurement because in each tube the fireball development would be similar. If one tube had an inner diameter of 10.2 cm (4 inch) and another had an inner diameter of 7.3 cm (2.87 inch), the front surface area would be reduced by 51 percent. If mixing were the only effect

to be considered, then approximately 50 percent less AlO emission would be expected to be measured for the smaller tube.

Experiments were conducted using the 10.2 cm diameter tube chamber and a 7.3 cm diameter tube, which was slid into and centered in the tube chamber to measure AlO emission from 20%-40-μm-Al charges. These charges were used, because in air they exhibited AlO emission signals longer than the first 30 μs. In air, one test was completed in each of the two tubes. One test was completed in the 7.3 cm diameter tube in N_2 to test whether in a confinement a longer AlO emission signal from only detonation product reactions can occur. A 2 μs time resolution was used and the same optics set up was used for each test. The optics set up used 25.4 mm (1 inch) lenses, having 60 mm focal lengths, that were focused slightly off the tube central axis.

The results from the AlO emission measurements from the three tests are presented in Figure 6.15. The optics alignment was not changed for the smaller tube setup, resulting in a slight misalignment for the 7.3 cm confinement, and thus the results are inconclusive because the effect of the misalignment is unknown. However, the tests in the 7.3 cm confinement in air and in N_2 show that only in air a longer AlO emission signal measured. Therefore, mixing with ambient O_2 is critical in the production and measurement of late-time AlO emission.

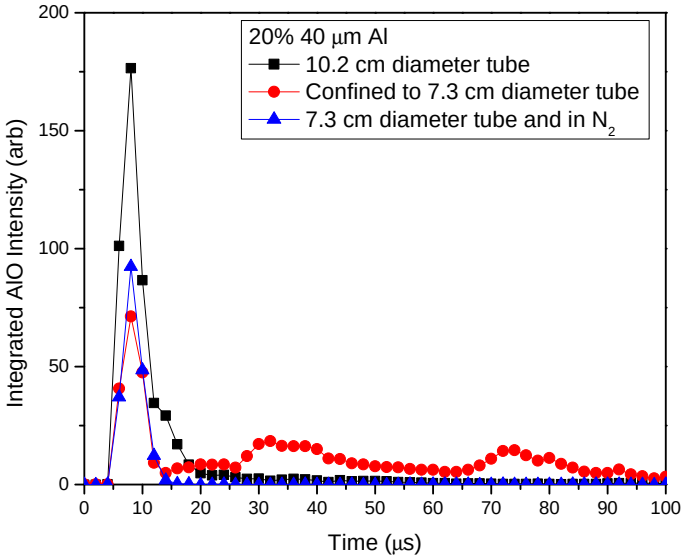

Figure 6.15: AlO emission measurements from tube confinement experiments in air and N_2.

Based on the results and analysis of the AlO emission from the two chambers, differences in the optical collection volume and the restriction of the fireball development can affect the duration and time-evolution of the AlO emission measured. It is important to note that in both chambers the later AlO emission was measured for the 40-μm-Al and the 50 percent loading. Therefore, regardless of the optical collection or the fireball expansion, the AlO emission measurements are representative of when the aluminum is burning inside the fireball. However, if a burn time were determined from each chamber's measurements, the results would be different because the time durations and time evolutions of the AlO emission measurements were different. In addition, detonation products mixing with ambient oxygen is necessary in order to measure late-time AlO emission. The effect of the mixing surface area on the AlO emission has not been isolated from the effect of restricting the fireball expansion and is not fully understood.

6.2.5 Particle Location

Since the optical depth of the fireball affects the optical measurements, the location of the particles is also important. Evidence about the effects of the particle location are found from the results of the grease layered charge tests, the end-loaded charge tests and the air-gap tests. Particle location has a strong influence on the amount of AlO emission measured; however, the edge particles add less to the initial impulse, and the late impulse overpressure than the pre-loaded charges. Therefore, an 'optical burn time' cannot be necessarily correlated to enhancement by the aluminum additive.

As shown in the results chapter, the end-loaded charges had fewer aluminum particles and a lower initial blast wave impulse, but longer AlO emission than the preloaded 20%-3-μm charges. In addition, the end-loaded charge having more aluminum powder, had more AlO emission measured than when less aluminum powder was used. Only two tests were completed using the end-loaded charges tested in air, and therefore absolute trends are difficult to make; however, the end-loaded charge enhancement was less than the pre-loaded charge in the initial blast wave. The late-time impulse comparison between the pre-loaded and the end-loaded is shown in Figure 6.16. The energy release of the end-loaded having 17.6 mg Al is approximately the same as the pre-loaded charge, and the long-term impulse was higher for the end-loaded charge having more aluminum. Therefore, the longer AlO emission time does not necessarily guarantee a significant late time enhancement.

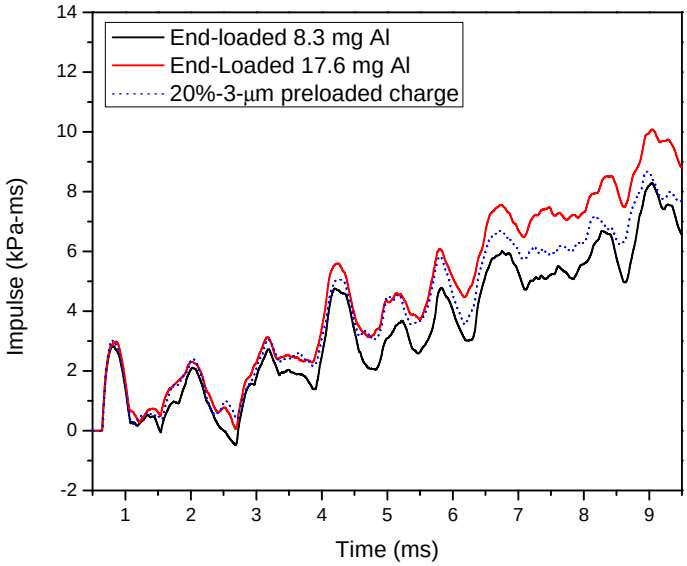

Figure 6.16: Comparison of the late-time impulse for the end-loaded and 20 percent pre-loaded charges.

For the gap experiments, there was no initial blast wave impulse enhancement from largest gap (0.562 inch) and aluminum pellet in air; however, there is a long term overpressure enhancement compared to SiO_2 pellets, as shown in Figure 6.17. The enhancement is not much above the inert SiO_2, but it indicates that some of the aluminum did burn and released energy. AlO emission was measured at the largest gap distance, indicating that part of the AlO emission may have been from aluminum reaction—as opposed to the oxide layer dissociation. Particles on the fireball edges that are not activated in the blast wave—because of distance from the charge—but are exposed to high temperatures and pressures via mixing with detonation products do not contribute to the initial blast enhancement, but do react, add to overpressure, and will have some AlO emission. However, the AlO emission is on a much shorter time scale—within the first 90 μs—than the overpressure enhancement—which occurs on the millisecond time scale, and is most pronouced between 5 and 9 ms after detonation.

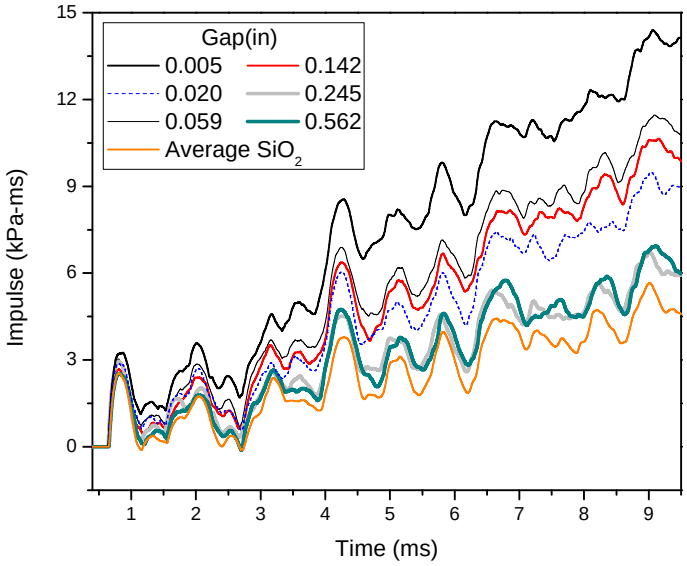

Figure 6.17: Long term impulse from the Al pellets in air compared to the average impluse of the SiO_2 pellets.

For the gap experiments in N_2 no initial and no overpressure enhancement was measured compared to the SiO_2 pellets, shown in Figure 6.18. Therefore, the enhancement of aluminum powder located further from the charge must be caused by aerobic reactions resulting from the mixing of detonation products and air.

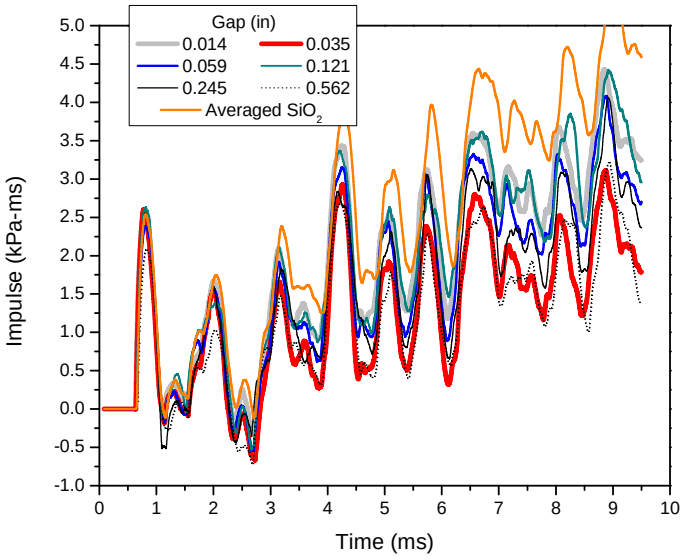

Figure 6.18: Long term inpulse from the Al pellets in N_2, and the average impluse of the SiO_2 pellets in air.

6.2.6 Grease Layer Effect

The effect of the grease layer on the charge tip has multiple aspects. It was shown that placing a thin layer of grease on the tip of a small charge has a large effect on the amount of AlO emission measured. It is possible that the grease layer creates an opaque layer which blocks the AlO emission from reaching the detector, or that the grease layer changes the breakout mechanism such that AlO emission is not produced or measurable in the same manner as without a grease layer. The effect of the grease layer is most likely not an isolated case[45], but rather other substances—such as an epoxy layer, or a cap on the charge—can increase the optical depth, change what is happening with respect to oxidizers, or change the initial detonation breakout.

The 20%-3-μm-Al charge having a grease layer had an initial blast wave impulse higher by 2 percent than the an ungreased 20%-3-μm-Al charge, though the millisecond overpressure enhancements are unknown. The initial blast wave impulse was also higher by 4 percent than an ungreased charge in N_2. Even though the measured initial blast wave impulses are within the measurement uncertainty, the initial blast wave impulse most likely still includes both aerobic and anaerobic effects, and therefore, there is still some mixing with the ambient environment. Since the initial blast wave impulse did not decrease, the aluminum must burn even when a layer of grease is present on the charge tip. The results also showed that AlO emission was measured in air and N_2, but very little AlO emission was measured from the grease-layered test during the same time frame, even though the aluminum was burning in both cases.

The same grease was used to attach the aluminum powder to the bare charge for the end-loaded experiments, and in this case the grease did not impede the AlO emission measurement, or at least more AlO emission was measured than in the grease-layed case compared to the ungreased aluminized charge. Therefore, the location of the grease layer with respect to the aluminum location does affect the amount of AlO emission measured.

One possible reason is that the grease creates an opaque buffer layer blocking the AlO emission measurement. While the grease used in the experiment is labeled as heat stable and inert, the MSDS of the silicone grease indicates that thermal breakdown during a fire or with very high heat can occur and may include carbon oxides, incomplete burned carbon compounds, silicone dioxide, and formaldehyde[92]. These substances could create a buffer layer which will prevent the AlO emission from being observed because the unburned carbon will act as soot, and may be a source of the light emission visible from the grease test seen in Figure 5.71.

Another reason that less AlO emission is measured is that the grease layer—or another layer on the charge tip—changes the breakout such that AlO emission is not produced or able to be observed. At breakout, a shock wave travels through the explosive material, initiating it, and creating a high pressure, high temperature area of detonation products behind the shock wave. At the contact surface between the high explosive and the ambient environment the shock or expansion wave is reflected back through the detonation products, as well as transmitted through the ambient environment. Across the contact surface the pressure and flow velocity are continuous, and thus the initial temperature jump across the shock will be large to maintain the continuity[80]. The effect of the breakout conditions on non-ideal explosives and additives—such as the charges in the current study—has not been studied. The results from the grease layer experiments indicate that if there is a change to the breakout, it can have significant consequences in the light output and the AlO emission measurement.

To test whether the effect of the grease layer is an opaque barrier or whether the grease affects the breakout, a series of experiments were completed using 20%-3-μm-Al and 20%-10-μm-Al charges in the tube chamber. Instead of a grease layer, Mylar strips—which also produce vapors at high temperatures —were used. The strips were the width of the charge diameter, and of similar thickness, approximately 50 μm, to the grease layer. In addition, a strip of glass—130 μm thick, and slightly wider than the charge diameter—was used in one

test. The glass will not produce a vapor in the same manner as the Mylar or grease, and will most likely break when the blast wave goes through it. The Mylar strip was tested in two ways—touching the charge tip and at a 2 mm—or a quarter charge diameter—offset from the charge tip. The tests are summarized in Table 6.7, and a schematic of the setup for the Mylar and glass strips is shown in Figure 6.19. The holders—used in each test, even those not using a Mylar or glass strip—were PVC tubes that had an inner diameter of 26 mm (1.02 inch) or was 3.5 times larger than the charge diameter. The Mylar and glass strips were held in place on the PVC holder by a piece of tape at the rim. All the tests were completed in air, and only AlO emission was measured using a time resolution of 1 μs in order to focus on the first 20 to 30 μs after the detonation.

Table 6.7: List of tests completed to investigate the effect of the grease layer.

Charge	Charge Tip	Notes
20%-3-μm-Al	-	baseline
20%-3-μm-Al	Mylar touching	
20%-3-μm-Al	Mylar offset 2 mm	
20%-10-μm-Al	-	baseline
20%-10-μm-Al	Mylar touching	
20%-10-μm-Al	Glass touching	

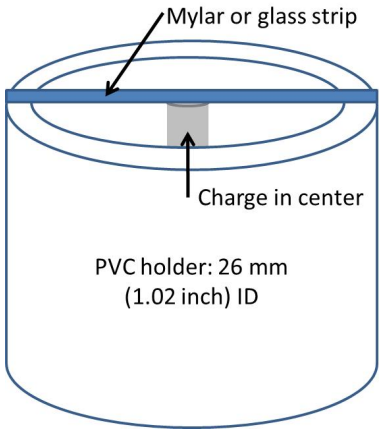

Figure 6.19: Schematic of holder for the Mylar and glass strips used to test the effect of a grease layer on the charge tip. (Sketch not to scale.)

The results of the AlO emission measurements from the tests using the 20%-3-μm-Al

and 20%-10-μm-Al charges are in Figures 6.20 and 6.21, respectively. For both the 3-μm and 10-μm aluminum charges, the total integrated AlO emission from 0 to 17 μs and the peak intensities were about half the baseline values for the tests using a Mylar layer. The test having the 2 mm offset of the Mylar sheet had the same total AlO emission, within measurement uncertainty, as the Mylar touching the charge. The glass layer test showed a reduction of the total AlO emission measured by 90 percent from the baseline charge, and the AlO emission from the glass layered charge was delayed by 5 μs.

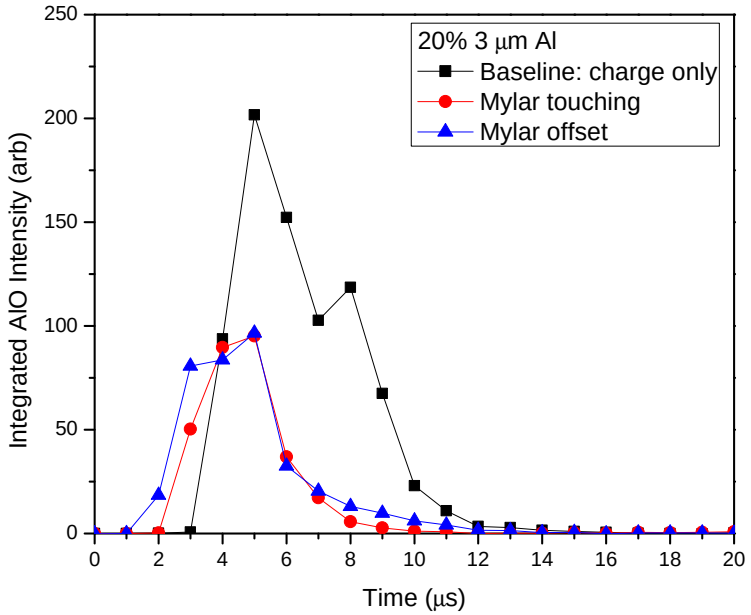

Figure 6.20: AlO emission from 20%-3-μm-Al charges—charge only, Mylar layer touching the charge tip, and Mylar layer offset 2 mm from the charge tip.

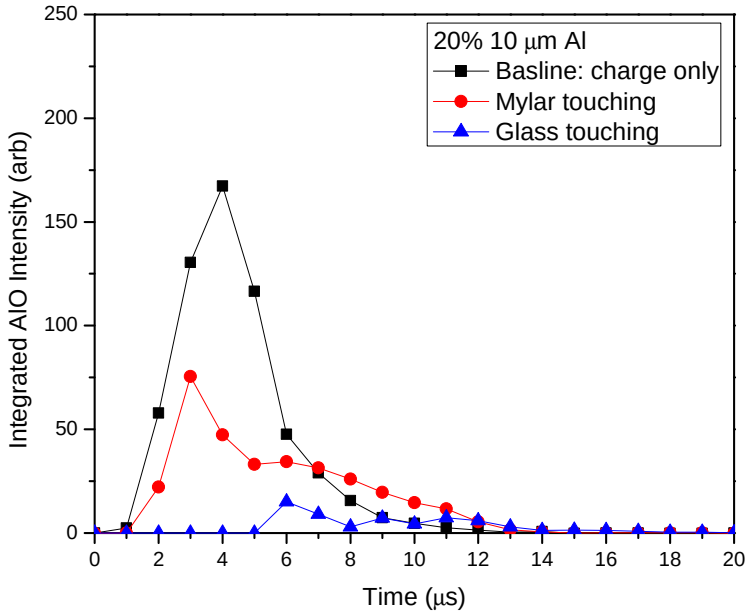

Figure 6.21: AlO emission from 20%-10-μm-Al charges—charge only, Mylar layer touching the charge, and a glass layer touching the charge tip.

The significant decrease in AlO emission measured for the glass layer—which does not create a gas environment in the same way as the Mylar—indicates that the grease layer or substance in front of the charge does alter the breakout, which explains why AlO emission was not observed. At detonation, the detonation wave travels through the solid explosive, then transitions to the ambient environment. At the interface between the solid explosive and the ambient environment, the wave is both transmitted and reflected through the detonation products/fireball. The reflected wave is most likely weaker than the stronger transmitted blast wave. AlO emission was still measured for the Mylar layers—the Mylar also affected the breakout—but the Mylar sheets had less mass than the glass layer, or grease layer, therefore the conditions—including the mass, density, and attenuating properties of the substances—at the explosive/environment interface govern the strength of the transmitted wave, and influences the degree to which the breakout is affected. In the case of the additional substance—glass, Mylar or grease—at the tip of the charge, the reflected wave may have been stronger and the transmitted wave weaker than for the charge alone. The mixing layer size and/or content may also change, changing the oxidizers available or quenching

that occurs. Mixing of the detonation products with the air behind the shock could also be affected. If the temperature of the mixing layer and detonation products is changed, then the speed of the aluminum reactions could be changed such that less AlO is produced. These changes to the breakout affect the AlO emission production and its subsequent measurement; however, as shown from the grease layer experiments, the initial blast wave enhancement is not necessarily affected.

6.2.7 Amount of Aluminum Powder

As seen from the end-loaded charges, and comparing the 50 percent to the 20 percent loaded charges, the more aluminum powder available, the more AlO emission is measured. The question is whether having more aluminum powder should indicate a longer burn time. Trzcinski et al.[42] measured light output duration using photo diodes—no specified wavelength measured—and in general the light duration increased as the percent of added aluminum increased. However, the relationship between percent loading and light duration is not consistent with the increasing amounts of aluminum, i.e., 15 aluminum percent had the same light duration as the zero percent aluminum. From zero to 60 percent added aluminum the light duration increased about 66 percent, but the two photo diodes did not always measure the same duration time[42].

A second consideration is whether the longer optical event indicates further enhancement. For the 50 percent and 20 percent loaded charges, the initial impulses were the same within the measurement uncertainty, and therefore it does not appear that the additional aluminum added to the initial blast enhancement. However, these were only two cases studied, and more experiments are needed to determine a trend. The study by Trzcinski et al.[42] found that peak pressure, impulse, and quasi-static pressure (QSP) all had slight increases as the percent added aluminum increased to a peak at 30 percent then decreased for larger amounts of aluminum; however, the differences between the different amounts of aluminum were not

as significant as the difference to having zero aluminum. The QSPs also fall between the calculated values for inert aluminum and fully active aluminum, and the study found that while the aluminum is reacting after the detonation, the influence of heat released on blast performance is weak[42].

Therefore, while the light duration is longer for more loaded aluminum particles, the actual additional contribution to the enhancement is minimal, or is at least not on the same order as the additional light output. Besides the evidence of this lack of correlation by comparing the 50 and 20 percent aluminum loaded cases, this relationship between loading and AlO emission is also evident from the end-loaded charges, as discussed in Section 6.2.5.

6.2.8 Expanding, Mixing, and Cooling Fireball

The late time AlO emission measured indicates that reactions are occurring producing AlO emission and may be an indicator that the temperature/oxidizers are such that those reactions can occur. As the fireball expands, not only does the fraction of the fireball volume the optics capture decreases significantly and the particle density decreases as $\sim 1/t^2$, but also the fireball is cooling. As the fireball expands, the probability that the aluminum particles travel into a cooler spot and quench increases. Since AlO emission is linearly related to concentration, as the particle density decreases, so will the AlO emission.

Any decrease in the combustion temperature will have an impact on the amount of AlO emission measured because AlO emission is exponentially dependent on temperature,. The adiabatic flame temperature of the aluminum—the theoretical maximum combustion temperature—is a function of the initial temperatures of both the aluminum and the oxidizers. The temperature of the oxidizers for the aluminum combustion is influenced by the fireball ambient temperature behind the shock, and the RDX/PETN detonation products temperature.

Using the Taylor blast similarity solution equations[76] and assuming a normal shock for

the bare charge case, the temperature of the air behind the shock would follow the curve shown in Figure 6.22. Within the first 25 μs, the temperature drops below 2000 K, and below 500 K by 150 μs. The adiabatic flame temperature of a bare charge and a 20 percent aluminum charge is shown in Figure 6.23. The adiabatic flame temperature is also decreasing with time because the pressure is decreasing with respect to time. The mixing of the fireball detonation products with the environment at ambient temperatures or the temperatures behind the shock can further decrease the combustion temperatures.

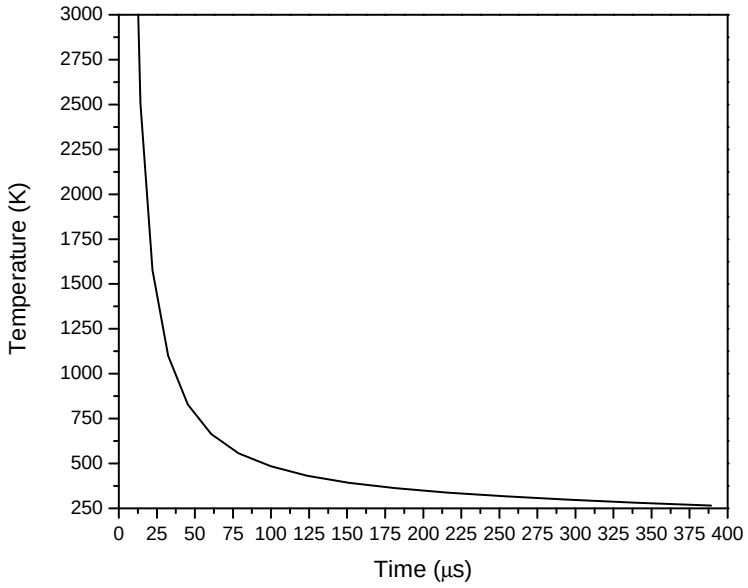

Figure 6.22: Temperaure behind an ideal shock wave from a bare charge.

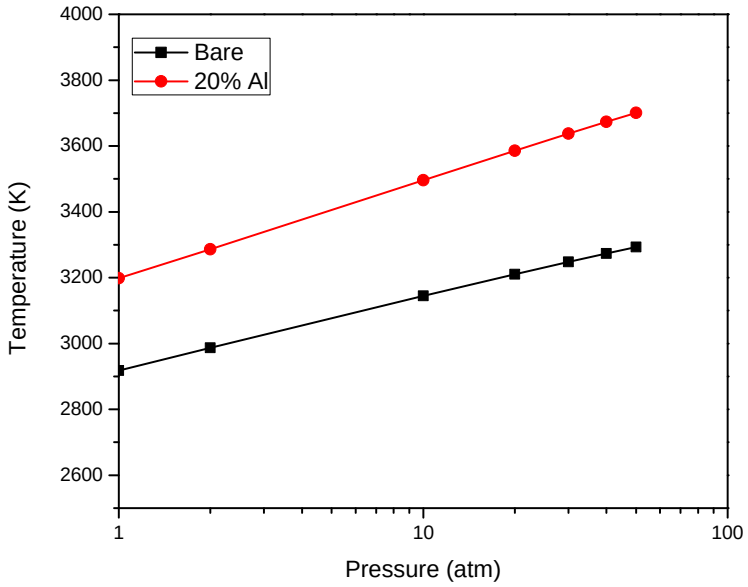

Figure 6.23: The adiabatic combustion temperature for a bare charge and a 20 percent aluminum charge in air.

Another factor that influences the aluminum combustion temperature, and thus the amount of AlO emission, is which oxidizer reacts with the aluminum. The adiabatic flame temperature is lower for reactions with CO_2 or N_2 than with O_2. Consequently, for equal amounts of AlO produced, systems burning in air will have more AlO emission, since AlO emission is exponentially related to temperature.

The air directly behind the shock is the air that mixes with the detonation products, and can not only enhance the aluminum burning—which is indicated by the enhancement of the tests in air compared to the tests in N_2—but it can also create cooler areas which will quench the aluminum combustion. According to Balakrishnan and Menon[51], the more particles at the edges of the fireball, the more that the mixing is enhanced. They also found that when the particles leave the mixing layer, there are cooler regions which will quench the aluminum. For the end-loaded and 50 percent aluminum charges in air, it is more likely that there are more particles on the fireball edges and the additional mixing brings in additional oxidizer, which enhances the after burn, and more AlO emission is measured because the particles continue to burn.

The mixing with oxidizer (air) enhances the after burn of not only the aluminum, but also of the RDX/PETN, both of which have negative oxygen balances. The impact of additional O_2 keeps the fireball hotter than mixing with N_2 or CO_2 because the RDX/PETN burns in the additional O_2. But mixing with N_2 or CO_2 will quench the combustion of the RDX/PETN. A more rapidly cooling fireball can explain why more AlO emission was not measured for the 50 percent aluminum charge, or end loaded cases in N_2 or CO_2, as it was in air.

6.2.9 Pressure in the Fireball

Typically, the optical event of the AlO emission is thought of in terms of a burn time, such that a longer AlO time indicates that the aluminum is burning longer. While there is some evidence that the longer AlO emission measured indicates that the aluminum is burning longer, the question is why different 'burn times' for the different cases—20%-3-μm-Al, 20%-40-μm-Al, 50%-3-μm-Al, and end-loaded charges—are measured.

One possible reason for a longer burn time includes pressure effects—on the edge of the fireball—where the AlO emission measurements are made. Based on the bare charge and using the Taylor blast similarity solution[76], the progression of the pressure at the shock front and shock radius as function of time is shown in Figure 6.24. The typical AlO emission signal from a 20%-3-μm-Al charge is also plotted for comparison purposes. While the pressure at shock front quickly reduces as function of time—$P \propto 1/t^{1.2}$—the typical peak AlO emission occurs at a time when the pressure is on the order of 10–11 atm.

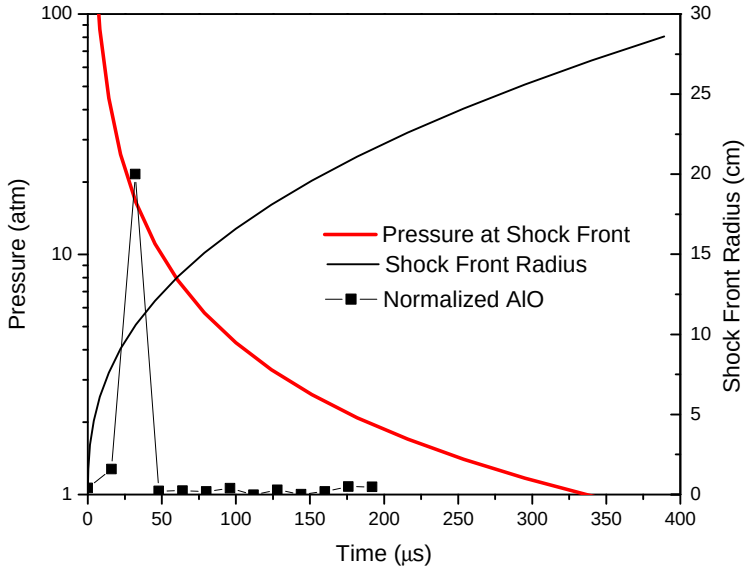

Figure 6.24: Based on bare case and ideal blast equations, progression of pressure and shock radius as a function of time. The normalized AlO is typical for 20%3-μm-Al charge.

As shown in Figure 6.25—which also compares the AlO emission from 20%-40-μm-Al and 50%-3-μm-Al charges—when the AlO emission lasts 100 μs, as for the 40-μm-Al charge and the end-loaded charges, the pressure has decreased to 4 atm in that time frame. For the 50 percent aluminum case—in which the AlO emission lasts for 400 μs—the pressure has decreased to 1 atm by the end of the AlO emission measurement. At particle sizes less than 20-μm, aluminum particle burn time is dependent on pressure;[2, 16] however, for the 40-μm aluminum the burn time is weakly dependent on the pressure[13]. Therefore, the reduced pressure should not have an effect on the 40-μm-Al particles (circles) burn time. For the 3-μm particles—at 50 percent compared to 20 percent loading—the pressure will influence the burn time by increasing the burn time as the pressure decreases. Subsequently, the changing pressures in the fireball is a possible explanation for why the 50 percent loading has a longer AlO emission event than the 20 percent loading—more particles take longer to burn, and the decreasing pressure further increases the apparent burn time and, therefore, the AlO emission measured.

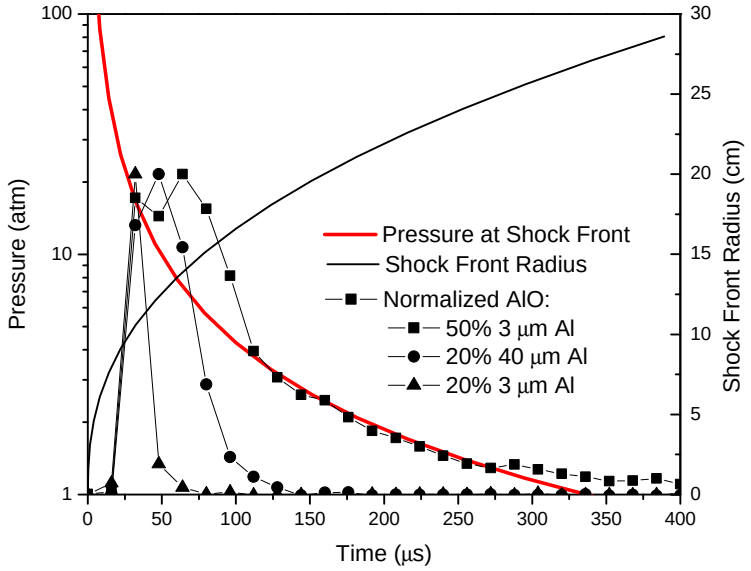

Figure 6.25: Ideal blast pressure and AlO emission from the 50%-Al and 20%40-μm-Al charges in addition to the 20%3-μm charge.

6.2.10 Summary: What AlO Emission Measurements Indicate

A summary of the effects on the AlO emission measurement and subsequent interpretation is as follows. The AlO emission dependence on the temperature is critical, especially during the high early transient temperatures, in which alumina dissociates and can emit AlO. The peak AlO emission measured occurs when the ratio of the collection volume to the fireball volume is the greatest, and it is during the time when the firball temporarily clears of most optical depth effects. Comparing the external AlO emission measurements to internal fiber probe AlO emission measurements showed that the external measurements are representative of the aluminum burning inside the fireball for pre-loaded charges. Therefore, the effect of the optical depth on the AlO emission measurement interpretation is not critical.

The aluminum particle density in the fireball can help explain why there is longer AlO emission for the 50 percent aluminum charge and end-loaded charges compared to 20%-3-μm-Al charge. When there were more aluminum particles at the fireball edges, then more AlO emission was measured, but fewer energy release enhancements were measured, indicating

that the AlO emission is not necessarily proportional to the enhancement. In addition, the end-loaded particles will more likely be located in the portion of the fireball that is less affected by the optical depth than the pre-loaded aluminum. The end-loaded are also less likely than the pre-loaded to be uniformly distributed, increasing the probability that more AlO emission is measured during the same time frame (assuming the end-loaded particles are more concentrated on the fireball surface where the AlO emission measurements are made).

For the 20%-3-μm-Al charges, independent of the environment, the collection volume size, confinement, aluminum particle density, or inside fireball measurements; the AlO emission is only observed within the first 30 μs after detonation. However, burn time calculations between the three experimental setups—tube chamber, blast chamber, and fiber probes—will give different values. For the 20%-40-μm-Al charges and 50 percent aluminum charges, the differences between the two chambers indicate that differences in confinement and optical measurements matter. More aluminum reactions are occurring for 40-μm-Al compared to the 20%-3-μm-Al; however, using the AlO emission as a quantitative burn time measurement is questionable because of the effects of the aluminum particle density, and the pressure in the fireball on the aluminum burn time.

A grease layer or a material on the tip of the charge was shown to affect the breakout of the detonation, changing the production of AlO and its ability to be observed. In addition, when more particles are at the fireball edges, then more mixing can occur and can enhance the after burn of both the RDX/PETN and the aluminum. The additional oxidizer in the air can increase the amount of AlO emission measured, but mixing with N_2 and CO_2 will reduce the fireball temperature quicker and produce cooler regions, which would quench the particles sooner than in air or O_2.

AlO emission was measured for longer than 30–40 μs for only a few cases—for 50 percent aluminum loading in air and pure O_2 ambient environments, and for the 20-%-40-μm-Al charge in air and pure O_2 environments. Since the late AlO emission occurred only in environments containing oxygen, the AlO emission is from aerobic reactions only. The

AlO emission is also an indication of sustained aluminum combustion during this time and signifies that the fireball temperatures are high enough to sustain (rather than quench) aluminum combustion.

When studying aluminum additives in explosives, the fireball will most likely be optically thick, and AlO emission measured will come from the outer edge of the fireball. However, as was demonstrated by comparing this study's AlO emission measurements to measurements made inside the fireball using fibers probes, the AlO emission measured from a pre-loaded aluminized fireball is representative of conditions throughout the fireball, and the external AlO emission measurements can be used to characterize the aluminum burning in an explosive fireball; however, a quanititive burn time measurement is questionable. Even taking into account AlO emission from alumina, AlO emission measurements can be used to confirm aluminum is burning, especially in air environments or during the time immediately following the detonation. In addition, any later AlO emission measured is also an indicator of continued aluminum combustion.

While it was shown that a quantitative burn time is not necessarily valid, determining a quasi burn time might be possible for early AlO emission measurements using a higher time resolution than was used in the blast chamber, such as 1 or 2 μs if possible. In addition, relative intensities of AlO emission can be used to determine the concentration of reactions occurring. High resolution spectra can also be used to determine the vibrational excitation temperature of the aluminum burning in the fireball.

Other configurations of the charge detonation, and/or optical collection techniques not used in this study may provide more information about when and/or where the aluminum is burning using AlO emission measurements. For example, spatially and time resolved AlO emission could be measured from the side of the fireball (as opposed to the leading edge). Different fireball and optical configurations might show AlO from mixing or from reactions with detonation products. In general, AlO emission measurements can be used to compare aluminum combustion from charges that have similar aluminum loading configurations, i.e.,

the different 20 percent pre-loaded charges used in this study, or all pre-loaded charges having different percent loadings, as opposed to comparing pre-loaded to end-loaded charges because of the particle location effects on the AlO emission measured.

In order to make meaningful AlO emission measurements from aluminized explosive fireballs the following ideas are suggested. Since AlO emission is typically measured only during the first 10s of microseconds, it would be beneficially to focus on the early time AlO emission by using as high of a time resolution as possible. As discussed earlier, the time resolved AlO emission may be able to be used to determine a quasi-burn time and can be used to compare similarly loaded aluminized charges. Simultaneous AlO emission measurements made from different angles into the fireball or of different areas of the fireball—such as one from the leading edge and one from the side—could be made, and the intensity and duration of the event compared to have a more complete view of when and where the aluminum is burning. The bright breakout was shown to have high temperatures and influence the amount of AlO emission measured, therefore, if the optics to measure AlO emission could be focused such that the bright breakout was not captured, the effect of the high temperatures on the early AlO emission would be reduced.

One solution for making AlO emission measurements is to use fiber probes inside the fireball. Using internal fiber probes resolves several of the issues shown to affect the AlO emission measurements. The fibers can be positioned to not capture the bright breakout, therefore reducing the influence of the high temperatures. As discussed, the optical depth of the fireball is no longer an issue, as well as the optical collection volume, since the fibers are representative of the total fireball. The effect of the fireball confinement is also reduced. Fiber probes, however, do not reduce the effect of the particle location in the case of the end-loaded charges or charges using an air-gap and aluminum pellet because the aluminum particles are more likely to be on the fireball surface, rather inside the fireball. Therefore it would be beneficial to use fiber probes for pre-loaded charges only.

CHAPTER 7

CONCLUSIONS AND RECOMMENDATIONS

7.1 Summary and Conclusions

7.1.1 Fireball Optical Thickness

The first part of the study focused on measuring the optical depth of an explosive fireball. Attenuation of 532 nm light by the fireball from an aluminized high explosive was measured as a function of space and time. The attenuation of the fireball was measured using two methods—photo diodes which measured the attenuation at five discrete locations as the fireball passed through laser lines, and a high speed framing camera which imaged the attenuation of a laser line or dot matrix through the fireball at eight different times.

The results show that the absorbance is above the optically thin assumption for the entire fireball, and during the entire time the fireball was imaged (up to 300 μs). The laser line images and data give information about the optical thickness near the centerline of the fireball, and the laser dot matrix images show that the edges of the visible fireball are also optically thick. In addition, as the fireball disperses it remains optically thick. The fireball is optically thick at times when key species for characterizing the combustion of aluminized explosives—such as Al and AlO—have been measured. Since the fireball is optically thick, the AlO emission that is measured comes from the outer edges of the fireball and will affect the amount of AlO emission measured and the subsequent measurement interpretation.

7.1.2 Aluminum Combustion inside an Explosive Fireball

One focus of the main part of the study was to better understand when, where and with what the aluminum burns inside the explosive fireball. Experiments were completed for six oxidizing environments—air, pure O_2, pure CO_2, pure N_2, 40%/60% O_2/N_2 and 20%/80% CO_2/N_2—to test the effect of ambient oxidizer on the aluminum combustion. To test the effect of aluminum particle size and percent loading, four distinct aluminized charges of varying aluminum particle size—3 μm, 10 μm and 40 μm—and loading amount—20 and 50 percent by mass—were used. Non-aluminized and 20%-Al_2O_3-loaded charges were used as baseline and inert comparisons, respectively. Experiments were conducted in two different chambers: the tube chamber—a 10.2 cm (4 inch) diameter steel tube—and the blast chamber—a 0.91 m (3 foot) semi-spherical steel enclosure. Both optical and non-optical measurement techniques were utilized, and included emission spectrometry, pyrometry, high speed imaging, pressure, and residue analysis.

Charges used in this study were fairly small, and thus scaling must be considered in interpretation of these results. In general, particles in an explosive will be exposed to longer times in hot gases for larger charges, and so the oxidation levels observed here may be a lower limit on those that would be expected for larger charges. With those caveats, the results indicate that there are four distinct stages of aluminum combustion for 20 percent aluminized PBX-9407 charges.

During the first stage of combustion, the explosive material is detonated and the aluminum particles are activated. The aluminum particles are not immediately activated, but as the detonation wave expands, the aluminum particles lose their aluminum oxide layer and begin to burn. Stage I contributes to the blast wave enhancement and temperatures are 10,000+ K at the breakout.

The implication of Stage II combustion is a stronger blast wave, indicated by higher peak pressures, higher initial blast wave impulses, and an earlier time of arrival of the blast wave

than the charge containing no aluminum and the 20%-Al_2O_3-loaded charge. An enhanced blast wave from the aluminized charges is independent of ambient environment, particle size and percent loading. The primary blast enhancement is consistent with full reaction of the metal in the period required to drive the blast wave. The blast driving reaction is approximately 50 percent aerobic and 50 percent anaerobic as determined by experiments in nitrogen environments. Stage II combustion temperatures are high—3000–4000 K.

During Stage II the aluminum reacts with the hot gaseous detonation products, increasing the energy output and driving the blast wave. In addition, mixing of ambient air and the detonation products at the fireball edge heats the ambient air rapidly and introduces additional oxidizer to the aluminum particles. As a result, fast aerobic reactions occur near the surface of the fireball in the mixing layers. The AlO emission measured is an indication of these fast reactions with the detonation products and the ambient air/O_2 after the initial breakout, even taking into account AlO emission from hot dissociating Al_2O_3 and other influences to the AlO emission measurements. As shown from the ideal blast analysis, some of the aluminum burns to enhance the blast wave in Stage II combustion; however, not all the available energy from the aluminum is released and some of the energy is available for overpressure enhancement during Stage III combustion.

The implications of Stage III combustion are overpressure, an increased impulse, and continued high temperatures. The overpressure enhancement is predominately a function of environment and particle size during this time—such that aerobic reactions are more important for the larger particles, and anaerobic reactions are more important for smaller particles. Quasi-static pressure measurements suggest that the oxygen in air is sufficient to fully oxidize the aluminum particles within 10 ms. In the absence of external oxygen, the aluminum is typically oxidized to the 50 percent level, except for the smallest particle size tested (3 microns), for which nearly full oxidation was observed. During Stage III, mostly aerobic reactions occur, but the anaerobic component is not negligible and cannot be neglected in simulation of aluminized charge oxidation. However, the oxygen in air plays a

significant, if not dominant, role in both early and late time oxidation of added aluminum.

Stage IV combustion is when the fireball is cooling and dispersing. Temperatures during Stage IV can be sustained above 1000 K for up to 1–2 seconds, which can contribute to continued aluminum oxidation. However, there was no measureable contribution to the energy output from the aluminum particles.

7.1.3 AlO Emission Measurement Characterization

The final goal of this study was to characterize AlO emission measurements from explosive fireballs, and determine when and how AlO emission can be used as an indicator of aluminum combustion in explosive fireballs. The variations in how much AlO emission was measured in the experiments indicate that interpreting AlO emission measurements from explosive fireballs is not straightforward with respect to correctly determining the amount of aluminum combusted or how long the aluminum reacted.

Time resolved emission measurements were made of aluminized explosive fireballs in air, O_2, N_2, and CO_2 in the tube chamber, and the residue products were collected and the amount of oxidation quantified. Results showed that AlO emission was detected in varying amounts for the aluminized charges in each environment, and there is evidence of an after burn of the aluminum particles in air and O_2 for the 50 percent aluminum loading and coarser (40 μm) aluminum particle charges. The recovered residue showed significant oxidation, 60–95%, from all tests—including the tests in N_2 and CO_2, which had significantly less AlO emission compared to the tests in air and O_2. The high oxidation in N_2 further indicates that the detonation products are important oxidizers in aluminized explosives and a significant amount of aluminim oxidation occurs as a result. However, a correlation between the total integrated AlO emission and completeness of combustion was not found.

Results from experiments in N_2 and CO_2 showed that AlO emission is produced by reactions with detonation products, However, since the duration was typically one 16 μs time

frame for the tests in the blast chamber, and was a similar time frame for the experiments in air and O_2, the AlO emission duration cannot be considered a burn time in the same understanding as for shock tube aluminum burn time measurements in these cases.

The AlO emission peaks were measured at the time of the highest temperatures and during the period when the temperature decreased most rapidly—the first 20–30 μs after the detonation. The high temperatures skew the AlO emission measurements to higher intensities because emission is an exponential function of temperature. The decrease in AlO emission with respect to time could be from a reduction in AlO production or from the decreasing temperature. As a result of high transient temperatures at breakout, the oxide layer found on the aluminum particles contributes to the AlO emission measured. Experiments showed only 50 percent of the AlO emission measured is from actual combusting aluminum particles contributing to the output energy during the first 20–30 μs after the detonation.

Other influences to the amount of AlO emission measured—and subsequently the measurement interpretation—include the location, amount, and particle density of the aluminum particles in the fireball; the restriction of the fireball development and subsequent mixing with the ambient environment; the optical collection volume; and the fireball optical depth. Differences in the optical collection volume and the restriction of the fireball development can affect the duration and time-evolution of the AlO emission measured, and subsequently a burn time calculation. In addition, mixing with ambient O_2 is critical in the production and measurement of late-time AlO emission.

While the light duration is longer when more aluminum particles are present—50 percent loaded compared to 20 percent loaded—the actual additional contribution to the enhancement is minimal, and is not on the same order as the additional light output. Additionally, the results show that the amount of AlO emission measured is influenced by the location of the burning aluminum particles—when more of the aluminum particles are on the outer surface of the fireball, the AlO emission intensity is greater than when the particles burn

throughout the full fireball volume. However, the edge particles added less to the initial blast wave impulse enhancement and the overpressure enhancement than the pre-loaded charges did. Therefore, an 'optical burn time' cannot be necessarily correlated to the enhancement by the aluminum additive.

The AlO emission that is measured externally appears to be *qualitatively* representative of the aluminum burning in the fireball, based on the comparison of two measurement techniques—external only and internal fiber optic probes—and therefore the optical thickness of the fireball does not affect the external AlO emission measurement interpretation when the measurements are used to confirm aluminum is burning. Using fiber probes may be a solution to AlO emission measurements for pre-loaded charges.

Analysis of the fireball size with respect to the light attenuation lengths measured for the fireball optical thickness study showed that the fireball temporarily clears—with respect to the optical thickness—during the time when the peak AlO emission is measured and can help explain why the peak AlO emission is measured at this time. The temporary clearing occurs when the fireball length scale is on the same order as the attenuation length scale. At other times, the attenuation length scale is much shorter than the fireball length scale, resulting in a smaller volume of the fireball from which AlO emission is measured than during the temporary clearing.

The air-gap experiments showed that particles on the fireball edges that are not activated in blast wave—because of their distance from the charge, but are exposed to high temperatures and pressures via mixing with detonation products—do not contribute to the initial blast enhancement, but do react, add to overpressure enhancement, and will have AlO emission. However, the AlO emission is on a much shorter time scale than the overpressure enhancement, indicating that hot burning—but not activated—aluminum will produce AlO emission. In addition, the enhancement of aluminum powder located further from the charge is caused by aerobic reactions resulting from the mixing of detonation products and air, since no enhancement was measured for the gap tests in N_2.

The tests using a charge having a grease layer on the charge tip showed a drop in measured AlO emission by 90 percent compared to the same charge not having a grease layer. It was determined the effect of the grease layer is that the breakout is changed, and is a function of the tip material mass, density, and attenuating properties.

From the results, it is clear that a greater AlO emission signal does not necessarily mean more aluminum combustion, and a lower AlO emission signal does not automatically denote little or no aluminum combustion. If aluminum is present in the fireball and AlO emission is measured, then the aluminum is burning; however, part of the AlO emission measured is from non-combusting Al_2O_3 in the first 20–30 μs. If an AlO emission signature is not detected, it does not necessarily mean that the aluminum is not burning inside the explosive fireball. The AlO emission measurement cannot be used as a quantitative burn time measurement in the traditional sense, nor can the AlO emission measurement be correlated to the amount of energy released by the aluminum in *all* cases and circumstances.

Suggested optical practices for making meaningful AlO emission measurement include making high time resolution measurements of the early AlO emission, simultaneously making measurements from different angles into the fireball or of different areas of the fireball, and focusing optics such that the bright breakout is not captured.

When AlO emission is measured it indicates that the temperatures are high enough to sustain aluminum combustion which produces AlO, and that oxidizers are present which react with aluminum to produce the AlO. For the same time frame, the relative intensities of AlO emission measured could be indicators about the temperature or the number of reactions occurring. AlO emission measured is a result of both anaerobic and aerobic reactions, and both types of reactions contribute to the aluminum combustion enhancement of the explosive charge.

7.2 Recommendations for Future Work

The results of the current study give insight into the aluminum combustion in an explosive fireball; however, questions remain. Specifically, how a material at the charge tip—such as grease—affects the breakout is not fully understood, and no clear relationship between the the enhancement and the aluminum percent loading of a charge was determined—for both the pre-loaded and the end-loaded charges. Nine influences to the production measurement of AlO emission were identified; however, the different influences affect each other, and investigating the effects separately or how to separate them is justified. The following are areas which merit further investigation.

The grease layered charge tests revealed that a small change at the charge tip—a thin layer of grease—resulted in a significant change in the amount of AlO emission measured. The results of the Mylar layer and glass layer experiments indicated that the main effect of a substance on the charge tip is that the breakout is changed. It was also shown that the mass of the material at the charge tip influences the degree to which the surface material affects the breakout. The detonation breakout is currently unstudied and further investigation is needed to understand how the breakout affects aluminum particle combustion in a non-ideal detonation. A substance on the charge tip most likely changes how the blast wave is reflected back through high explosive (HE) and detonation products, and affects the blast wave speed, the temperature, and the mixing layer. The mixing layer size and/or content may change and thereby change the oxidizers available or quenching that occurs.

Therefore, it is proposed that an in-depth and detailed study be completed to investigate the breakout of a non-ideal explosive, the effect the breakout has on aluminum particle additives, and the effect of changing the breakout using a material on the charge tip. More work needs to be completed to fully understand how the mass and density of the substance on the charge tip affects the breakout. Other variations which may influence how the breakout is affected include the thickness of the tip material, and the location of the material, e.g.,

only on part of the tip, either in the very middle leaving some of the HE exposed, or around the edge of the tip leaving most of the HE exposed. The effect of two dissimilar layers on the charge tip could also be investigated, and determine the effect of the relative location of each layer with respect to the HE has on the breakout and AlO emission observed. It is also suggested to use fiber probes to measure the AlO emission of pre-loaded charges having a material at the tip to investigate the AlO production in the middle of the fireball, since the current studied showed little AlO emission is measured using external measurements.

In addition to investigating the breakout effect on aluminum particles added to a HE, using charges containing Al_2O_3 would give insight to the effect a material has on the charge tip on the dissociation of the aluminum oxide at high temperatures. While the breakout occurs within the first 20 to 30 μs after detonation, the effect of a substance on the charge tip has on late AlO emission is also unknown. Therefore, it would be interesting to conduct a smaller investigation focused on determining what the influence, if any; a material on the charge tip has on late AlO emission.

The different loading amounts—20 and 50 percent—had similar initial impulses and peak pressures, but the higher loaded charges have potentially more energy that, in theory, could be released later. Pressure and impulse data for the 50 percent aluminum loading after the initial blast wave is needed for comparisons to the 20 percent loading. In addition, having only two different percent loading is not enough to determine any clear relationship between the percent loading and the energy output. It is necessary to expand this part of the study to include additional percent loading amounts. Using an expanded set of charges having different aluminum percent loadings will allow an in-depth investigation exploring the effects of aluminum loading has on the enhancement, and possibly on the AlO emission measurements. This study could include also investigating the effect the particle density has on the AlO emission measurements. It would be beneficial to conduct this study in a smaller chamber than the blast chamber, because in a smaller chamber differences in the overpressure could be more easily measured. Since the aluminum will burn with N_2, to

be able to separate the enhancement from anaerobic and aerobic reactions of aluminum, experiments in a true inert environment, such as Ar, should be conducted.

The comparison of the ideal blast similarity solution of a RDX/PETN charge and aluminum additives to the experimental results indicated that the blast wave from the charges is not ideal, as expected. In order to be able to better compare the experimental results to ideal calculations, experiments should be completed that more closely emulate an ideal blast detonation. One technique is to perform the experiment in a larger chamber than the blast chamber, and place the charge in the bottom center of the chamber, and the pressure transducers further away than in the current study and above the charge location. Measuring the pressure further away than the current set up and in a more open setting will allow the blast wave to develop more symmetrically, and mimic an ideal spherical blast wave at the pressure transducer.

In addition to ideal blast wave comparisons, a CFD model of an RP80 charge should be developed in order to investigate the effect of mixing on the aluminum particle combustion. A simple CFD model could start by modeling the RP80 in a tube in which the fluid flow and mixing can be approximated as 1D, rather than a 3D modeling of the fireball in the blast chamber. A CFD model would further the understanding of where in the fireball the aluminum is burning, where after burn can occur as a result of enhanced mixing, and identify cooler regions which could quench the combustion. It is important to understand how the mixing region of the fireball affects the aluminum combustion and the potential for after burn. Taking the model one step further would be to incorporate the results of the grease layer affecting the breakout into the model to be able to better understand the effect of the breakout on the aluminum particles.

The effects of confinement, mixing, and optical collection on the AlO emission measurements were not entirely separated, nor are completely understood. Experiments which more clearly separate these effects would be useful in further determining when AlO emission can be used as an indicator of aluminum combustion. In addition, the particle location was

shown to effect the amount of AlO emission measured, and is not fully understood yet. Additional studies investigating the effects of end-loading on the energy output and using AlO emission as a combustion indicator are warranted.

APPENDIX A

EXPERIMENTAL PROCEDURES AND EQUIPMENT

This appendix contains standard operating proceedures, details of equipment settings used, and additional pictures of the experimental setup. Equipment technical data and technical drawings for parts manufactured in-house can be found in Appendix B. The purpose of the appendix is to aid future graduate students in the continuing of this work and/or using the same equipment.

A.1 Standard Operating Procedures

Tube Chamber—MEL 2314

Date/ Time:
Detonator Designation:
Environment:
Data File Name Extension:

Tube Chamber Test Standard Operating Procedure

Safety Precautions

- NG or HK must be present for all detonator tests.
- Everyone must wear eye protection during all handling of the detonator and during the test.
- Before testing, ensure the chamber is securely supported and all electronic/chamber parts are in working order.
- The detonator is not to in the room until pre-tests are completed, step 4 of the pre-test set-up check list.
- Before handling the detonator, ensure no cables or wires can be tripped over or pose a hazard to safe moving in or exiting the room.

- Have a designated location on a table to store the detonator before testing and to load the detonator in the holder.
- Inform everyone where detonator is at all times and when it is being moved.
- Detonator needs to be transported in wooden box.
- Make sure there is a clear lab exit path at all times.
- Wear conductive shoes in the lab and any gloves are to be anti-static to reduce static electricity.
- No removal of outer wear in the lab which can cause static electricity charge.
- No tape on the chamber or set up - removal causes static electricity.
- Discharge possible static electricity on tools before using them by touching them to a grounded wire.
- Only a RISI approved firing set should be used with the detonator.
- Use only RISI approved firing cable. Hook-up is recommended through either pig-tailing the detonator cable with the hook-up wire or connecting via a RISI approved RISI firing connector. Always be aware of exposed wire. We are working with high voltage that when uncontrolled can arc and result in a misfire.
- Make sure everyone in the room is familiar with the safety precautions and emergency procedures. Each person must comply to be in the room during the test.

Pre-Test Set Up

1. Ensure all electrical connections are correct and in working order
   (a) Check connection from the pulse generator to fire set.
   (b) Check connection from the pulse generator to FK camera & spectrometer
   (c) Inspect wire from the fire set to the detonator wires, shunt wires at the fire set.
2. Insert feed-through tube through the chamber wall and into the chamber with wires.
   (a) With the top of the feed-through wires shunted, pull wire out of tube.
   (b) Tighten the brass cap.
3. Test set up and settings with bridge wire
   (a) Place a piece of aluminum wire between alligator clips and connect to the wires in the chamber from the feed through tube. Arrange so that the wires do not touch the chamber wall or each other
   (b) Close chamber with flanges following steps 5 through 7 below.
   (c) Follow testing procedure below
   (d) After test is over, end flange, first disconnecting any gas supply
   (e) Repeat bridge wire test until satisfied that all settings are correct
4. Roll plastic liner into a 4 inch diameter tube and insert into the chamber so that entire length of chamber is covered. Line up notch in liner with feed through tube. Insert a steel ring into chamber such that it protects the liner at the detonator location.

5. Load detonator (last step before sealing chamber) Follow all safety precaution listed above.

   (a) Ensure that the wires from the feed through tube to the fire set are shunted at the fire set end. These wires are to remain shunted until firing.
   (b) Ensure chamber is grounded properly.
   (c) Check that the chamber, optic equipment and electronic equipment are in the correct positions. Double check the integrity of all cables and wires.
   (d) On a table, carefully insert the detonator into the chuck, wires first, and tighten around plastic head.
   (e) Slid block into chamber until it is against the steel ring and under the feed through port.
   (f) Place another steel ring behind the block.
   (g) Attach the two feed-thorough wires to the detonator via the alligator clips, preventing the two leads from touching each other or the chamber walls
   (h) Attach feed-through wires from detonator to shunted firing set wires

6. Bolt end flanges

   (a) Make sure o-rings are in place
   (b) Use 8 bolts for each flange, tighten to 50 ft-lb of torque per bolt. Use a washer with each bolt and nut.
   (c) The gas port flange is at the detonator side of chamber.
   (d) The window flange is downstream of detonator.

7. Attach vacuum pump and inlet gas supply if necessary for flushing, otherwise ensure the inlet valve is closed

8. If firing in environments besides air:

   (a) Flush chamber with working gas four times.
   (b) Fill chamber with working gas at slightly above atmospheric pressure
   (c) Close inlet valve when finished with flushing and turn off vacuum pump (gate valve also closed)

Testing Procedure - Make sure Safety Precautions listed above are followed before proceeding.

1. Make sure FK camera and spectrometer are turned on and ready for testing
2. Make sure Andor software for FK camera is on and ready to trigger.
3. Reinspect all cables and wires.
4. Turn on hallway red warning light.
5. Leave room and close door. Lock door.
6. Remove shunt from firing set wires and connect to firing set. Inform room when this is being done.

7. Turn on Fire Set, arm and charge to 4 kV (Say "Arming")
8. Warn everyone when capacitor is charged (Say "Ready")
9. Trigger the pulse generator (Say "3-2-1-Fire")
10. Immediately after test, turn off the Fire Set, and shunt the wires. Discharge any static electricity at the fire set by touching the leads with grounded wire before removing and shunting the fire set wires.

Post-Test Procedure

1. Vent chamber to atmospheric pressure by loosening one of the set screws near the middle of the chamber.
2. Reverse setup steps 3 - 5 from pretest procedure:
   (a) Unbolt and roll gas port flange out of the way
   (b) Remove the detonator mount by disconnecting the feed-through wires
   (c) Unscrew brass cap and remove feed-through tube
   (d) Slide plastic liner out of the chamber; take special care not to lose debris
3. Collect particles from the liner
   (a) Lay the liner flat on a table
   (b) Using a spray bottle with distilled water, gently mist the entire liner surface
   (c) Squeegee in one direction, collecting water in one area; tilt liner to pour this sample into a Petri dish
   (d) Repeat spray and squeegee steps 2 or 3 times until debris can no longer be seen in the water; set sample aside
   (e) Wipe down the liner with water and alcohol for future use, if undamaged
4. Thoroughly clean inside of the test chamber and flanges
5. Remove the remains of the detonator from the adapter mount

Delay Generator Settings
1. Channel To: Fast Kinetics Camera (Trigger)
2. Channel A: Fire Set (95 s delay)
Ensure all channels are TTL, High Z, Normal

Emergency Procedures - MEL 2314
Room Phone Number - 244-3650
Room Location in MEL - 2nd floor, 2nd most northern east-west hallway in building

Miss-Fire:
If a misfire is suspected, e.g. the blast is not heard, then follow this procedure.

1. The fire set is designed to discharge once the firing button is pushed or an external pulse is provided, whether or not the detonator fires. If the fire set does not discharge, then fully discharge the capacitor in the fire set by releasing the arm button and waiting until the voltage reads 0 V on the fire set voltage meter. Turn off fire set.

2. Shunt fire set wires.
3. Wait 30 minutes outside the lab.
4. Check connections of all other wires.
5. Check power source of pulse generator.
6. Retry test.
7. If the detonator does not fire a second time, discharge and turn off the fire set, and shunt wires at the fire set. Call University EOD unit. Lt. Skip Frost is in charge of the EOD unit; his direct phone number is 244-4874, or call the non-emergency Division of Public Safety number, 333-1216, to reach Lt. Frost. The EOD unit will remove and dispose of the detonator safely.

Chamber Breach:

1. If there is a fire, follow Fire Procedure below.
2. Ensure no one is hurt. If so, follow Medical Emergency Procedure below.
3. Determine damage to chamber, room, and other equipment.

Fire:
Fire Alarm locations: at either end of hallway
Fire Extinguisher location: on wall next to MEL 2314 doorway

1. If feasible put out fire with fire extinguisher.
2. Evacuate room closing lab doors to contain fire.
3. Evacuate building, pulling fire alarm on the way out.
4. Inform firemen the location of the fire by calling 911 and/or talking to the firemen when they arrive.

Medical Emergency (from DRS website):

1. Life Threatening Injury or Situation
   Call 9-911 (METCAD) for immediate response.

2. Non-life Threatening Injury or Situation
   Employees should seek treatment at the Occupational Medicine Departments identified by the Workers' Compensation program. Currently, these facilities are:

   Carle Occupational Medicine (602 W. University Ave., Urbana): Normal hours are 7:00 am - 5:00 pm weekdays. Phone: (217) 383-3077. Employees can go to the Carle Emergency Room (611 W. Park St, Urbana) after normal hours, on weekends, and holidays. Phone: (217) 383-3313.

   Christie Occupational Medicine (101 W. University Ave., Champaign, 4th floor): Normal hours are 8:00 am - 5:00 pm weekdays. Phone: (217) 366-1310. Employees can go to the Provena Covenant Emergency Room (1400 W. Park St, Urbana) after normal

hours, on weekends, and holidays. Phone: (217) 337-2131.

When seeking treatment, bring the following: (1) a note from your supervisor verifying that the injury took place during work OR the name and number of your supervisor (who will be called the following day to verify that the injury occurred during work), and (2) a Material Safety Data Sheet (MSDS) if a chemical was involved in the injury (if an MSDS cannot be found, do not delay seeking medical attention).

Non-employees should seek treatment at the emergency room of either Carle Foundation Hospital or Provena Covenant Medical Center. Students may seek basic medical care at the McKinley Health Center or with their personal physician. Costs associated with most injuries incurred during unpaid activities are the responsibility of the individual and their health insurance.

If needed there is a first aid kit in MEL 2314 on the shelf above the table near the main door.

Emergency Contacts
Nick Glumac
Herman Krier
Bob Coverdill

Blast Chamber—MEL 1304, 1308

Date & Time	Detonator	Environment	Data Code Prefix

1. Pressure Gauges

   (a) Adjust locations
   (b) Record setup details:

Transducer Number	Cable Ltr.	Orientation	Distance

2. Pressure Amplifiers

   (a) Verify pressure wires from tank match wires connected to transducers
   (b) Set sensitivity on amplifiers,
   (c) choose and record output scaling: mV/PSI
   (d) Connect amp outputs to picoscope inputs
   (e) Record setup details

Amp Channel	Input Cable Letter	Sensitivity	Picoscope Port

3. Picoscope Computers Settings

   (a) Set Single Simple Trigger, Channel D, 5% Pre-data, 1 V Threshold
   (b) Set Channels A, B to +/- 10 V
   (c) Set Channel D to +/- 2 V
   (d) Set 500 μs/Div.
   (e) Set samples collected to 1 MS

4. Pyrometer

   (a) Is there a ND filter installed? Y,#: N:
   (b) Connect Power cords, power on photodiodes
   (c) Connect BNC cords
   (d) Record setup details

Photo Diode	Cable colors	Picoscope port	Gain
730 nm			
940 nm			

5. Flash

   (a) Set flash to manual mode, ASA 100.
   (b) Check that flash is connected to power cord.
   (c) Secure flash to optics table.

6. FK Settings
   Exposure:
   Number in Series:
   Light Calibration Exposure: Count:

7. Phantom Camera

   (a) Connect camera trigger cable, Ethernet cable, and power cable.
   (b) Start camera software
   (c) Verify image size settings in software. Dimensions: X pixels
   (d) Aim camera, focus camera, secure camera
   (e) Change camera settings for high speed capture: FPS, μs exposure

8. Triggering

   (a) Check BNC connection between trigger and picoscope.
   (b) Check BNC connection to camera.
   (c) Check connections between trigger and circuit, and between circuit and flash.
   (d) Check BNC connection between fireset and trigger.
   (e) Record Settings:

Trigger Channel	Equipment Connection	Delay (usec)

9. Flash Test

   (a) Close front hatch, secure with 3 bolts, hand tightened.
   (b) Begin Capture on the camera, check that flash is on and charged.
   (c) Trigger the flash and camera (and picoscope).
   (d) Check for flash centering, shadow offset. Adjust flash position / orientation.
   (e) Check for adequate lighting over enough frames ($\sim$15). Improper positioning can result in low lighting, so ensure the flash is in the correct location before taking other measures to increase the amount of light.

(f) Repeat Step 7 until flash duration, brightness, and shadow overlap is acceptable.

10. Bridge Wire or Al/potassium perclorite powder Test

    (a) Attach bridge wire clips to the detonator wire leads inside the chamber.
    (b) Install brigde wire, wire running front to back in the tank.
    OR
    (c) Attach additional length of lead wire taped to a block to the detonator wire leads inside the chamber.
    (d) Place a pile of Al/potassium perclorite powder on top of two exposed wires.
    (e) Close the front port, 3 bolts, hand tightened.
    (f) Follow test procedure below
    (g) Adjust flash timing relative to detonation, examine pressure data & pyrometry data
    (h) Repeat bridge wire test until satisfied

11. Install Detonator - NG or HK present from this point on

    (a) Before retrieving detonator from the safe, ensure that all necessary components are present:

        i. Steel detonator holder block and brass sleeve insert
        ii. Wire shunts
        iii. Hardware for securing detonator block to U channel
        iv. Hardware for securing front port
        v. Wrenches for securing front port

    (b) Ensure that the area is clear to move about, that the room exit is not blocked, and that there are no wires or other trip hazards on the ground.
    (c) Check that everyone present has proper personal protective equipment
    (d) Retrieve detonator - Only N. Glumac and H. Krier may handle detonators.
    (e) Insert detonator into brass sleeve, then into steel block. Thread wires through and bend $\sim 90°$, tape wire to bottom of block.
    (f) Place detonator in U-holder, insert bolts.
    (g) Ensure O-ring is present and correctly seated in front flange, and that no tools are inside the chamber.
    (h) Rotate front port into place and secure with two hand tightened bolts and nuts.
    (i) Insert and hand tighten remaining bolts and nuts, 6 total, in every other hole.
    (j) Tighten in criss-cross pattern, with wrench, in 2 steps.

12. If firing in environments besides air

    (a) Ensure all valves are closed (including green air supply valve).
    (b) Attach vacuum pumps to piping system behind tank at the black needle valve
    (c) Turn on vacuum pumps
    (d) Slowly open black valve until fully open
    (e) Open green valve to also evacuate supply line.
    (f) Evacuate chamber until pressure is at -25 inHG

(g) Close all valves
(h) Turn off vacuum pumps
(i) Slowly fill with N_2
(j) Repeat process to have 4 evacuations, filling the final time with desired environment gas.

13. Test

(a) Do trigger test, if all diognostics triggered properly, then reset.
(b) Ensure all valves to tank are closed
(c) Final check of camera settings
(d) Set camera to capture
(e) Final check of charge amp settings
(f) Final check of picoscope settings
(g) Set picoscope to wait for trigger
(h) Attach detonator leads to the fireset poles
(i) Turn Key to on
(j) Final Check of tigger settings
(k) Clear 1304 of everyone, ensure door is locked.
(l) Hold down Arm - "Arming"
(m) When ∼4000 V, - "Ready"
(n) Trigger Test with Pulse generator (EXC) - "3, 2, 1, Fire"
(o) Once fire set reads ¡ 100 V, Remove detonator wires and shunt together.

14. Vent Chamber

(a) Turn on Exhaust fan
(b) Open exhaust valve behind tank (plastic valve)
(c) Turn on air (green valve on west wall)
(d) Slowly open needle valve at tank until air is flowing quickly
(e) Vent for 10 minutes before opening chamber

15. Post-Test / Save Data

(a) Save Pyrometry Data (all waveforms) as .mat
(b) Save Pressure Data (all waveforms) as .csv and .mat
(c) In Camera Software, find and select frames relevant to detonation
(d) Save as .cine
(e) Save as .tif image sequence
(f) Save spectrometry data

16. Clean Up / Reset

(a) Remove detonator remnants from chamber
(b) Clean chamber / check screen for dust
(c) Remove debris from the detonator block

17. Calibrations

    (a) Pyrometry

Calibration	Lt	Dk	Difference
730 nm			
940 nm			

    (b) Spectrometer: light and wavelength (Hg lamp)
    (c) HSC Calibration image

ALTERNATE PROCEDURES
Misfire

1. Release the arm button and wait for voltage to discharge back to 0 V. Turn off fire set.
2. Unscrew and shunt the detonator wires.
3. Check pulse generator to ensure proper trigger is being delivered.
4. Check wiring to ensure trigger signal is being received by fire set.
5. After 30 minutes, retry test.
6. If detonator does not fire on second attempt, follow step 1 and 2 again. Call University EOD unit. Lt. Skip Frost is in charge of the unit; his direct phone number is 244-4874. Alternatively, call non-emergency university police at 333-1216 to reach Lt. Frost. The EOD unit will remove and dispose of the detonator.

Chamber Breach

1. Check for a fire. If there is a fire, follow procedures below.
2. Check for injuries. If anyone is injured, follow procedures below.
3. Determine extent of damage to equipment, chamber, and lab.

Fire—Alarms at either end of hallway, Extinguisher to the left.

1. Attempt to put out the fire with a fire extinguisher if it is small enough.
2. Evacuate room, close doors after exiting.
3. Pull the fire alarm and evacuate the building.
4. Talk to firemen by calling 911 or in person when they arrive. Inform them of the location, size and type of the fire.

Medical Emergency (from DRS website)

1. Life Threatening Injury or Situation: Call 9-911 from UIUC phone or 911 from cell phone (METCAD).

2. Non-life Threatening Injury or Situation

(a) Employees should seek treatment at the Occupational Medicine Departments identified by the Workers' Compensation program. Currently, these facilities are:

   i. Carle Occupational Medicine (602 W. University Ave., Urbana): Normal hours are 7:00 am - 5:00 pm weekdays. Phone: (217) 383-3077. Employees can go to the Carle Emergency Room (611 W. Park St, Urbana) after normal hours, on weekends, and holidays. Phone: (217) 383-3313.

   ii. Christie Occupational Medicine (101 W. University Ave., Champaign, 4th floor): Normal hours are 8:00 am - 5:00 pm weekdays. Phone: (217) 366-1310. Employees can go to the Provena Covenant Emergency Room (1400 W. Park St, Urbana) after normal hours, on weekends, and holidays. Phone: (217) 337-2131.

(b) When seeking treatment, bring the following: (1) a note from your supervisor verifying that the injury took place during work OR the name and number of your supervisor (who will be called the following day to verify that the injury occurred during work), and (2) a Material Safety Data Sheet (MSDS) if a chemical was involved in the injury (if an MSDS cannot be found, do not delay seeking medical attention).

(c) Non-employees should seek treatment at the emergency room of either Carle Foundation Hospital or Provena Covenant Medical Center. Students may seek basic medical care at the McKinley Health Center or with their personal physician. Costs associated with most injuries incurred during unpaid activities are the responsibility of the individual and their health insurance.

Checklist for multiple testing days

Date:
Pressure

Transducer #	Cable Ltr.	Distance	Amp Channel	Sensitivity	Picoscope Port

Photo Diode	Cable colors	Picoscope port	Gain
730 nm			
940 nm			

Calibration	Lt	Dk	Difference
730 nm			
940 nm			

Trigger Channel	Equipment Connection	Delay (μs)

FK Settings
Exposure:
Number in Series:
Light Calibration Exposure: Count:

Phantom Camera
Dimensions: X pixels
FPS, μs exposure
Calibration:

Test/time	Detonator	Environ	Name

A.2 Equipment Settings

Tube Chamber Experiments

Table A.1 lists the settings for the pulse generator used to control the timing of the spectrometer and fireset. In Table A.2, the settings for the Andor FK CCD detector are listed.

Table A.1: Pulse Generator—Tube Chamber.

Trigger Channel	Equipment Connection	Delay	Output
T	Andor FK CCD	-	HighZ, TTL, Normal
A	Fireset	95 μs	HighZ, TTL, Normal

Table A.2: FK Andor CCD Detector—Tube Chamber.

Acquisition Mode	Fast Kinetics
Trigger Mode	External Start
Readout Mode	Full Vertical Binning
Acquisition Parameters	
Sub-area Height	1 row
Exposure time	2 μs
Number in Series	100
FK Vertical Shift Speed	2 μs

Blast Chamber

The pulse generator settings used for the blast chamber tests are listed in Table A.3. Table A.4 lists the setting for the Andor FK CCD detector. The data aquisition using a picoscope for the pressure transducers is listed in A.5. For the peizoresistive transducers, the DC amplifier settings are listed in Table A.6, and the calibration equations are listed in Table A.7. The picoscope settings used for the pyrometer are found in Table A.8.

Table A.3: Pulse Generator—Blast Chamber.

Trigger Channel	Equipment Connection	Delay	Output
T	Andor FK CCD	-	HighZ, TTL, Normal
A	Phantom 5.2 Camera	T + 600 μs	HighZ, TTL, Normal
A $\sqcap$ B	Flash, Picoscopes	B = A + 5 ms	HighZ, TTL
C	-	A + 80 μs	HighZ, TTL, Normal
C $\sqcap$ D	Fireset	D = C + 1 ms	HighZ, TTL

Table A.4: FK Andor CCD Detector—Blast Chamber.

Acquisition Mode	Fast Kinetics
Trigger Mode	External Start
Readout Mode	Full Vertical Binning
Acquisition Parameters:	
Sub-area Height	1 row
Exposure time	16 μs
Number in Series	100
FK Vertical Shift Speed	16 μs

Table A.5: Picoscope for pressure transducers.

Collection Time	1 ms/div (10 ms total)
Number of Samples	1 MS
Channels A/B Range	$\pm$ 10 V
Channel D Range	$\pm$ 2 V
Trigger Mode	Single
Rising Edge	
Trigger Channel	D
Threshold	1 V
Pretrigger	5%

Table A.6: DC Amplifier for peizoresistive pressure transducers.

Endevco Transducer #	B95N	B78T
Voltage Excitation (V)	10	10
Sensitivity (mV/EU)	5.29	5.21
Output Scaling (mV/EU)	200	200
LP Filter	OFF	OFF
Auto Zero	OFF	OFF
Shunt Calibration	OFF	OFF
Monitoring State	OFF	OFF

Table A.7: Calibration equations for peizoresistive pressure transducers.

Endevco Transducer #	Equation
B78T	$P(psi) = 5.8826V(V)$
B95N	$P(psi) = 5.5489V(V)$

Table A.8: Picoscope for pryometer.

Collection Time	500 μs/div (5 ms total)
Number of Samples	1 MS
Channels A/B Range	$\pm$ 10 V
Channel D Range	$\pm$ 2 V
Trigger Mode	Single
Trigger Channel	D
Threshold	1 V
Pretrigger	5%

A.3 Setup Pictures

Tube Chamber

From the tube chamber tests, the optics are shown in Figure A.1 and the charge mount in Figure A.2. Details on the design and construction of the tube chamber can be found in [45].

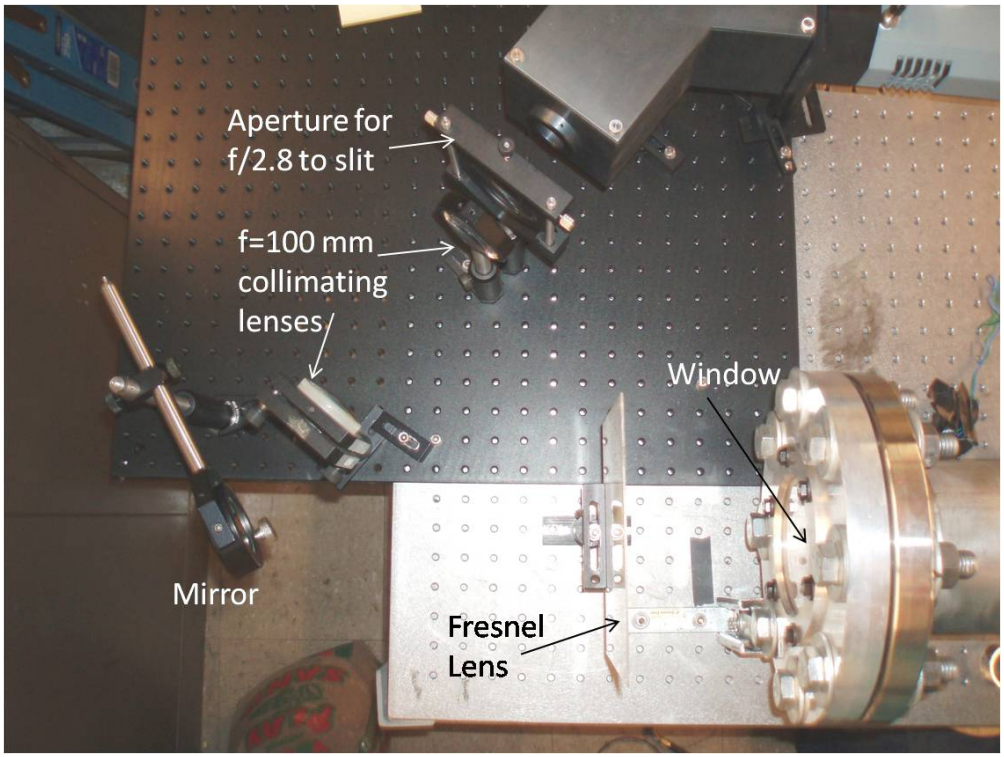

Figure A.1: Collection and focusing optics to spectrometer for the tube chamber tests.

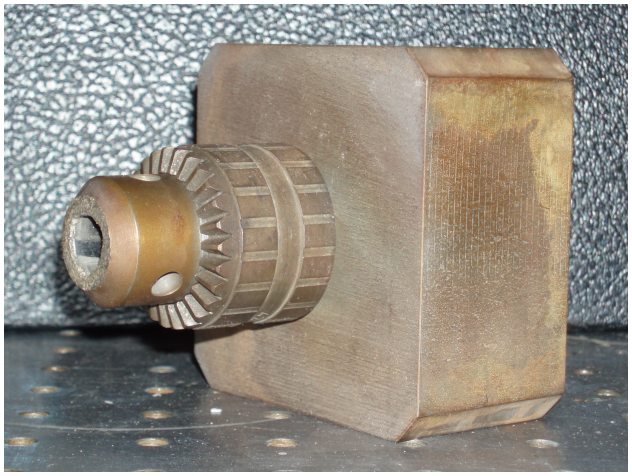

Figure A.2: Chuck mount for the tube chamber tests.

Blast Chamber

The interior of the blast chamber is shown in Figure A.3, in which the detonator mount, side-on piezoelectric pressure transducer and retroreflective screen are visible.

Figure A.3: Interior of the blast chamber—detonator mount, side-on piezoelectric pressure transducer and retroreflective screen.

The detonator mount blocks are shown in more detail in Figure A.4. The blocks were 2.5 inch wide by 2.5 inch long by 2 inches tall. Each block used disposable brass pieces—which can be seen in Figures A.4b and A.5 to enclose the charge. The brass piece is held in place by a brass tube inside the block—Figure A.5b left—and a washer and aluminum tape on the bottom of the block. A new brass piece was used for each test. Manufacturing diagrams of the brass pieces and top plates are in Appendix B.3. The brass tube—7/16 inch ID x 0.014 inch thick—was cut to length for each brass piece.

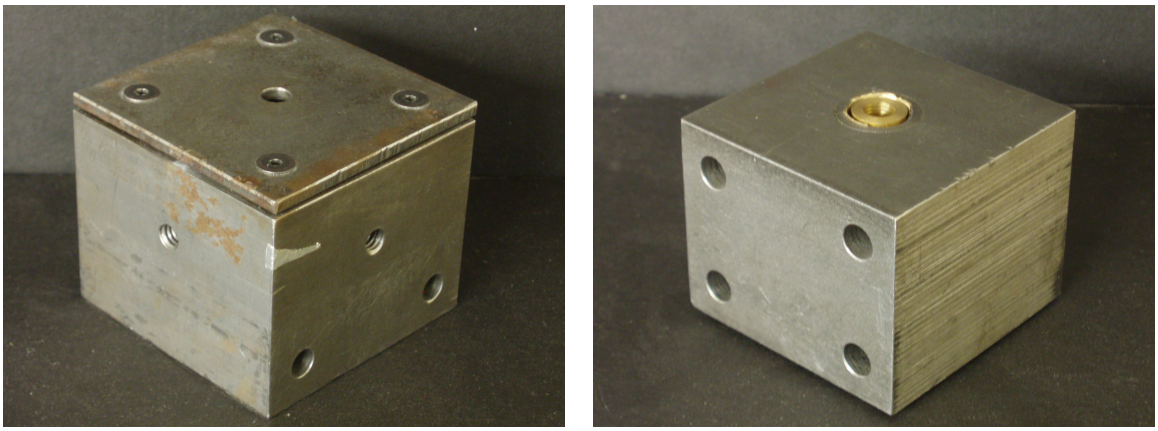

(a) First block (b) Second block

Figure A.4: Mount blocks used to hold charge in blast chamber tests. (a) block used for the weakly confined fireball and Al_2O_3-, Al- and Al+grease-loaded tests. (b) block used for weakly confined fireball environment and air gap tests.

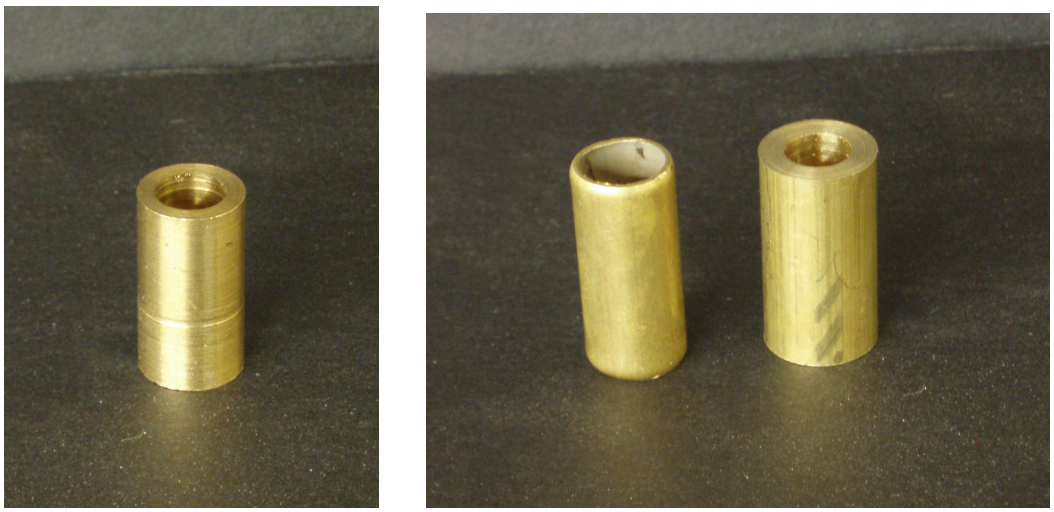

(a) First block (b) Second block

Figure A.5: Disposable mount brass used to hold charge in the block for the blast chamber tests. (a) brass piece used for the weakly confined fireball and Al_2O_3-, Al- and Al+grease-loaded tests. (b) brass piece (right) and brass tube support (left) used for weakly confined fireball environment and air gap tests.

From the blast chamber tests, the optics for the spectrometer—from the fiber to slit—are shown in Figure A.6, and the entrance fiber optic is shown in Figure A.7.

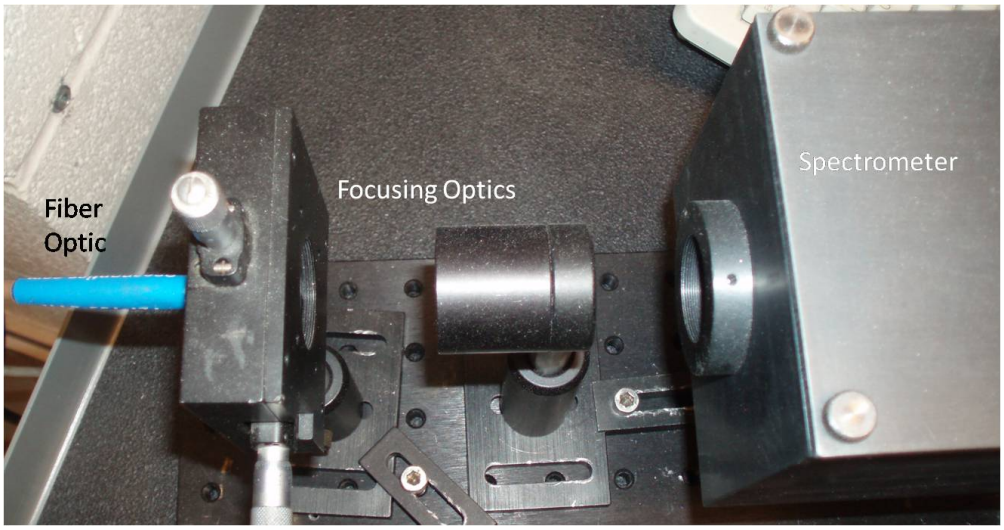

Figure A.6: Focusing optics from fiber optic to spectrometer slit.

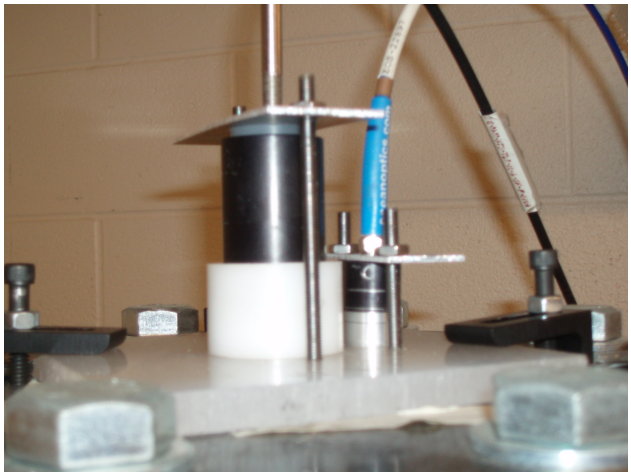

Figure A.7: Fiber optic at tank top for the pyrometer (left) and spectrometer (right).

The first version of the pyrometer, shown schematically in Figure A.8a, was built using a notch filter to split the light through the two interference filters to the photodiodes, and was mounted to the top of the blast chamber as shown in Figure A.8b. The hard mounting on the chamber resulted in gradual misalinement of the optics as a result of jarring during tests. To address this problem, the pyrometer was moved and connected remotely using a fiber optic as described in section 4.2.2. The inlet fiber is shown above in Figure A.7 and the newer pyrometer setup is shown in Figure A.9.

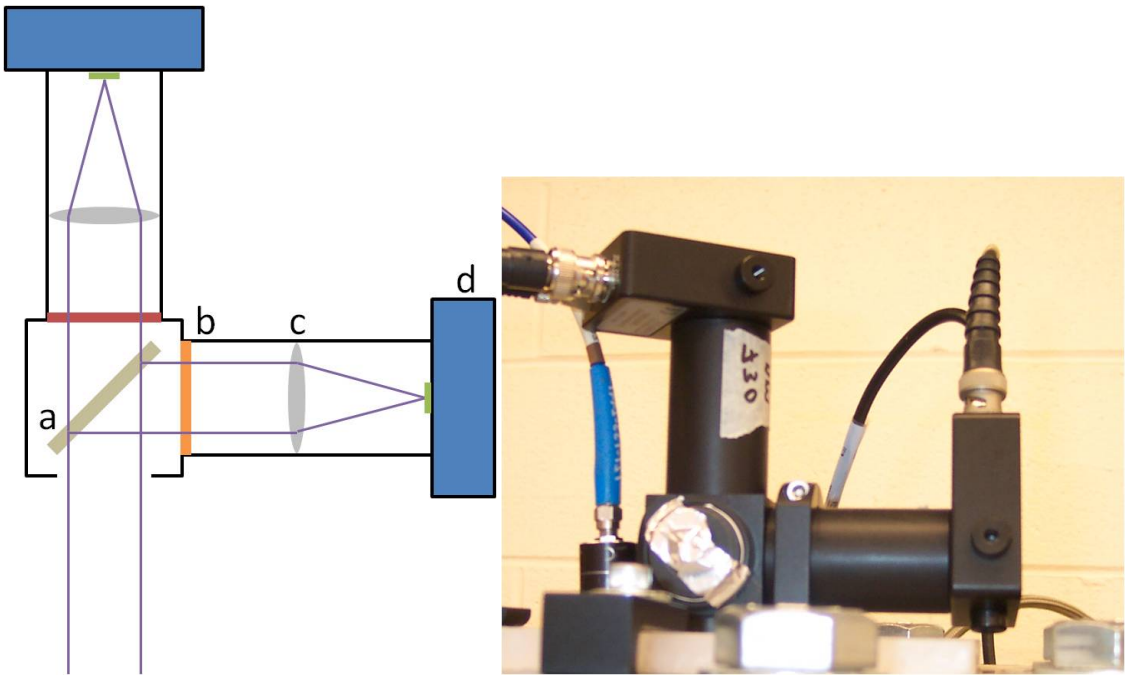

(a) Schematic (b) Picture

Figure A.8: Schematic[73] and picture of old pyrometer setup: a. 800 nm shortpass filter, b. notch filter (730 nm, 940 nm), c. f=24 mm lens, d. photodiode.

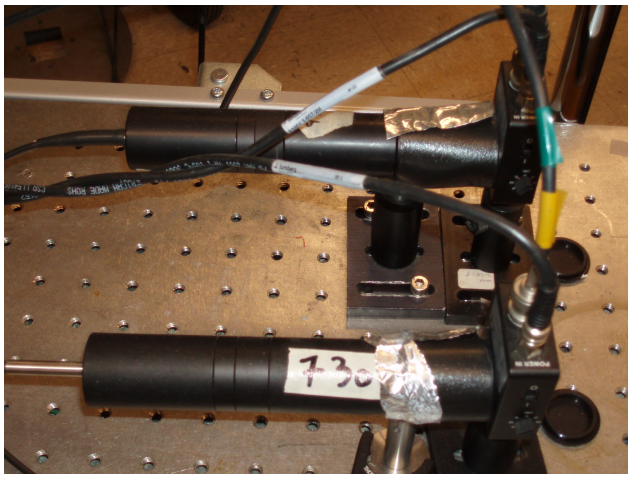

Figure A.9: Optics for newer version of the pyrometer.

The mounted piezoresistive pressure transducers are shown in Figure A.10. Manufacturing drawings for the mounts and knife-edge plates can be found in Appendix B.3.

(a) (b)

Figure A.10: Front (a) and side (b) views of mounted piezoresistive pressure transducers.

APPENDIX B

EXPERIMENTAL EQUIPMENT

B.1 Equipment Technical Data

Tables B.1 through B.5 list techinical data for the equipment used in the experiments.

Table B.1: Spectrometer.

Item & Model Number	Characteristics
Fast Kinetics Andor DV420 UV-FK	0–65535 Counts, 16 bit signal resolution
Ocean Optics P600-10-UV/VIS	Fiber Optic Cable
Nikon Series E	100 mm F/2.8 collimating lens
Volume Holographic grating	1800 grooves
Mintolta MC-Rokkor-PG	F/1.4 focusing lens

Table B.2: Shadowgraph and High Speed Camera.

Item & Model Number	Characteristics
Vision Reseach Phantom 5.2	
Tamron M12MV412	9-12 mm C mount lens
3M 7610	High gain reflective tape
50/50 Beam Splitter	
Vivitar 352 Flash	3.8 mm pinhole

Table B.3: Pyrometer.

Item & Model Number	Characteristics
Edmund Optics NT47-896	800 nm short pass filter
Edmund Optics NT62-178	730 ±2 nm bandpass filter
Edmund Optics NT62-187	940 ±2 nm bandpass filter
Anchor Optics AX27248	f=25 mm lens
Thor Labs AC254-050-B	NIR Achromatic f=50 mm lens
Thor Labs PDA 100	photodiode
Picoscope 3424	12 bit resolution digital oscilloscope

Table B.4: Pressure Transducers.

Item	Model Number & Characteristics
Peizoelectric	Kistler 603B1 100 psi range, ABS
Amplifier	Kistler 5004
Peisoresistive	Endevco 8530C 50 psi range, ABS
Amplifier	Endevco 136

Table B.5: Other Equipment.

Item	Characteristics
Firing Control System	Teledyne RISI FS-43
Pulse Generator	Stanford Research System DG 535
Shims	Plain steel, 1 3/8″ OD, 7/8” ID
	1008/1010 Carbon Steel
Silicon Grease	Dow Corning high vacuum grease
Mylar sheets 2.5 μm thick	Chemplex Industries 106 Thin Film Mount Support
	2.5” Dia (6.4 cm)
High Speed Camera	Phantom 5.2

B.2 Pressure Ratio Analysis

An ideal blast wave pressure scales as $1/r^3$,[76] and some difference between the ratios is expected for the experimental data. The pressure ratios are plotted in Figures B.1 to B.3. Also plotted are lines denoting the $(r_2/r_1)^3$ ratio, the average pressure ratio for all the tests, and 10 percent and 25 percent lower than the radius ratio.

In Figure B.1, the ratio for each experiment test is plotted as a function of the test date. The average pressure ratio of the experimental data is 25 percetn lower than the ideal radius ratio. The tests were completed over a three month time interval, and as the plot shows, there is no clear relationship between the tests as a function of time or the type of experiment test.

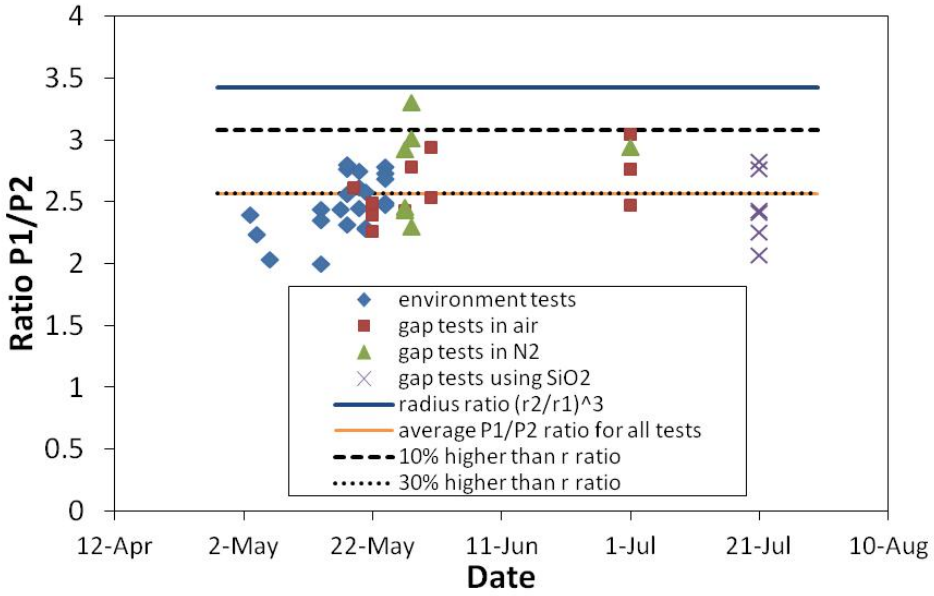

Figure B.1: Pressure ratio for all experiments as a function of day of test.

The pressure ratios from some of the environment experiment tests are shown in Figure B.2 as a function of the ambient environment and Al particle size (or none as in the case of the bare and Al_2O_3-loaded charges). For the Al-loaded charges the pressure ratio varies more than for the bare charges. No clear relationship between atmosphere and the pressure ratio exists. Most of the other tests have pressure ratios around 25 percent lower than the radius ratio.

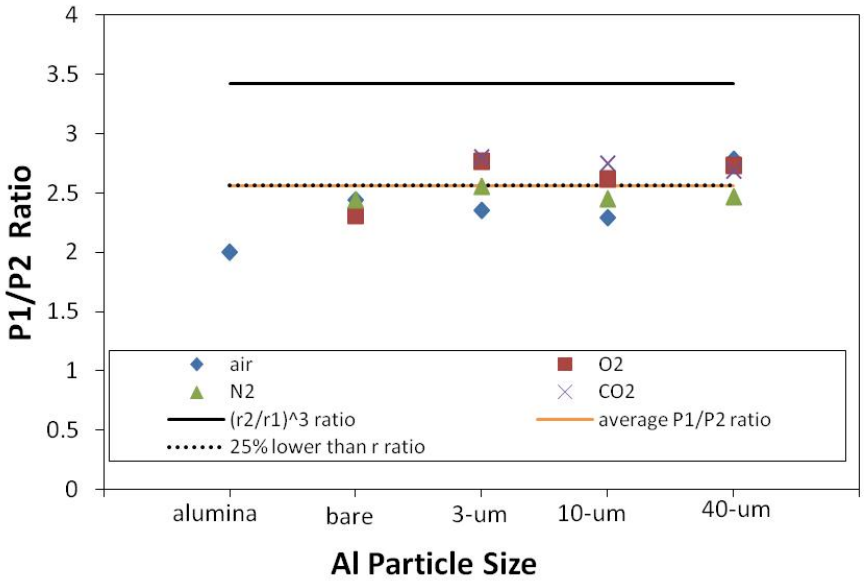

Figure B.2: Pressure ratio for environment experiments as a function of ambient atmosphere and Al particle size.

The pressure ratios from the gap experiment as a function of the gap distance, pellet type and atmosphere are shown in Figure B.3. As seen in Figure B.1, no clear relationship exists between the pressure ratios and the type of experiment. The gap tests do have more variability than the environment tests and most are within 25 percent of the radius ratio.

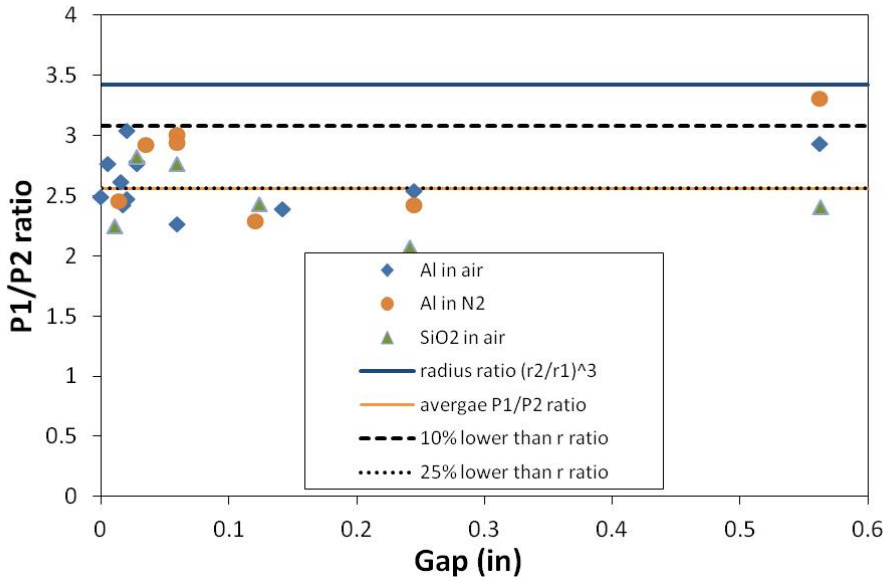

Figure B.3: Pressure ratio for gap experiments a function of the gap distance between the charge and the pellet.

The pressure transducers used in these experiments are Endevco piezoresistive pressure transducers, which measure the absolute pressure. For piezoresistive devices, mechanical stress causes a change in resistance, which is then measured. These particular pressure transducers have a strain gage bridge diffused into a silicon diaphragm. The pressure transducers were calibrated using static pressure.

B.3 Technical Drawings

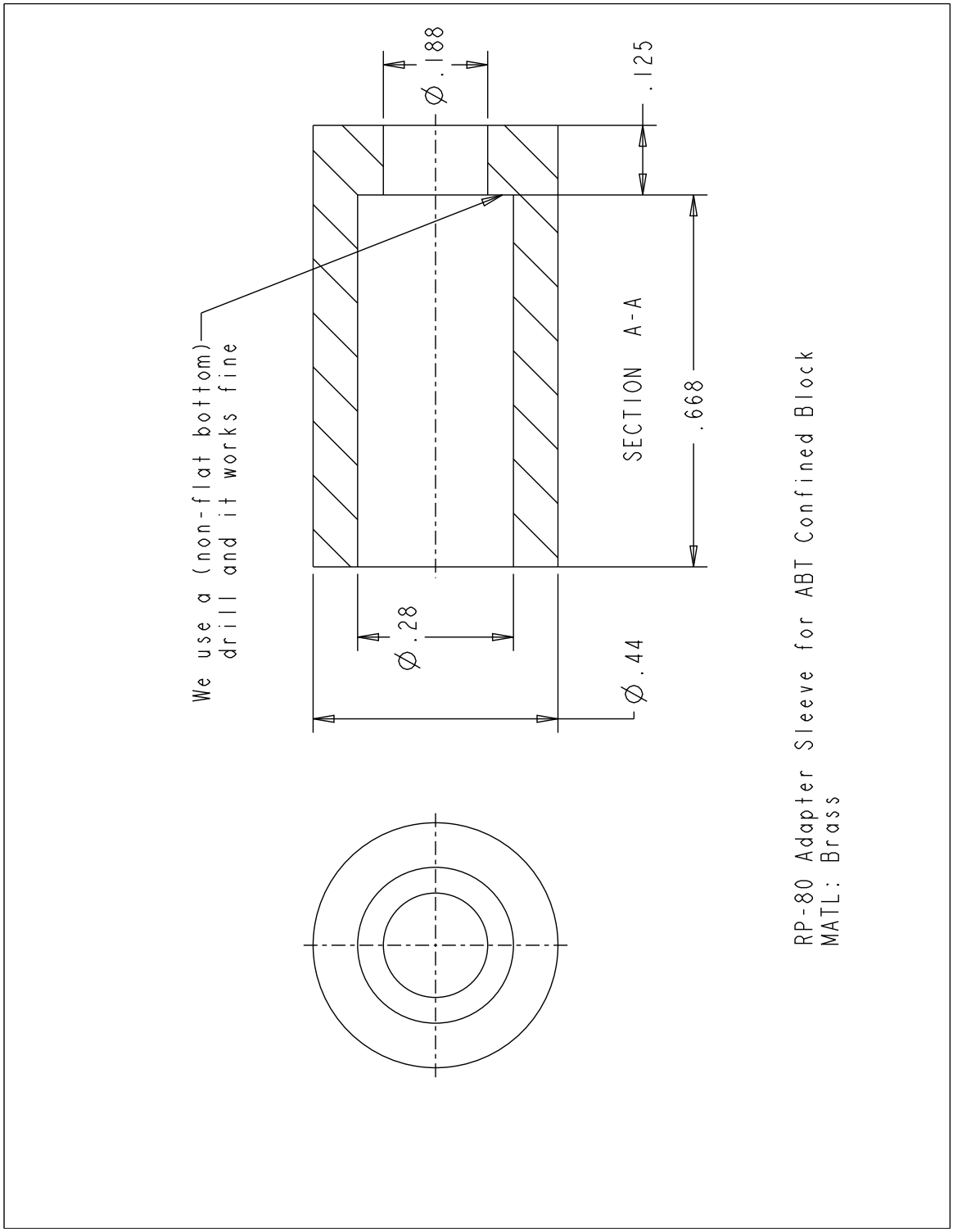

Figure B.4: Brass piece used to hold charge in block. Dimensions are for first block and top plate. Modifications for the second block are the diameter at 0.5 inch and the internal counter sink is 0.817 inch long instead of 0.668 for full enclosure of the charge. The overall length of the piece does not need to be exact. Units are in inch. Adapted from Drew Coverdill.

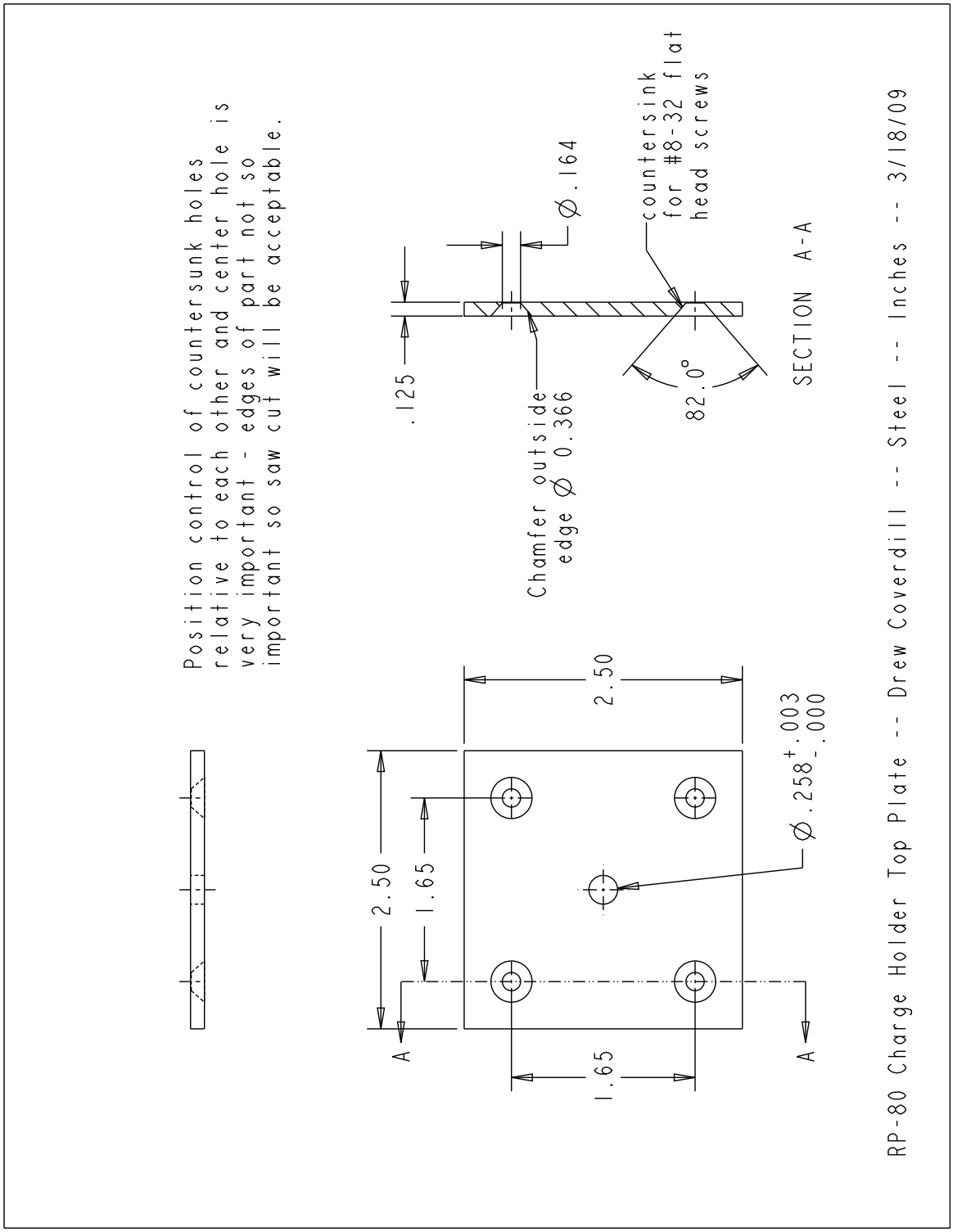

Figure B.5: Top plate used with the first block for mounting in the blast chamber. Units are in inch. Adapted from Drew Coverdill.

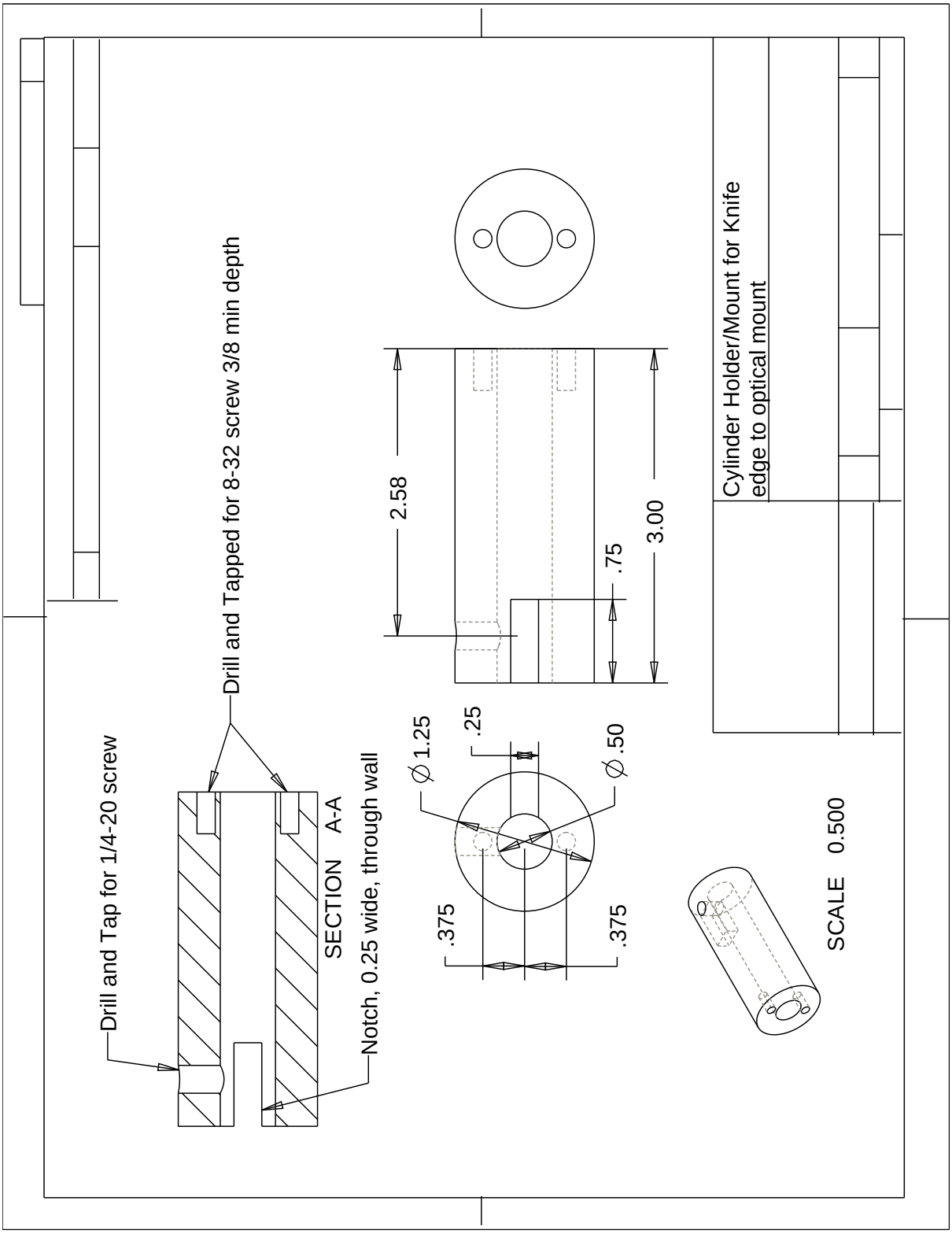

Figure B.6: Cylindrical mount for knife edge and piezo-resistive pressure transducer. Units are in inch.

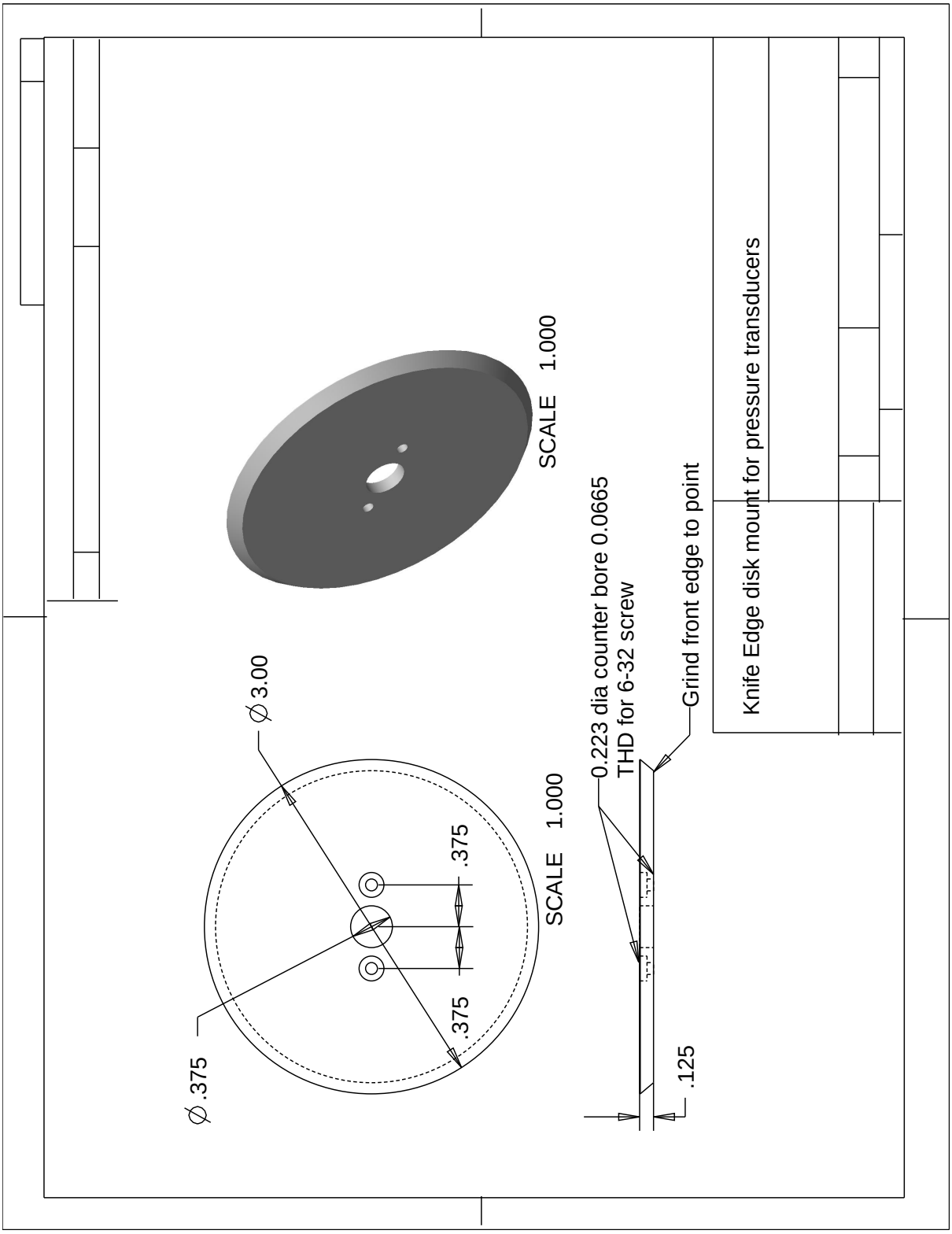

Figure B.7: Knife edge flat plate for piezo-resistive pressure transducer mount. Units are in inch.

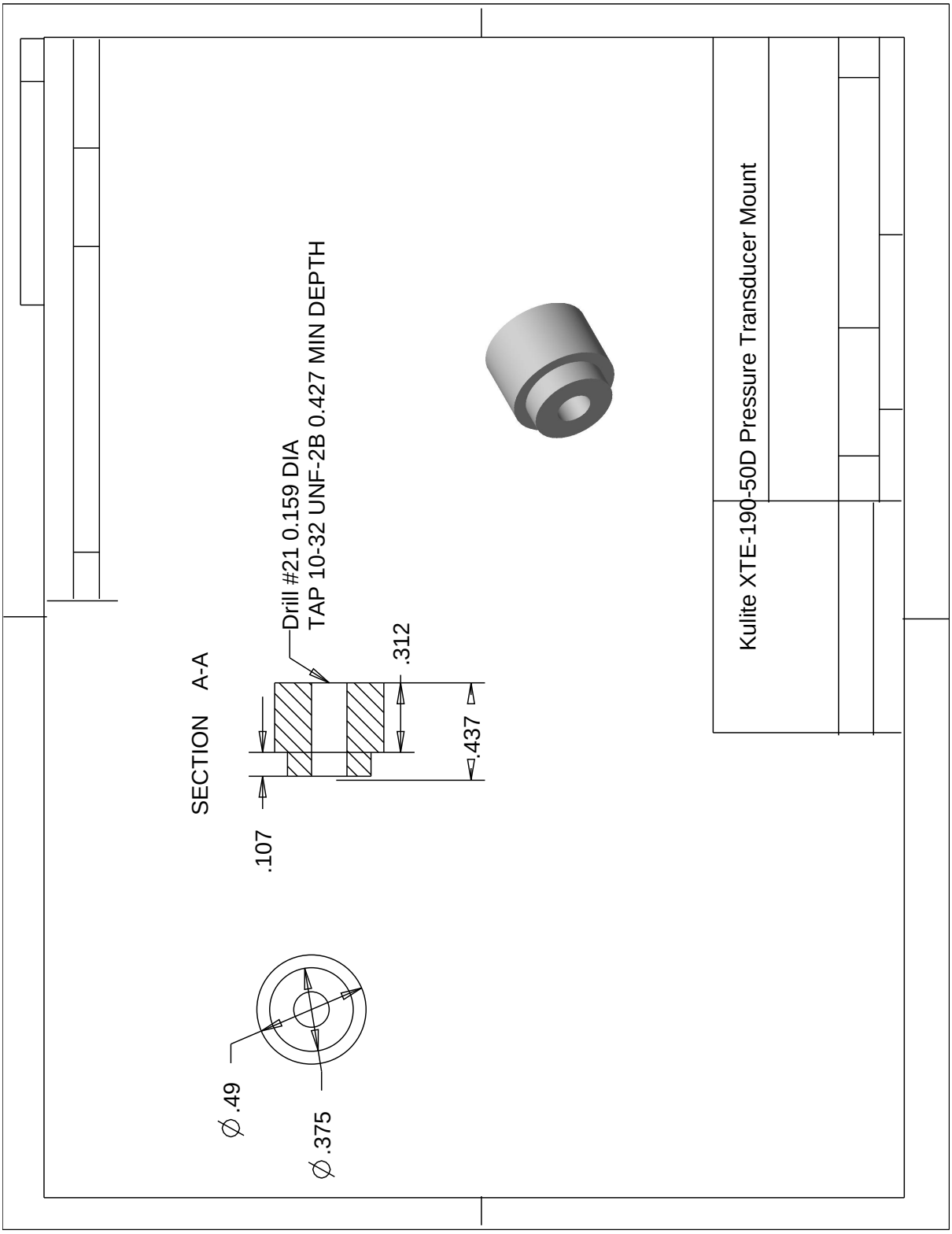

Figure B.8: Plastic mount for piezo-resistive pressure transducer. Units are in inch.

APPENDIX C

CALCULATIONS METHODOLOGY AND DETAILS

C.1 Effect of Temperature on AlO B State Population

The AlO B state population ratio as a result of two different temperatures—3000 K and 4000 K—was determined using the following equations and methodology. All equations, state energy levels, and other constants for the molecule AlO are from Laurendeau[93].

The number density, n_j, of a molecule at a particular internal energy level can be found using:

$$\frac{n_j}{n} = \frac{g_j}{Z} exp\left(-\frac{\epsilon_j}{kT}\right) \tag{C.1}$$

where n is the total number density, g_j is the degeneracy, and ϵ_j is the energy, each of level j; Z is the total molecular partition function and is dependent on temperature; T is the temperature, and k is the Boltzmann constant equal to $1.397 \times 10^{-23}\ J/K$. The population ratio n_1/n_2 for the same energy level of ϵ, but at different temperatures, can be determined by:

$$\frac{n_1}{n_2} = \frac{Z_2}{Z_1} exp\left(\frac{\epsilon(T_1 - T_2)}{kT_1T_2}\right) \tag{C.2}$$

where the subscripts denote values at the two temperatures T_1 and T_2.

In equation C.2, the total molecular partition function, Z, at each temperature is found by multiplying the partition functions from the translational, rotational, vibrational, and electronic modes: $Z_{tot} = Z_{tr}Z_{rot}Z_{vib}Z_{el}$. The translational mode partition function is

$$Z_{tr} = \left(\frac{2\pi mkT}{h^2}\right)^{(3/2)} V \tag{C.3}$$

where h is Planck's constant, V is the volume and m is the total mass of the nuclei of AlO. Only the ratio of $Z_{tr,2}/Z_{tr,1}$ is needed for the population ratio calculation, and therefore the ratio of the two translational mode partition function reduces to

$$\frac{Z_{tr,2}}{Z_{tr,1}} = \left(\frac{T_2}{T_1}\right)^{(3/2)} \tag{C.4}$$

for the two temperatures. Since $T/\theta_r < 30$ for both temperatures—3000 K and 4000 K—the rotational mode partition function is

$$Z_{rot} = \frac{T}{\sigma\theta_r} \tag{C.5}$$

In equation C.5, θ_r is the rotational temperature and is equal to $\frac{hc}{k}B_e$, where c is the speed of light and B_e is the rotational constant for the AlO $X^2\Sigma^+$ state. The symmetry factor, σ, is equal to 2, which is the case for heteronuclear diatomic molecules. The vibrational mode partition function is

$$Z_{vib} = \frac{1}{1 - exp\,(-\theta_v/T)} \tag{C.6}$$

where θv is the vibrational temperature equal to $\frac{hc}{k}w_e$ in which w_e is the vibrational frequency for the AlO $X^2\Sigma^+$ state. The electronic mode partition function is

$$Z_{el} = \sum g_j exp(-\epsilon/kT) \tag{C.7}$$

and becomes

$$Z_{el} = g_1 exp(-\epsilon_1/kT) + g_2 exp(-\epsilon_2/kT) + g_3 exp(-\epsilon_3/kT) \tag{C.8}$$

for the three electronic states of AlO. In determining the total partition function for AlO at each temperature, the energies, $\epsilon_1,\ \epsilon_2$ and ϵ_3 were based on the T_e tabulations in Table K.2 of [93]. The vibrational frequency, w_e, and rotational constant, B_e, values were also found

in Table K.2 of [93]. The degeneracies were determined using $\phi(2S+1)$.

The resulting population ratio was calculated to be 9.6, where T_1 is 4000 K and T_2 is 3000 K, as stated in Section 5.4.

C.2 Taylor Similarity Solution to Blast Equations

The ideal pressure curves shown in Chapter 6 were determined using the Taylor similarity solution to the blast equations from Baker[76]. The assumptions for the equations are

- Spherically symmetric blast wave
- Strong shock such that $P_1 \gg P_o$, where P_o is the ambient pressure in front of the shock
- An instantaneous energy release of amount E, which remains nearly constant for some period of time
- Ambient environment is air at STP, and $\gamma = 1.4$

The similarity solution gives the pressure P_{max}—the maximum pressure in Pa—at the shock front:

$$P_{max} = P_1 = 0.155 R^{-3} E \tag{C.9}$$

and at time, t:

$$R = \left(\frac{5}{2} A t\right)^{2/5}, \quad \text{where} \quad A = \frac{E^{1/2}\rho_o^{-1/2}}{\sqrt{5.36}} \tag{C.10}$$

where R is the radius of the shock wave in meter, E is the instantaneous energy that is released in Joule, and ρ_o is the density of the ambient air in kg/m^3. Using equation C.9, and the data from the bare charge test—a peak pressure of 204,715 Pa absolute at $R = 0.2134$ m (8.4 in)—the ideal energy output was calculated. Equations C.9–C.10 were combined into equation C.11 to determine the pressure versus time plot. The plot is the pressure curve at one radius location.

$$P = C E^{2/5} \rho_o t^{-6/5}, \quad \text{where} \quad C = \frac{0.155}{\left(\frac{2.5^{0.4}}{5.36^{0.2}}\right)^3} = 0.141 \tag{C.11}$$

The impulse in Pa-s was determined by integrating equation C.11 from the time of arrival, t_a, to the time when the pressure decayed to 1 atm, t_{atm}.

$$I = \frac{C_1}{-0.2}\left(t_{atm}^{-0.2} - t_a^{-0.2}\right) \quad \text{where} \quad C_1 = CE^{2/5}\rho_o \tag{C.12}$$

where

$$t_a = 0.926R^{(3/2)}\rho_o^{1/2}E^{-1/2} \tag{C.13}$$

and t_{atm} was found using equation C.11 for the known pressure.

The Chapman-Jouguet (CJ) detontation pressure for pure RDX and PETN vary between 100 and 300 kbar (10,000–30,000 MPa) depending on the initial density,[94] which is on the same order as the ideal shock wave pressure at a radius of less than 1 cm from the blast location.

C.3 Explosive Energy Calculations

Separately, the energy of explosion of each case—bare, inert Al, 20% Al, and 50% Al—was determined using the methodology and equations from Kinney and Graham[87]. For the inert Al case, it was assumed that the amount of explosive was 20 percent less than for the bare case. For the two aluminum cases—20 percent and 50 percent—all of the aluminum was assumed to fully oxidize.

$$\text{Energy of explosion} = \int_1^2 PdV \simeq -\Delta A \simeq -\Delta E + T\Delta S \tag{C.14}$$

Where ΔE is the Heat of Explosion found using the explosive chemical equation and decomposition:

$$\Delta E = \sum (nE_f^o)_{products} - \sum (nE_f^o)_{reactants} \tag{C.15}$$

And ΔS is the entropy of explosion, and is the difference $S_{products}$–$S_{reactants}$, where

$$S_{products} = \sum(nS^o) \tag{C.16}$$

$$S_{reactants} = \sum(nS^o) + S_{mix} \tag{C.17}$$

The entropy of mixing, S_{mix}, was estimated using $S_{mix} = 9\Delta n$, where Δn is the increase in the number of product gas moles[87].

Using the relative amounts of explosive energy, the value of E calculated using equation C.9 was modified to determine the maximum pressure and pressure vs. time and impulse for the three other charge mixtures using equations C.11–C.12.

The curves for the plot of pressure vs. time and the radius vs. time were determined using equations C.11 and C.13 for a constant energy E—which was initial found at $R = 0.2134$ m—and varying the radius R to determine the pressure and time of arrival as a function of radial distance.

C.4 Comparison of Energy Calculations

Listed in Table C.1 are the equations to determine the explosive heat or energy, and available tabulated values, which are compared to the calculated values of the pure RDX and PETN substances using the method of each reference. As the table shows, there are variations for the tabulated explosive heat or energy. The values of the RDX/PETN mixture—as in the bare charge case—were in between the pure values of RDX and PETN as expected.

Table C.1: Comparison of methods to calculate explosive energy and tabulated values for pure RDX and PETN.

Ref.	Value	Equation	Value Listed	Computed Value	Notes
[1]	Heat of Detonation	$Q_v \simeq Q_p = \sum \Delta H^o_{f(reactants)}$	RDX: 5036 kJ/kg	RDX: 5040 kJ/kg	Treats
		$-\sum \Delta H^o_{f(products)}$	PETN: 5794 kJ/kg	PETN: 5791 kJ/kg	$\Delta H \sim \Delta E$
[87]	Heat of Explosion	$\Delta E = \sum (nE^o_f)_{products}$	-	RDX: 5139 kJ/kg	No tabulated
		$-\sum (nE^o_f)_{reactants}$	-	PETN: 5860 kJ/kg	values
[87]	Energy of Explosion	$\int_1^2 PdV \simeq -\Delta A$	-	RDX: 7234 kJ/kg	No tabulated
		$\simeq -\Delta E + T\Delta S$	-	PETN: 7396 kJ/kg	values
[95]	Explosion Energy	$\Delta Q_v = \sum (nE^o_f)_{products}$	RDX: 5540 kJ/kg	RDX: 5139 kJ/kg	
		$-\sum (nE^o_f)_{reactants}$	PETN: 6120 kJ/kg	PETN: 5860 kJ/kg	

A comparison of the Taylor blast determined energy released E, and the available Energy of Explosion for the actual amount of explosive (PETN/PBX-9407) using the described method are compared in Table C.2. For the first method, the Taylor blast energy for the 20% aluminum case was determined from the relative amounts of the explosive energy values and the bare energy determined from pressure data. The calculated Energy of Explosion was used to determine the peak pressure for the second method. While the energy amounts between the two different methods differ significantly, the ratios between the peak ideal pressures of the bare and 20% Al charges are the same for each determination of energy and at each distance. The difference between the energies indicates that the assumptions of an ideal blast wave are invalid; however, comparisons between the peak pressures can still give some insight into when/how the energy of the explosive is used, e.g., to drive the blast wave or to increase the overpressure of the ambient environment.

Table C.2: Comparison of the Taylor blast solution using different energy calculations.

Distance from blast		Method 1 Taylor Blast Energy		Method 2 Energy of Explosion[87]	
		E (J)	P (Pa)	E (J)	P (Pa)
21.3 cm	Bare	12828	204716	1400	22342
	20% Al	15342	244840	1675	26731
32.1 cm	Bare	30752	143693	1400	6542
	20% Al	36779	171856	1675	7827
21.3 cm	P_{20A}/P_{bare}		1.196		1.196
32.1 cm	P_{20A}/P_{bare}		1.196		1.196

The time history of the pressure for the two different starting pressures are different owing to the relationship between P, E, and t in equation C.11 above, in which the pressure is related to $E^{2/5}t^{-6/5}$.

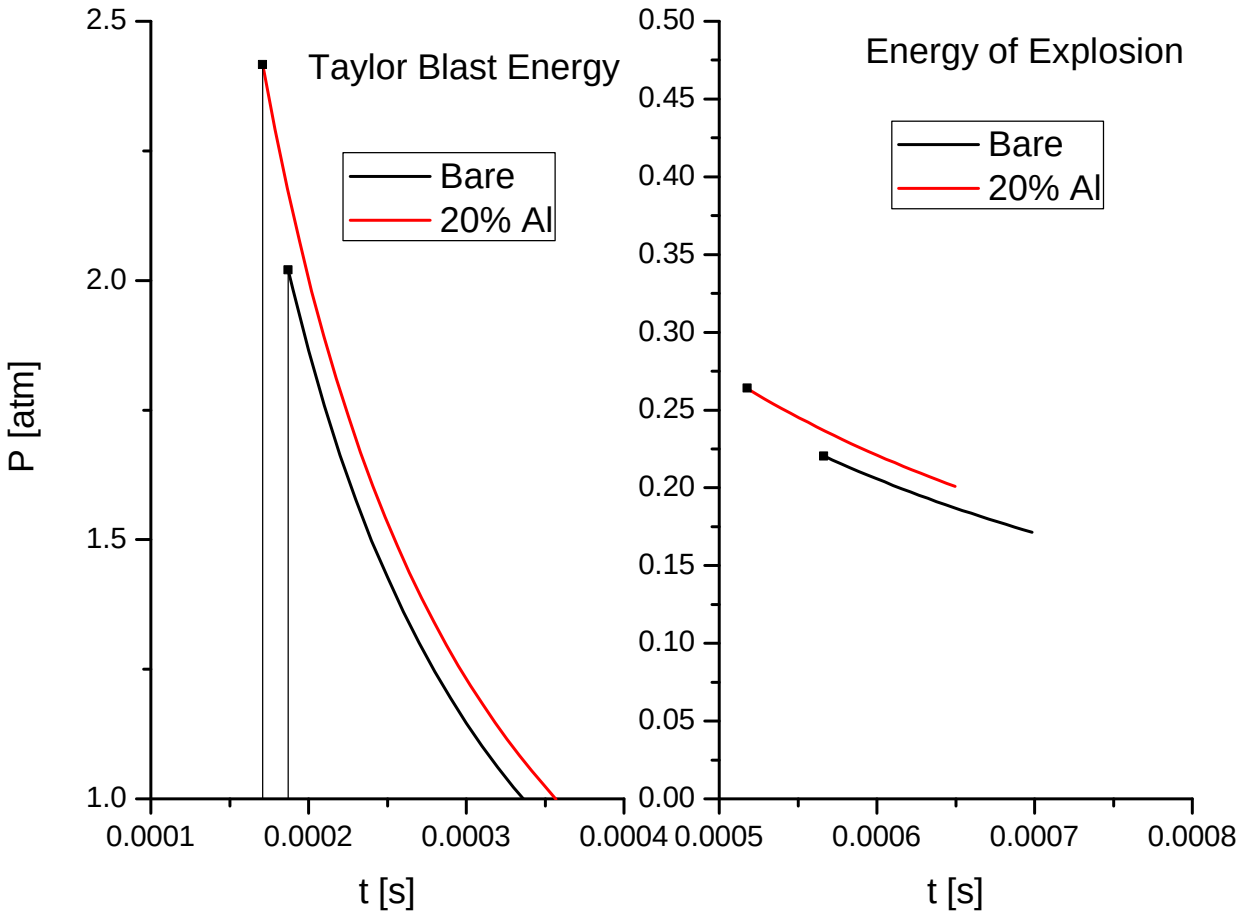

Figure C.1: Comparison of pressure traces for different energy determinations.

REFERENCES

[1] Jacqueline Akhavan. *The Chemistry of Explosives*. Royal Society of Chemistry Information Services, Cambridge England, 1998.

[2] Patrick Lynch, Herman Krier, and Nick Glumac. A correlation for burn time of aluminum particles in the transition regime. *Proceedings of the Combustion Institute*, 32(2):1887–1893, 2009.

[3] Joel R. Carney and J. M. Lightstone. Post-detonation combustion of aluminum particles: Aluminum particle size dependence. In *Proceedings of the 6th U.S. National Combustion Meeting*, May 18-20, 2009.

[4] Paul E. Anderson, Paula Cook, Wendy Balas, Andy Davis, and Kyle Mychajlonka. An overview of comined effects explosives formulations. Technical report, PEA ICT Paper 100506, 2009.

[5] Wendy Balas, Steve Nicolich, Paula Cook, Christos Capellos, Jack Pincay, and Leonard Stiel. Development, optimization, and application of combined effects explosives. In *2009 NDIA Insensitive Munitions Energetic Materials Technology Symposium*, May 12 2009.

[6] Terry R. Gibbs and Alphonse Popolato. *LASL Explosive Property Data*. University of California Press, Berkeley and Los Angeles, CA, 1 edition, 1980.

[7] T. D. Tran, C. M. Tarver, J. Maienschein, P. Lewis, M. Moss, R. S. Lee, and F. Roesk. Characterization of detonation wave propagation in lx-17 near the critical diameter. In *12th international Detonation Symposium*, August 11-26 2002.

[8] Mikhaylo A. Trunov, Mirko Schoenitz, and Edward L. Dreizin. Ignition of aluminum powders under different experimental conditions. *Propellants, Explosives, Pyrotechnics*, 30(1):36–43, 2005.

[9] W. A. Trzcinski, S. Cudzilo, Jozef Paszula, and James Callaway. Study of the effect of additive particle size on non-ideal explosive performance. *Propellants, Explosives, Pyrotechnics*, 33(3):227–235, 2008.

[10] S. D. Gilev and V. F. Anisichkin. Interaction of aluminum with detonation products. *Combustion Explosion and Shock Waves*, 42(1):107–115, 2006.

[11] P. Bucher, L. Ernst, F. L. Dryer, R. A. Yetter, T. P. Parr, and D. M. Hanson-Parr. *Detailed Studies on the Flame Structure of Aluminum Particle Combustion*, volume 185 of *Solid Propellant Chemistry, Combustion, and Motor Interior Ballistics*, pages 689–722. AIAA, Reston, VA, 2000.

[12] I. Glassman. *Combustion*. Academic Press, Orlando, FL, 1987.

[13] M. Beckstead. Correlating aluminum burning times. *Combustion, Explosion, & Shock Waves*, 41(5):533–546, 2005.

[14] J. C. Melcher, H. Krier, and R. L. Burton. Burning aluminum particles inside a laboratory-scale solid rocket motor. *Journal of Propulsion and Power*, 18(3):631–640, 2002.

[15] J. C. Melcher, R. L. Burton, and H. Krier. *Combustion of Aluminum Particles in Solid Rocket Motor Flows*, volume 185 of *Progress in Astronautics and Aeronautics*, pages 723–747. AIAA, Washington, DC, 2000.

[16] T. Bazyn, H. Krier, and N. Glumac. Oxidizer and pressure effects on the combustion of 10 μm aluminum particles. *Journal of Propulsion and Power*, 21(4):577–582, 2005.

[17] Patrick Lynch, Nick Glumac, and Herman Krier. Combustion of 5 μm aluminum particles in high temperature, high pressure, water vapor environment. In *43rd AIAA/ASME/SAE/ASEE Joint Propulsion Conference & Exhibit*. AIAA, July 8-11 2007.

[18] T. Bazyn, H. Krier, and N. Glumac. Evidence for the transition from the diffusion-limit in aluminum particle combustion. *Proceedings of the Combustion Institute*, 31:2021–2028, 2007.

[19] Patrick Lynch, Nick Glumac, and Herman Krier. Combustion of aluminum particles in the transition between the diffusion and kinetic limits. In *44th AiAA/ASME/SAE/ASEE joint Propulsion Conference & Exhibit*, July 21-23 2008.

[20] M. Beckstead, Y. Liang, and K. Pudduppakkam. Numerical simulation of single aluminum particle combustion (review). *Combustion, Explosion, & Shock Waves*, 41(6):622–638, 2005.

[21] P. Bucher, R. A. Yetter, F. L. Dryer, T. P. Parr, D. M. Hanson-Parr, and E. P. Viceni. Flames structure measurement of single, isolated aluminum particles burning in air. *Symposium (International) on Combustion*, 26(2):1899–1908, 1996.

[22] Fan Zhang and Keith Gerrard. Reaction mechanism of aluminum-particle-air detonation. *Journal of Propulsion and Power*, 25(4):845–858, 2009.

[23] Nancy L. Garland and H. H. Nelson. Temperature dependence of the kinetics of the reaction Al+O_2 $\rightarrow$ AlO+O. *Chemical Physics Letters*, 191(3-4):269–272, 4/3 1992.

[24] Arthur Fontijn and William Felder. HTFFR kinetics studies of Al+CO_2 → AlO+CO from 300 to 1900 K, a non-arrhenius reaction. *The Journal of chemical physics*, 67(4):1561–1569, August 1977.

[25] Roy E. McClean, H. H. Nelson, and Mark L. Campbell. Kinetics of the reaction Al($^2P^0$) + H_2O over an extended temperature range. *The Journal of physical chemistry*, 97(38):9673–9676, 09 1993.

[26] R. W. B. Pearse and A. G. Gaydon. *The Identification of Molecular Spectra*. Chapman and Hall, London, 1976.

[27] Jennifer Mott Peuker, Patrick Lynch, Herman Krier, and Nick Glumac. Optical depth measurements of fireballs from aluminized high explosives. *Optics and Lasers in Engineering*, 47(9):1009–1015, 9 2009.

[28] S. E. Olsen and M. W. Beckstead. Burn time measurements of single aluminum particles in steam and CO_2 mixtures. *Journal of Propulsion and Power*, 12(4):662–671, 1996.

[29] James Servaites, Herman Krier, J. C. Melcher, and R. L. Burton. Ignition and combustion of aluminum particles in shocked H_2O/O_2/Ar and CO_2/O_2/Ar mixtures. *Combustion and Flame*, 125(1-2):1040–1054, 2001.

[30] P. Bucher, R. A. Yetter, F. L. Dryer, T. P. Parr, and D. M. Hanson-Parr. PLIF species and ratiometric temperature measurements of aluminum particle combustion in O_2, CO_2 and N_2O oxidizers, and comparison with model calculations. *Symposium (International) on Combustion*, 27(2):2421–2429, 1998.

[31] Edward L. Dreizin. On the mechanism of asymmetric aluminum particle combustion. *Combustion and Flame*, 117(4):841–850, 1999.

[32] P. Bucher, R. A. Yetter, F. L. Dryer, T. P. Parr, and D. M. Hanson-Parr. Aluminum particle gas-phase flame structure. In *34th JANNAF Combustion Subcommittee Meeting, CPIA Pub 662*, volume II, pages 295–305, October 1997.

[33] P. Bucher, R. A. Yetter, F. L. Dryer, E. P. Viceni, T. P. Parr, and D. M. Hanson-Parr. Observations on aluminum particles burning in various oxidizers. In *33rd JANNAF Combustion Subcommittee Meeting CPIA Pub. 653*, volume II, pages 449–458, November 1996.

[34] P. Bucher, R. A. Yetter, F. L. Dryer, E. P. Vicenzi, T. P. Parr, and D. M. Hanson-Parr. Condensed-phase species distributions about al particles reacting in various oxidizers. *Combustion and Flame*, 117(1-2):351–361, 1999.

[35] T. Bazyn, H. Krier, and N. Glumac. Combustion of nanoaluminum at elevated pressure and temperature behind reflected shock waves. *Combustion and Flame*, 145(4):703–713, 2006.

[36] T. Bazyn, N. Glumac, H. Krier, T. S. Ward, M. Schoenitz, and E. L. Dreizin. Reflected shock ignition and combustion of aluminum and nanocomposite thermite powders. *Combustion Science and Technology*, 179(3):457–476, 2007.

[37] Ying Huang, Grant A. Risha, Vigor Yang, and Richard A. Yetter. Effect of particle size on combustion of aluminum particle dust in air. *Combustion and Flame*, 156(1):5–13, 2009.

[38] Lisa Orth and Herman Krier. Shock physics for nonideal detonations of metallized energetic explosives. *Symposium (International) on Combustion*, 27(2):2327–2333, 1998.

[39] Patrick Brousseau, Helen E. Dorsett, Matthew D. Cliff, and C. John Anderson. Detonation properties of explosives containing nanometric aluminum powders. In *12th international Detonation Symposium*, pages 11–21, August 11-26 2002.

[40] M. F. Gogulya, M. N. Makhov, A. Y. Dolgoborodov, M. A. Brazhnikov, V. I. Arkhipov, and V. G. Shchetinin. Mechanical sensitivity and detonation parameters of aluminized explosives. *Combustion, Explosion, and Shock Waves*, 40(4):445–457, 2004.

[41] W. A. Trzcinski, S. Cudzilo, and L. Szymanczyk. Studies of detonation characteristics of aluminum enriched RDX compositions. *Propellants Explosives Pyrotechnics*, 32(5):392–400, 2007.

[42] W. A. Trzcinski, S. Cudzilo, and Jozef Paszula. Studies of free field and confined explosions of aluminium enriched RDX compositions. *Propellants, Explosives, Pyrotechnics*, 32(6):502–508, 2007.

[43] A. M. Grishkin, L. V. Dubnov, V. Y. Davidov, Yu A. Levshina, and T. N. Mikhailova. Effect of powdered aluminum additives on the detonation parameters of high explosives. *Combustion, Explosion, and Shock Waves*, 29(2):239–241, 1993.

[44] Joel R. Carney, J. S. Miller, J. C. Gump, and G. I. Pangilinan. Atmospheric effects on the combustion of detonating aluminized explosives. *CP845 Shock Compression of Condensed Matter*, pages 948–951, 2005.

[45] Kim Chesterfield. Effect of detonation on the combustion of 20 micron aluminum particles embedded in high explosives. Master's thesis, Department of Mechanical Science and Engineering, University of Illinois, 2008.

[46] J. Scott Miller and G. I. Pangilinan. Measurements of aluminum combustion in energetic formulations. volume 706, pages 867–870. AIP, 2004.

[47] Joel R. Carney and John Wilkinson. Atmospheric effects on time-resolved emission measurements of detonation and combustion products. In *13th International Detonation Symposium*, Norvolk, VA, July 23-28 2006.

[48] Joel R. Carney, James M. Lightstone, Thomas P. McGrath II, and Richard J. Lee. Fuel-rich explosive energy release: Oxidizer concentration dependence. *Propellants, Explosives, Pyrotechnics*, 34(4):331–339, 2009.

[49] Richard H. Granholm, Harold W. Sandusky, Jeremy E. Monat, and Richard J. Lee. Small-scale internal blast measurements and predictions. In *14th International Detonation Symposium*, April 11-16 2010.

[50] David Frost, Samuel Goroshin, Robert Ripley, and Fan Zhang. Interaction of a blast wave with a metalized explosive fireball. In *14th International Detonation Symposium*, April 11-16 2010.

[51] K. Balakrishnan and S. Menon. On the role of ambient reactive particles in the mixing and afterburn behind explosive blast waves. *Combustion Science and Technology*, 182(2):186, 2010.

[52] G. Baudin, Fabien Petitpas, and Richard Saurel. Thermal non equilibrium modeling of the detonation waves in highly heterogeneous condensed phase he: a multiphase approach for metalized high explosives. In *14th International Detonation Symposium*, April 11-16 2010.

[53] Mary Brown, Mike Anderson, Charles Needham, and Craig Watry. The effects of metal loading on the detonation properties of explosive mixes. In *14th International Detonation Symposium*, April 11-16 2010.

[54] E. L. Baker, D. J. Murphy, P. Anderson, P. Cook, E. Wrobel, and Leonard I. Stiel. Eigenvalue detonation theory and analytic cylinder test model for a new generation of combined effects explosives. 27th Army Science Conference `http://www.armyscienceconference.com`, Nov 29 to Dec 2 2010. accessed April 25, 2011.

[55] E. L. Baker, W. Balas, C. Capellos, J. Pincay, and L. Stiel. Combined effects aluminized explosives. Technical report, 07 2010.

[56] C. Capellos, E. L. Baker, S. Nicolich, W. Balas, J. Pincay, and L. I. Stiel. Eigenvalue detonation of combined effects aluminized explosives. *AIP Conference Proceedings*, 955(1):357–60, 12/12 2007.

[57] Per-Anders Persson, Bertil Andersson, and Sven-Olof Stahl. A technique for detailed time-resovled radiation measurements in the reaction zone of condensed explosives. In *4th International Symposium on Detonation*, pages 602–608, Silver Spring, MD, October 12-15 1965.

[58] Kevin C., Glen P. Perram, and Ronald F. Tuttle. Modeling infrared spectral intensity data from bomb detonations. In *Targets and Backgrounds XI: Characterization and Representation*, volume 5811, pages 100–111. SPIE, 2005.

[59] Joel R. Carney, J. Scott Miller, Jared C. Gump, and G. I. Pangilinan. Time-resolved optical measurements of the post-detonation combustion of aluminized explosives. *Review of Scientific Instruments*, 77(6), 2006.

[60] V. Bouyer, G. Baudin, and C. Le Gallic. Temperature profile calculation from emission spectroscopy measurements in nitromethane submitted to plate impacts. In *12th International Detonation Symposium*, pages 743–751, San Diego, Ca, August 11-16 2002.

[61] Craig F. Bohren and Donald R. Huffman. *Absorption and Scattering of Light by Small Particles*. John Wiley and Sons, New York, 1983.

[62] James D. Ingle and Stanley R. Crouch. *Spectrochemical analysis*. Prentice Hall, Englewood Cliffs, N.J., 1988.

[63] Cook Corporation. HSFC Pro Intensified Camera. `http://www.cookecorp.com/fileadmin/user_upload/db/products/datasheet/hsfc_pro_TCC_20080714_web.pdf`. accessed November 5, 2008.

[64] ImageJ documentation. `http://rsb.info.nih.gov/ij/docs/index.html`.

[65] Teledyne RISI Inc. RP80 EBW Detonator. `http://www.teledynerisi.com/products/0products_1ebw_page23.asp`. accessed November 5, 2008.

[66] Mansoor A. Khan, Charly Allemand, and Thomas W. Eagar. Noncontact temperature measurement. I. interpolation based techniques. *Review of Scientific Instruments*, 62(2):392, 1991.

[67] Patrick Lynch, Herman Krier, and Nick Glumac. Emissivity of aluminum-oxide particle clouds: Application to pyrometry of explosive fireballs. *Journal of Thermophysics and Heat Transfer*, 24(2):301–308, April-June 2010.

[68] N. Glumac, H. Krier, T. Bazyn, and R. Eyer. Temperature measurements of aluminum particles burning in carbon dioxide. *Combustion Science and Technology*, 177(3):485–511, 2005.

[69] Thorlabs. *PDA100A Operating Manual—Switchable Gain, Amplified Silison Detector*, September 1, 2011.

[70] S. Rahman, E. Timofeev, and H. Kleine. Pressure measurements in laboratory-scale blast wave flow fields. *Review of Scientific Instruments*, 78(12):125106, 12 2007.

[71] Jim Mabon. phone conversation, March 2 2010.

[72] Jim Mabon. conversation, May 9 2011.

[73] A. R. Coverdill, N. Glumac, and H. Krier. Characterization of the energetic response of reactive materials to a detonation stimulus. In *2010 Spring Technical Meeting of the Central States Section of the Combustion Institute*, March 21-23 2010.

[74] Andrew Coverdill. Explosive initiation of tungsten based reactive materials in air. Master's thesis, Department of Mechanical Science and Engineering, University of Illinois, 2010.

[75] Dupont Teijin Films. *Health and safety aspects of 'Melinex' polyester films*. Imperical Chemical Industries Limited, July 1980.

[76] Wilfred E. Baker. *Explosions in Air*. University of Texas Press, Austin and London, 1973.

[77] Bonnie J. McBride and Sanford Gordon. *Computer Program for Calculation of Complex Chemical Equilibrium Compositions and Applications, II Users Manual and Program Description*, 1996.

[78] G. Schlöffel, A. Eichhon, H. Albers, Ch. Mundt, F. Seiler, and F. Zhang. The effect of a shock wave on the ignition behavior of aluminum particles in a shock tube. *Combustion and Flame*, 157(3):446–454, 3 2010.

[79] K. Roodenko, M. D. Halls, Y. Gogte, O. Seitz, J. F. Veyan, and Y. J. Chabal. Nature of Hydrophilic Aluminum Fluoride and Oxyaluminum Fluoride Surfaces Resulting from XeF(2) Treatment of Al and Al(2)O(3). *JOURNAL OF PHYSICAL CHEMISTRY C*, 115(43):21351–21357, NOV 3 2011.

[80] Nick Glumac and Herman Krier. Early time spectroscopic measurements during high explosive detonation breakout into air. In *JANNAF Sub-Committee Meeting*, April 18-22 2011.

[81] Kevin L. McNesby, Barrie E. Homan, John J. Ritter, Zachary Quine, Rachel Z. Ehlers, and Brendan A. McAndrew. Afterburn ignition delay and shock augmentation in fuel rich solid explosives. *Propellants, Explosives, Pyrotechnics*, 35(1):57–65, 2010.

[82] Thuvan Piehler, Avi Birk, Richard Benjamin, Vincent Boyle, Eugene Summers, and Stephen Aubert. Near-field impluse loading measuremetn techniques for evaluating explosive blast. Technical report, ARL-RP-235, 2009.

[83] D. H. Edwards, G. O. Thomas, A. Milne, G. Hooper, and D. Tasker. Blast wave measurements close to explosive charges. *Shock Waves*, 2:237–243, 1992. 10.1007/BF01414759.

[84] Gregory J. Hutchens. Approximate cylindrical blast theory: Near-field solutions. *Journal of Applied Physics*, 77(7):2912, 1995.

[85] J.D. Baum, E.L. Mestreau, H. Luo, R. Löhner, D. Pelessone, M.E. Giltrud, and J.K. Gran. Modeling of near-field blast wave evolution. In *Collection of Technical Papers - 44th AIAA Aerospace Sciences Meeting*, volume 4, pages 2310–2320, 2006.

[86] Manfred Held. Near field blast load. *Propellants, Explosives, Pyrotechnics*, 27(4):244–246, 2002.

[87] Gilbert F. Kinney and Kenneth F. Graham. *Explosive Shocks in Air*. Springer, Verlag, New York, 1985.

[88] Kevin C. Gross. *Phenomenological model for infrared emissions from high-explosive detonation fireballs*. PhD thesis, Department of Engineering Physics, Air Force Institute of Technology, 2007.

[89] J. M. Gordon. *Shock wave dynamics of novel aluminized detonations and empirical model for temperature evolution from post detonation combustion fireballs*. PhD thesis, Air Force Institute of Technology, 2011.

[90] M. Marion, C. Chauveau, and I. Gokalp. Studies on the ignition and burning of levitated aluminum particles. *Combustion Sci.Technol.*, 115(4):369–390, 1996.

[91] Patrick Lynch. *High Temperature Spectroscopic Measurments of Aluminum Combustion in a Heterogeneous Shock Tube*. PhD thesis, Department of Mechanical Science and Engineering, University of Illinois, 2010.

[92] Dow Corning. Dow Corning High Vacuum Grease MSDS. `http://www2.dowcorning.com/DataFiles/090007b2815a669d.pdf`. accessed April 6, 2011.

[93] Normand M. Laurendeau. *Statistical Thermodynamics*. Cambridge University Press, New York, NY, 2005.

[94] C. H. Johansson and Per-Anders Persson. *Detonics of High Explosives*. Academic Press, London, 1970.

[95] Per-Anders Persson, Roger Holmberg, and Jaimin Lee. *Rock Blasting and Explosives Engineering*. CRC Press, Boca Raton, FL, 1994.